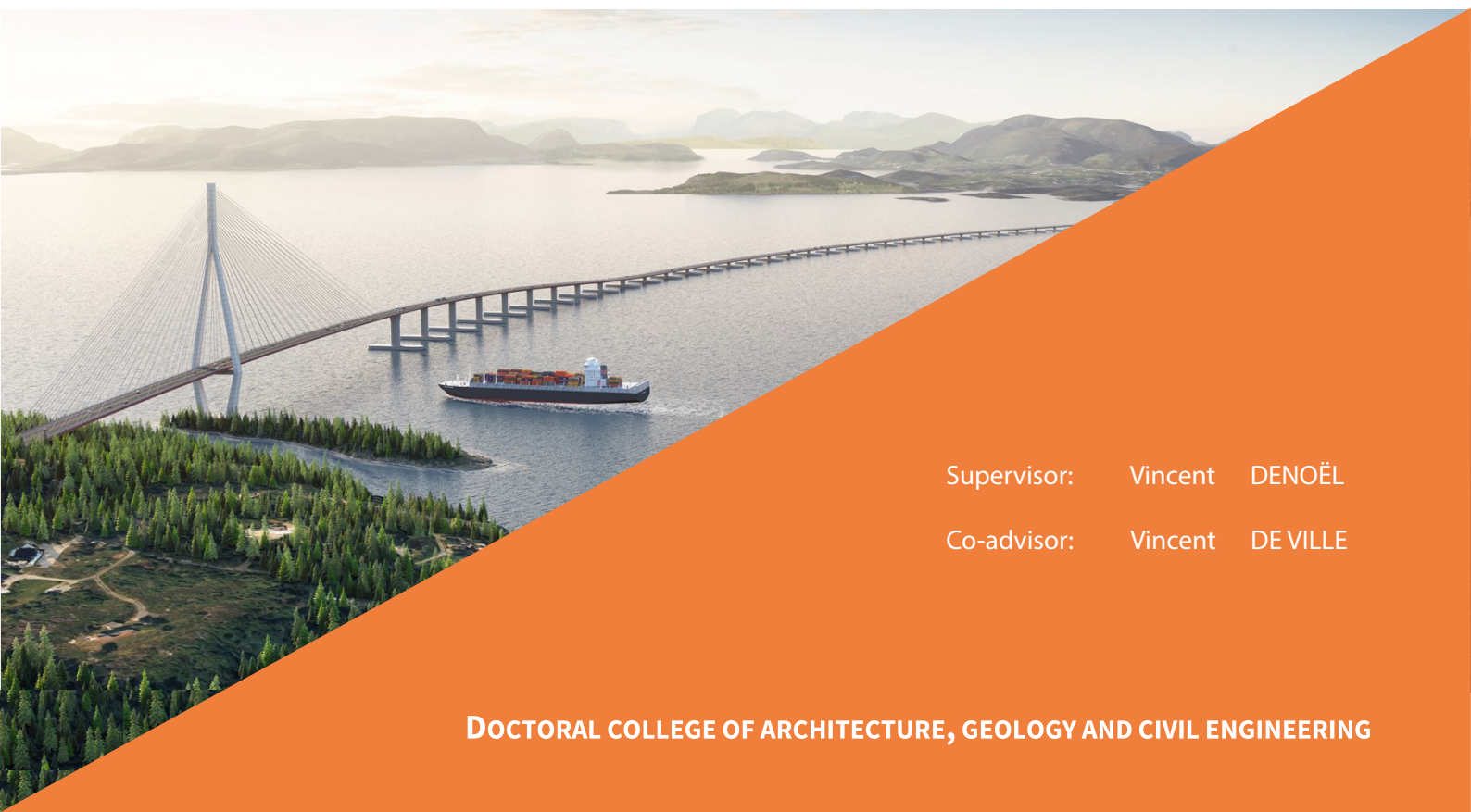


# Multiple Timescale Spectral Analysis of Wave-Loaded Floating Structures

A thesis submitted in partial fulfilment of the requirements for the  
degree of Doctor of Philosophy (Ph.D.) in Engineering Sciences

by

**Margaux Geuzaine**



Supervisor: Vincent DENOËL

Co-advisor: Vincent DE VILLE







# Multiple Timescale Spectral Analysis of Wave-Loaded Floating Structures

by

Margaux Geuzaine

A thesis submitted in partial fulfillment of the requirements for  
the degree of Doctor of Philosophy in Engineering Sciences

April 2022



### **Members of the Jury**

President Prof. Philippe RIGO  
University of Liège

Advisor Prof. Vincent DENOËL  
University of Liège

Co-Advisor Prof. Vincent DE VILLE  
University of Liège

Dr. Ir. Thomas ANDRIANNE  
University of Liège

Prof. Ole Andre ØISETH  
NTNU Trondheim

Prof. Federico PEROTTI  
Politecnico di Milano



*À mes bonnes étoiles,*



# Abstract

Today, floating structures are widely recognized as one of the main keys to unlock a number of problematic situations. This includes for instance floating wind turbines and solar panels which are envisioned to play a big role in the energy transition; floating platforms and facilities which offer an economically and environmentally sustainable solution to reclaim land from the water when the urban density, the space scarcity and the climate change are making it necessary; and also floating bridges and tunnels which enable the crossing of large and deep bodies of water.

But determining the statistics of their responses to the loading of the waves is intense, although it can typically be achieved in a more efficient way than in time domain already, by integrating the appropriate spectra. In this context, the computational burden is currently driven by the fact that heavy operations need to be repeated at all integration points, which are actually numerous. This is because the spectra usually exhibit sharp peaks as a result of the typical separation observed between the frequency bands where either the energy of the loading concentrates, either the resonance of the structure occurs.

This problem is thus addressed in the following with the help of the Multiple Timescale Spectral Analysis. This method hinges in fact on the perturbation theory to turn the existence of distinct peaks in the spectra into an advantage and to develop simple expressions for approximating their integrals with a small but controllable discrepancy. In particular, these semi-analytical formulas are intended to reduce the number of integration points and, above all, to find alternatives to bypass the most demanding operations. This approach can essentially be seen as a generalization of Davenport's background-resonant decomposition, which is very well known in wind engineering. It is by the way in this field that the Multiple Timescale Spectral Analysis has been applied until now, and more especially for the response of structures whose natural frequencies are all much higher than the characteristic frequency of the loading. But, when dealing with wave-loaded floating structures, the roles of the slow and the fast timescales are likely to be interchanged for a few of the lowest natural frequencies.

This is the main reason why the Multiple Timescale Spectral Analysis needs to be extended first, before the resulting formulas can be employed to solve the problem at hand. In this thesis, we therefore derive the expressions that are still missing to calculate the second and the third order statistics of a linear oscillator's response under a non-Gaussian loading, whose bispectrum is possibly complex-valued. At second order, the same is done for the crossed statistics of the multiple structural responses obtained when a modal state formulation of the governing equations is adopted. As a result, these equations of motion are perfectly decoupled even if the damping is not classical. It is the first time that such a feature is handled with the Multiple Timescale Spectral Analysis, the main difference being that the eigenfrequencies and the eigenmodes are consequently complex-valued as well. Overall, these expressions drastically reduce the number of integration points required as they decrease the order of integration by one at least, or else they depend on a few costly operations only, which do no longer have to be repeated at all integration points. In the sequel, they are validated, verified and eventually shown to degenerate to the formulas that have formerly been derived under more restrictive circumstances.

Besides these substantial additions to the state-of-the-art, three significant novelties are also reported in this thesis. First, a completely new technique is introduced to find the local approximations of the spectra for the resonant components. Second, a unified expression is developed and acts as a matching in the sense of the perturbation theory for the background and the inertial components. Third, two different strategies are proposed to decouple the equations of motion when fluid structure interactions are included, depending on whether the frequency sensitivity of the mass, the damping, and the stiffness matrices is negligible or not.





# Acknowledgements

C'était il y a quatre ans déjà que j'avais ma première entrevue avec Vincent Denoël, au sujet du doctorat. Moi qui avais toujours imaginé dimensionner des ponts dans un bureau d'études, j'envisageais alors de m'embarquer dans une toute autre voie, celle de la recherche. C'était il y a quatre ans déjà aussi, que Vincent De Ville De Goyet invitait Ketil Aas-Jakobsen à venir parler de ces ponts flottants incroyables qui allaient être construits en Norvège et qui mettaient des rêves un peu fou dans la tête de tellement d'ingénieurs en construction.

Par le plus beau des hasards, ou l'impulsion discrète d'une bonne étoile, ces deux évènements ont donné naissance à la thèse que vous vous apprêtez à lire et que je termine justement d'écrire à Trondheim, en Norvège (d'où je vais peut-être enfin pouvoir partir à la découverte de ces ponts flottants autrement qu'en numérique). C'est assez impressionnant de voir le chemin qui a été parcouru entre-temps ainsi que le nombre d'organismes ou de personnes qui ont de près ou de loin contribué à cet aboutissement et que j'aimerais commencer par remercier.

First of all, since all scientific research requires funding, I gratefully acknowledge the financial support of a four-year FRIA Fellowship granted by the F.R.S.-FNRS (the Belgian Fund for Scientific Research). Part of my thesis has also been conducted during a stay at the Norwegian University of Science and Technology in Trondheim, which was funded by a Research Stay Grant awarded by the Federation Wallonia-Brussels, a District Grant attributed by the Rotary Club of Seraing and a Scientific Mission Subsidy received from the University of Liège. In this regard, my special thanks are also going to Ole Øiseth and Aksel Fenerci, who welcomed me and accompanied me during these periods of time.

D'un point de vue plus personnel maintenant, mes remerciements vont d'abord à Vincent, mon superviseur certes, mais aussi mon ami. Parce qu'au delà de tout ce qu'il m'a appris en termes de connaissances techniques, scientifiques et académiques, de cette manière bien spéciale de réfléchir qui devient l'apanage de tout membre du SSD Crew, il y a évidemment eu tout le reste, toutes nos discussions, tous nos échanges et toutes nos aventures qui m'ont fait tellement grandir, humainement parlant. Alors merci !

Quant à la Team d'ailleurs, merci à vous tous d'avoir été là à chaque fois qu'il le fallait également, et même quand il ne le fallait pas forcément. Votre compagnie a été précieuse. François depuis le début, puis Anass, Julien, Michele et Kevin, mais aussi temporairement Francesco. J'ai passé des moments géniaux avec vous, et je retiendrai en particulier nos repas divers, à la pizzeria, pour Noël et chez Vincent, ainsi que nos découvertes sportives, le badminton tout récemment, le kayak un peu avant et l'escalade il y a plus longtemps.

J'aimerais aussi en profiter pour mentionner toutes ces personnes qui ont, en fait sans trop le savoir, participé à la conservation de mon équilibre psychologique. Vous n'imaginez pas comme ça a été important pour moi de pouvoir décompresser de temps en temps avec et grâce à vous. Je pense à Sara, qui a ancré un peu plus profondément en moi cet amour naissant pour l'escalade, puis à tous les chercheurs que je retrouvais le temps d'un repas à la cuisine, ou parfois à la grande cafet', ceux qui étaient là avant moi et ceux qui seront encore là après. Vous allez peut-être me prendre pour une folle mais ils se reconnaîtront, merci aussi aux Bananes, à l'Equipe, aux Ingénieuses, ainsi qu'au Variety Orchestra et au Manège Pégase.

Ensuite, pour leur soutien inconditionnel en toutes circonstances, je remercie mon Papa, ma Maman, Brieuc et Valérie, puis aussi Romane, pour nos conversations distrayantes et déstressantes lorsque nous covoiturions et que tu venais me rejoindre au bureau. J'adresse également des remerciements particuliers à mon Papy et ma Mamy, qui ont toujours cru en moi et en mes rêves, à la famille de Maxime et à Lutti, pour nos séances de puppy-therapy.

Pour finir bien sûr, merci infiniment à lui, mon fiancé Maxime, l'amour de ma vie, qui s'est révélé être un compagnon de route formidable, tout comme un soutien sans faille, et ce encore plus dans les moments difficiles que j'ai pu traverser.



# Contents

<b>Abstract</b>	<b>i</b>
<b>Acknowledgements</b>	<b>iii</b>
<b>Contents</b>	<b>v</b>
<b>INTRODUCTION</b>	<b>1</b>
<b>Problem Addressed in This Thesis</b>	<b>1</b>
<b>The Multiple Timescale Spectral Analysis</b>	<b>6</b>
<b>My Personal Contributions</b>	<b>10</b>
<b>Outline of the Thesis</b>	<b>11</b>
<b>List of Publications</b>	<b>12</b>
<b>I SDOF SYSTEMS</b>	<b>15</b>
<b>1 Contextualization</b>	<b>17</b>
1.1 Context and Propositions . . . . .	17
1.2 Governing Equations in Time Domain . . . . .	17
1.3 Dimensionless Formulation of the Equations . . . . .	19
1.4 Spectral Formulation of the Equations . . . . .	21
1.5 Need for MTSA Extension . . . . .	24
<b>2 Second Central Moment</b>	<b>27</b>
2.1 Introduction and Preliminary Considerations . . . . .	27
2.2 Formulation of the Necessary Assumptions . . . . .	27
2.3 Derivation of the Resonant Component . . . . .	29
2.4 Derivation of the Inertial Component . . . . .	30
2.5 Validation and Parametric Analysis . . . . .	33
<b>3 Third Central Moment</b>	<b>41</b>
3.1 Introduction and Preliminary Considerations . . . . .	41
3.2 Identification of the Main Components . . . . .	42
3.3 Formulation of the Necessary Assumptions . . . . .	47
3.4 Background Bi-Resonant Decomposition . . . . .	49
3.5 Bi-Resonant Inertial Decomposition . . . . .	50
3.6 Validation and Parametric Analysis . . . . .	52

<b>II</b>	<b>MDOF SYSTEMS</b>	<b>61</b>
<b>4</b>	<b>Contextualization</b>	<b>63</b>
4.1	Context and Propositions . . . . .	63
4.2	Governing Equations in Frequency Domain . . . . .	63
4.3	Modal State Formulation of the Equations . . . . .	65
4.4	Decoupling of the Equations - Scenario 1 . . . . .	68
4.5	Decoupling of the Equations - Scenario 2 . . . . .	70
4.6	Recombination of the Modal Responses . . . . .	75
4.7	Need for MTSA Extension . . . . .	76
<b>5</b>	<b>Covariances, Excluding Frequency-Dependency</b>	<b>79</b>
5.1	Introduction and Preliminary Considerations . . . . .	79
5.2	Formulation of the Necessary Assumptions . . . . .	80
5.3	Derivation of the Resonant Component . . . . .	82
5.4	Derivation of the Loading Component . . . . .	83
5.5	Verification with a Parametric Analysis . . . . .	86
<b>6</b>	<b>Covariances, Including Frequency-Dependency</b>	<b>95</b>
6.1	Introduction and Preliminary Considerations . . . . .	95
6.2	Formulation of the Necessary Assumptions . . . . .	96
6.3	Derivation of the Resonant Component . . . . .	97
6.4	Derivation of the Loading Component . . . . .	98
6.5	Specialization to Former Approximations . . . . .	101
<b>7</b>	<b>Applications</b>	<b>105</b>
7.1	Bergsøysund Bridge . . . . .	105
7.2	Bjørnafjorden Bridge . . . . .	124
	<b>CONCLUSION</b>	<b>129</b>
	<b>APPENDICES</b>	<b>135</b>
	<b>Appendix A</b>	<b>137</b>
	<b>Nomenclature</b>	<b>145</b>
	<b>Bibliography</b>	<b>155</b>

---

NOTE – In this thesis, the power spectral densities are two-sided and need to be integrated from  $-\infty$  to  $+\infty$  on the circular frequencies,  $\omega$ , to provide the variances of the processes they are associated to. The same convention applies to higher order spectra. In addition: lowercase and capital bold letters are respectively used for denoting vectors and matrices while italic letters are employed for their elements; the superscripts  $(\cdot)^*$ ,  $(\cdot)^\top$  and  $(\cdot)^\dagger$  stand for the conjugate, the transpose and the conjugate transpose (hermitian) operators; overhead tildes and hats indicate approximations and residual functions.





# INTRODUCTION

## Problem Addressed in This Thesis

In the past several decades, the design of very large floating structures has attracted considerable attention because they offer affordable solutions to respond to many of our needs and problems [1, 2]. Several major and strategical ongoing projects aiming at the crossing of wide and deep fjords or straits, such as the \$20-billion E39 coastal highway project in Norway [3] or the various versions of the Messina Straits crossing [4], are even not feasible at all unless floating bridges or tunnels technologies are used [5, 6]. Floating facilities also provide extensions for coastal areas where land reclamations are not economically nor environmentally reasonable while floating solar platforms and energy hubs are expected to strongly support the energy transition [7].

In general, floating structures are subjected to the action of wind and wave loads. Although they are stochastic by nature and specified in the frequency domain by their power spectral densities, see Figure 3, as well as frequency-dependent mass, damping, and stiffness matrices, this problem is also specific by the various nonlinearities associated with the loading processes and with the structural behavior. As long as they are limited in magnitude, the dynamic analysis of such floating structures can be conducted in both the time domain and the frequency domain, but the latter option is known to be much more efficient [8, 9].

Interestingly enough, in the frequency domain, the so-called spectral approach makes it quite clear that several timescales coexist in the response of a slender bridge deck to wind forces, and similarly for a slender floating body to wave excitations. This is for instance illustrated for one of the floating bridge concepts proposed to complete the crossing of the Bjørnafjorden bridge in Norway, which is represented in Figure 1, see the ranges attributed to the natural frequencies of the structure with respect to the location of the wind and wave load spectra in Figure 2.

Moreover, this separation of timescales is known to provide approximate expressions to compute the statistics of the structural responses to buffeting winds with a small but controllable discrepancy, cutting the time it takes by 10 to 100 compared to the traditional frequency domain analysis method [10, 11, 12, 13, 14]. But these approximations are yet to be established when dealing with wave loads and this is thus the purpose of the present thesis, as further detailed below.

### Four reasons to rely on a time domain analysis.

At start, there are four main reasons to justify the use of a time domain analysis instead of a frequency domain analysis. First, the nonlinearity of the wind loading [16] which is weak though, and takes the simple form of a quadratic-type transformation of the stochastic wind field [17]. Second, the nonlinearity of the wave forces, as expressed by the Morison equation [18]. Third, the nonlinearity of the structural behavior, which is typically attributable to the nonlinear behavior of the cables [19]. At last but not least, fourth, the non Gaussianity of the response, which results from the nonlinear transformation of the known (and assumed Gaussian) input fields, namely the wind velocity field and the wave height profile.

Because of these four reasons, conducting the analysis of floating structures in the time domain, based on extensive simulations is naturally appealing [20, 21, 22, 23]. It indeed quite simply consists in generating synthetic Monte Carlo realizations of the wind and wave loads [24, 25, 26], then solving the equations of motion with a step-by-step integrator to determine the time evolution of the design quantities (displacements, stresses, cable forces) and finally performing a statistical treatment of these quantities in order to provide extreme value distributions for the final design, see Figure 3.



FIGURE 1: A three-span suspension bridge with tension-leg platforms as pylons, one of the proposed floating bridge concepts for crossing the Bjørnafjorden strait in Norway. Illustrated by Arne Jørgen Myhre, Statens Vegvesen. Courtesy of [15].

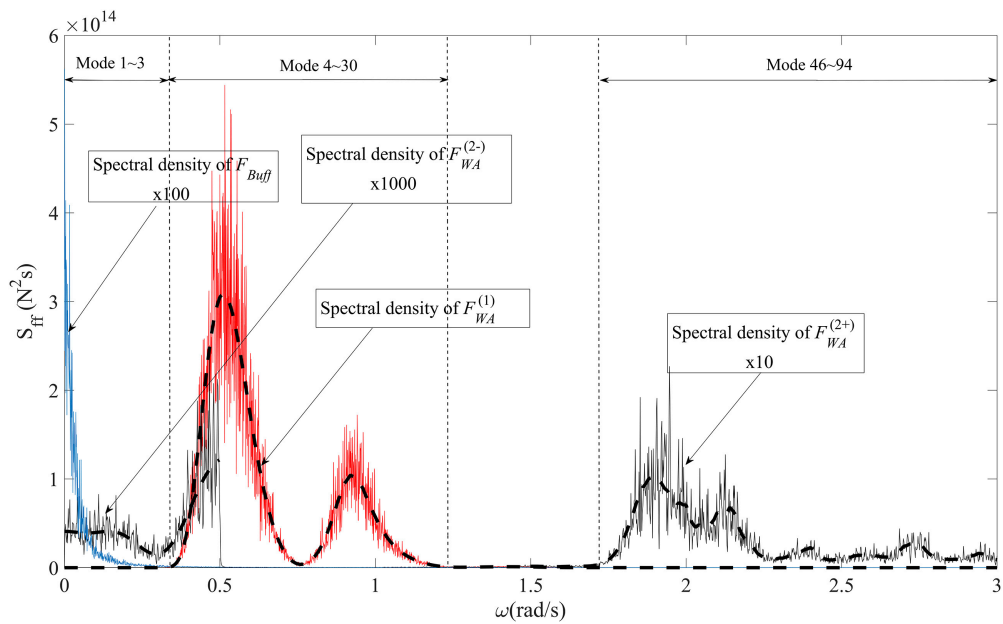


FIGURE 2: Autospectral density of the wind (blue) and the wave (red) forces on the bridge represented in Figure 1. Courtesy of [15].



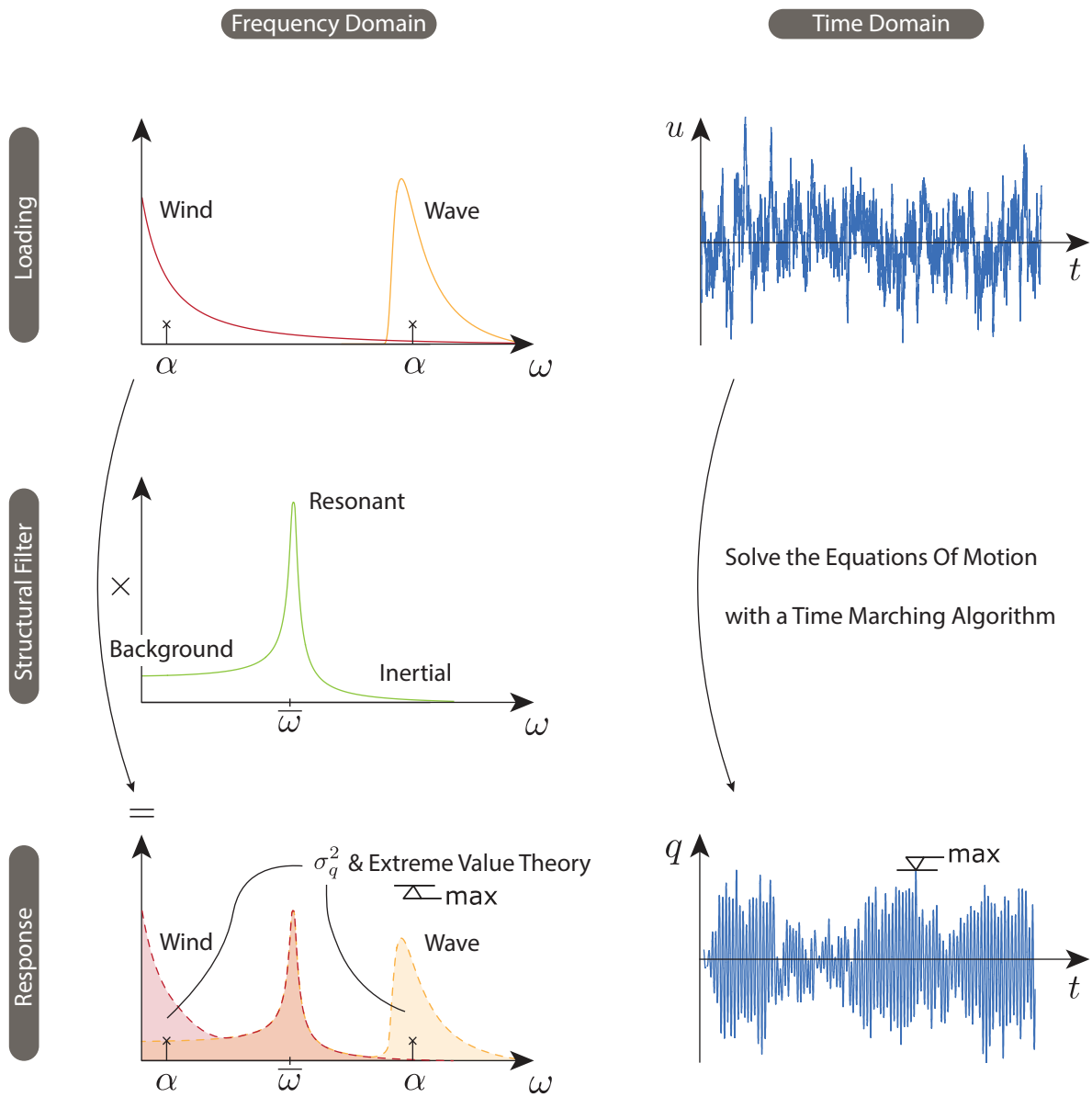


FIGURE 3: Schematic representation of the traditional analysis methods.

But this traditional method actually struggles to evaluate the extreme response of large floating structures to the actions of winds and waves in a reasonable amount of time when the timescales associated with the motions of either the structure, either the loadings, are clearly separated. The surge response of a compliant structure, for instance, have to be simulated long enough to capture the slow dynamics of the floaters, and with a sufficiently short time step to detect the fast oscillations of the waves [27, 28]. This is all the more accentuated if higher order statistics such as the skewness and the kurtosis are to be estimated since they require to use even longer response histories.

### **The four reasons, revisited in the frequency domain.**

In the wind engineering community, the equivalence between time and frequency domains has been utilized and recognized for a while [14]. The design of large span bridges subjected to buffeting wind loads is typically done in the frequency domain [29], then spread over to the time domain in order to take advantage of the great flexibility of the Monte Carlo simulations [30]. One should also admit that the nonlinearity of the wind loading is not strong and equivalent linearized models have proven very accurate [29]. It thus justifies the regular use of linear models to evaluate the buffeting and aeroelastic responses of large span bridges [29].

In the marine engineering community as well, many works have highlighted the possibility to provide an equivalent linear [20], quadratic [31] or cubic [32] modeling of the problem. Based on these equivalences and on the theory of Volterra and Wiener systems [33], the analysis of marine structures such as tension leg and floating platforms can also be performed in the frequency domain [34], by means of a spectral approach.

In its most simple form, it consists in the multiplication of the power spectral density of the loading by the frequency response function of the system in order to establish the power spectral density of the response, which contains the necessary information for the design [35]. Extensions to the non Gaussian case exist and rely on the bispectrum of the loading and the higher order frequency response functions of the system [12]. This allows, through a simple multiplication again, to tackle non Gaussian and slightly nonlinear systems [36].

The second and third statistical moments of the response can then be obtained by integrating these spectra over a one or a two-dimensional frequency space, respectively. These statistics are particularly useful to determine the short-term extreme response distribution [37] and accumulated damage state of the structure [38]. However and although less than in time domain, their computation is known to be demanding as well, even if modal truncation techniques are used.

### **The remaining computational burden in the frequency domain.**

First, time consuming operations have to be repeated at each integration point, e.g. the establishment of the loading spectra in three dimensions for all combinations of the numerous structural degrees-of-freedom, or the projection of such a large number of loading spectra into the modal basis [13]. Second, computing these integrals accurately enough necessitates to use many closely spaced points because the spectra of the response typically feature several sharp peaks related to the resonance of the structure in its multiple modes and to the particular energy content of the wave loads [11]. Third, a large panel of such short-term analyses have to be executed for many different sea states. Depending on their probability of occurrence, the results can then be weighted and concatenated to provide long-term extreme distributions [39] and fatigue accumulations [40].

Over the years, many studies have explored the possibility to improve the computational efficiency of the long-term analyses for various marine structures [41, 42]. They tried to reduce the number of short-term analyses that are required, by using for instance the first and second order reliability methods, the inverse reliability method, the environmental contour approach but also

surrogate modelling and learning algorithms [43, 44, 45, 46, 47]. Besides, they attempted to accelerate each of these many short-term analyses. With this in mind, Giske et al. recently proposed to estimate the cross-spectral densities of the wave loads by using Fourier series [48]. But, although they are obtained much more rapidly than before, they still have to be projected into the modal basis for a lot of frequencies.

### **How is the reduction of this complexity addressed in the current thesis?**

Whereas the sharpness and the distinctness of the peaks in the spectra to integrate constitute a huge drawback for a traditional frequency domain analysis, it can in fact be turned into an advantage as it allows to use the Multiple Timescale Spectral Analysis [11].

This general framework is based on the perturbation theory and hinges on the existence of well separated timescales in the responses of structures. It has been formulated to provide rapid and accurate estimations for the main components of the response statistics in the form of semi-analytical expressions. These formulas are actually derived with the aim to reduce the number of points that are needed to integrate such spectra with sharp peaks, and especially avoid to project the forces into the modal basis so many times.

For the moment, though, the Multiple Timescale Spectral Analysis concerns the response of slightly-damped structures to the loading of buffeting winds, whose characteristic frequency is typically much lower than the natural frequencies of the structures [10, 11, 12, 13]. They are hence excited in their background and resonant regimes. By contrast, when dealing with wave loads on floating structures, the roles of the slow and fast timescales are likely to be interchanged, as this is schematically represented for the power spectral densities in Figure 3.

In brief, the purpose of this thesis is thus to **extend the Multiple Timescale Spectral Analysis** further, in order to efficiently tackle the analysis of large and slender structures which are expected to respond in the inertial regime as well, leaving aside the wind loads for which solutions already exist. Other novelties reported in this thesis also aim at handling the non-classical damping and the frequency-dependent nature of the structural properties which can result from the consideration of fluid-structure interactions.

### **What are the expected outcomes of the proposed developments?**

As the Multiple Timescale Spectral Analysis is supposed to be much more efficient than any other method, while providing a small and controllable discrepancy, it is the perfect tool to analyze very rapidly numerous possible layouts and configurations. It should thus be used at the early stage of the design, in order to guide engineers with graspable information, while a heavier time domain simulation (as performed today) would be used for the final design.

At last but not least, many floating structures have also been constructed over the recent years and today's monitoring possibilities allow comparison between numerical predictions and real operating conditions of a bridge [29-30]. In this context, it is not surprising to observe that the comparison is based on frequency domain information (power spectral density, coherence and related information in the modal basis) and on the dispatching of the structural response between the background and resonant components, while this thesis makes it possible to examine also the inertial ones.

Altogether, these two expected outcomes certainly show that the spectral approach is the best way to understand the actual behaviour of the structures and is definitely much richer than what the comparison of time series could give.

## The Multiple Timescale Spectral Analysis

### Where does it come from?

Historically, in wind engineering, Davenport formulated an approximate expression for the variances of the modal responses [14]. It yielded the well-known background/resonant decomposition, which relies on a single projection of the forces. Then, Gu [49] and Denoël [13] independently did the same for the covariances of the modal responses, which can sometimes not be ignored in the reconstruction of the nodal statistics. To do so, the power spectral densities of the wind loads were just replaced by a constant value over the whole domain of integration.

However, such a substitution was not fully justified at this point, mathematically speaking [12]. Besides, it also appeared that this approach could not be extended as is to higher orders [12]. To solve these issues, Denoël identified some small parameters in the definition of the response spectra, which allowed them to be integrated with one of the perturbation methods proposed by Hinch [50]. Nevertheless, Denoël adapted it to deal with the third order analysis of a wind-excited oscillator in [12] and this is what subsequently gave birth to the Multiple Timescale Spectral Analysis [11].

### How does it work?

The Multiple Timescale Spectral Analysis consists in the sequential evaluation of the major contributions to these integrals with sharp peaks. This is achieved by looping around the same steps: (i) select the peak that contributes the most, then (ii) find a local approximation of the integrand that is sufficiently accurate over the extent of the peak considered, integrable in the far field, and in an explicit way. After integration, it thus provides a simple expression for the statistical component associated to the considered peak. Except for these requirements of precision, integrability and simplicity, freedom is left to the user on how to find such a closed-form formula.

Next move is to (iii) subtract the approximate function from the integrand in order to obtain a residual. The sequence (i)-(iii) is then repeated for the following contribution. Bit by bit, the peaks that have already been treated disappear from the residual function until a proper balance is reached between the accuracy and the complexity of the formulas developed for the main components of the statistics. At this point, the iterative process is stopped and the last remainder is neglected.

Whenever in step (ii), an arbitrary small parameter is most often introduced together with a stretching. It usually relates to a particular feature of the problem and it helps to find a proper estimation for the analytical functions over the zone of interest, which is justified from an asymptotic standpoint. According to the perturbation theory, this number eventually disappears from the final results because it is arbitrarily chosen.

### How about an example?

For the sake of the understanding, let us exemplify this procedure with the variance of the response of a linear oscillator subjected to the loading of the wind, or equivalently, in a decoupled setting, a modal response of a linear structure to such a wind excitation. At start, it reads

$$\sigma_q^2 = \int_{-\infty}^{+\infty} S_q(\omega) d\omega \quad (1)$$

where  $S_q(\omega)$  stands for the power spectral density of the response and is schematically represented by a black line in Figure 4-(A).

As mentioned earlier, the power spectral density of the response can actually be expressed as the following product

$$S_q(\omega) = S_f(\omega) |H(\omega)|^2 \quad (2)$$

where  $S_f(\omega)$  is the power spectral density of the force and  $|H(\omega)|^2$  is the structural kernel of the system. In the current situation, it is given by

$$|H(\omega)|^2 = \frac{1}{k^2} \frac{1}{\left(1 - \left(\frac{\omega}{\bar{\omega}}\right)^2\right)^2 + (2\xi\frac{\omega}{\bar{\omega}})^2} \quad (3)$$

where  $k$  is the stiffness,  $\xi$  is the damping ratio and  $\bar{\omega}$  is the natural circular frequency.

The wind loading is usually seen as a slow driving process, which means that the center of gravity of its power spectral density is located at  $\alpha \ll \bar{\omega}$ . The integrand in Equation (1) thus exhibits a peak in the background region. It also features two additional peaks related to the resonance of the system, at  $\pm\bar{\omega}$ .

**Loop 1:** Based on the available information, it is not possible to rank these three peaks according to the importance of their contribution. When applying the Multiple Timescale Spectral Analysis, any of them can therefore be selected at Step (i) but it is customary to start with the background one.

In order to complete Step (ii), the stretched coordinate  $\omega = \alpha\eta$  can first be introduced. It interestingly rescales the range  $\omega = \text{ord}(\alpha)$  to an order-one in  $\eta$ , see the resulting functions in the gray box in Figure 4-(A). Using this scaling, the structural kernel reads

$$|H(\omega[\eta])|^2 = \frac{1}{k^2} \frac{1}{\left(1 - \left(\frac{\alpha}{\bar{\omega}}\eta\right)^2\right)^2 + (2\xi\frac{\alpha}{\bar{\omega}}\eta)^2} \quad (4)$$

and can then be expanded in an asymptotic series for  $\alpha/\bar{\omega} \ll 1$ . At leading order, it can consequently be approximated by  $1/k^2$ . Substituting this coefficient in Equation (2) subsequently provides

$$S_b(\omega) = \frac{S_f(\omega)}{k^2} \quad (5)$$

which is an appropriate approximation of the integrand in the sense of the Multiple Timescale Spectral Analysis. As shown by the red dashed line in Figure 4-(A), it is indeed locally accurate in the low frequencies. It is also bounded in the far field and integrable in an explicit way as it yields the simple expression

$$\sigma_b^2 = \frac{\sigma_f^2}{k^2} \quad (6)$$

where  $\sigma_f^2$  is the variance of the wind load, for the background component of the response. Proceeding with Step (iii), the first residual function

$$\hat{S}_q(\omega) = S_q(\omega) - S_b(\omega) \quad (7)$$

$$= S_f(\omega) \left( |H(\omega[\eta])|^2 - \frac{1}{k^2} \right) \quad (8)$$

is eventually built and has obviously no more peak in the vicinity of the origin, see the black line in Figure 4-(B).

**Loop 2:** Starting back at Step (i), the rightmost peak is then selected. As shown in the gray box in Figure 4-(B), the introduction of the strained coordinate  $\omega = \bar{\omega}(1 + \xi\eta)$  allows to focus on this peak, whose extent is known to scale with  $\xi \ll 1$ . Indeed, the smaller the damping ratio, the sharper the peaks of the structural kernel. Please notice that this choice is commonly made to add such a physical insight in the derivation, although any small number  $\varepsilon \ll 1$  could be employed and would disappear anyways in the end.

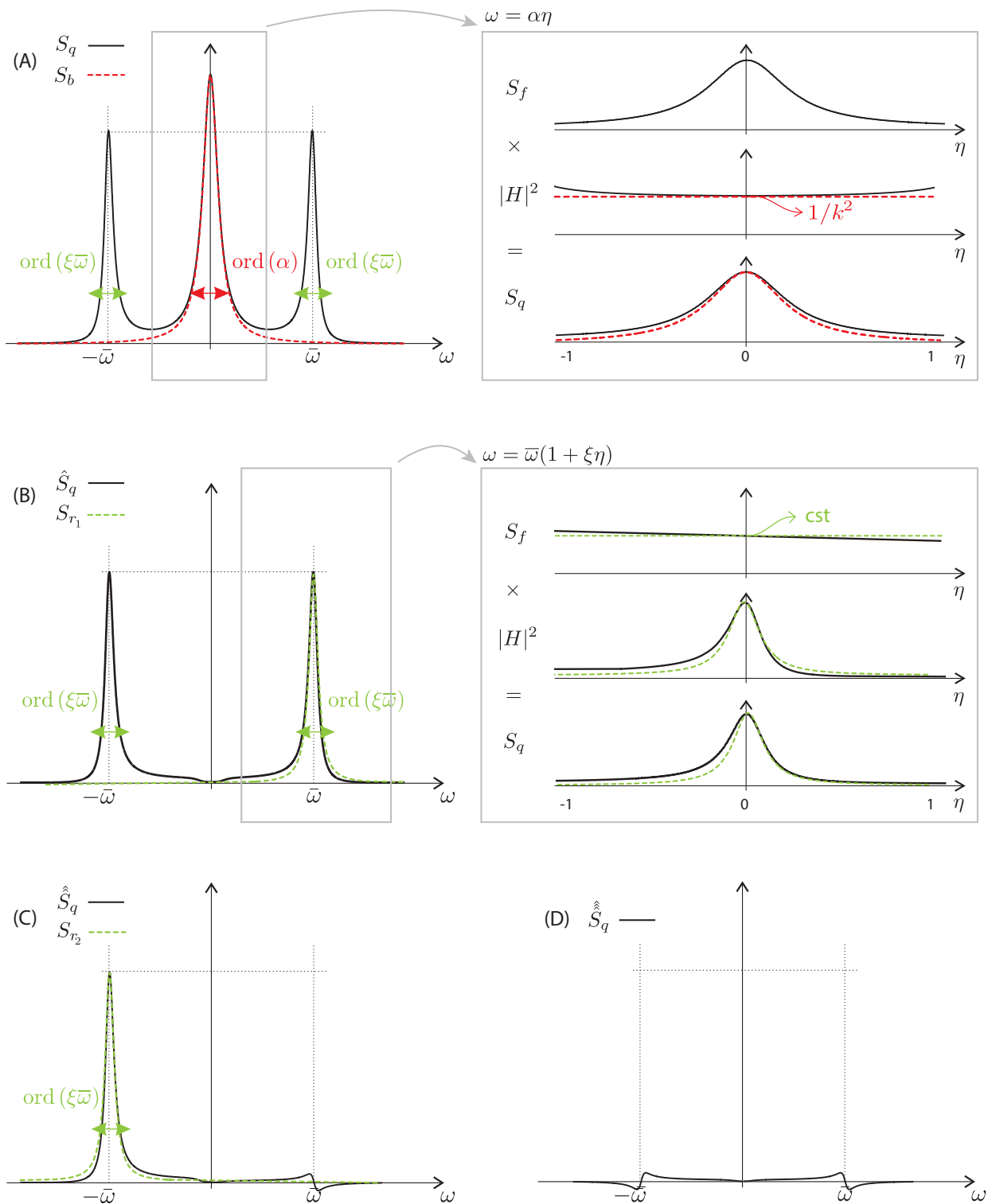


FIGURE 4: Schematic representation of how the Multiple Timescale Spectral Analysis applies to the second order response of a linear oscillator and allows to express the background/resonant decomposition of the variance.

Then in Step (ii), among other possibilities [11], it is decided to expand the residual structural kernel in an asymptotic series for  $\xi \ll 1$ . It reads as follows

$$|H(\omega[\eta])|^2 - \frac{1}{k^2} = \frac{1}{4k^2\xi^2(\eta^2+1)} - \frac{\eta}{4k^2\xi^2} \frac{(\eta^2+2)}{(\eta^2+1)^2} \xi + \text{ord}(\xi^2) \quad (9)$$

and it can satisfactorily be truncated at leading order provided that the damping ratio is effectively very small. Meanwhile, the power spectral density of the loading is replaced by the constant value  $S_f(\bar{\omega})$  across the width of the resonant peak. To justify this from a Taylor series perspective, it is necessary to check that  $\bar{\omega}\partial_\eta^i S_f(\bar{\omega}) \ll S_f(\bar{\omega})$  to keep the asymptoticness of the series

$$S_f(\omega[\eta]) = S_f(\bar{\omega}) + \eta\partial_\eta S_f(\bar{\omega})\xi + \text{ord}(\xi^2) \quad (10)$$

in the neighborhood of  $\eta = 0$ , with  $\partial_\eta^i$  indicating the  $i$ -th order differentiation with respect to the stretched coordinate  $\eta$ . Under these conditions, the local approximation

$$S_{r_1}(\omega) = \frac{1}{4\xi(\eta^2+1)} \frac{S_f(\bar{\omega})}{k^2} \quad (11)$$

is supposed to be sufficiently accurate over the range of interest. It is also integrable in the far field and in an explicit way. It can therefore be considered as appropriate in the sense of the Multiple Timescale Spectral Analysis. Integrating Equation (11) thus gives the simple expression

$$\sigma_{r_1}^2 = \frac{\pi\bar{\omega}}{4\xi} \frac{S_f(\bar{\omega})}{k^2} \quad (12)$$

for the contribution of the rightmost resonant peak to the response.

**Loop 3:** Repeating these steps one last time, or taking the symmetry of the integrand into account, subsequently yields

$$S_{r_2}(\omega) = S_{r_1}(-\omega) \quad (13)$$

for the local approximation of the leftmost resonant peak, meaning that  $S_{r_1}(\omega)$  is just mirrored with respect to the y-axis, see Figure 4-(C). Therefore,  $\sigma_{r_1}^2 = \sigma_{r_2}^2$  and the resonant component of the response is expressed by

$$\sigma_r^2 = \sigma_{r_1}^2 + \sigma_{r_2}^2 = \frac{\pi\bar{\omega}}{2\xi} \frac{S_f(\bar{\omega})}{k^2} \quad (14)$$

once the two resonant peaks are considered.

**Globally:** In the end, the last residual is negligible, see Figure 4-(D), and the background/resonant decomposition thus reads

$$\sigma_x^2 = \sigma_b^2 + \sigma_r^2 \quad (15)$$

with

$$\sigma_b^2 = \frac{\sigma_f^2}{k^2} \quad (16)$$

and

$$\sigma_r^2 = \frac{\pi\bar{\omega}}{2\xi} \frac{S_f(\bar{\omega})}{k^2} \quad (17)$$

which correspond to Davenport's formulas [14].

## My Personal Contributions, see Blue Boxes in Figure 5

Figure 5 provides an overview of the existing and the missing pieces in the Multiple Timescale Spectral Analysis of linear structures. It currently covers: the background and the resonant components of the variance, the skewness and the kurtosis of the response of a single degree-of-freedom system as well as the covariances between the two-by-two responses of a multi degree-of-freedom system, provided that they are decoupled in the modal basis [12, 13, 11, 10].

The initial input of Davenport for the background/resonant decomposition of the variance is acknowledged by being represented in green, even if it was then revisited in the light of the Multiple Timescale Spectral Analysis. Meanwhile, the background/resonant components of the higher order statistics, which grant access to the skewness and the kurtosis, and the crossed statistics at second order are displayed in yellow. Their expressions have been provided by Denoël [12, 13, 11, 10].

The new elements whose formula will be derived in this thesis are coloured in dark blue. To do so, we will follow the principles of the Multiple Timescale Spectral Analysis, as illustrated in the previous section, but applied to much more complicated situations. Meanwhile, the light blue shading indicates a case which is not discussed in the manuscript but results directly from it.

Although they all represent a substantial extension of the state-of-the-art, these components are not the only novelties presented herein. In particular, (i) a brand new way of finding the approximations for the resonant components is introduced, (ii) a unified expression is developed for the background and the inertial components, as shown by the bracket symbols in Figure 5, and (iii) two strategies are proposed to decouple the equations of motion when fluid structure interactions are included. They rely on a state space formulation (SSF) of the governing equations and depend on either constant, either frequency dependent mass (M), damping (C) and stiffness (K) matrices. They are respectively denoted by the symbols  $(\omega)$  and  $(\omega)$  in Figure 5.

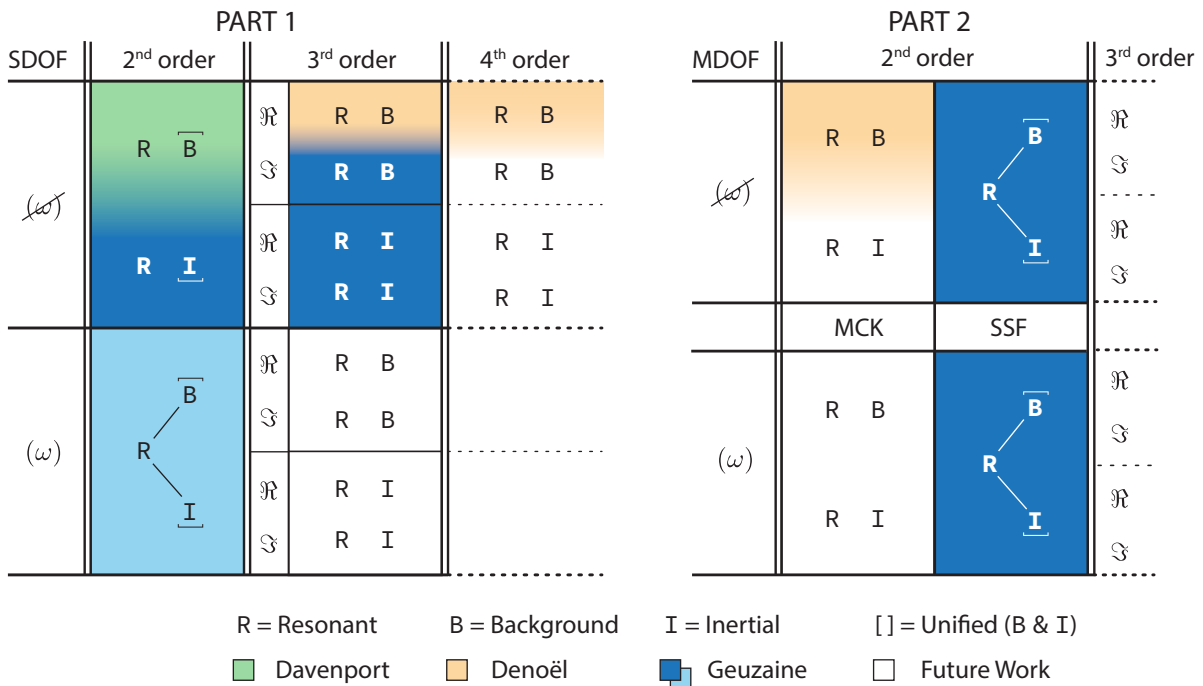


FIGURE 5: Application range for the Multiple Timescale Spectral Analysis of a linear structure.



## Outline of the Thesis

As the reader can see in Figure 5, two axes of complexity are explored in this thesis:

- In Part 1 The response of a single degree-of-freedom system is studied under a non-Gaussian loading. In this case, the difficulty lies in the consideration of higher order statistics.
  
- In Part 2 The response of a multi-degree-of-freedom system is studied under a Gaussian loading. In this case, the difficulty arises in examining the crossed statistics of the responses, at second order only.

At the beginning of Part 1, **Chapter 1** establishes the governing equations of an oscillator, such as a tension-leg platform, which is excited by a Morison wave load. The nondimensionalization and the simplification of the problem are discussed. The first and second order spectra of such an oscillator's response under a linearized, quadratized and non-polynomial forcing process are also examined.

In **Chapter 2**, the Multiple Timescale Spectral Analysis is applied to the power spectral density of the response in order to formulate simple expressions to estimate the main components of the variance in an efficient way. Several variants are tested and are eventually compared in a parametric analysis.

**Chapter 3** focuses on the developments of the closed-form expressions required to approximate rapidly the third central moments of the response to a non-normal loading, whose bispectrum is possibly complex-valued. A parametric analysis is conducted to validate these formulas and evaluate their limitations as well.

As we enter the second part of the thesis, **Chapter 4** presents the specificities of the governing equations obtained when dealing with the responses of a multi degree-of-freedom system to the forces of the waves, which include fluid-structure interactions. In order to decouple the equations of motion, two different strategies are introduced together with a modal state formulation.

**Chapter 5** contains the derivations of the simple expressions which are dedicated to the rapid estimation of the spectral densities and the second moments of the responses given by the first decoupling strategy. Their validity is assessed with a parametric analysis, performed on a minimalistic example.

In **Chapter 6**, simple expressions are derived for approximating the spectral densities and the second moments of the responses which result from the implementation of the second decoupling strategy. A demonstration is provided regarding on how well they degenerate to the formulas obtained by Denoël and Davenport in more restrictive circumstances.

Finally, **Chapter 7** aims at validating the decoupling strategies and the approximate decompositions proposed in the second part of the thesis by using them for the stochastic analysis of realistic multi-degree-of-freedom structures subjected to hydroelastic loads.

## List of Publications

### Main Papers Related to this thesis:

- Geuzaine, M. , Fenerci, A., Øiseth O., Denoël, V. (under external review). Multiple timescale spectral analysis of floating structures subjected to hydrodynamic loads. *Journal of Engineering Mechanics*.
- Geuzaine, M., Fenerci, A., Øiseth O., Denoël, V. (2022). Importance of the inertial components in modal state covariances. *Proceedings of the 41<sup>st</sup> International Conference on Ocean, Offshore and Arctic Engineering* (OMAE 2022) [51].
- Fenerci, A., Geuzaine, M., Denoël, V. , Øiseth O. (2022). Efficient long-term extreme response analysis of floating bridges using multiple timescale spectral analysis. *Proceedings of the 41<sup>st</sup> International Conference on Ocean, Offshore and Arctic Engineering* (OMAE 2022) [52].
- Geuzaine, M., & Denoël, V. (2020). Efficient estimation of the skewness of the response of a wave-excited oscillator. *Proceedings of the 11<sup>th</sup> International Conference on Structural Dynamics* (EURODYN 2020), pp. 3467–3480 [53].
- Geuzaine, M., Esposito Marzino, M., & Denoël, V. (2020). Efficient estimation of the skewness of the response of a linear oscillator under a non-Gaussian loading. *Proceedings of the Engineering Mechanics Institute Conference and Probabilistic Mechanics & Reliability Conference*, New York, United States [54].
- Geuzaine, M., & Denoël, V. (2019). A framework for the efficient spectral analysis of large wind- and wave-loaded structures. *Proceedings of the 15<sup>th</sup> International Conference on Wind Engineering*, Beijing, China [55].
- Geuzaine, M., & Denoël, V. (2019). Estimation of modal correlation coefficients in wind buffeting spectral analysis. *Proceedings of the 2<sup>nd</sup> Romanian National Conference on Wind Engineering*, Bucharest, Romania [56].

### Main Papers Related to Side Topics:

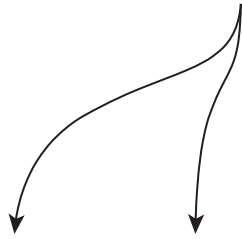
- Geuzaine, M., Jaspert, J. P., Demonceau, J. F., & Denoël, V. (2022). Influence of a small flexibility of connections on the elastic structural response of frames. *Journal of Structural Engineering*, 148(5), 04022033 [57].
- Geuzaine, M., Foti, F., & Denoël, V. (2021). Minimal requirements for the vibration-based identification of the axial force, the bending stiffness and the flexural boundary conditions in cables. *Journal of Sound and Vibration*, 511, 116326 [58].
- Foti, F., Geuzaine, M., & Denoël, V. (2021). On the identification of the axial force and bending stiffness of stay cables anchored to flexible supports. *Applied Mathematical Modelling*, 92, 798-828 [59].
- Felder, S., Geuzaine, M., Dewals, B., & Erpicum, S. (2019). Nappe flows on a stepped chute with prototype-scale steps height: Observations of flow patterns, air-water flow properties, energy dissipation and dissolved oxygen. *Journal of Hydro-Environment Research*, 27, 1-19 [60].





# Part I

## SDOF SYSTEMS



Chapter 2

Chapter 3

SDOF	2 <sup>nd</sup> order	3 <sup>rd</sup> order	4 <sup>th</sup> order	MDOF	2 <sup>nd</sup> order	3 <sup>rd</sup> order
$(\omega)$	<div style="background-color: #4CAF50; color: white; padding: 5px; display: flex; justify-content: space-around;"> <span>R</span> <span><math>\overline{B}</math></span> </div>	$\mathfrak{R}$	<div style="background-color: #4CAF50; color: white; padding: 5px; display: flex; justify-content: space-around;"> <span>R</span> <span>B</span> </div>	<div style="background-color: #FFCC80; color: white; padding: 5px; display: flex; justify-content: space-around;"> <span>R</span> <span>B</span> </div>	<div style="background-color: #FFCC80; color: white; padding: 5px; display: flex; justify-content: space-around;"> <span>R</span> <span>B</span> </div>	$\mathfrak{R}$
		$\mathfrak{S}$	<div style="background-color: #0070C0; color: white; padding: 5px; display: flex; justify-content: space-around;"> <span>R</span> <span>B</span> </div>			$\mathfrak{S}$
	<div style="background-color: #0070C0; color: white; padding: 5px; display: flex; justify-content: space-around;"> <span>R</span> <span><math>\overline{I}</math></span> </div>	$\mathfrak{R}$	<div style="background-color: #0070C0; color: white; padding: 5px; display: flex; justify-content: space-around;"> <span>R</span> <span><math>\overline{I}</math></span> </div>	<div style="background-color: #0070C0; color: white; padding: 5px; display: flex; justify-content: space-around;"> <span>R</span> <span><math>\overline{I}</math></span> </div>	<div style="background-color: #0070C0; color: white; padding: 5px; display: flex; justify-content: space-around;"> <span>R</span> <span><math>\overline{I}</math></span> </div>	$\mathfrak{R}$
		$\mathfrak{S}$	<div style="background-color: #0070C0; color: white; padding: 5px; display: flex; justify-content: space-around;"> <span>R</span> <span><math>\overline{I}</math></span> </div>			$\mathfrak{S}$
$(\omega)$	<div style="background-color: #ADD8E6; color: white; padding: 5px; display: flex; justify-content: space-around;"> <span>R</span> <span><math>\overline{B}</math></span> </div>	$\mathfrak{R}$	R B	MCK	<div style="background-color: #ADD8E6; color: white; padding: 5px; display: flex; justify-content: space-around;"> <span>R</span> <span><math>\overline{B}</math></span> </div>	$\mathfrak{R}$
		$\mathfrak{S}$	R B			$\mathfrak{S}$
	<div style="background-color: #ADD8E6; color: white; padding: 5px; display: flex; justify-content: space-around;"> <span>R</span> <span><math>\overline{I}</math></span> </div>	$\mathfrak{R}$	R I	SSF	<div style="background-color: #ADD8E6; color: white; padding: 5px; display: flex; justify-content: space-around;"> <span>R</span> <span><math>\overline{I}</math></span> </div>	$\mathfrak{R}$
		$\mathfrak{S}$	R I			$\mathfrak{S}$

R = Resonant      B = Background      I = Inertial       $\overline{[]}$  = Unified (B & I)  
■ Davenport      ■ Denoël      ■ Geuzaine       Future Work

Figure A



## Chapter 1

# Contextualization

### 1.1 Context and Propositions

In this first part of the thesis, we focus on the second and the third central moments of the response of a linear single-degree-of-freedom system to a non-Gaussian wave loading, neglecting fluid-structure interactions.

To start, the equations of motion are introduced, first in the time domain, in Section 1.2, and then in the frequency domain, in Section 1.4. Once the second and the third order spectra of the response are established, they can eventually be integrated in order to determine the second and the third central moments of the response. These operations are performed in a much more efficient way, by using the simple expressions derived for the major components of these statistics with the help of the Multiple Timescale Spectral Analysis. However, as explained in the introduction and detailed further, in Section 1.5, some of them are still missing or are not yet applicable in a marine engineering context.

Chapter 2 and Chapter 3 therefore aim at addressing these issues for the second and the third central moments, respectively. At the end of each chapter, the resulting decompositions are eventually validated and verified for a wide range of parameters against the numerical integration of the response spectra obtained from analytical formulations and simulated data.

### 1.2 Governing Equations in Time Domain

The surge response of an oscillator, which can typically represent a tension-leg platform as shown in Figure 1.1, is governed by the nonlinear second order differential equation

$$m\ddot{x}(t) + c\dot{x}(t) + kx(t) = f(t) \quad (1.1)$$

where  $x(t)$  is the displacement,  $\dot{x}(t)$  is the velocity and  $\ddot{x}(t)$  is the acceleration of the oscillator,  $k$  is the stiffness,  $c$  is the viscosity, and  $m = m_s + m_a$  is the effective mass (i.e. the mass of the structure plus the mass of fluid accelerating with the structure). Also, the horizontal force exerted by random waves on such an oscillating point-like structure, which is elastic and small compared to the wavelength of the waves, can be expressed according to Morison's equation [18] by the sum of two loading components

$$f(t) = f_m(t) + f_d(t) \quad (1.2)$$

where  $f_m(t)$  and  $f_d(t)$  are respectively an inertia and a drag force. The inertia force reads

$$f_m(t) = k_m \dot{u}(t) \quad (1.3)$$

and is due to the pressure gradient generated by the acceleration of the flow,  $\dot{u}(t)$ . It resembles a buoyancy force and results from a linear transformation, as the overhead dot denotes differentiation in time of  $u(t)$  being the fluctuations of the water velocity around  $u_c$ , the constant current speed.

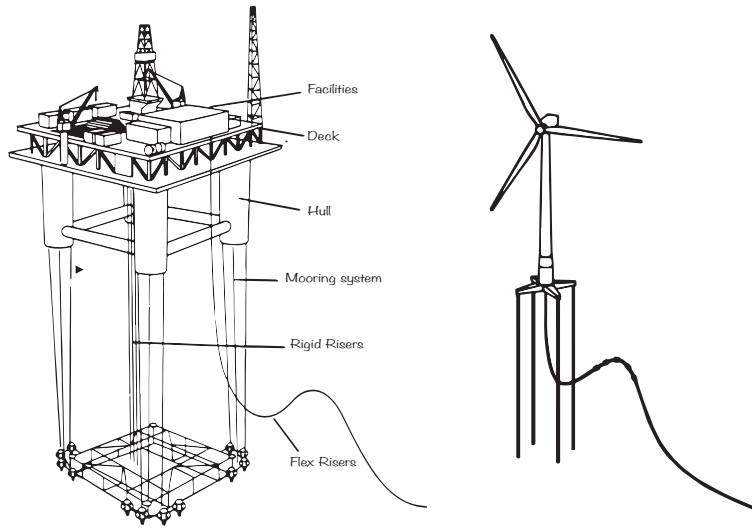


FIGURE 1.1: Examples of tension-leg structures.

The drag force reads

$$f_d(t) = k_d |u_c + u(t) - \dot{x}(t)| (u_c + u(t) - \dot{x}(t)) \quad (1.4)$$

and acts in the same direction as the relative velocity of the fluid with respect to the speed of the structure,  $\dot{x}(t)$ . This is the reason why this relative velocity enters a nonlinear function involving the product of its absolute value and its signed value. At last, the coefficients  $k_m$  and  $k_d$ , are related to geometric and hydrodynamic properties through

$$k_m = c_m v_w d_w \quad \text{and} \quad k_d = \frac{1}{2} c_d a_w d_w \quad (1.5)$$

where  $d_w$  is the density of the water while  $c_m$  is the inertia coefficient,  $c_d$  is the drag coefficient, and  $a_w$  is the cross-sectional area of  $v_w$ , the volume of the submerged part of the body.

Because of the memoryless and the feedback type nonlinearities included in the drag loading component, the response of the structure is expected to be non-normal. It is therefore necessary to determine not only the variance but also the higher order statistics of the response in order to describe its probability density, and especially the tail of the distribution in an unambiguous and accurate way.

These developments are presented next. They are valid regardless of the analytical, numerical or experimental definition selected for the power spectral density of the random process  $u(t)$ . This sole input of the dynamical system is for its part supposed to be zero-mean, Gaussian, stationary, and is thus fully defined by its power spectral density

$$S_u(\omega, s) = F_h(\omega, s) S_h(\omega) \quad (1.6)$$

where  $F_h(\omega, s)$  is a wave elevation-to-velocity amplitude operator, depending on the depth  $s$ , and  $S_h(\omega)$  is a wave elevation power spectral density. This being said, for the sake of the illustrations, the structure is assumed to be located at the still-water level in deep water. Thus, the application of the Linear Airy Wave Theory [61] gives

$$F_h(\omega, s) = \omega^2 \quad (1.7)$$



and it is also decided herein to model the wave elevation process,  $h(t)$ , by using the two-sided Pierson Moskowitz spectrum

$$S_h(\omega) = \frac{5}{32} \frac{\omega_h^4}{|\omega|^5} h_s^2 \exp\left(-\frac{5\omega_h^4}{4\omega^4}\right) \quad (1.8)$$

with two parameters,  $h_s$  and  $\omega_h$ . They are typically referred to as the significant wave height and the peak frequency of the wave elevation spectrum [61]. Please notice that the power spectral densities employed in this thesis are two-sided and can thus be integrated from  $-\infty$  to  $+\infty$  to provide the variances of the processes they are associated to. For the wave elevation and velocity processes, for instance, it yields

$$\sigma_h^2 = \left(\frac{h_s}{4}\right)^2 \quad \text{and} \quad \sigma_u^2 = \sqrt{\frac{3\pi}{4}} \omega_u^2 \sigma_h^2 \quad (1.9)$$

where

$$\omega_u = \sqrt[4]{\frac{5}{3}} \omega_h \quad (1.10)$$

is the peak frequency of  $S_u(\omega)$  and can also be obtained by cancelling the  $\omega$ -derivative of  $S_u(\omega)$ .

### 1.3 Dimensionless Formulation of the Equations

Equation (1.1) can then be written in a non-dimensional form by introducing a time duration, a structural response and a water velocity of reference:  $t_r$ ,  $x_r$ , and  $u_r$  respectively. The associated dimensionless quantities

$$\tau = \frac{t}{t_r} \quad ; \quad \chi = \frac{x}{x_r} \quad \text{and} \quad v = \frac{u}{u_r} \quad (1.11)$$

can hence be defined. They are subsequently substituted into Equation (1.1). After division by  $kx_r$ , it yields

$$\frac{m}{kt_r^2} \chi'' + \frac{c}{kt_r} \chi' + \chi = \frac{k_m u_r}{k x_r t_r} v' + \frac{k_d u_c^2}{k x_r} \left| 1 + \frac{u_r}{u_c} v - \frac{x_r}{t_r} \frac{1}{u_c} \chi' \right| \left( 1 + \frac{u_r}{u_c} v - \frac{x_r}{t_r} \frac{1}{u_c} \chi' \right) \quad (1.12)$$

where the new independent time coordinate,  $\tau$ , is omitted for conciseness. In order to ease the comparison with the equation obtained for a wind-excited oscillator in [36], the reference response and reference time are chosen as

$$kx_r = 2k_d u_c u_r \quad \text{and} \quad t_r = \frac{1}{\omega_0} \quad (1.13)$$

where  $\omega_0 = \sqrt{k/m}$  is the natural frequency of the undamped system. These choices allow to obtain a unitary coefficient in front of the highest order derivative as it is usually recommended. Lastly, the reference water velocity is also set equal to  $\sigma_u$  being the standard deviation of the process  $u(t)$ .

As a consequence, the presence of the turbulence intensity of the waves,  $\lambda_u = \sigma_u/u_c$ , is revealed in the dimensionless formulation of the governing equation

$$\chi'' + 2\xi_s \chi' + \chi = \kappa_f v' + \frac{1}{2\lambda_u} |1 + \lambda_u v - 2\xi_a \lambda_u \chi'| (1 + \lambda_u v - 2\xi_a \lambda_u \chi') \quad (1.14)$$

where the symbol  $'$  denotes differentiation with respect to  $\tau$ . Similarly, Equation (1.6) is rewritten dimensionlessly as

$$S_v(\Omega) = \sqrt{\frac{3}{\pi}} \frac{\alpha_v^2}{|\Omega|^3} \exp\left(-\frac{3\alpha_v^4}{4\Omega^4}\right) \quad (1.15)$$

where  $\Omega = \omega t_r$  is the nondimensional circular frequency and  $\alpha_v = \omega_u/\omega_0$  is the frequency ratio of the wave velocity process. Besides, the integration property of the power spectral densities holds true for the rescaled processes as well and can thus be applied to the water velocity process,  $v(\tau)$ , to demonstrate that, given the chosen non-dimensionalization, this input is characterized by a unit variance,  $\sigma_v^2 = 1$ , regardless the value of the frequency ratio.

According to the Vashy-Buckingham theorem, the problem described by Equation (1.14) and Equation (1.15) is ruled out by a set of five dimensionless numbers. They are listed as follows

$$\lambda_u = \frac{\sigma_u}{u_c}, \quad \xi_s = \frac{c}{2\sqrt{km}}, \quad \xi_a = \frac{k_d u_c}{\sqrt{km}}, \quad \kappa_f = \frac{k_m \omega_0}{2k_d u_c}, \quad \alpha_v = \frac{\omega_u}{\omega_0} \quad (1.16)$$

and they are readily identified as the turbulence intensity, the structural damping ratio, the added damping ratio, the loading ratio and the frequency ratio.

In marine engineering applications, the structural and the added damping ratios ( $\xi_s$  and  $\xi_a$ ) are usually small numbers, ranging between  $10^{-3}$  and  $10^{-1}$ , but the turbulence intensity ( $\lambda_u$ ) can reach values from zero up to approximately 3 [62]. All the more so, the frequency ratio ( $\alpha_v$ ) associated to the surge motion is typically much greater than unity when compliant wave-loaded structures, such as floating offshore wind turbines or floating bridges, are considered [27, 28]. Besides, the loading ratio ( $\kappa_f$ ) also starts at zero and is theoretically unbounded, meaning that the inertia force can sometimes be neglected in front of the drag force [63], and vice versa [64]. Also, it is more appropriate to relate  $\lambda_u$  to the relative length of the waves by writing it as follows

$$\lambda_u = \sqrt[4]{\frac{5\pi}{1024} \frac{h_s}{u_c}} \omega_h$$

instead of the turbulence intensity.

For an oscillating flow then, the relative importance of the drag forces over the inertia forces is usually related to the Keulegan-Carpenter number [65]. It is expressed as

$$N_{kc} = \frac{UT_u}{W} \quad (1.17)$$

which is the ratio between the amplitude of the waves and the characteristic lengthscale of the immersed body. Alternatively, it can be rewritten as

$$N_{kc} = 2 \frac{\Omega_v}{\kappa_f} \quad (1.18)$$

where  $\Omega_v = \omega_0/\omega_u$  is the inverse of the frequency ratio. Equation (1.18) therefore highlights the fact that larger Keulegan-Carpenter numbers are associated with smaller loading ratios, and thus a relatively smaller influence of the inertia forces. In order to focus on the nonlinear nature of the loading process, it is considered as drag-dominated. Being linear and independent anyways, the inertia force are thus discarded in the sequel, by setting the loading ratio equal to zero.

Moreover, since the purpose of the present chapter is to study the surge motion of such floating structures, which is much slower than the water particles for most wave loading conditions, an alternative formulation can actually be adopted for the nondimensional drag force [32]. It reads

$$\varphi_d(\tau) = \frac{1}{2\lambda_u} (1 + \lambda_u v(\tau)) |1 + \lambda_u v(\tau)| - \xi_a |1 + \lambda_u v(\tau)| \chi'(\tau) \quad (1.19)$$

where the term  $\xi_a |1 + \lambda_u v(\tau)| \chi'(\tau)$  is in general supposed to contribute substantially to the overall

damping. For practical reasons, though, it is typically replaced by a time invariant substitute<sup>1</sup>. Various procedures exist to do so but the most common consists in using the mean value of  $|1 + \lambda_u v(\tau)|$  instead [66].

As a result of this simplification, the velocity-feedback disappears from the definition of the loading process and transformed into an additional damping parameter. The motion of the system in surge is consequently governed by the differential equation

$$\chi''(\tau) + 2\xi\chi'(\tau) + \chi(\tau) = \varphi_f(\tau) \quad (1.20)$$

whose homogeneous part is linear. The non-normality of the response is thus solely due to the nonlinear transformation of the zero-mean, stationary and Gaussian process  $v(\tau)$

$$\varphi_f(\tau) = \frac{1}{2\lambda_u} (1 + \lambda_u v(\tau)) |1 + \lambda_u v(\tau)| \quad (1.21)$$

which is still necessary to define the loading process.

## 1.4 Spectral Formulation of the Equations

In a spectral approach, it is necessary to determine the power spectral density, but also the higher order spectra of these non-Gaussian loading and response processes, for them to be completely described in a probabilistic sense [67]. In particular, the power spectral density, the bispectrum, and so on, of the response can basically be obtained once their loading counterparts are introduced.

Although the power spectral density and the bispectrum of the loading,  $S_\varphi(\Omega)$  and  $B_\varphi(\Omega_1, \Omega_2)$ , can theoretically be defined in an analytical way based on the power spectral density of the water velocity fluctuations, this possibility is generally disregarded because the expressions at stake are practically intractable<sup>2</sup>.

As a consequence, the preferred solution usually consists in polynomializing the loading, first, so that the spectra are much more simple to establish [68]. In principle, the higher the relative wave length, the higher the degree of the polynomial required to reproduce the actual nonlinearities of the loading in a satisfactory way [62].

For the purpose of this thesis, however, a degree two at most is considered because the next ones do no longer alter the topology of the spectra in the low frequency range. It thus reads

$$\varphi_p(\tau) = p_0 + p_1 v(\tau) + p_2 v^2(\tau) \quad (1.22)$$

where the coefficients of the polynomialization are herein obtained by minimizing the mean-square error between the actual nonlinear loading and its polynomial approximation. Interestingly enough, they are actually expressed in closed-form as

$$p_0 = b_1 + b_2 \quad ; \quad p_1 = 2\lambda_u p_0 \quad \text{and} \quad p_2 = \lambda_u^2 b_1 \quad (1.23)$$

with

$$b_1 = \frac{1}{2\lambda_u} \operatorname{erf}\left(\sqrt{\frac{1}{2\lambda_u^2}}\right) \quad \text{and} \quad b_2 = \sqrt{\frac{1}{2\pi}} \exp\left(-\frac{1}{2\lambda_u^2}\right) \quad (1.24)$$

by applying this rationale to Equation (1.21) and Equation (1.22) as in [69].

With such a polynomial formulation, the power spectral density of the loading process can therefore be expressed in very simple terms by

<sup>1</sup>Handling a time-variant coefficient is manageable but complicated because it would be dealt with by means of a convolution operation after the application of a Fourier transform.

<sup>2</sup>If only they have already been developed, which is not the case for the bispectrum

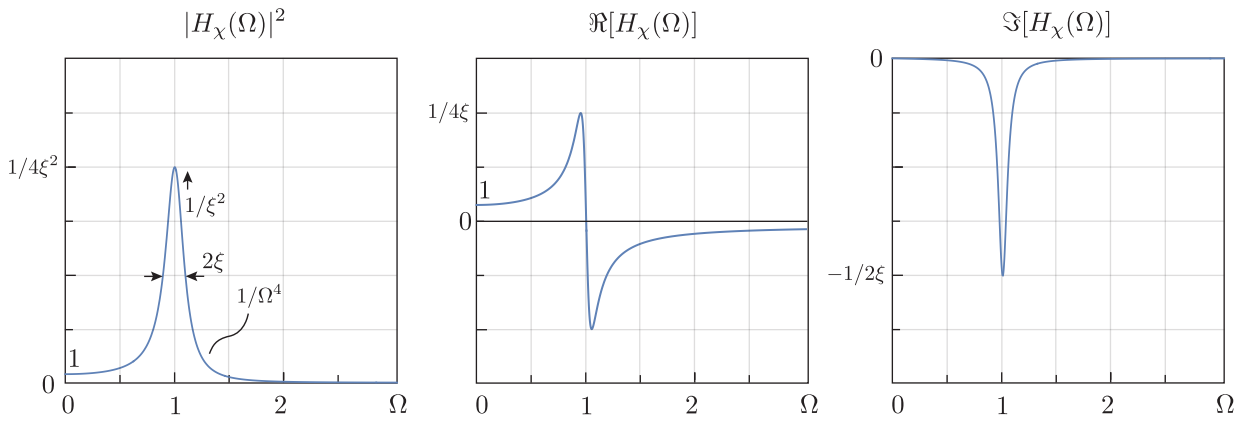


FIGURE 1.2: Structural kernel, real and imaginary parts of the frequency response function.

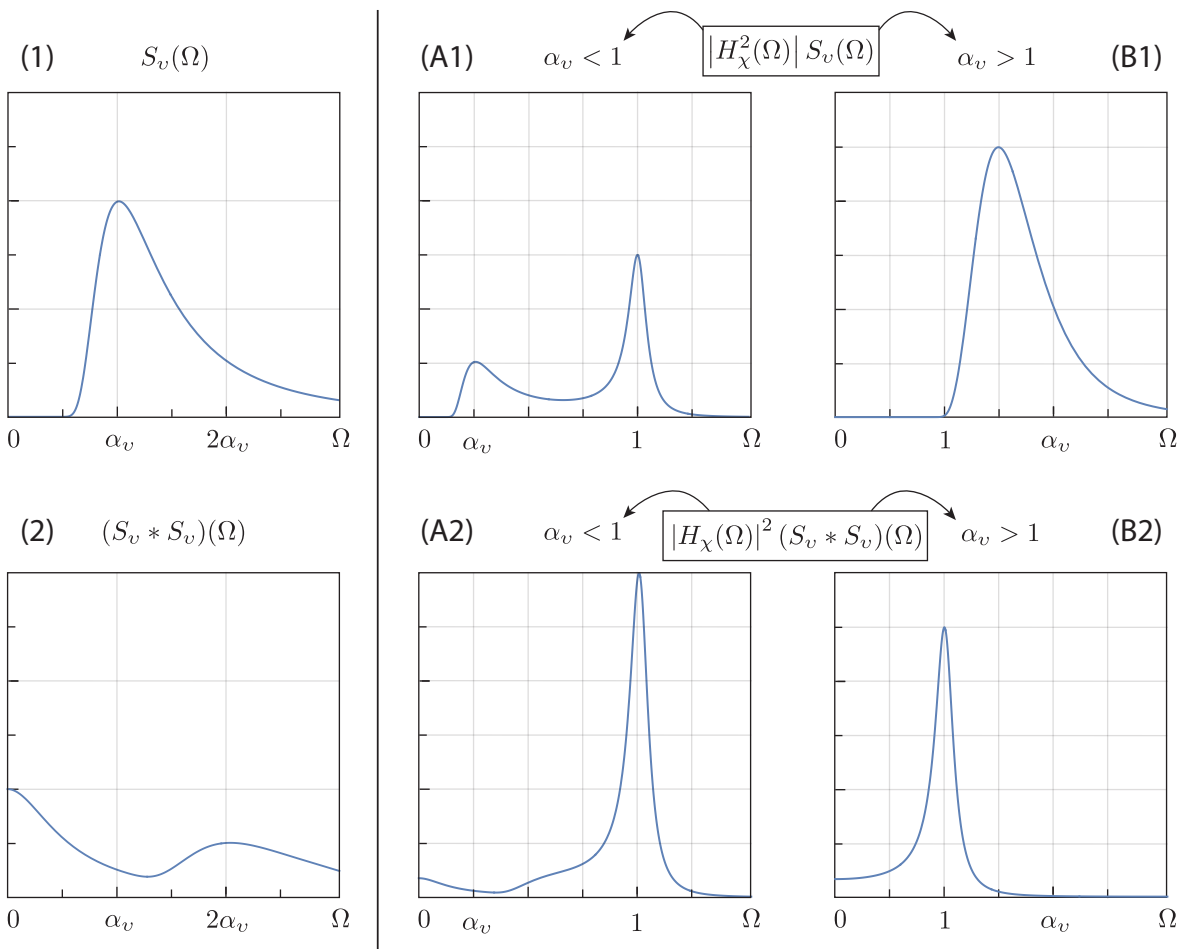


FIGURE 1.3: Power spectral density of the response to a quadratized loading process.

$$S_\varphi(\Omega) = S_{\varphi_1}(\Omega) + S_{\varphi_2}(\Omega) \quad (1.25)$$

$$\text{with } S_{\varphi_1}(\Omega) = p_1^2 S_v(\Omega) \quad (1.26)$$

$$\text{and } S_{\varphi_2}(\Omega) = 2p_1^2 p_2 \int_{-\infty}^{+\infty} S_v(\Omega_1) S_v(\Omega - \Omega_1) d\Omega_1 \quad (1.27)$$

$$\text{while } B_\varphi(\Omega_1, \Omega_2) = B_{\varphi_1}(\Omega_1, \Omega_2) + B_{\varphi_2}(\Omega_1, \Omega_2) \quad (1.28)$$

$$\text{with } B_{\varphi_1}(\Omega_1, \Omega_2) = 2p_1^2 p_2 (S_v(\Omega_1) S_v(\Omega_2) + S_v(\Omega_1) S_v(\Omega_1 + \Omega_2) + S_v(\Omega_1 + \Omega_2) S_v(\Omega_2)) \quad (1.29)$$

$$\text{and } B_{\varphi_2}(\Omega_1, \Omega_2) = 8p_2^3 \int_{-\infty}^{+\infty} S_v(\Omega + \Omega_1) S_v(\Omega_1 - \Omega) S_v(\Omega) d\Omega \quad (1.30)$$

corresponds to the bispectrum of the loading process. When the loading is linearized and  $p_2 = 0$ , the power spectral density is thus proportional to the power spectral density of the water velocity fluctuations while the bispectrum trivially vanishes. When the loading is quadratized, however, the power spectral density is complemented by  $S_{\varphi_2}(\omega)$ , which contains some energy in the low frequency range, and the bispectrum is no longer nil.

According to Equation (1.20), the power spectral density and the bispectrum of the response are eventually given by

$$S_\chi(\Omega) = G_s(\Omega) S_\varphi(\Omega) \quad \text{and} \quad B_\chi(\Omega_1, \Omega_2) = G_b(\Omega_1, \Omega_2) B_\varphi(\Omega_1, \Omega_2) \quad (1.31)$$

where

$$G_s(\Omega) = |H_\chi(\Omega)|^2 \quad \text{and} \quad G_b(\Omega_1, \Omega_2) = H_\chi(\Omega_1) H_\chi(\Omega_2) H_\chi^*(\Omega_1 + \Omega_2) \quad (1.32)$$

are the structural kernels at second and third orders. They both depend on the frequency response function

$$H_\chi(\Omega) = \left(1 - \Omega^2 + 2i\xi\Omega\right)^{-1} \quad (1.33)$$

which completely characterizes the dynamical behavior of the considered oscillator. To get a first overview of the problem at second order, illustrations are provided in in Figure 1.2 and Figure 1.3 for the structural kernel and the power spectral density of both the loading and the response, respectively, whereas the constitutive functions of the bispectrum will be represented later on, in Chapter 3.

Since the power spectral density of the loading is divided into two parts, the same is done for the power spectral density of the response. The resulting functions are therefore shown separately and for two different loading cases, in Figure 1.3 (A1)-(A2) for  $\alpha_v = 1/4 < 1$  and in Figure 1.3 (B1)-(B2)  $\alpha_v = 2 < 1$ , respectively.

However, the structure responds in the background and the resonant regimes in Figure 1.3 (A1), (A2), and (B2), surprisingly, while the structure is exclusively excited in the inertial regime in Figure 1.3 (B1). In order to discriminate these two types of compositions, it consequently seems more appropriate to introduce a new parameter,  $\alpha_\varphi$ , which corresponds to the location of the main peak in the power spectral density of the loading instead of the water velocity fluctuations. More specifically, in the power spectral densities at stake, it means that  $\alpha_{\varphi_1} = \alpha_v$  and  $\alpha_{\varphi_2} = 0$ .

In the end, the probabilistic description of the response usually requires to calculate its statistics. The second and third central moments of the response can in particular be obtained by integrating the corresponding spectra of the response as follows

$$\sigma_\chi^2 = \int_{-\infty}^{+\infty} S_\chi(\Omega) d\Omega \quad \text{and} \quad \beta_\chi = \iint_{-\infty}^{+\infty} B_\chi(\Omega_1, \Omega_2) d\Omega_1 d\Omega_2 \quad (1.34)$$

and subsequently be used to compute the skewness of the response

$$\gamma_\chi = \frac{\beta_\chi}{\sigma_\chi^3} \quad (1.35)$$

which characterizes the extremes. Nevertheless, these operations are numerically expensive to perform due to the presence of sharp and distinct peaks in the integrands, as shown for the power spectral density of the response in Figure 1.3. This is thus what motivates the use of the Multiple Timescale Spectral Analysis. Unfortunately, some pieces are still missing to do so, as detailed in the upcoming section. The objective of this work is therefore to develop them.

## 1.5 Need for MTSA Extension

For the record, the inertia force can directly be discarded by imposing  $\kappa_f = 0$  in a wind engineering setting because the flow is not periodically oscillating as the waves are. In addition, in this specific context, the other dimensionless numbers listed in Equation (1.16), i.e.  $\lambda_u$ ,  $\xi_s$ ,  $\xi_a$ , and  $\alpha_v$ , are typically recognized as being all small [36]. The absolute value in Equation (1.20) can therefore be dropped based on the smallness of the turbulence intensity and the added damping. Indeed, it indicates that the mean velocity of the flow is much larger than the velocity of its fluctuations and of the structure itself. The direction of the relative wind velocity is therefore expected to stay in line with the mean flow and the absolute value is not needed anymore, because its argument is always positive.

Implementing this brings us directly back to the governing equation of a wind-excited oscillator when a quasi-steady assumption is made. It is accordingly given by

$$\chi'' + 2\xi\chi' + \chi = \frac{1}{2\lambda_u} (1 + \lambda_u v)^2 \quad (1.36)$$

and it can be expanded as

$$\chi'' + 2\xi\chi' + \chi = \frac{1}{2\lambda_u} + v + \frac{\lambda_u}{2} v^2 \quad (1.37)$$

where  $\xi := \xi_s + \xi_a$  is the total damping ratio, by definition. The smallness of this damping ratio also suggests that the memory of the structure is relatively long and, last but not least, the smallness of the frequency ratio indicates that the wind loading is much slower than the motion of the structure.

Calculating the statistics of the structural response to a buffeting wind excitation in the time domain consequently necessitates resorting to realizations that are long enough to capture the slow dynamics of the forces, but whose time steps are short enough to detect fast oscillations of the structure. And this is all the more accentuated if higher order statistics are to be estimated as well.

Alternatively, since the wind loading process is shown to be defined as a quadratic transformation of a Gaussian process, the response spectrum, bispectrum, and so on, can easily be expressed in the frequency domain and can then be integrated to get the same response statistics as in time domain. But again, the smallness of the frequency and the damping ratios imply that these spectra, in possibly multiple dimensions, exhibit sharp peaks whose accurate integration requires using many close quadrature points. In either way, obtaining the response statistics is therefore computationally demanding.

This is the reason why the Multiple Timescale Spectral Analysis has been used on these integrands with sharp peaks in the past as well. For instance, it helped to derive semi-analytical expressions for the second, third and fourth central moments of such an oscillator's response to a wind loading, without velocity feedback, first, in [12] and with a velocity feedback, then, in [36]. These statistics can therefore be computed much more efficiently than before, at the extra cost of a small but controllable discrepancy.

To do so, it was however assumed that the frequency ratio and the turbulence intensity (a.k.a. the relative wave length) were small, which is however not systematically valid for marine engineering applications and especially not when floating structures are moving in surge, as explained in Section 1.3.

The wave loads are thus expected to activate the system in its inertial regime, resulting in the emergence of other contributions than the background ones in the statistics of the response which are yet to be taken into account by the Multiple Timescale Spectral Analysis as well.

In Chapter 2, it is desired to overcome these restrictions and to develop solutions for the inertial components of the variance, first, that are valid no matter the power spectral density of the loading. A unified formulation is eventually sought in order to match the two limit cases that are observed when the frequency ratio is either much smaller, either much greater than unity and the contribution which is due to the peaks of the loading spectrum is either background, either inertial. This also aims at discovering to what extent it is possible to lower the level of the errors that are committed when the timescales are not well separated and the frequency ratio approaches unity.

Besides, the bispectrum of the response and its two-dimensional integral, which gives access to the third central moment of the response, are also intended to be examined in the light of the Multiple Timescale Spectral Analysis, in Chapter 3. After combination with the second moment, it is supposed to provide an efficient tool to compute the skewness of the response.

As at second order, the background and resonant components have already been derived in [12] and revisited in the light of the Multiple Timescale Spectral Analysis in [11]. However, in these studies, the loading bispectrum was assumed to be real-valued only. This was of course fully justified since the wind loading was expressed, as usual, as a quadratic transformation of a Gaussian process [70].

But when trying to apply this decomposition to the experimental wind data collected at Tokyo Polytechnic University [71], Michele Esposito discovered that a component seemed to be missing [72]. It then appeared that the imaginary part of the loading bispectrum is sometimes of the same order of magnitude as the real part for signals recorded in real conditions and therefore contributes to the third moment of the response as well [73]. Besides, evidences show that this is also likely to be observed with wave loads and this is even more widely recognized in this field [74, 75, 76, 77].

Although the current wind and wave loading models are not able to reproduce this particular feature because they are expressed as static transformations of a Gaussian process, they should theoretically be refined to include memory effects in the future.

In Chapter 3, the Multiple Timescale Spectral Analysis is thus applied to derive some expressions for the components of the third order response which are due to the existence of an imaginary part in the bispectrum of the loading when the loading is background, in order to complete the former decomposition of Denoël. Then, the contributions which originate from the product of the third order kernel with both the real and the imaginary parts of the loading bispectrum are tackled in a similar fashion when the loading is inertial.





## Chapter 2

# Second Central Moment

### 2.1 Introduction and Preliminary Considerations

In this chapter, simple expressions are formulated for the main components of the variance of an oscillator's response to a given wave loading. To do so, the integration of the power spectral density

$$S_\chi(\Omega) = G_s(\Omega) S_\varphi(\Omega) \quad (2.1)$$

where the structural kernel reads

$$G_s(\Omega) = |H_\chi(\Omega)|^2 \quad (2.2)$$

is handled with the help of the Multiple Timescale Spectral Analysis.

Following the discussion held in Section 1.5, it is anticipated that there are essentially a resonant contribution, which is due to the peaks of the structural kernel, and a loading contribution, which is either background, either inertial, but anyways always pertaining to the peaks of the loading spectrum.

As evidenced in the introduction for the background resonant decomposition and according to the perturbation theory, some assumptions need to be verified for the proposed approximations to be sufficiently accurate. They are therefore listed and adapted to the novel case of concern, i.e. the resonant inertial decomposition, at start, in Section 2.2.

Then, and contrary to the custom application of this general Multiple Timescale Spectral Analysis framework, the resonant component is first investigated, in Section 2.3. Second, the focus is placed on the inertial component, in Section 2.4, and a unified formula is ultimately sought for the so-called loading component, which reduces seamlessly to either the inertial, either the background component as they are both pertaining to the peak contained in the power spectral density of the loading.

### 2.2 Formulation of the Necessary Assumptions

Before anything else, the first step of the Multiple Timescale Spectral Analysis consists in identifying the origin of the main contributions to the integral at stake, and thus to the variance. Being readily related to the peaks of the loading spectrum and the structural kernel, the following hypotheses must be respected, then, in order to discern them from one another:

- (i) The power spectral density of the loading varies smoothly and moderately across the peaks of the structural kernel. In mathematical formalism, it signifies that the derivatives of the function are relatively much smaller than the value of the function itself in the vicinity of  $\Omega = \pm 1$ :

$$\left| (\Omega \mp 1)^i \partial_\Omega^i [S_\varphi(\pm 1)] / i! \right| \ll \left| S_\varphi(\pm 1) \right| \quad (2.3)$$

where  $\partial_{\Omega}^i(\cdot)$  denotes the  $i$ -th derivative with respect to the dimensionless frequency. In this event, the Taylor series expansion of the loading spectrum can be truncated at leading order as follows

$$S_{\varphi}(\Omega) = S_{\varphi}(\pm 1) \quad (2.4)$$

in the neighborhood of the poles. Such a constant term provides a proper approximation of  $S_{\varphi}(\Omega)$  in an interval where

$$\left| (\Omega \mp 1)^i / i! \right| \ll \left| S_{\varphi}(\pm 1) / \partial_{\Omega}^i [S_{\varphi}(\pm 1)] \right| \quad (2.5)$$

according to Equation (2.3).

- (ii) The peak frequency of the loading spectrum is significantly greater than the natural frequency of the oscillator. The frequency ratio and its inverse accordingly read

$$\alpha_{\varphi} = \frac{\omega_p}{\omega_0} \gg 1 \quad \Leftrightarrow \quad \Omega_{\varphi} = \frac{\omega_0}{\omega_p} \ll 1 \quad (2.6)$$

and are respectively much greater, or much smaller than unity. As a consequence, the system is expected to respond in its resonant regime, still, but also in its inertial regime, a contrario to the background one. Given that the perturbation theories usually rely on the use of small parameters, the inverse of the frequency ratio is therefore employed in the following when dealing with an inertial loading whereas, on the flip side, the frequency ratio is manipulated when the loading is background, since

$$\alpha_{\varphi} = \frac{\omega_p}{\omega_0} \ll 1 \quad \Leftrightarrow \quad \Omega_{\varphi} = \frac{\omega_0}{\omega_p} \gg 1 \quad (2.7)$$

in this respective event.

These assumptions reveal the existence of several small parameters which will subsequently be used from a perturbation perspective to decompose the power spectral density of the response into several parts. In these circumstances, the response spectrum is expected to be approximately given by

$$\tilde{S}_{\chi}(\Omega) = S_{\varrho}(\Omega) + S_{\varsigma}(\Omega) \quad (2.8)$$

where the subscripts  $\varrho$  and  $\varsigma$  respectively stand for the resonant and the inertial contributions to the function. Provided that these local approximations are accurate over the considered zones, bounded in the far field and integrable in an explicit way, we will demonstrate that the variance of the response can be estimated by the sum of two components with simple expressions

$$\tilde{\sigma}_{\chi}^2 = \sigma_{\varrho}^2 + \sigma_{\varsigma}^2 \quad (2.9)$$

which are again associated to either the resonance of the oscillator, either the inertial nature of the loading through the subscripts  $\varrho$  and  $\varsigma$ .

In brief, in Section 2.3 and Section 2.4, these two components and their dimensional counterparts are shown to be expressed as

$$\sigma_{\varrho}^2 = \frac{\pi}{2\xi} S_{\varphi}(1) \quad \Leftrightarrow \quad \sigma_{\varsigma}^2 = \frac{\pi\omega_0}{2\xi} \frac{S_f(\omega_0)}{k^2} \quad (2.10)$$

and

$$\sigma_{\zeta}^2 = \left(1 - \frac{S_{\varphi}(1)}{S_{\varphi}(\alpha_{\varphi})}\right) \sigma_{\text{ff}_{\varphi}}^2 \Leftrightarrow \sigma_i^2 = \left(1 - \frac{S_f(\omega_0)}{S_f(\omega_p)}\right) \frac{\sigma_{\text{ff}_f}^2}{k^2} \quad (2.11)$$

where

$$\sigma_{\text{ff}_{\varphi}}^2 = \int_{-\infty}^{+\infty} \frac{C_{\varphi} S_{\varphi}(\Omega)}{C_{\varphi} + \Omega^4} d\Omega \Leftrightarrow \sigma_{\text{ff}_f}^2 = \int_{-\infty}^{+\infty} \frac{C_f S_f(\omega)}{C_f + \omega^4} d\omega \quad (2.12)$$

with

$$C_{\varphi} = \frac{\alpha_{\varphi}^4}{|H_{\chi}(\alpha_{\varphi})|^{-2} - 1} \Leftrightarrow C_f = \frac{\omega_p^4}{|H_x(\omega_p)|^{-2} - 1} \quad (2.13)$$

and

$$H_{\chi}(\Omega) = (1 - \Omega^2 + 2i\xi\Omega)^{-1} \Leftrightarrow H_x(\omega) = (k - m\omega^2 + 2i\xi\omega)^{-1} \quad (2.14)$$

when  $\alpha_{\varphi} > 1$ . Besides, when  $\alpha_{\varphi} < 1$ , the inertial component extends in a unified way to the well-known background component by replacing the fourth powers in the above equations with zeroth powers as follows

$$\sigma_{\text{ff}_{\varphi}}^2 = \int_{-\infty}^{+\infty} \frac{S_{\varphi}(\Omega)}{1 + 1/C_{\varphi}} d\Omega \Leftrightarrow \sigma_{\text{ff}_f}^2 = \int_{-\infty}^{+\infty} \frac{S_f(\omega)}{1 + 1/C_f} d\omega \quad (2.15)$$

where

$$C_{\varphi} = \frac{1}{|H_{\chi}(\alpha_{\varphi})|^{-2} - 1} \Leftrightarrow C_f = \frac{1}{|H_x(\omega_p)|^{-2} - 1} \quad (2.16)$$

accordingly tend towards zero as  $\alpha_{\varphi}$  decreases.

## 2.3 Derivation of the Resonant Component

Starting with the resonant component, as explained hereabove, two contributions of equal magnitude are to be taken into account. They are originating from the peaks of the structural kernel which lie at  $\Omega = \pm 1$  and span a width of about a few damping ratios. Given that the general framework of the Multiple Timescale Spectral Analysis leaves some freedom to the user on how to find a locally accurate and explicitly integrable approximation for the power spectral densities over the range of interest, two options are explored in the following.

**First Option.** Although the focus is currently placed on finding an approximate expression for the original function instead of the residual one, the procedure presented for the resonant component in the introduction can be applied to the functions at stake and delivers the exact same leading order solution.

Accounting for the even nature of the loading spectrum, the local approximation of the response spectrum over the present zone of interest thus reads

$$S_{\varrho_1}(\Omega) = S_{\varphi}(1) \left( \frac{1/4}{(\Omega + 1)^2 + \xi^2} + \frac{1/4}{(\Omega - 1)^2 + \xi^2} \right) \quad (2.17)$$

in the initial coordinates and its integral gives the very simple expression

$$\sigma_{\varrho}^2 = \frac{\pi}{2\xi} S_{\varphi}(1) \quad (2.18)$$

for the resonant component of the variance of the response.

**Second Option.** The possibility to expand the structural kernel in partial fractions is investigated. It is shown to offer an interesting alternative for the resonant component because it allows to split the peaks without having to use and to truncate an asymptotic series.

On the real axis, the structural kernel under consideration can be decomposed into simple elements of the second kind only but they still feature two peaks, which are positioned in mirror image with respect to the y-axis. To succeed in separating them, the complex poles of the structural kernel are considered. They correspond to the roots of the four monomials  $(\Omega - B)$ ,  $(\Omega - B^*)$ ,  $(\Omega + B)$  and  $(\Omega + B^*)$  with  $B = \sqrt{1 - \xi^2} + \xi i$ . Thus, the structural kernel can equivalently be written

$$G_s(\Omega) = \left( \frac{A}{\Omega - B} \right) + \left( \frac{A^*}{\Omega - B^*} \right) - \left( \frac{A^*}{\Omega + B} \right) - \left( \frac{A}{\Omega + B^*} \right) \quad (2.19)$$

with

$$A = \left[ 8\xi^2 \sqrt{1 - \xi^2} + 8\xi (1 - \xi^2) i \right]^{-1} \quad (2.20)$$

after some standard algebra. In this sum, the first two and the last two terms are respectively responsible for the apparition of a peak on the right and a peak on the left of the y-axis.

The power spectral density of the response can consequently be separated into four pieces as well. Then, the appropriate stretched coordinate among  $\Omega = (\Xi\Upsilon + 1)$  and  $\Omega = (\Xi\Upsilon - 1)$ , with  $\Upsilon$  being of order one at most and  $\Xi$  being an arbitrary small number, can be introduced into the former and the latter two terms in order to focus on their respective resonant peak.

Being symmetric, the loading spectrum can ultimately be replaced by the constant value  $S_{\varphi}(+1) = S_{\varphi}(-1)$  in these specific zones, under Assumption (i), and the local approximation of the response spectrum thus reads

$$S_{\varrho_2}(\Omega) = G_s(\Omega) S_{\varphi}(1) \quad (2.21)$$

at leading order. This expression is simpler than Equation (2.17) and the residual it provides is expected to be more convenient to handle with the Multiple Timescale Spectral Analysis in the next step.

Nevertheless, integrating Equation (2.17) and Equation (2.21) yield the same formula for the resonant component of the variance. This illustrates the freedom in choosing the local, accurate and far-field integrable approximations of the power spectral densities, which are effectively not unique, when using the Multiple Timescale Spectral Analysis.

## 2.4 Derivation of the Inertial Component

Following the method described in [11] and briefly recalled in the introduction, these first approximations are subtracted from the original integrands to yield the residual functions

$$\hat{S}_{\chi_1}(\Omega) = S_{\chi}(\Omega) - S_{\varrho_1}(\Omega) \quad \text{and} \quad \hat{S}_{\chi_2}(\Omega) = S_{\chi}(\Omega) - S_{\varrho_2}(\Omega) \quad (2.22)$$

which do no longer contain any significant contribution in the vicinity of the poles, see the dashed lines in Figure 2.1 for instance. As a consequence, the remaining peaks in these new integrands are

twofold. They are attributed to the loading spectrum and are distributed symmetrically about the y-axis again.

To make this more evident, the loading spectrum can be factored out in the residual functions. Thus, for the first and the second option, they respectively read

$$\hat{S}_{\chi_1}(\Omega) = \hat{G}_{s_1}(\Omega) S_\varphi(\Omega) \quad \text{and} \quad \hat{S}_{\chi_2}(\Omega) = \hat{G}_{s_2}(\Omega) S_\varphi(\Omega) \quad (2.23)$$

where

$$\hat{G}_{s_1}(\Omega) = G_s(\Omega) - \frac{S_{\vartheta_1}(\Omega)}{S_\varphi(\Omega)} \quad \text{and} \quad \hat{G}_{s_2}(\Omega) = \left(1 - \frac{S_\varphi(1)}{S_\varphi(\Omega)}\right) G_s(\Omega) \quad (2.24)$$

are further referred to as the *residual kernels*.

The coordinate stretching  $\Omega = (1 + \Xi\Upsilon)/\Omega_\varphi$  with  $\Upsilon \sim \text{ord}(1)$  and  $\Xi \ll 1$  again is injected into the residual kernels in order to zoom on their rightmost peaks, which are positioned at  $\Omega = 1/\Omega_\varphi$ . The equations are then expanded in series for small values of the frequency ratio,  $\Omega_\varphi \ll 1$ . It gives

$$\hat{G}_{s_1}(\Upsilon) = -\frac{1}{2} \frac{S_\varphi(\Psi)}{S_\varphi(\Upsilon)} \frac{\Omega_\varphi^2}{(1 + \Xi\Upsilon)^2} + \frac{\Omega_\varphi^4}{(1 + \Xi\Upsilon)^4} + \mathcal{O}(\Omega_\varphi^6) \quad (2.25)$$

and

$$\hat{G}_{s_2}(\Upsilon) = \left(1 - \frac{S_\varphi(\Psi)}{S_\varphi(\Upsilon)}\right) \frac{\Omega_\varphi^4}{(1 + \Xi\Upsilon)^4} + \mathcal{O}(\Omega_\varphi^6) \quad (2.26)$$

with  $\Xi\Psi = (\Omega_\varphi - 1)$ , respectively. As it can clearly be appreciated at this point, the expression is indeed more complicated in the first case than in the second. Theoretically, the identification of the leading term in Equation (2.25) requires to formulate an additional condition regarding the relative smallness of  $S_\varphi(\Psi)/S_\varphi(\Upsilon)$  with respect to  $\Omega$ . It is however not necessary to do so in Equation (2.25) and this justifies why the second option is kept from there on. In the neighborhood of the origin,  $\Upsilon = 0$ , the inverse of the loading spectrum can also be rewritten as follows

$$\frac{1}{S_\varphi(\Upsilon)} = \frac{1}{S_\varphi(0)} - \Upsilon \partial_\Upsilon [S_\varphi(0)] \frac{1}{S_\varphi^2(0)} + \mathcal{O}(\Upsilon^2) \quad (2.27)$$

by making use of Taylor series expansion. Given that the loading spectrum reaches its maximum value at this specific location, its inverse can actually be considered as small enough to maintain the convergence of the series and to be replaced by a constant value over the whole range of interest. Finally, in the region spanned by the strained coordinate, the kernel therefore appears to be properly estimated by a monomial of  $(-4)$ -th degree. After returning to the original coordinates, it can consequently be approximated by

$$\tilde{G}_s(\Omega) = G_s(1/\Omega_\varphi) (\Omega\Omega_\varphi)^{-4} \quad (2.28)$$

which replicates well this decreasing trend but also the value of the initial function at the location of the considered peak. However, it has the disadvantage of tending towards infinity as the circular frequency approaches zero. It is not a problem as long as the loading spectrum decreases rapidly enough to ensure that the local approximation of the response spectrum

$$S_\zeta(\Omega) = \left(1 - \frac{S_\varphi(1)}{S_\varphi(1/\Omega_\varphi)}\right) \tilde{G}_s(\Omega) S_\varphi(\Omega) \quad (2.29)$$

is integrable in the vicinity of the origin. This condition is commonly satisfied when the loading corresponds to a linear transformation of a water-particle velocity process, whose power spectrum is defined as in Equation (1.26).

In this event, the inertial component of the variance is eventually independent of any structural property and can be established a priori, maybe even in closed-form, for a given loading spectrum. In general, however, it reads

$$\sigma_{\zeta}^2 = \left(1 - \frac{S_{\varphi}(1)}{S_{\varphi}(1/\Omega_{\varphi})}\right) \Omega_{\varphi}^{-4} G_s(1/\Omega_{\varphi}) \sigma_{\mathbb{J}_1}^2 \quad (2.30)$$

where

$$\sigma_{\mathbb{J}_1}^2 = \int_{-\infty}^{+\infty} \Omega^{-4} S_{\varphi}(\Omega) d\Omega \quad (2.31)$$

is the spectral moment of order  $-4$  of the loading. It seems interesting to notice that the multiplicative factor  $(1 - S_{\varphi}(1)/S_{\varphi}(1/\Omega_{\varphi}))$  in Equation (2.30) is expected to be approximately equal to unity on the basis of Assumption (ii), provided that the loading spectrum exhibits a relatively sharp peak at  $\Omega = 1/\Omega_{\varphi}$ .

But otherwise, it is important to consider its exact value because it ensures that the proposed decomposition is also suitable to deal with a flatter loading spectrum. In the limit case of a white-noise forcing process, for instance, the power spectral density is constant,  $S_{\varphi}(1) = S_{\varphi}(1/\Omega_{\varphi})$ , and the multiplicative factor drops down to zero. The loading component consequently disappears and the variance of the response is eventually given by the resonant component only, as it is supposed to.

This being said, the local approximation (2.29) of the response spectrum provided hereabove might not always be integrable. To overcome this problem, instead of (2.28), the kernel can alternatively be replaced by

$$\tilde{G}_s(\Omega) = \frac{C}{C + \Omega^4} \quad (2.32)$$

where

$$C = \frac{G_s(1/\Omega_{\varphi})}{\Omega_{\varphi}^4 - \Omega_{\varphi}^4 G_s(1/\Omega_{\varphi})} \quad (2.33)$$

is selected so that this  $(0, 4)$  Padé approximant is bounded and matches the initial function at the origin. With this specific choice, the inertial component of the response spectrum is given by

$$S_{\zeta}(\Omega) = \left(1 - \frac{S_{\varphi}(1)}{S_{\varphi}(1/\Omega_{\varphi})}\right) \tilde{G}_s(\Omega) S_{\varphi}(\Omega) \quad (2.34)$$

again, with a different definition of the approximate kernel though, and the variance reads

$$\sigma_{\zeta}^2 = \left(1 - \frac{S_{\varphi}(1)}{S_{\varphi}(1/\Omega_{\varphi})}\right) \sigma_{\mathbb{J}_2}^2 \quad (2.35)$$

where

$$\sigma_{\mathbb{J}_2}^2 = \int_{-\infty}^{+\infty} \frac{C S_{\varphi}(\Omega)}{C + \Omega^4} d\Omega \quad (2.36)$$

seems less advantageous to evaluate, at first glance, than Equation (2.31) because it mixes structural and loading characteristics.

Nevertheless, Equation (2.31) and Equation (2.36) boil down to the same expression if the fourth powers of  $\Omega_{\varphi}$  and  $\Omega$  are replaced by zeroth powers as it should for the background component. It

thus reads

$$S_\zeta(\omega) = \left(1 - \frac{S_\varphi(1)}{S_\varphi(1/\Omega_\varphi)}\right) G_s(1/\Omega_\varphi) S_\varphi(\Omega) \quad (2.37)$$

and

$$\sigma_\zeta^2 = \left(1 - \frac{S_\varphi(1)}{S_\varphi(1/\Omega_\varphi)}\right) G_s(1/\Omega_\varphi) \sigma_\varphi^2 \quad (2.38)$$

which implies that the background component presented in Equation (15) can eventually be recovered by acknowledging that  $1/\Omega_\varphi \ll 1$ .

## 2.5 Validation and Parametric Analysis

The simple expressions derived hereabove for the resonant and the loading components of the spectral densities and the second moments of the responses to a given loading are assessed in this section. To this aim, the results they provide under a linearized, or quadratized and a non-polynomial loading are compared to the values obtained by integrating the power spectral densities of the corresponding responses.

### Presentation of the results

To begin with, the dimensionless definition derived in the end of Section 1.4 for the power spectral density of the water velocity fluctuations is employed. For the record, it reads

$$S_v(\Omega) = \sqrt{\frac{3}{\pi}} \frac{\alpha_v^2}{|\Omega|^3} \exp\left(-\frac{3\alpha_v^4}{4\Omega^4}\right) \quad (2.39)$$

and solely depends on  $\alpha_v$ . In the following, this parameter is set equal to 5 for illustrating the power spectral densities of the responses under a fast loading, see Figure 2.1. The variances, however, are represented for  $\alpha_v \in [10^{-2}, 10^2]$ , see Figure 2.2. It means that both the background and the inertial components are examined depending on whether  $\alpha_v < 1$  or  $\alpha_v > 1$ . They are pictured by orange patches and lines in Figure 2.1 and Figure 2.2, respectively, whereas the resonant components are colored in green. As shown in these figures, three turbulence intensities are also picked:  $\lambda_u = \{0.1, 0.3, 1\}$ .

First, a linearized wave forcing process is considered. It is expressed as a linear transformation of the water velocity fluctuations. As a consequence, its power spectral density is given by

$$S_{\varphi_1}(\Omega) = p_1^2 S_v(\Omega) \quad (2.40)$$

and contains a peak at  $\alpha_{\varphi_1} = \alpha_v$ . The values of the coefficient,  $p_1$ , are also computed in an analytical way as explained in Section 1.4 and are listed in Table 2.1 with respect to the selected relative wave length. The power spectral densities of the responses are subsequently calculated through the analytical definition

$$S_{\chi_1}(\Omega) = G_s(\Omega) S_{\varphi_1}(\Omega) \quad (2.41)$$

for  $\alpha_v = 5$  and  $\xi = \{0.1\%, 1\%, 10\%\}$ . They are illustrated by black lines in Figure 2.1-(A). When using the Multiple Timescale Spectral Analysis, the resonant and the inertial components of these power spectral densities are approximated by Equation (2.21) and Equation (2.34). They are represented in Figure 2.1-(A). The sums of these two contributions are then pictured by black dots in Figure 2.1-(A).

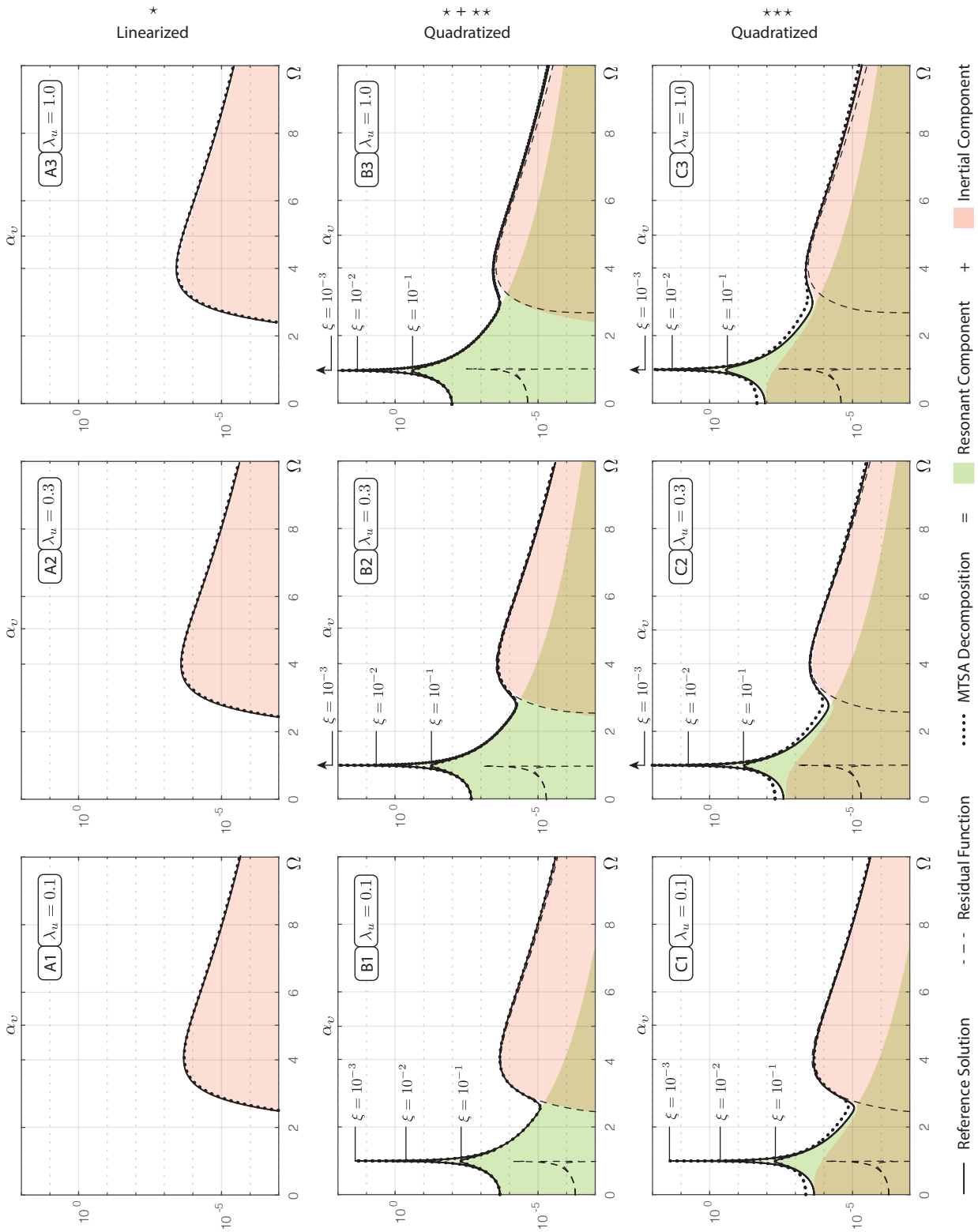


FIGURE 2.1: Power spectral densities of the response to a linearized and a quadraticized drag loading for different turbulence intensities of the waves and damping ratios of the system.



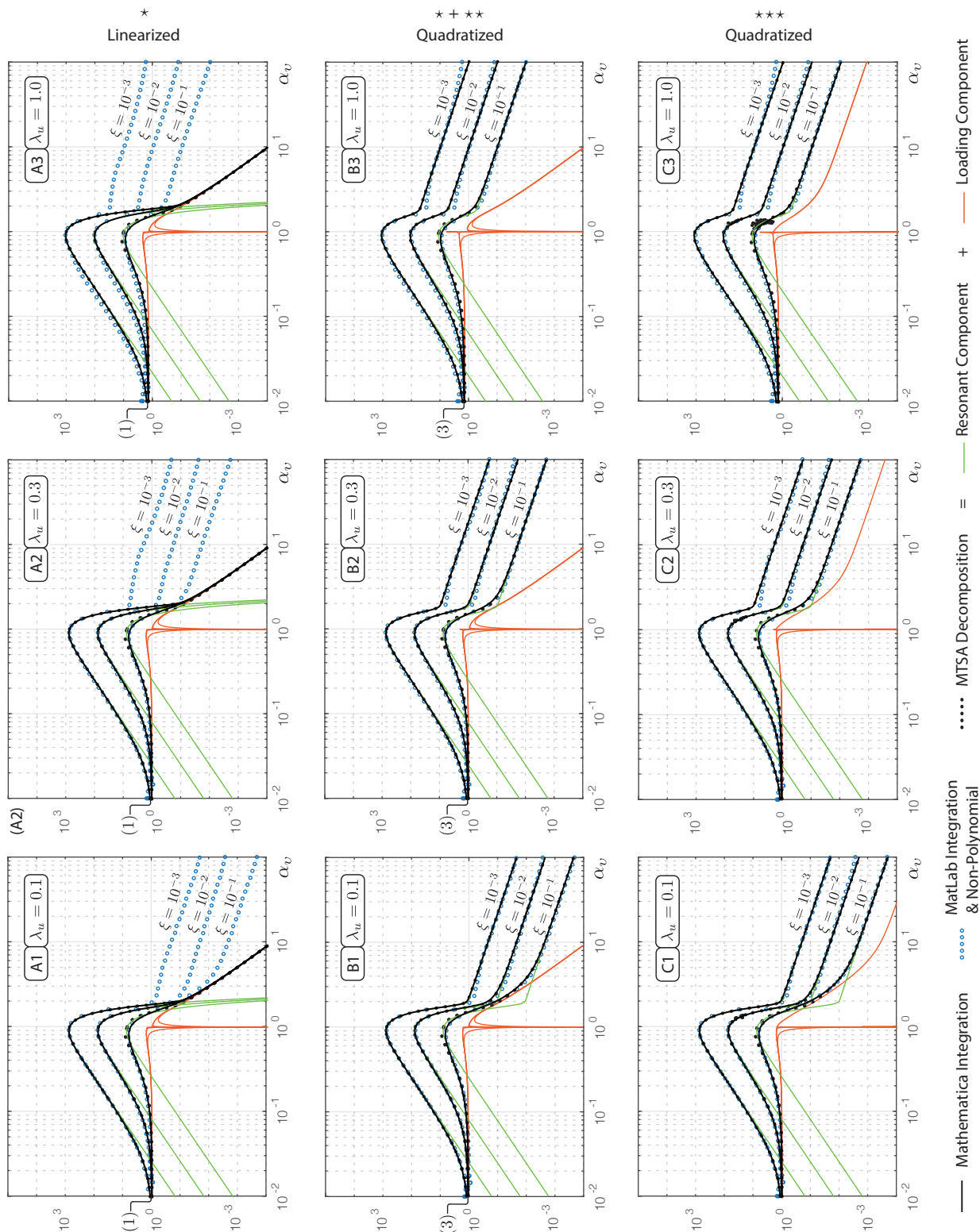


FIGURE 2.2: Variances of the response to a linearized, a quadratized and a non-polynomial drag loading for different turbulence intensities of the waves and damping ratios of the system.

Similar results are shown for the variances in Figure 2.2-(A), for various values of  $\alpha_v$ . Black lines are obtained through the numerical integration of Equation (2.41) which is handled by using the adaptive algorithm with default parameters implemented in Version 12.0.0.0 of Wolfram Mathematica. Green and orange lines represent respectively the resonant and the loading (background or inertial) components, which are given by Equation (2.21) and Equation (2.37), or Equation (2.21) and Equation (2.34), depending on whether  $\alpha_v < 1$  or  $\alpha_v > 1$ . Their sums are then depicted by black dots, which thus correspond to the approximation provided by the Multiple Timescale Spectral Analysis.

Second, a quadratized wave loading process is considered. The corresponding results are illustrated in Figure 2.1-(B,C) and Figure 2.2-(B,C). The power spectral density of the loading is now complemented by an additional contribution which is obtained by auto-convolving the power spectral density of the water velocity fluctuations as follows

$$S_{\varphi_2}(\Omega) = 2p_1^2 p_2 \int S_v(\Omega_1) S_v(\Omega - \Omega_1) d\Omega_1 \quad (2.42)$$

and where  $p_2$  is the second coefficient of the polynomialization, see Table 2.1 for their values. This second part of the loading spectrum consequently features a bump around the origin, as well as another one of half the size at twice the peak frequency of the waves, see Figure 1.3.

The power spectral densities of the responses to such a quadratized loading are represented by black lines Figure 2.1-(B,C). Two scenarios are then investigated regarding the use of the approximate expressions derived with the help of the Multiple Timescale Spectral Analysis. Either the second part of the loading spectrum is considered independently of the first one and the results it provides in terms of response,  $(\star\star)$ , are just added to those obtained with the linearized loading,  $(\star)$ . This option is denoted by  $(\star + \star\star)$  and presented in Figure 2.1-(B) and Figure 2.2-(B). Either the first and the second parts of the loading spectrum are considered as a whole to get the results in terms of response which are denoted by  $(\star\star\star)$  and presented in Figure 2.1-(C) and Figure 2.2-(C).

When the loading is background, the power spectral densities of the responses can be approximated by the sum of a resonant and a background component, as given by Equation (2.21) and Equation (2.37), in both scenarios. Likewise, the resonant and the background components of the variance are thus provided by Equation (2.18) and by Equation (2.38). Please notice that the background components respectively correspond to the integral of  $S_{\varphi_1}(\Omega)$ ,  $S_{\varphi_2}(\Omega)$  and  $S_{\varphi_3}(\Omega)$ , which can be expressed in closed-form as  $p_1^2 = (1)$ ,  $2p_2^2 = (2)$  and  $(1) + (2) = (3)$ . The values of these components for  $\lambda_u = \{0.1, 0.3, 1\}$  are gathered in Table 2.1.

Otherwise, when the loading is inertial, the power spectral densities and the variances of the responses are treated in two different ways, as explained above.

- $(\star + \star\star)$  In the first scenario, the center of gravity of  $S_{\varphi_2}(\Omega)$  is identified as being located in the low frequency range. The second part of the response spectrum is therefore approximated by the sum of a resonant and a background contribution, instead of an inertial one, even if  $\alpha_v \gg 1$ . They are respectively given by Equation (2.21) and Equation (2.37).
- $(\star\star\star)$  In the second scenario, however, the main peak is located at  $\alpha_\varphi \approx \alpha_v$  in the global loading spectrum. In addition, this power spectral density is not exponentially small in the neighborhood of the origin, by contrast with  $S_{\varphi_1}(\omega)$ . The power spectral density of the response is hence approximated by the sum of the resonant and the inertial contributions given by Equation (2.21) and Equation (2.34), respectively.

Again, similar results are eventually computed for the variances. In order to ease the understanding, information regarding the equations employed when applying the Multiple Timescale Spectral Analysis are summarized in Table 2.2 and Table 2.3, depending on whether  $\alpha_v \ll 1$  or  $\alpha_v \gg 1$ .

Globally, the same color code as before is used for the power spectral densities in Figure 2.1-(B,C) and the variances in Figure 2.2-(B,C).

TABLE 2.1: Polynomial coefficients and background components.

$\lambda_u$	$p_1$	$p_2$	(1)	(2)	(3)
0.1	1.0	0.05	1.0	0.005	1.005
0.3	1.0	0.15	1.0	0.045	1.045
1.0	1.17	0.34	1.4	0.231	1.631

TABLE 2.2: Numbers of the equations employed when  $\alpha_v < 1$ .

Load Case	Freq. Ratio	$S_\varrho(\Omega)$	$S_\zeta(\Omega)$	$\sigma_\varrho^2$	$\sigma_\zeta^2$
★	$\alpha_{\varphi_1} \ll 1$	Eq. (2.21)	Eq. (2.37)	Eq. (2.18)	Eq. (2.38)
★★	$\alpha_{\varphi_2} \ll 1$				
★★★	$\alpha_{\varphi_3} \ll 1$				

TABLE 2.3: Numbers of the equations employed when  $\alpha_v > 1$ .

Load Case	Freq. Ratio	$S_\varrho(\Omega)$	$S_\zeta(\Omega)$	$\sigma_\varrho^2$	$\sigma_\zeta^2$
★	$\alpha_{\varphi_1} \gg 1$	Eq. (2.21)	Eq. (2.29)	Eq. (2.18)	Eq. (2.30)
★★	$\alpha_{\varphi_2} \approx 1$		Eq. (2.37)		Eq. (2.38)
★★★	$\alpha_{\varphi_3} \gg 1$		Eq. (2.34)		Eq. (2.35)

Last but not least, a non-polynomial Morison drag loading, as derived in Equation (1.21), is considered in order to provide reference values for the variances which are independent of the polynomialization. The power spectral density of such a loading can actually be defined in an analytical way as well but, since it involves cumbersome expressions, it will not be done herein. Instead, it is calculated from generated signals.

To do so, the power spectral density of the nondimensional water velocity fluctuations is first computed for the corresponding set of dimensionless numbers, according to Equation (2.39). Next, a time history of the Gaussian process  $v(\tau)$  is generated by computing the inverse Fourier transform of

$$\mathcal{F}[v(\tau)](\omega) = \sqrt{N_f \Omega_s S_v(\omega_i)} \exp(i\theta_i) \quad (2.43)$$

where  $\Omega_s = \max(20, 20\alpha_v)$  is the sampling frequency,  $N_f = 10^7$  is the number of frequencies employed to represent the power spectral density in the range  $[-\Omega_s, \Omega_s]$  and  $\theta_i$  is a phase angle, randomly distributed in the interval  $[0, 2\pi[$ . This realization then feeds Equation (1.21) and provides a loading sample whose power spectral density can subsequently be computed by using standard algorithms [78].

Although it looks like a Monte Carlo simulation at the beginning, this loading history is not considered as an input for the equations of motion and the recourse to a time marching algorithm is bypassed afterwards. To do so, the power spectral density of the response is directly calculated by multiplying the power spectral density of the non-polynomial loading by the structural kernel and the variances are eventually obtained by integrating them with a trapezoidal scheme. In total, 5000 points are distributed over the frequency domain, in the positive range. Among those, a fine mesh of 1000 points is considered in the interval  $[1 - 4\xi, 1 + 4\xi]$  in order to properly capture the area under the resonant peaks, which become sharper as the damping decreases. These values are

considered for reference only. Thus, they are not approximated with the expressions derived in this chapter.

## Discussion of the results

Overall, the validation of these expressions is endorsed by the good agreement of the results obtained for a large range of frequency ratios, damping ratios and turbulence intensities. As a consequence, the proposed decomposition appears to provide accurate estimations for the variances of various systems, be they subjected to quasi-static or inertial loads expressed as a linear, polynomial or whatever transformation of a Gaussian process.

However and although the Multiple Timescale Spectral Analysis is not to blame, the power spectral densities, and hence the variances of the responses, do not contain any resonant component when the loading is linearized and inertial, see the right parts of the graphs in Figure 2.2-(A) for the statistics. As well established in the field, this is due to the exponential decay observed at low frequencies in the power spectral density of the wave velocities. This specificity implies that Equation (2.40) is integrable and thus Equation (2.30) can be used to get the inertial components of the statistics. But, in the meantime, the value of  $S_{\varphi_1}(1)$  is so small that the resonant peaks do not emerge at all in this zone, no matter how slightly damped the structure is and thus how sharp the peaks are in the kernel.

Accounting for the nonlinear nature of the loading by means of its quadratic or non-polynomial formulations solves this problem and allows to observe the typical increase of the resonant components for small damping ratios, which is suggested by the apparition of this specific parameter in the denominator of Equation (2.18). The resonant components also grow with the relative wave length. This effect, in turn, can be explained by looking at the expression provided in Equation (2.42) for  $S_{\varphi_2}(\Omega)$ . This additional part in the power spectral density of the loading is proportional to the square of the second polynomial coefficient. Therefore, and as shown in Table 2.1 as well, the stronger the relative wave length, the larger the coefficient and hence the power spectral density. Moreover, this additional contribution features a bump in the low frequency range, near the resonant peaks, as well as another half one at twice the peak frequency of the waves.

In the first scenario, once the resonant component is removed, the residual function is thus expected to provide (i) a background component, which is due to the bump located in the vicinity of the origin, and (ii) an inertial component, which is due to the bump located at twice the peak frequency of the waves. Interestingly enough, the contribution of (i) can approximately be ignored on the basis that the characteristic frequency for this second part of the loading spectrum is actually close to one and the multiplicative factor  $(1 - S_{\varphi}(1)/S_{\varphi}(\alpha_{\varphi}))$  approaches zero. Besides, the contribution of (ii) can be discarded as well on the basis that the corresponding bulge is half the size of the former and is placed in an area where the kernel is also much smaller.

In fact, it is precisely because these effects cannot be treated aside in the second scenario that the contribution of (i) is accounted for twice, in both the resonant component and the inertial component, resulting in the slight overestimation of the response spectrum which is observed near the origin, in Figure 2.1-(C). Nevertheless, it does not seem to affect the variances.

Although it is expected that the proposed decomposition is a little less reliable when the peak frequency of the loading is close to the natural frequency of the system, meaning that Assumption (ii) is violated, the multiplicative factor interestingly helps to limit the errors over there. This is all the more verified when the damping is small since the resonant peaks are then much sharper than the loading peaks. This, in turn, ensures that Assumption (i) is respected even if all of these peaks are almost superimposed. The resonant component is therefore expected to cover them both at once while the background/inertial component drops down to zero thanks to cancelation of the multiplicative factor.





## Chapter 3

# Third Central Moment

### 3.1 Introduction and Preliminary Considerations

The objective of this chapter is to derive a semi-analytical approximation for the third central moment of the response, in a similar fashion as the decomposition provided for the second central moment in the previous chapter. To do so, the Multiple Timescale Spectral Analysis is applied to the bispectrum of the response which can be written in the canonical form

$$B_\chi(\Omega_1, \Omega_2) = G_b(\Omega_1, \Omega_2) B_\varphi(\Omega_1, \Omega_2) \quad (3.1)$$

where  $G_b(\Omega_1, \Omega_2)$  and  $B_\varphi(\Omega_1, \Omega_2)$  correspond respectively to the structural kernel and the loading bispectrum.

For symmetry reasons, the imaginary part of the response bispectrum does not contribute at all to the third central moment of the response, as it is to be expected because this process, and hence its central moments, are real-valued. It is therefore possible to compute the third central moment as follows

$$\beta_\chi = \iint \Re[B_\chi(\Omega_1, \Omega_2)] d\Omega_1 d\Omega_2 \quad (3.2)$$

instead of integrating the imaginary part of the response bispectrum as well.

To get familiar with the derivation of semi-analytical formulations dedicated to such an integration in two dimensions, this chapter firstly deals with the third central moment of an oscillator's response to a non-normal and quasi-static loading because it has already been treated in [12]. It has then led to the development of the Multiple Timescale Spectral Analysis method, and it has eventually been revisited in the light of this general framework in [11].

In the present configuration, however, the loading is not supposed to be expressed as a static nonlinear transformation of a Gaussian process. As a consequence, the loading bispectrum is theoretically complex-valued and the real part of the response bispectrum reads

$$\Re[B_\chi(\Omega_1, \Omega_2)] = \Re[G_b(\Omega_1, \Omega_2)] \Re[B_\varphi(\Omega_1, \Omega_2)] - \Im[G_b(\Omega_1, \Omega_2)] \Im[B_\varphi(\Omega_1, \Omega_2)] \quad (3.3)$$

where the second term can no longer be discarded. A new component is therefore required to take the product of the imaginary parts into account. A simple expression for this specific term is derived for the first time in this thesis, in Section 3.4.

In parallel, this chapter also focuses on the third moment of the response of an oscillator subjected to a non-normal but inertial loading, and in particular on two other new contributions. They come from the emergence of high-frequency peaks in the bispectrum of the response, which are due to those of either the real, either the imaginary parts of the loading bispectrum. The expressions of these two components are formulated in Section 3.5.

### 3.2 Identification of the Main Components

Before determining the conditions under which the Multiple Timescale Spectral Analysis is able to operate, it seems appropriate to start by describing the functions under consideration in more details because their characteristics are not so commonly known, although these functions are particularly useful in a non-linear and non-normal setting. This section therefore aims at identifying the areas where peaks are intended to protrude in the bispectrum of the response, or where the volume below the surface is significant, in order to pave the way for the effective inclusion of their contributions to the third central moment of the response in a multiple timescale context.

Being defined as the product of three frequency response functions whose poles are respectively located on the lines of equation

$$\{\Omega_1 = \pm 1, \Omega_2 \in \mathbb{R}\} \quad , \quad \{\Omega_1 \in \mathbb{R}, \Omega_2 = \pm 1\} \quad \text{and} \quad \{\Omega_1 \in \mathbb{R}, \Omega_2 = \pm 1 - \Omega_1\} \quad (3.4)$$

as shown in Figure 3.1, the structural kernel exhibits six *crest/ditch* lines around these zones, on frequency bands whose width is of order  $\xi$ , and some bi-resonant peaks at their two-by-two crossings, on frequency patches whose size is of order  $\xi \times \xi$ . These peaks are called as such in order to indicate that they are due to the interaction of two poles from either two out of three frequency response functions. Meanwhile, the third frequency response function is activated in its background region for six of these peaks. They are therefore higher than the six other ones for which the third frequency response function is excited in its inertial region, see Figure 3.2.

Overall, the real part of the structural kernel discloses essentially:

- six *background bi-resonant* peaks centered at  $(\Omega_1, \Omega_2) = (\pm 1, 0)$ ,  $(0, \pm 1)$  and  $(\pm 1, \mp 1)$ ;
- six *bi-resonant inertial* peaks centered at  $(\Omega_1, \Omega_2) = \pm(1, -2)$ ,  $\pm(2, -1)$  and  $\pm(1, 1)$ ;
- six triangular basins in-between the ridges, the background and the inertial peaks;
- a flat *tri-background zone* whose height is of order one in the vicinity of  $(\Omega_1, \Omega_2) = (0, 0)$ .

Similar features are observed in the imaginary part of the structural kernel, except that the height of the background zone drops down to zero and the peaks are called *double* because they are spiking on the two sides of the pole lines, reaching opposite values at these locations and passing by zero in between. In order to get a better picture of what this function looks like, it is represented in Figure 3.2 as well.

This figure also illustrates the symmetries which are theoretically observed in the real and the imaginary parts of both the structural kernel and the bispectrum of the loading. It is interesting to notice for a further understanding of how the product of their imaginary parts looks like, although the bispectrum of the loading is just real-valued in here, as explained before.

As shown in Figure 3.3, the real part of the loading bispectrum is characterized by a twelve peaks pattern like the structural kernel, except that the high versus low peaks are switched and are now positioned at  $(\Omega_1, \Omega_2) = (\pm 2\alpha_\varphi, 0)$ ,  $(0, \mp 2\alpha_\varphi)$ ,  $(\pm 2\alpha_\varphi, \mp 2\alpha_\varphi)$  or  $(\Omega_1, \Omega_2) = (\pm \alpha_\varphi, 0)$ ,  $(0, \mp \alpha_\varphi)$ ,  $(\pm \alpha_\varphi, \mp \alpha_\varphi)$ , respectively. This inversion of their aspect ratio is due to the faster decay of the bispectrum towards the origin than towards infinity, in contrast with the structural kernel.

If the loading is quasi-static (i.e.  $\alpha_\varphi \ll 1$ ), these peaks will appear as such amid the tri-background zone, in the bispectrum of the response, see Figure 3.4-①. Then, given the rapid decrease of the loading bispectrum as the frequencies increase, the smallness of the bi-resonant inertial peaks with respect to the background bi-resonant peaks, see Figure 3.4-②, is all the more accentuated and it results in the possibility to simply neglect their contribution.

If the loading is inertial (i.e.  $\alpha_\varphi \gg 1$ ), the bi-resonant inertial peaks do not disappear from the response bispectrum, see Figure 3.5-③. In addition, the crest/ditch arrangements in the structural



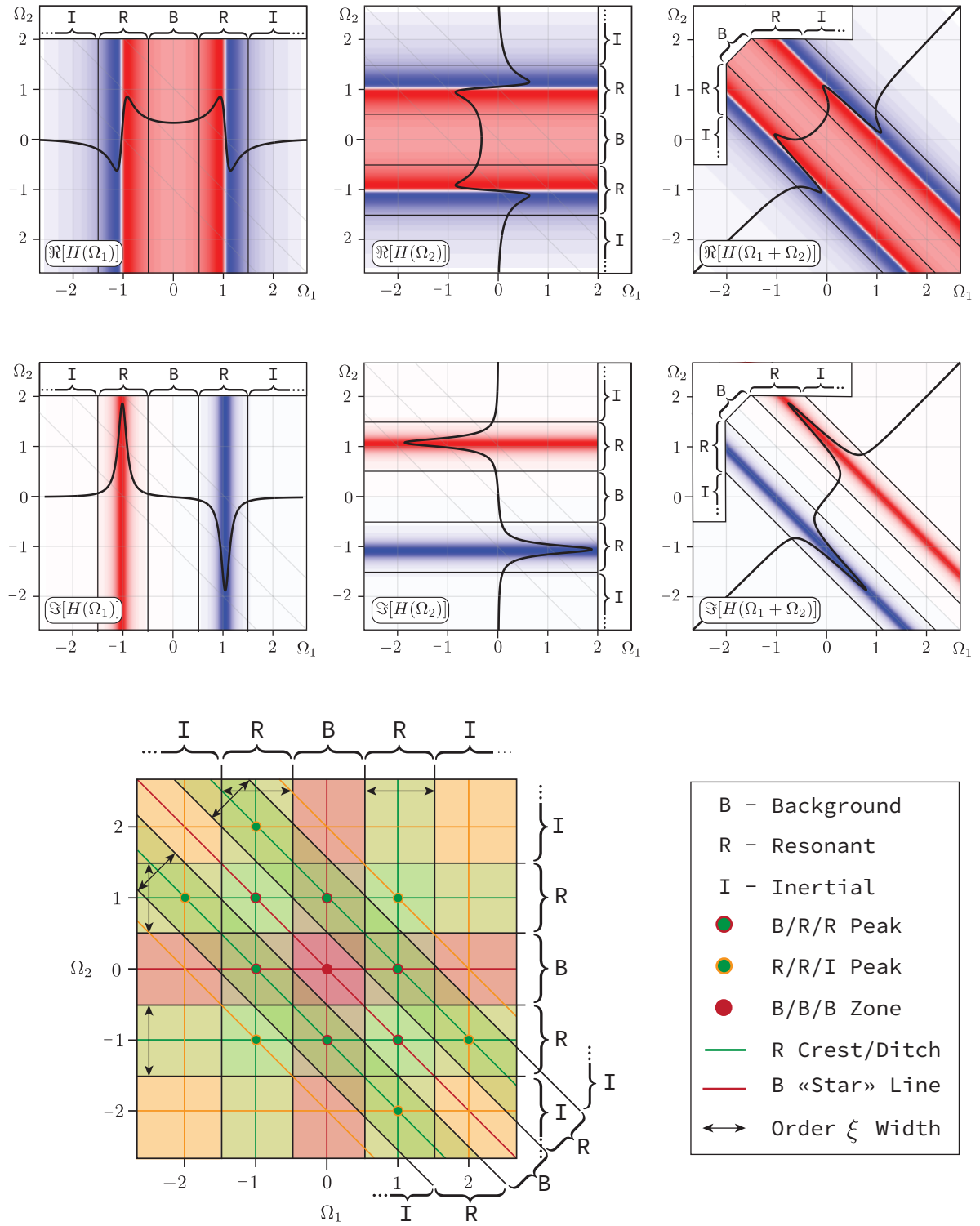


FIGURE 3.1: Frequency Response Functions - B/R/I Zones

kernel create some pairs of double peaks in the resonant bi-inertial frequency ranges, see Figure 3.5-④.

To summarize, the bispectrum of the response eventually exhibits six background bi-resonant peaks centered at  $(\Omega_1, \Omega_2) = (\pm 1, 0)$ ,  $(\pm 1, 0)$  and  $(\pm 1, \mp 1)$ , which come from the products of both the real and the imaginary parts of the loading spectrum and the structural kernel, plus a background zone with twelve bumps close to the origin, which is due to the product of the real parts only, when the loading is associated to the slow timescale, or six background bi-resonant peaks centered at  $(\Omega_1, \Omega_2) = (\pm 1, 0)$ ,  $(\pm 1, 0)$  and  $(\pm 1, \mp 1)$ , plus six bi-resonant inertial peaks centered at  $(\Omega_1, \Omega_2) = \pm(1, -2)$ ,  $\pm(2, -1)$  and  $\pm(1, 1)$ , which originate from the product of the real parts only, and six resonant inertial peaks centered at  $(\Omega_1, \Omega_2) = (\pm \alpha_\varphi, 0)$ ,  $(0, \pm \alpha_\varphi)$  and  $(\pm \alpha_\varphi, \mp \alpha_\varphi)$  when the loading is related to the fast timescale.

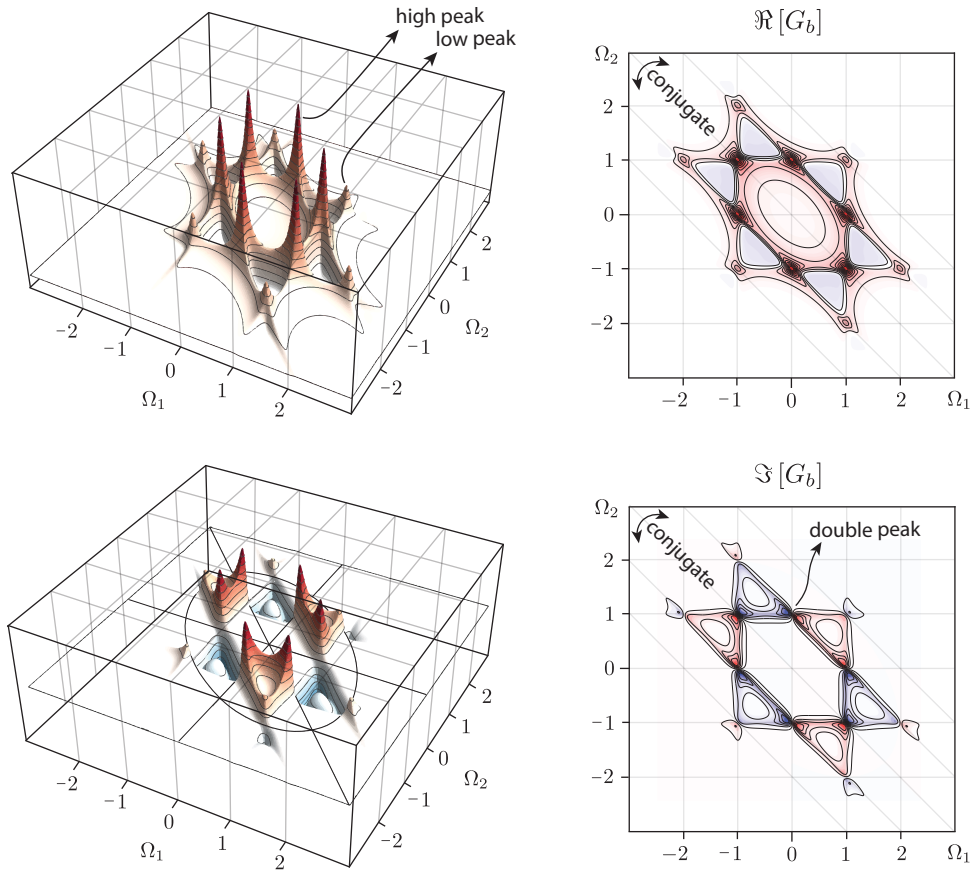


FIGURE 3.2: Real and imaginary parts of the structural kernel,  $G_b(\Omega_1, \Omega_2)$ .

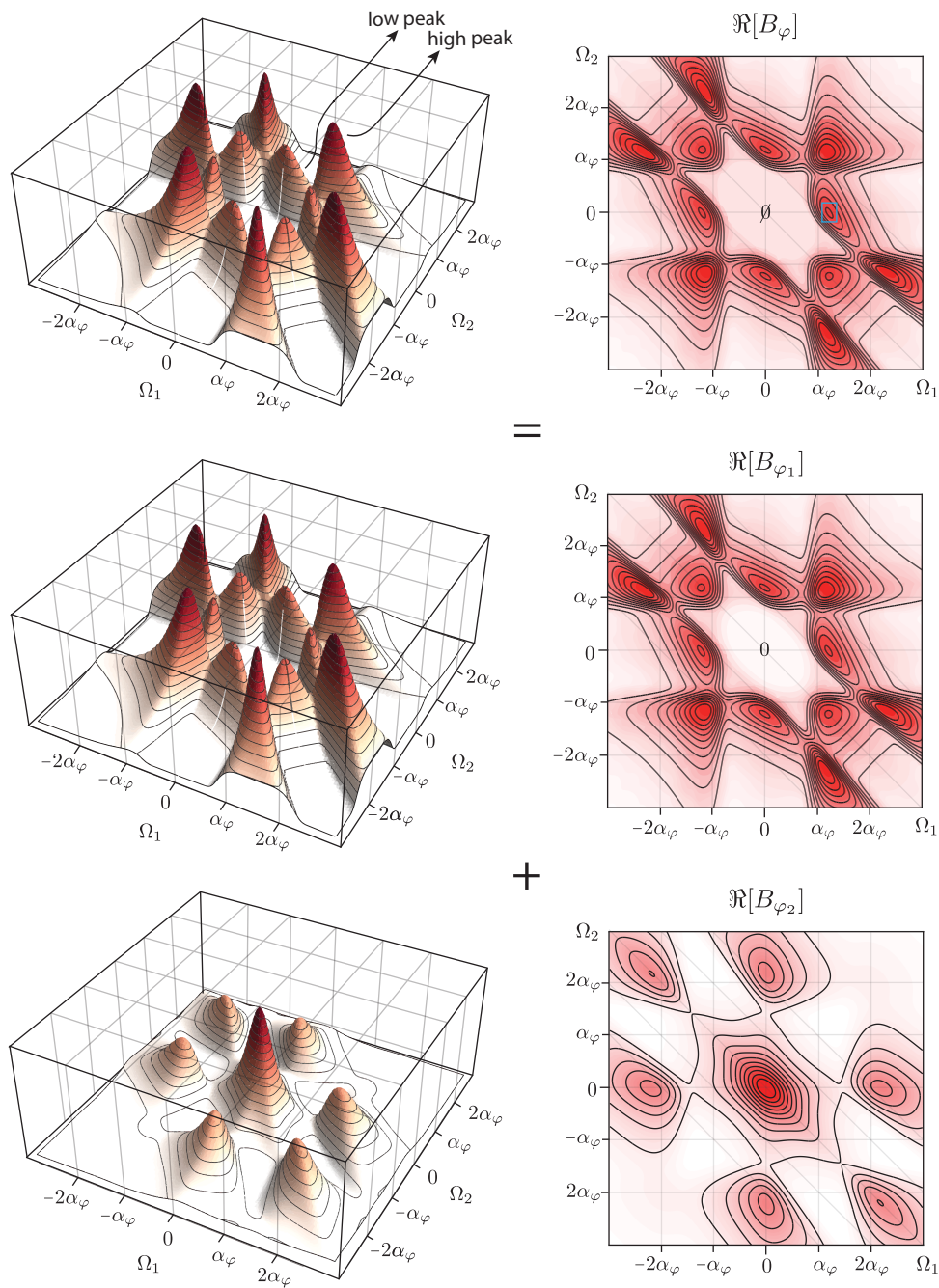


FIGURE 3.3: Real-valued bispectrum of the quadratic loading process,  $B_\varphi(\Omega_1, \Omega_2)$ . Decomposition as the sum of  $B_{\varphi_1}(\Omega_1, \Omega_2)$  and  $B_{\varphi_2}(\Omega_1, \Omega_2)$ .

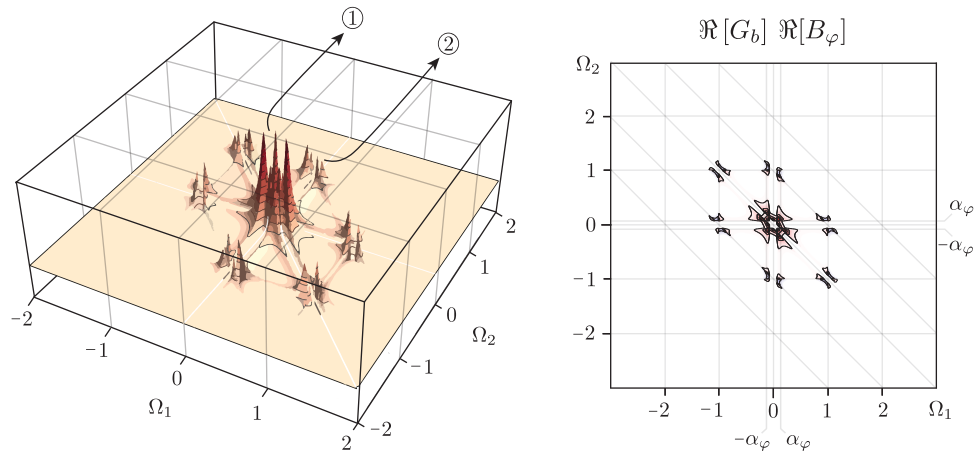


FIGURE 3.4: Bispectrum of the response when the loading is background,  $\alpha_\varphi \ll 1$ . Contributions of the real parts only since the loading bispectrum is real-valued.

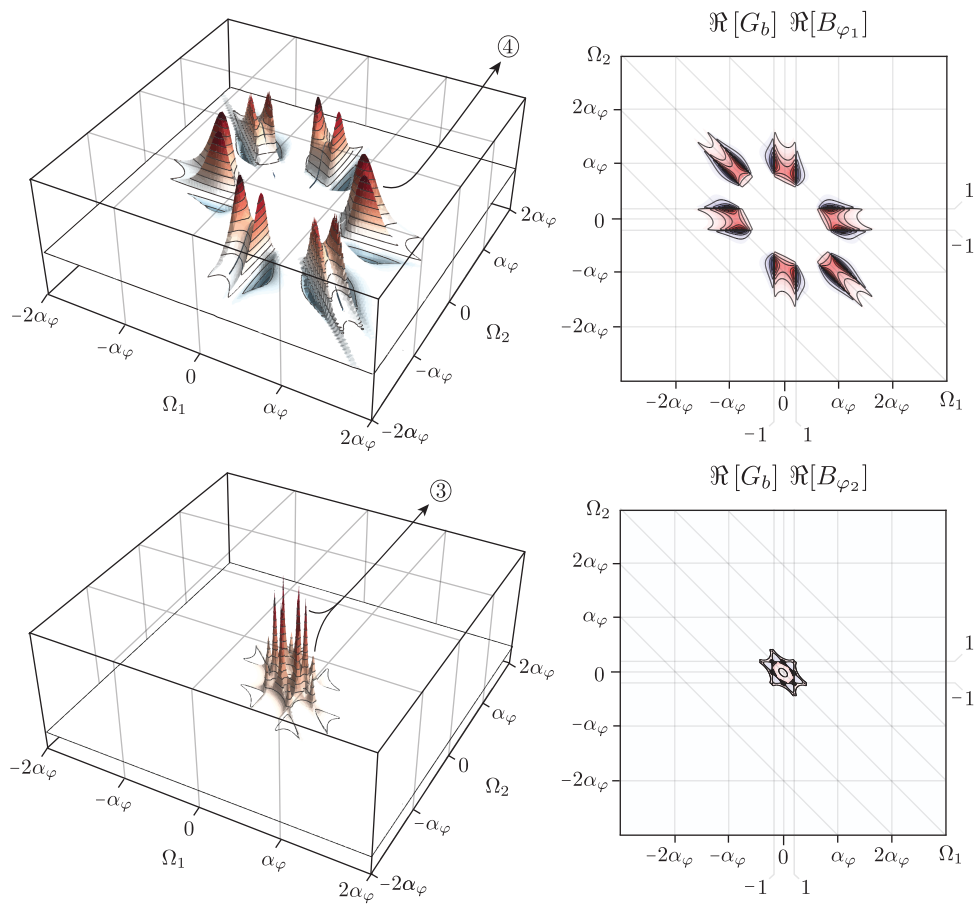


FIGURE 3.5: Bispectrum of the response when the loading is inertial,  $\alpha_\varphi \gg 1$ . Contributions of the real parts only since the loading bispectrum is real-valued.

### 3.3 Formulation of the Necessary Assumptions

To succeed in the derivation of semi-analytical formulas for the contributions to the third central moment of the response, which enable to reduce the order of integration by one at least, it is required to ensure that the structural kernel and the loading bispectrum interact in one direction at most in the areas of concern. This is subject to the following provisions.

**First possibility, see Section 3.4:**

- (B1) The peak frequency of the loading bispectrum is considerably smaller than the natural frequency of the system. Mathematically speaking, it yields

$$\alpha_\varphi \ll 1 \quad \text{and} \quad \Omega_\varphi \gg 1 \quad (3.5)$$

for the frequency ratio and its inverse. In this event, the structural kernel is relatively flat across the peaks of the loading bispectrum. Therefore, and unlike the loading bispectrum, the structural kernel does not vary at all in the background region, no matter the direction considered. This is typically formalized by admitting that the structural kernel is approximately equal to the leading order term of its Taylor series expansion in the vicinity of the origin while the asymptoticness of such an expression is not ensured for the loading bispectrum.

- (B2) Around the background bi-resonant peaks, on the other hand, the structural kernel varies rapidly in all directions. The loading bispectrum fluctuates significantly in parallel to the crests as well but moderately in the perpendicular direction. It is hence supposed that the variation of the structural kernel can be regarded alone in this direction while the interaction of the two functions should be accounted for in the other one.

Under these specific assumptions, the Multiple Timescale Spectral Analysis allows to decompose the third central moment of the response into the following sum of contributions

$$\tilde{\beta}_\chi = \beta_{bbb} + 6\beta_{\Re[brr]} + 6\beta_{\Im[brr]} \quad (3.6)$$

which are respectively identified, in accordance with the previous section, as a tri-background component, six  $\Re \times \Re$  and six  $\Im \times \Im$  background bi-resonant components, being attributed to the peaks in the products of either the real, either the imaginary parts of the structural kernel and the loading bispectrum.

In Section 3.4, we demonstrate that these three components can be expressed as

$$\beta_{bbb} = \beta_\varphi \quad , \quad (3.7)$$

$$\beta_{\Re[brr]} = 2\xi \frac{\pi}{2} \int_{-\infty}^{+\infty} \frac{\Re[B_\varphi(1, \Omega_2)]}{4\xi^2 + \Omega_2^2} d\Omega_2 \quad (3.8)$$

and

$$\beta_{\Im[brr]} = -\frac{\pi}{2} \int_{-\infty}^{+\infty} \Omega_2 \frac{\Im[B_\varphi(1, \Omega_2)]}{4\xi^2 + \Omega_2^2} d\Omega_2. \quad (3.9)$$

**Second possibility, see Section 3.5:**

- (I1) The peak frequency of the loading bispectrum is significantly greater than the natural frequency of the system. The frequency ratio and its inverse thus read

$$\alpha_\varphi \gg 1 \quad \text{and} \quad \Omega_\varphi \ll 1 \quad (3.10)$$

respectively. As opposed to Assumption (B1), the bispectrum of the loading is approximately constant over the zones where the peaks of the structural kernel arise. But, although their roles are interchanged, these two functions are still not interacting at all in the low frequency range.

- (I2) By contrast with Assumption (B2), the variations of the loading bispectrum are smooth in the direction perpendicular to the crests with respect to those of the structural kernel, whereas both functions fluctuate more strongly along these ridgelines. For a number of reasons which will appear clear in the light of the mathematical developments, it is however not possible to completely discard the slow evolution of the loading bispectrum perpendicularly to the crests. Nevertheless, as it is moderate enough, the order of integration will be reduced anyways by having recourse to more advanced techniques.

Under these particular hypotheses, the third central moment is in principle given by the sum of several contributions as follows

$$\tilde{\beta}_\chi = \beta_{rr} + 6\beta_{\Re[r ii]} + 6\beta_{\Im[r ii]} \quad (3.11)$$

via the application of the Multiple Timescale Spectral Analysis. These components are respectively pertaining to the activation of the background bi-resonant and the bi-resonant inertial regimes, first, as well as the resonant bi-inertial ones in both the real and the imaginary parts of the structural kernel, second and third.

In Section 3.5, we demonstrate that these three components can be expressed as

$$\beta_{rr} = \frac{8\pi^2}{3(1+8\xi^2)} \Re[B_\varphi(0,0)] \quad , \quad (3.12)$$

$$\beta_{\Re[r ii]} = \int_{-\infty}^{+\infty} \frac{\Re[H_\chi(\Omega_2)]}{P_0 + P_2\Omega_2^2} d\Omega_2 \quad \text{and} \quad \beta_{\Im[r ii]} = -\frac{\pi}{2} \int_{-\infty}^{+\infty} \Im\left[\frac{B_\varphi(\Omega_1, 1)}{1 + \Omega_1^4}\right] d\Omega_1 \quad (3.13)$$

where

$$P_0 = \mathcal{I}_\Re(0) \quad \text{and} \quad P_2 = \frac{1}{\mathcal{I}_\Re(1)} - \frac{1}{\mathcal{I}_\Re(0)} \quad (3.14)$$

with

$$\mathcal{I}_\Re(\Omega_2) = \int_{-\infty}^{+\infty} \frac{C_\varphi}{C_\varphi + \Omega_1^4} \Re[B_\varphi(\Omega_1, \Omega_2) - B_\varphi(0,0)] d\Omega_1 \quad ,$$

$$C_\varphi = \frac{\alpha_\varphi^4}{|H_\chi(\alpha_\varphi)|^{-2} - 1} \quad \text{and} \quad H_\chi(\Omega) = (1 - \Omega^2 + 2i\xi\Omega)^{-1} \quad . \quad (3.15)$$

### 3.4 Background Bi-Resonant Decomposition

When the excitation is quasi-static, the background region of the response bispectrum can first be targeted by zooming on the origin. In this zone, the structural kernel can be replaced by a constant, according to Assumption (B1). The response bispectrum is thus trivially approximated by

$$B_{bbb}(\Omega_1, \Omega_2) = G_b(0, 0) B_\varphi(\Omega_1, \Omega_2) \quad (3.16)$$

whose double integral reads

$$\beta_{bbb} = G_b(0, 0) \beta_\varphi \quad (3.17)$$

with  $\beta_\varphi$  being the third central moment of the loading. Given the non-dimensionalization employed in Chapter 1,  $G_b(0, 0)$  is equal to one but this is not implemented in Equation (3.17) for the reader to think about it when returning to the dimensional variables.

Taking this approximation out of the initial function then yields the first residual of the response bispectrum

$$\hat{B}_\chi(\Omega_1, \Omega_2) = B_\chi(\Omega_1, \Omega_2) [G_b(\Omega_1, \Omega_2) - G_b(0, 0)] \quad (3.18)$$

which mainly complements the third moment due to the bi-resonant peaks. Among those, the peak located at  $(\Omega_1, \Omega_2) = (\pm 1, 0)$  is subsequently looked at more closely by introducing the stretched coordinates  $\Omega_1 = (1 + \varepsilon\eta_1)$  and  $\Omega_2 = \varepsilon\eta_2$  with  $\eta_1$  and  $\eta_2$  being of order one at most into Equation (3.18). Meanwhile, the parameter  $\varepsilon$  is a small number which reflects the extent of the peak considered in the structural kernel.

Next, the loading bispectrum and the structural kernel are expanded in series for  $\varepsilon \ll 1$ . Under Assumption 3.3, the loading bispectrum is given by

$$\tilde{B}_\varphi(\Omega_1, \Omega_2) = B_\varphi(1, \varepsilon\eta_2) \quad (3.19)$$

at leading order and is thus made independent of  $\eta_1$ . The structural kernel can therefore be integrated along  $\eta_1$  before being multiplied by the loading bispectrum and eventually integrated along  $\eta_2$ . At leading order again, it reads

$$\tilde{G}_b(\eta_1, \eta_2) = \frac{(\eta_1^2 + \eta_1\eta_2 + 1) + i\eta_2}{(\eta_1^2 + \eta_1\eta_2 + 1)^2 + \eta_2^2} \quad (3.20)$$

for the structural kernel whose integral can subsequently be worked out in closed form as follows

$$\int_{-\infty}^{+\infty} \tilde{G}_b(\eta_1, \eta_2) d\eta_1 = \frac{\pi}{2} \left( \frac{2 + i\eta_2}{4 + \eta_2^2} \right) \quad (3.21)$$

and contains a real and an imaginary part which are respectively even and odd. Since this statement also holds true for the real and the imaginary part of the loading bispectrum, two out of four terms in the integral are strictly equal to zero. They are directly discarded and the background bi-resonant components associated to the peak of interest are finally expressed as

$$\beta_{\Re[brr]} = 2\xi \frac{\pi}{2} \int_{-\infty}^{+\infty} \frac{\Re[B_\varphi(1, \Omega_2)]}{4\xi^2 + \Omega_2^2} d\Omega_2 \quad \text{and} \quad \beta_{\Im[brr]} = -\frac{\pi}{2} \int_{-\infty}^{+\infty} \Omega_2 \frac{\Im[B_\varphi(1, \Omega_2)]}{4\xi^2 + \Omega_2^2} d\Omega_2 \quad (3.22)$$

with the initial coordinates. For symmetry reasons, these contributions will simply be multiplied by 6, in the end, to account for the other background bi-resonant peaks.

### 3.5 Bi-Resonant Inertial Decomposition

Regarding the response of an oscillator to a loading whose bispectrum contains peaks in the high frequency range now, the bi-resonant peaks of the response bispectrum, which are due to the poles of the structural kernel, can first be studied by looking at the region where both  $\Omega_1$  and  $\Omega_2$  are of order one. Being so already, it is therefore not required to stretch these coordinates in order to focus on the considered peaks.

According to Assumption (I1), the bispectrum of the loading is also sufficiently flat to be replaced by a constant value in the neighborhood of  $(\Omega_1, \Omega_2) = (0, 0)$ . As a consequence, the bispectrum of the response behaves as

$$B_{rr}(\Omega_1, \Omega_2) = \Re[G_b(\Omega_1, \Omega_2) B_\varphi(0, 0)] \quad (3.23)$$

in this area. This approximation of the bi-resonant peaks is local indeed because the structural kernel decreases rapidly as  $\Omega_1$  and  $\Omega_2$  increase. Given that this last function is also integrable in an explicit way as follows

$$\iint_{-\infty}^{+\infty} G_b(\Omega_1, \Omega_2) d\Omega_1 d\Omega_2 = \frac{8\pi^2}{3(1+8\xi^2)} \quad (3.24)$$

and that the imaginary part of the loading bispectrum is exactly equal to zero at the origin, the integration of  $B_{rr}(\Omega_1, \Omega_2)$  over the two dimensional frequency space gives the following expression

$$\beta_{rr} = \frac{8\pi^2}{3(1+8\xi^2)} \Re[B_\varphi(0, 0)] \quad (3.25)$$

for the background and inertial bi-resonant components which is hence real-valued, as expected.

The subtraction of  $B_{rr}(\Omega_1, \Omega_2)$  from the response bispectrum of the response subsequently provides the first residual bispectrum which reads

$$\hat{B}_\chi(\Omega_1, \Omega_2) = G_b(\Omega_1, \Omega_2) \hat{B}_\varphi(\Omega_1, \Omega_2) \quad (3.26)$$

with

$$\hat{B}_\varphi(\Omega_1, \Omega_2) = B_\varphi(\Omega_1, \Omega_2) - B_\varphi(0, 0) \quad (3.27)$$

and does no longer contain any bi-resonant peak. The coordinate stretching  $\Omega_1 = \Upsilon_1/\Omega_\varphi$  and  $\Omega_2 = \Upsilon_2$ , with  $\Upsilon_1$  and  $\Upsilon_2$  being of ord (1) at most, can then be injected into Equation (3.26) to zoom on one of the remaining resonant inertial contributions, which is located at  $(\Omega_1, \Omega_2) = (\alpha_\varphi = 1/\Omega_\varphi, 0)$ . By recalling that the inverse of the frequency ratio is small in the current context, the structural kernel can be expanded in series for  $\Omega_\varphi \ll 1$  and hence be given by

$$\tilde{G}_b(\Upsilon_1, \Upsilon_2) = H(\Upsilon_2) |H(\Upsilon_1)|^2 \quad (3.28)$$

at leading order. Interestingly enough, each term of this product depends on its own single strained coordinate. Moreover, the latter one relates to the second order structural kernel and can therefore be approximated by the same (0, 4) Padé approximant as before in the interval of interest, see Equation 2.32 in Section 2.4.

Such an evolution of the kernel with respect to  $\Upsilon_1$  cannot be discarded. It might indeed change significantly across the zone of concern because this area needs to be relatively large to cover the peaks of the loading bispectrum. In other words, any function with a small gradient but extending over a long distance can fluctuate as importantly in total as if the gradient was larger and the distance was shorter. Besides, nor can the respective variations of the loading bispectrum and the structural kernel about  $\Upsilon_1$  and  $\Upsilon_2$  be neglected either, since they are responsible for the peculiar



shape of the peaks. If they were to be dropped, the local approximation would not adequately suit the original function.

As regards the real part of the loading bispectrum, its slightly curved nature along  $\Upsilon_2$ , although almost flat when zoomed at, is actually essential to obtain a non-zero result for the resonant bi-inertial component. To picture this, imagine stretching the blue box in Figure 3.3. Otherwise, the local approximation of the response bispectrum would read

$$\tilde{G}_b(\Upsilon_1, \Upsilon_2) \hat{B}_\varphi(\Omega_1, \Omega_2) = \Re[H(\Upsilon_2)] \tilde{G}_s(\Upsilon_1) \hat{B}_\varphi(\Omega_1, \Omega_2)$$

and its integral with respect to  $\Upsilon_2$  would be computed independently of the variations in the other direction. But it unfortunately yields

$$\int_{-\infty}^{+\infty} \Re[H(\Upsilon_2)] d\Upsilon_2 = 0 \quad (3.29)$$

and it would thus directly cancel the result by multiplying the remaining integral along  $\Upsilon_1$ .

Nevertheless, for this precise contribution, the number of points where the bispectrum of the loading has to be evaluated can be drastically reduced by acknowledging that the integral

$$\mathcal{I}_{\Re}(\Omega_2) = \int_{-\infty}^{+\infty} \tilde{G}_s(\Omega_1) \Re[\hat{B}_\varphi(\Omega_1, \Omega_2)] d\Omega_1$$

is properly matched by the following (0, 2) Padé approximant

$$\mathcal{P}(0, 2)[\mathcal{I}_{\Re}(\Omega_2)] = \frac{1}{P_0 + P_2\Omega_2^2} \quad (3.30)$$

with

$$P_0 = \mathcal{I}_{\Re}(0) \quad \text{and} \quad P_2 = \frac{1}{\mathcal{I}_{\Re}(1)} - \frac{1}{\mathcal{I}_{\Re}(0)} \quad (3.31)$$

guaranteeing that the Padé approximant and the original function are perfectly matched at the origin,  $\Omega_2 = 0$ , and at the location of the resonant peaks,  $\Omega_2 = \pm 1$ . In the end, the  $\Re \times \Re$  resonant bi-inertial component of the third central moment of the response is therefore given by

$$\beta_{\Re[r_{ii}]} = \int_{-\infty}^{+\infty} \frac{\Re[H(\Omega_2)]}{P_0 + P_2\Omega_2^2} d\Omega_2 \quad (3.32)$$

which only requires to compute the bispectrum of the loading on two lines –within  $\mathcal{I}_{\Re}(0)$  and  $\mathcal{I}_{\Re}(1)$ – instead of on the entire two-dimensional domain.

Meanwhile, vis-à-vis the imaginary part of the loading bispectrum, it is not especially its variation between the two peaks of  $\Im[H(\Omega_2)]$  that matters, but rather its change of sign which makes these two peaks end up on the same side of the axis, whereas they are opposite at start, see Figure 3.6. Their respective contributions can hence be isolated and accounted for in a separate way. To do so, the imaginary part of the frequency response function under consideration is first rewritten as follows

$$\Im[H(\Omega_2)] = \Im\left[\frac{D}{\Omega_2 - B^*}\right] - \Im\left[\frac{D}{\Omega_2 + B}\right] \quad (3.33)$$

with

$$B = \sqrt{1 - \xi^2} + \xi i \quad \text{and} \quad D = 1/\sqrt{4 - 4\xi^2} \quad (3.34)$$

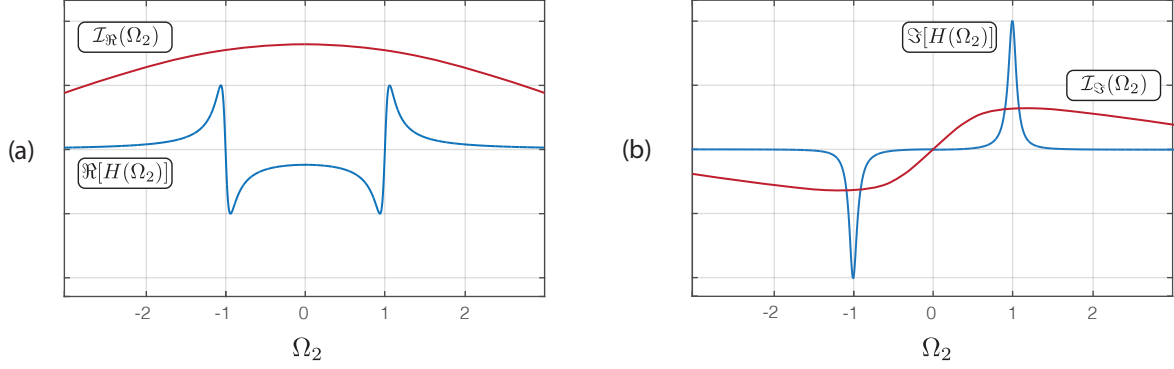


FIGURE 3.6: Schematic representation of the functions discussed in this section.

by being expanded in partial fractions. Each term of Equation (3.33) accordingly features a single peak, in the vicinity of  $\Omega_2 = -1$  or  $\Omega_2 = +1$  for small damping ratios, across which the loading bispectrum is deemed to be constant. At last, the response bispectrum is consequently approximated by

$$B_{\Im[rii]}(\Omega_1, \Omega_2) = \left( \frac{D}{\Omega_2 - B^*} + \frac{D}{\Omega_2 + B} \right) \Im \left[ \frac{B_\varphi(\Omega_1, 1)}{1 + \Omega_1^4} \right] \quad (3.35)$$

and its double integral gives

$$\beta_{\Im[rii]} = -\frac{\pi}{2} \int_{-\infty}^{+\infty} \Im \left[ \frac{B_\varphi(\Omega_1, 1)}{1 + \Omega_1^4} \right] d\Omega_1 \quad (3.36)$$

for the  $\Im \times \Im$  resonant bi-inertial component of the third central moment of the response.

## 3.6 Validation and Parametric Analysis

### Presentation of the results

The expressions derived hereabove for the main contributions to the integral of the response bispectrum are assessed in this section. To this aim, the results they provide are compared to the values obtained through the implementation of a numerical quadrature algorithm for  $\lambda_u = \{0.1, 0.3, 1.0\}$  and for  $\xi = \{1\%, 3\%, 10\%\}$ , see Figure 3.7 and Figure 3.8. They are eventually combined with the outcomes of Chapter 2 to see how the errors committed by using the proposed decompositions for the second and the third central moments affect the skewnesses of the response as well, see Figure 3.9 and Figure 3.10. Overall, these four figures are grouped at the end of this section.

These comparisons are additionally conducted for three different definitions of the loading bispectrum, in order to evaluate the appropriateness of the simplifications that are required to get handy formulas for computing the loading bispectrum in an analytical way. The results obtained for these three options are respectively represented in the (A), (B), and (C) graphs of the figures. From the least to the most complicated, the definitions of the loading bispectrum in each of these three scenarios are given as follows.

- (A) The loading is quadratized, first, and its bispectrum is expressed as the first term of Equation (1.28) only. Meanwhile, the second term of Equation (1.28) is considered as being negligible. As it will be shown later on, this is in principle conditioned upon the smallness of the relative wave length,  $\lambda_u$ , which indirectly modifies the values of the

polynomialization coefficients, see Table 3.1. In this first scenario, the bispectrum of the loading therefore reads

$$B_{\varphi_1}(\Omega_1, \Omega_2) = 2p_1^2 p_2 (S_v(\Omega_1) S_v(\Omega_2) + S_v(\Omega_1) S_v(\Omega_1 + \Omega_2) + S_v(\Omega_1 + \Omega_2) S_v(\Omega_2)) \quad (3.37)$$

where

$$S_v(\Omega) = \sqrt{\frac{3}{\pi}} \frac{\alpha_v^2}{|\Omega|^3} \exp\left(-\frac{3\alpha_v^4}{4\Omega^4}\right) \quad (3.38)$$

solely depends on  $\alpha_v$  being the frequency ratio of the water velocity fluctuations.

- (B) The loading is quadratized, again, but the second term of Equation (1.28) is no longer discarded. Thus, the bispectrum of the loading reads

$$B_\varphi = B_{\varphi_1}(\Omega_1, \Omega_2) + B_{\varphi_2}(\Omega_1, \Omega_2) \quad (3.39)$$

where

$$B_{\varphi_2}(\Omega_1, \Omega_2) = 8p_2^3 \int_{-\infty}^{+\infty} S_v(\Omega + \Omega_1) S_v(\Omega_1 - \Omega) S_v(\Omega) d\Omega \quad (3.40)$$

is actually much more cumbersome to compute than  $B_{\varphi_1}(\Omega_1, \Omega_2)$  as it involves a convolution alike operation.

- (C) The non-polynomial loading is kept as is and its bispectrum is computed from simulated time series, in a similar fashion as the power spectral density of the loading in Section 2.5 [78]. This third scenario is therefore regarded as the reference one and the results obtained through the numerical integration of the response bispectrum are hence watermarked on the (A) and (B) graphs to help visualize the discrepancies which are attributable to the polynomialization and to the omission of  $B_{\varphi_2}(\Omega_1, \Omega_2)$ .

In the first and the second scenarios, the numerical integration of the response bispectrum is performed by using the adaptive integration algorithm of Wolfram Mathematica, Version 12.0.0.0, with predefined parameters. In the third scenario, however, a trapezoidal scheme is employed. In total, 5000 points are distributed over both the positive and the negative frequency ranges, for both  $\Omega_1$  and  $\Omega_2$ . Among those, a fine mesh of 1000 points is implemented in the intervals  $\Omega_1|\Omega_2 \in [-1 - 4\xi, -1 + 4\xi]$  and  $\Omega_1|\Omega_2 \in [1 - 4\xi, 1 + 4\xi]$  in order to properly capture the volumes under the resonant peaks and ridges, which become sharper as the damping decreases. The ensuing results are represented by blue lines in Figure 3.7 and Figure 3.8, for ten uniformly spaced values of  $\alpha_v$  within the intervals [0.1, 0.3] and [4, 6], respectively.

The graphs in Figure 3.7 and Figure 3.8 are therefore associated to either a quasi-static loading, either an inertial loading. In Figure 3.7, the black lines are thus given by the sum of the tri-background component as introduced in Equation (3.17), which is also displayed in red, and the background bi-resonant component as presented in Equation (3.22), which is pictured in green as well. In Figure 3.8, however, the black lines correspond to the sum of the complete bi-resonant component as expressed in Equation (3.25), which is also shown in green, and the resonant bi-inertial component as given by Equation (3.32), which is represented in yellow.

Likewise, the skewnesses of the response are computed for the same sets of  $\alpha_v$  values, by combining the blue and the black colored results from both the previous and the current chapter. This is done graph-by-graph, meaning that the second central moments, which are computed as those shown in Figure 2.2-(A1) for instance, are compiled with the third central moments, which are calculated as those enclosed in Figure 3.7-(A1) or Figure 3.8-(A1), depending on whether  $\alpha_v < 1$  or not, and so on.

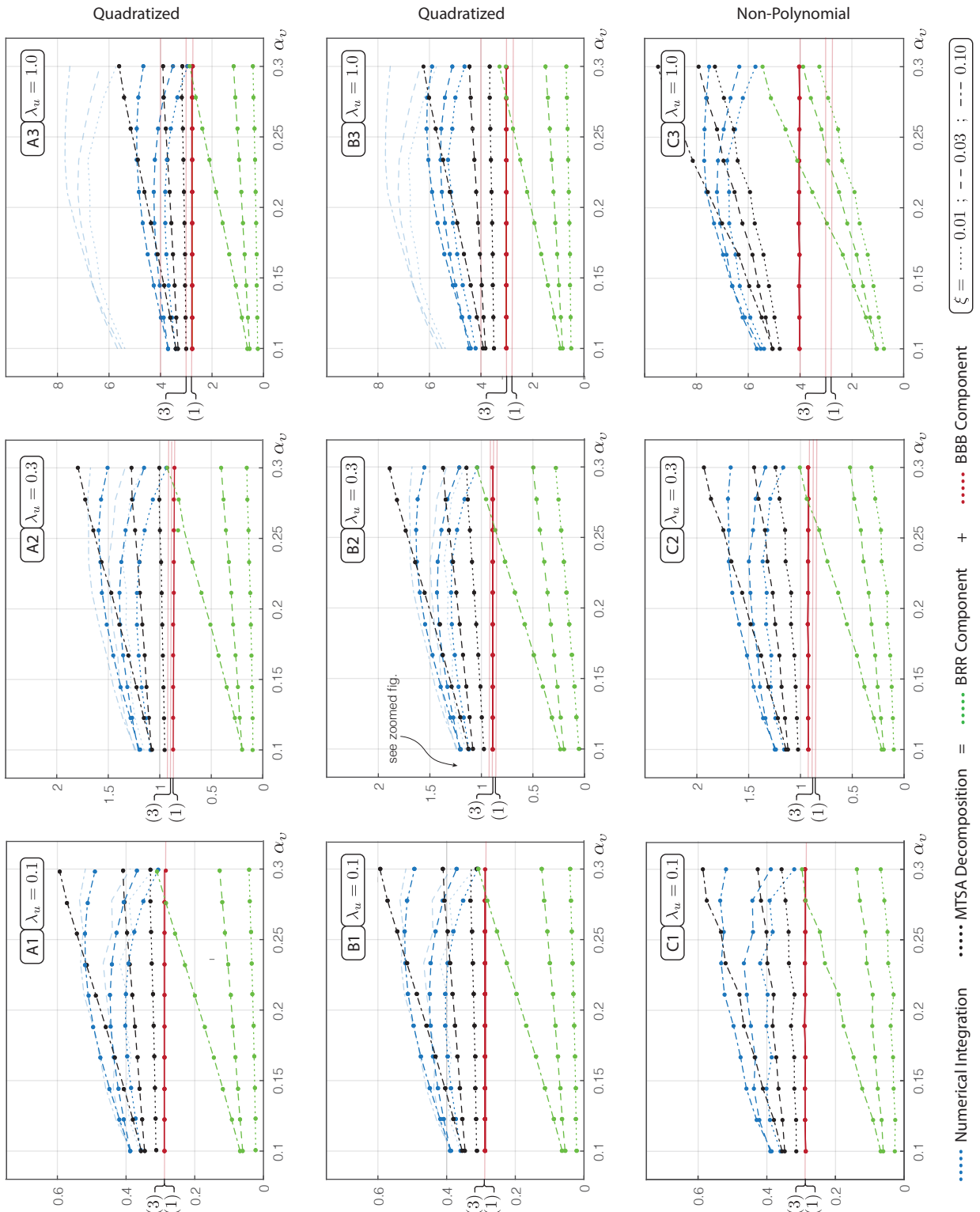


FIGURE 3.7: Third central moment of the response when the loading is background,  $\alpha_v \ll 1$ .

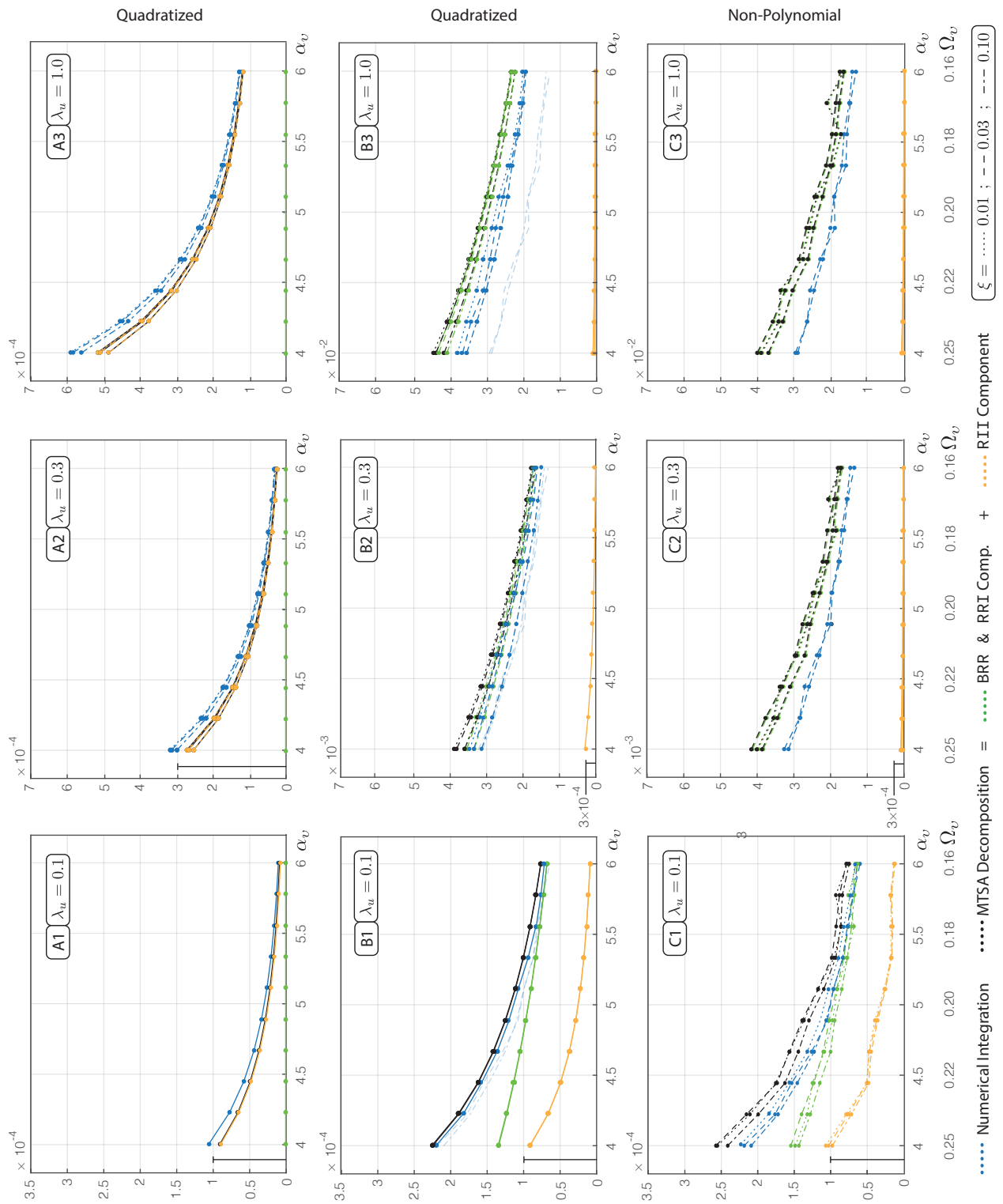


FIGURE 3.8: Third central moment of the response when the loading is inertial,  $\alpha_v \gg 1$ .

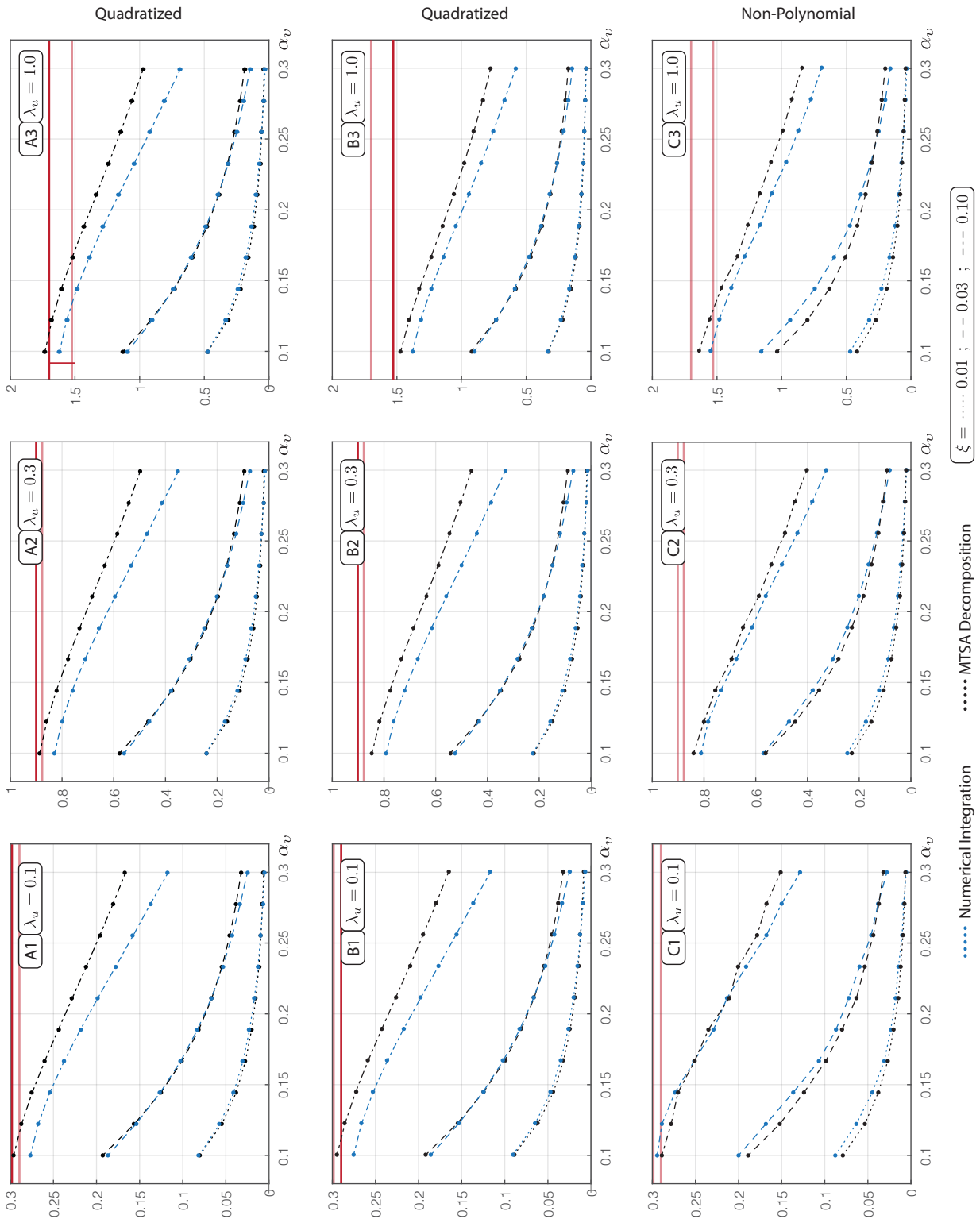


FIGURE 3.9: Skewness of the response when the loading is background,  $\alpha_v \ll 1$ .

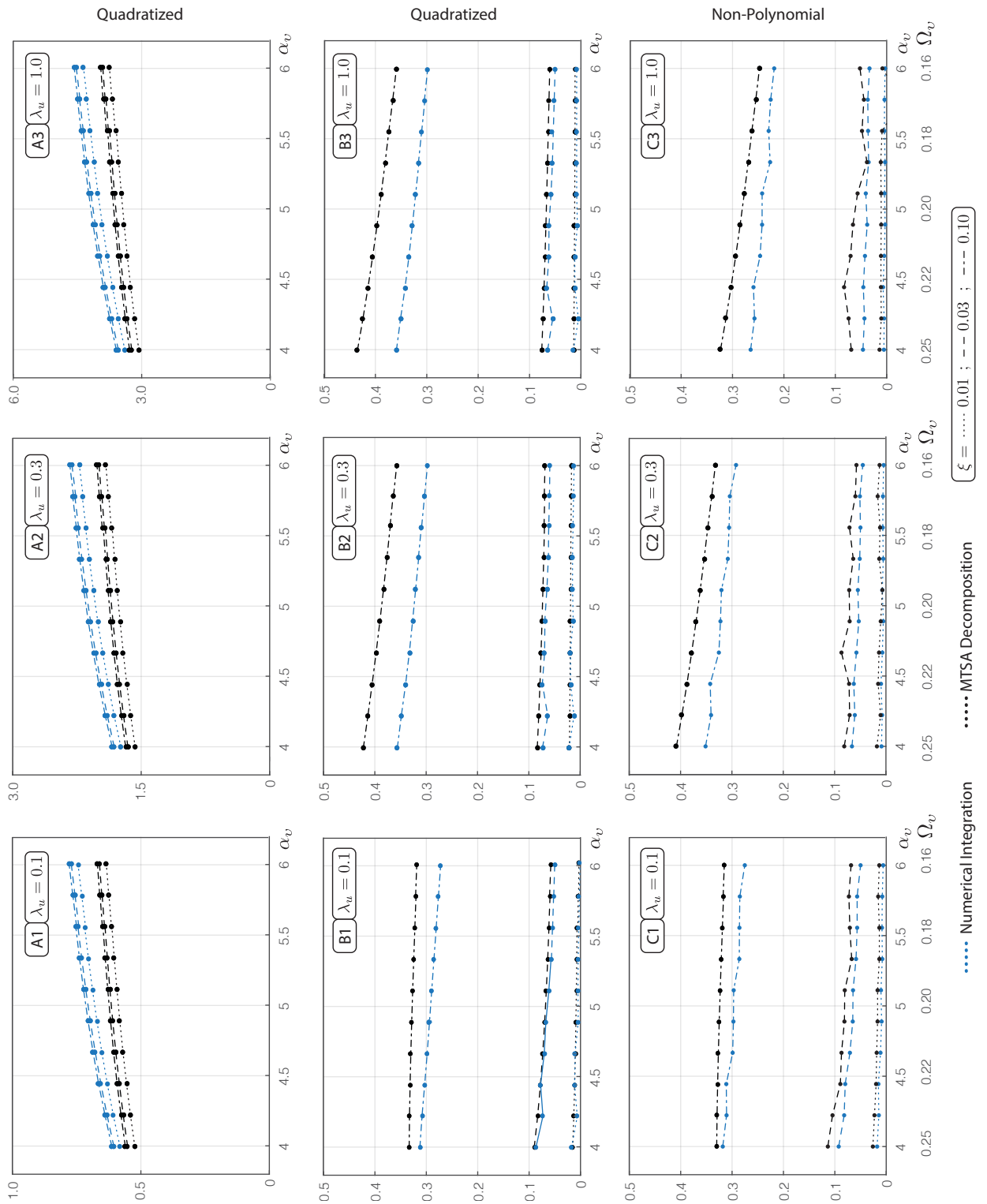


FIGURE 3.10: Skewness of the response when the loading is inertial,  $\alpha_v \gg 1$ .

TABLE 3.1: Polynomial coefficients and background components.

$\lambda_u$	$p_1$	$p_2$	(1)	(2)	(3)	$\gamma_{(1)}$	$\gamma_{(3)}$
0.1	1.00	0.05	0.300	0.001	0.301	0.30	0.29
0.3	1.00	0.15	0.899	0.027	0.926	0.90	0.87
1.0	1.17	0.34	2.787	0.318	3.105	1.70	1.53

In the end, please notice that the tri-background components related to  $B_{\varphi_1}(\Omega_1, \Omega_2)$  and  $B_{\varphi_2}(\Omega_1, \Omega_2)$  can in fact be expressed in closed-form by (1) =  $6p_1^2p_2$  and (2) =  $8p_2^3$ , respectively. Their numerical values and their sums, (3) = (1) + (2), are listed in Table 3.1, with respect to the relative wave length of concern. They are also indicated on the relevant graphs.

### Discussion of the results

Globally, there is a good agreement between the third central moments calculated via the numerical integration, in blue, and via the proposed formulations, in black. These results are all the more accurate if the damping ratio and the frequency ratio drop, as it is expected from a perturbation standpoint. The background bi-resonant decomposition additionally tends to be more sensitive to the smallness of the frequency ratio than the bi-resonant inertial decomposition because  $\alpha_\varphi$  has to reach smaller values than  $\Omega_\varphi$  for the third moments to be affected by the same level of error. However, as shown in Figure 3.11, the results eventually tend to be equal to the third central moment of the loading for  $\alpha_\varphi \ll 1$ , meaning that the response becomes fully background. This is due to the fact that the bi-resonant peaks arise in a zone where the loading bispectrum is very low.

The same applies to the skewness in Figure 3.9 and Figure 3.10 where the greater the damping, the faster the convergence. But, on the opposite, the response is less skewed than the loading when the frequency ratio approaches unity and the damping ratio decreases. This corroborates the central limit theorem even if, contrary to what would be anticipated based on the behavior of the second moments, the reduction in the amount of damping is not accompanied by an increment in the resonant proportion for the third moment of the response. Indeed, although the bi-resonant peaks are sharper, they are consequently concentrated in the frequency bands where the loading bispectrum is almost zero, on the other hand.

The results are however significantly biased when the relative wave length reaches unity. Nevertheless, this is not due to the use of the multiple timescale spectral analysis. These discrepancies can actually be attributed to the polynomialization because they are shown to decrease with the relative wave length. In practice, a loading of higher degree should indeed be considered when the relative wave length is not so small [79].

In addition, when the loading is also quasi-static, it appears that  $B_{\varphi_2}(\Omega_1, \Omega_2)$  is well negligible for the lowest value of the relative wave length, as shown by the similarity between Figure 3.7-(A1) and Figure 3.7-(B1). Thus the outcomes of the numerical integration and the proposed decomposition match quite closely.

A contrario, when the loading is inertial, its bispectrum is however exponentially small in the neighborhood of the origin, and hence of the resonant peaks, in the first scenario. The resonant components are therefore completely obliterated in Figure 3.8-(A) whereas, in principle, they are responsible for a substantial part of the third central moments, no matter the smallness of the relative wave length, as indicated in Figure 3.8-(B).

This is akin to what was observed with the power spectral densities of the response in the previous chapter, although the loading bispectrum is herein simplified on the premise that the relative wave length is small but remains associated to a quadratized, and not a linearized, forcing process. The second part of the bispectrum can therefore be treated like the second part of the



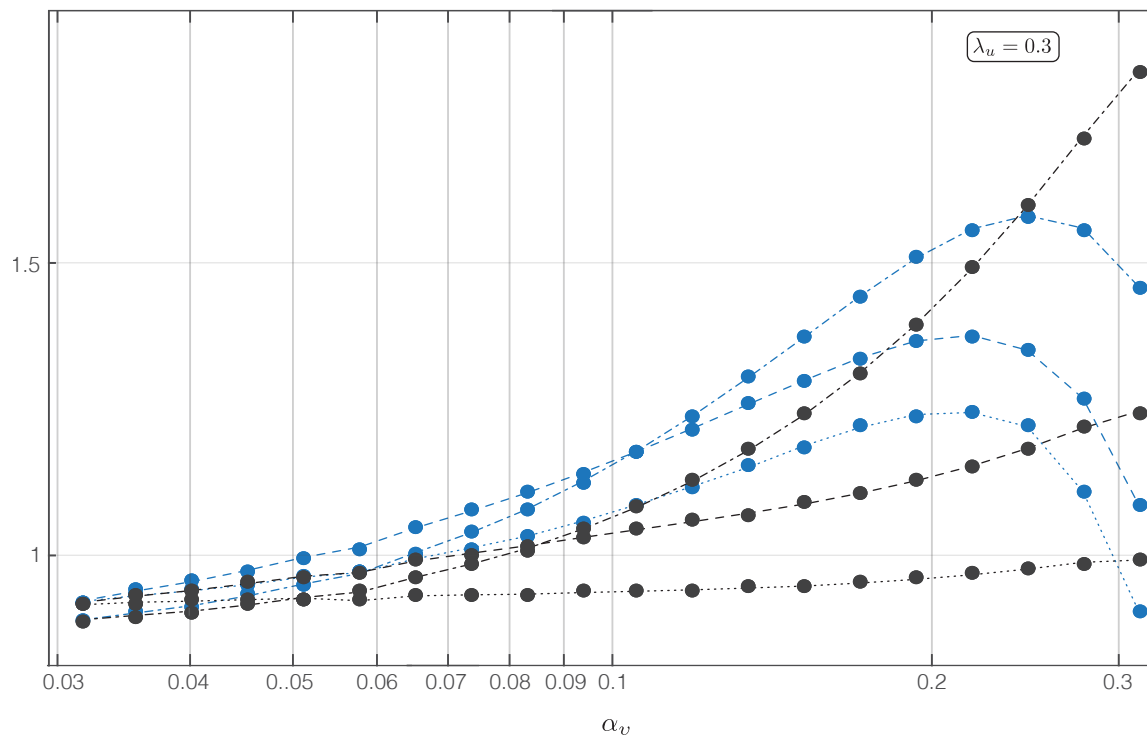


FIGURE 3.11: Close-up view on Figure 3.7-(B2) for smaller  $\alpha_v$ .

power spectrum. For the record, in Section 2.5, it yielded a resonant contribution only because of its low frequency content and the presence of the multiplicative factor  $(1 - S_\varphi(1)/S_\varphi(1/\Omega_\varphi))$ .

Although it does not appear so clearly for the bispectrum in the above formulas, it seems that the addition of a bi-resonant component only also provides the adequate complement for the results to match with the reference values in Figure 3.8-(B). The inertial components, in yellow, therefore remain the same as in the first-row graphs. Overall, it indicates that the second part of the loading bispectrum cannot be neglected at all when the loading is inertial, even if the relative wave length is very small.



# Part II

## MDOF SYSTEMS

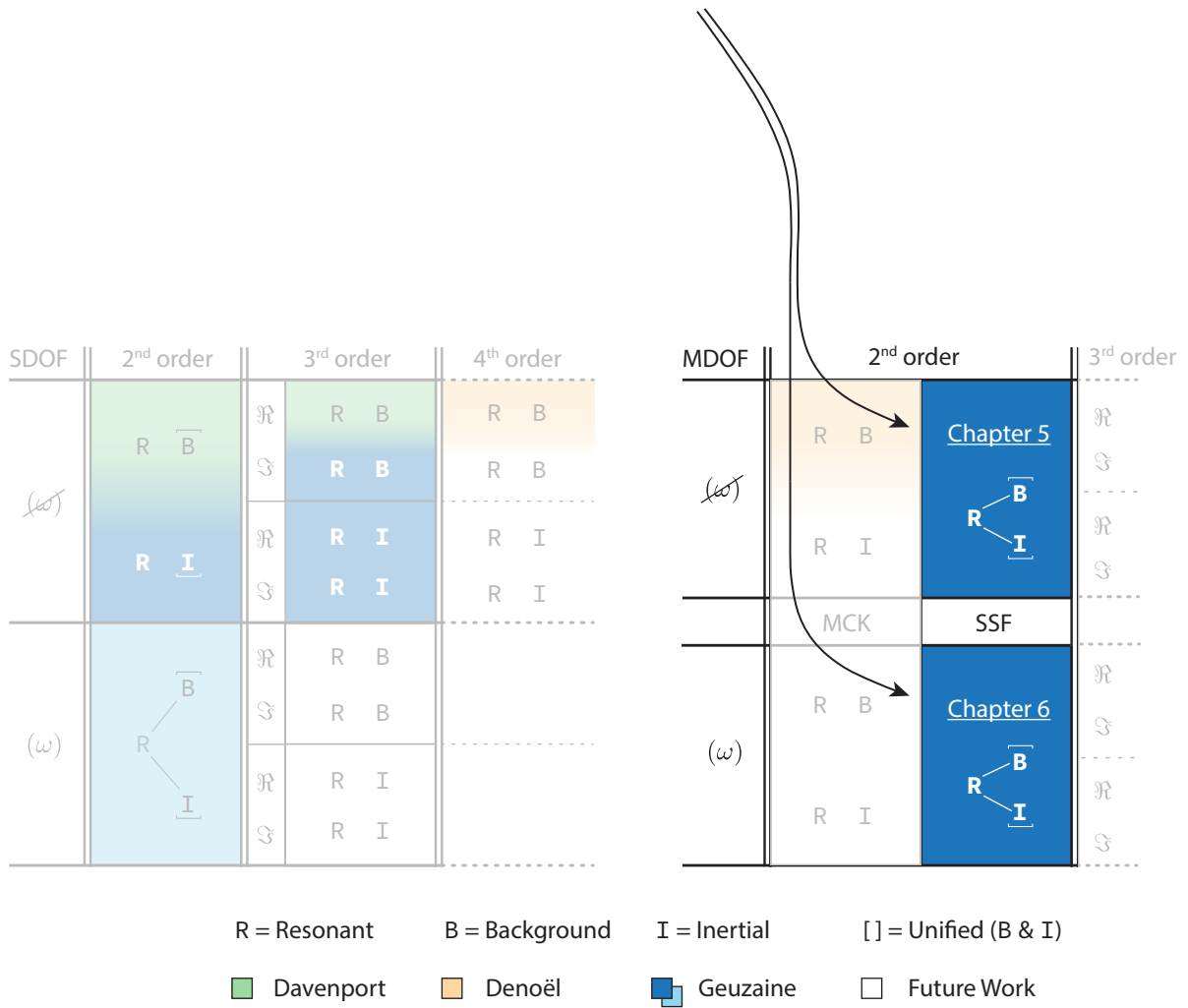


Figure B



## Chapter 4

# Contextualization

### 4.1 Context and Propositions

In this second part of the thesis, the Multiple Timescale Spectral Analysis is specialized to calculate the second central moments of the responses of a linear multi-degree-of-freedom (MDOF) system to the forces of the waves.

As shown in Section 4.2, these hydroelastic loads typically include fluid-structure interaction effects which are represented herein by additional stiffness, damping and mass matrices. They are usually defined in the frequency domain, and so are therefore expressed the equations of motion. In this thesis, their decoupling is then achieved by adopting a modal state-space formulation (SSF), in Section 4.3, and by proposing two decoupling strategies, in Section 4.4 and Section 4.5, respectively. The former supposes that the frequency sensitivity of the matrices can actually be neglected while the latter transforms it into a small correction of the spectral densities. Hence, they are respectively denoted by the symbols  $(\omega)$  and  $(\omega)$  in Figure B.

However, as explained in Section 4.7, the Multiple Timescale Spectral Analysis has never been used in such a decoupled setting. The method is therefore applied to derive simple expressions for the main components of the second order statistics that are obtained with either the first, either the second decoupling strategy, in Chapter 5 and Chapter 6 respectively, as represented in Figure B. In the first scenario, the proposed decompositions are validated on a minimalistic example for several sets of parameters. In the second scenario, it is not possible to do so and they are instead shown to degenerate to the formulas that have been developed in the past under more restrictive conditions. These two possibilities are eventually verified and compared with examples of realistic floating bridges in Chapter 7.

### 4.2 Governing Equations in Frequency Domain

The dynamics of a linear elastic structure with  $N$  degrees-of-freedom subjected to sea waves is governed by a set of  $N$  second order differential equations whose Fourier transform reads

$$\left[ \mathbf{K}_s + i\omega \mathbf{C}_s - \omega^2 \mathbf{M}_s \right] \mathbf{x}(\omega) = \mathbf{f}_h(\omega) \quad (4.1)$$

where  $\mathbf{x}(\omega)$  and  $\mathbf{f}_h(\omega)$  are two  $N \times 1$  vectors containing the frequency-domain representations of the structural displacements in every degree-of-freedom around the static equilibrium configuration and the total hydrodynamic loads acting on each of them, respectively. The symbols  $\mathbf{K}_s$ ,  $\mathbf{C}_s$ , and  $\mathbf{M}_s$  denote the  $N \times N$  static stiffness, damping and mass matrices of the structure. They are typically real and symmetric within a finite element modelling framework [80, 81].

More explicitly, the total hydrodynamic actions can generally be expressed in the frequency domain by

$$\mathbf{f}_h(\omega) = \mathbf{f}(\omega) - \left[ \mathbf{K}_h(\omega) + i\omega \mathbf{C}_h(\omega) - \omega^2 \mathbf{M}_h(\omega) \right] \mathbf{x}(\omega) \quad (4.2)$$

where the first term is due to the undisturbed waves and the other ones are originating from the interactions between the relative motion of the fluid and the structure. It gives rise to additional elastic, viscous and inertial forces, as indicated by the hydrodynamic stiffness, damping and mass matrices,  $\mathbf{K}_h(\omega)$ ,  $\mathbf{C}_h(\omega)$ , and  $\mathbf{M}_h(\omega)$ . In numerical studies, their determination usually relies on the potential theory, which is fundamentally linear and thus allows to superimpose the well-known flow fields obtained with the panel method when the body is supposed to oscillate in still water or when it is fixed and exposed to sinusoidal waves of unit height by assuming that the steepness of the waves is small, the fluid motion is irrotational and the water is inviscid and incompressible [82]. In this context, the added damping and mass matrices basically depend on the frequency of the oscillations whereas the supplemental stiffness matrix does not, i.e.  $\partial_\omega \mathbf{K}(\omega) = 0$ . However, in order to remain completely generic, this specificity is not implemented in here and moving the hydrodynamic matrices to the left-hand side of Equation (4.1) yields

$$\left[ \mathbf{K}(\omega) + i\omega \mathbf{C}(\omega) - \omega^2 \mathbf{M}(\omega) \right] \mathbf{x}(\omega) = \mathbf{f}(\omega) \quad (4.3)$$

where the global hydroelastic matrices are given by  $\mathbf{K}(\omega) = \mathbf{K}_s + \mathbf{K}_h(\omega)$ ,  $\mathbf{C}(\omega) = \mathbf{C}_s + \mathbf{C}_h(\omega)$ , and  $\mathbf{M}(\omega) = \mathbf{M}_s + \mathbf{M}_h(\omega)$ . By keeping such a general formulation, the methodology developed in this thesis can be used in other fields of applications, and for instance help to deal with the aeroelastic problems in wind engineering. In this context, though, the mass matrix is actually fixed while the stiffness matrix is function of the frequency.

The static analysis of the structure is supposed to be performed beforehand to define the reference position of each degree-of-freedom. Hence, the dynamic parts of the loadings are zero-mean random processes. They are additionally deemed to be stationary over a given time interval and Gaussian when deep water waves of moderate heights are considered [83]. Under such conditions, these processes are completely described, in a probabilistic sense, by the matrix  $\mathbf{S}_f(\omega)$  which gathers the cross-spectral densities of all  $i$ -th and  $j$ -th nodal forces,  $S_{f,ij}(\omega)$ . Establishing them is not the purpose of the present thesis, see e.g. [84] for that matter, but a few of their peculiarities are worthy to be highlighted for further discussion. In brief, they are typically obtained by using a wave elevation spectrum whose unified expression reads

$$S_w(\omega) = \left( \frac{\omega_p^5}{\omega^5} \right) \exp \left( -\frac{5}{4} \frac{\omega_p^4}{\omega^4} \right) \quad (4.4)$$

and whose maximum is reached at  $\omega_p$  in the positive frequency range [61]. Equation (4.4) is then commonly multiplied by some filters, which include for instance the influence of directional spreading effects, spatial correlations, and wave elevation-to-force amplitude operators. Despite these modifications, the spectral densities of the hydrodynamic forces habitually feature a similar exponential decay as  $S_w(\omega)$  when the circular frequencies are approaching the origin. In addition, their energy content remains relatively massed around  $\omega_p$  which is hence referred to as the characteristic frequency of the loading in the sequel [11].

Once filled, the matrix  $\mathbf{S}_f(\omega)$  is used to compute the matrix which contains the spectral densities of the responses as follows

$$\mathbf{S}_x(\omega) = \mathbf{H}_x(\omega) \mathbf{S}_f(\omega) \mathbf{H}_x^\dagger(\omega) \quad (4.5)$$

where

$$\mathbf{H}_x(\omega) = \left[ \mathbf{K}(\omega) + i\omega \mathbf{C}(\omega) - \omega^2 \mathbf{M}(\omega) \right]^{-1} \quad (4.6)$$

is the matrix of frequency response functions. Given that the behavior of the structure is supposed to be linear, the responses inherit the zero-mean Gaussian nature of the forces. Their probabilistic properties are therefore fully defined on the sole basis of their spectral densities. In particular, the second order statistics of the structural responses and their time derivatives are respectively given

by

$$\boldsymbol{\Sigma}_x = \int_{-\infty}^{+\infty} \mathbf{S}_x(\omega) d\omega \quad \text{and} \quad \boldsymbol{\Sigma}_{\dot{x}} = \int_{-\infty}^{+\infty} \omega^2 \mathbf{S}_x(\omega) d\omega \quad (4.7)$$

whose diagonal elements are the variances of the corresponding processes. The overhead dots will be adopted in this part of the thesis to represent the differentiation in time. Please remember that this operator is equivalently written as the product of the factor  $(i\omega)^i$  and the Fourier transform of the process at stake in the frequency domain, e.g.  $\dot{x}(\omega) = i\omega x(\omega)$  and  $\ddot{x}(\omega) = i\omega \dot{x}(\omega) = -\omega^2 x(\omega)$ .

The quantities derived in Equation (4.7) are essential from a design point of view because they enter into the definition of the peak factors [85, 86], the cumulative probability distributions of the extreme responses [37, 39], and the fatigue accumulated damage [38, 40], to cite just a few examples. They are also employed when Equation (4.1) is the result of the stochastic linearization performed on a set of nonlinear equations and is solved through an iterative procedure because the stiffness, damping and mass matrices are depending on  $\boldsymbol{\Sigma}_x$  and  $\boldsymbol{\Sigma}_{\dot{x}}$  as well [87, 88].

Nevertheless, the system and hence the matrix  $\mathbf{H}_x(\omega)$  to be inverted are possibly very large. First, this operation is computationally demanding. Second, it has to be repeated for as many frequencies as the number of points  $n_\omega$  that are necessary to compute the integrals in Equation (4.7). Unfortunately, on top of that, the spectral densities of the responses are expected to exhibit sharp and distant peaks when the structures are slightly damped. Their numerical integration therefore requires using a lot of closely spaced points to give accurate results. Globally, it means that huge matrices of size  $N \times N \times n_\omega$  are to be handled. Sometimes, they cannot even be stored in their entirety. To avoid such problems, the structural responses are most often defined by using a limited number  $M$  of modal responses, with  $M \ll N$  for large structures. This approach is usually intended to dissociate the equations of motion as well, so that they can be solved independently of one another, without requiring any costly matrix inversion.

### 4.3 Modal State Formulation of the Equations

Being impracticable to evaluate explicitly [89], the static damping matrix is traditionally expressed as a linear combination of the static mass and stiffness matrices, following the simple proportional damping rule proposed by Rayleigh [83, 90]. As a consequence, these three matrices satisfy the Caughey-O'Kelly commutativity condition but this criterion, or any equivalent one [91], is however hardly verified by the matrices that are originating from fluid-structure interactions [92], especially when they are functions of the frequency as  $\mathbf{K}_h(\omega)$ ,  $\mathbf{C}_h(\omega)$ , and  $\mathbf{M}_h(\omega)$ . The three static matrices ( $\mathbf{K}_s$ ,  $\mathbf{C}_s$ , and  $\mathbf{M}_s$ ) are therefore simultaneously diagonalizable by resorting to an appropriate projection space but the three hydrodynamic ones are never, no matter the basis considered [93, 94]. For instance, projecting the equations of motion into a subspace formed by the eigenmodes of the undamped structure, as usual, would diagonalize the global mass and stiffness matrices but not the damping. It would contain non-zero off-diagonal terms which are responsible for a remaining coupling between the modal responses. These entries can unfortunately not always be ignored since high levels of damping can be generated by the fluid-structure interactions, again [83, 95].

Overall, the above remarks imply that decoupling cannot be achieved in a satisfactory way unless additional hypotheses are introduced. First, if the frequency sensitivity of the hydrodynamic matrices is negligible, a modal state formulation can be introduced in order to separate the governing equations. Being just two instead of three, the state matrices can indeed be diagonalized in a simultaneous way even though the hydrodynamic damping is neither classical [92, 94], nor negligible [83, 89]. This first condition is also trivially met when analyzing a structure whose properties do not depend at all on the frequencies. Second, if the frequency sensitivity of the hydrodynamic matrices can no longer be discarded, but remains somewhat limited, the transfer matrix of the modal state

responses is not supposed to be exactly diagonal anymore but is still diagonally dominant. It can therefore be expanded in series on the basis that the off-diagonal entries are small with respect to the diagonal ones, in order to virtually decouple the set of governing equations [96, 97]. These two strategies are detailed in Section 4.4 and Section 4.5, respectively, after the reference modal state approach is presented in this section.

To start, the structural responses are combined with their time derivatives to describe the system in state-space. The state variables thus read

$$\mathbf{y}(\omega) = \begin{bmatrix} \mathbf{I} & i\omega\mathbf{I} \end{bmatrix}^T \mathbf{x}(\omega) \quad (4.8)$$

with  $\mathbf{I}$  being a  $N \times N$  identity matrix. An additional set of equations is subsequently introduced to create a system of  $2N$  first order equations whose constitutive matrices aim at conserving the symmetry and the positive definiteness of the initial ones:  $\mathbf{K}(\omega)$ ,  $\mathbf{C}(\omega)$ , and  $\mathbf{M}(\omega)$  [98, 99, 100]. To do so, the state forces are defined as

$$\mathbf{g}(\omega) = \begin{bmatrix} \mathbf{I} & \mathbf{0} \end{bmatrix}^T \mathbf{f}(\omega) \quad (4.9)$$

where  $\mathbf{0}$  is a  $N \times N$  zero matrix. They allow to recast the set of  $N$  second-order equations, (4.3), into  $2N$  first-order equations as follows

$$[\mathbf{A}(\omega) + i\omega\mathbf{B}(\omega)]\mathbf{y}(\omega) = \mathbf{g}(\omega) \quad (4.10)$$

where

$$\mathbf{A}(\omega) = \begin{bmatrix} \mathbf{K}(\omega) & \mathbf{0} \\ \mathbf{0} & -\mathbf{M}(\omega) \end{bmatrix} \quad \text{and} \quad \mathbf{B}(\omega) = \begin{bmatrix} \mathbf{C}(\omega) & \mathbf{M}(\omega) \\ \mathbf{M}(\omega) & \mathbf{0} \end{bmatrix} \quad (4.11)$$

are designated as the state matrices.

Considering that they are symmetric and positive definite, these matrices are actually very convenient to handle in order to find an adequate subspace in which the first  $2M \ll 2N$  contributing modal state responses are sufficient to perform the analysis of the structure with an acceptable level of accuracy. In general, the higher modes are legitimately discarded because they tend to be less excited by the hydrodynamic loads and to be more affected by discretization errors [89, 92].

Although the eigendecomposition can be numerically expensive as well, the eigensystem associated to the homogeneous part of the governing equations is interestingly written in the standard form

$$i\mathbf{A}(\psi_m)\boldsymbol{\theta}_m = \lambda_m\mathbf{B}(\psi_m)\boldsymbol{\theta}_m \quad (4.12)$$

when it is expressed in the state coordinates. This complex eigenproblem will be referred to as EVP- $\Omega$  in the rest of the thesis. Despite being nonlinear, it can be solved with well-established and time-efficient algorithms to get the matrix of eigenvalues,  $\boldsymbol{\Lambda} = \text{diag}(\lambda_1, \dots, \lambda_m, \dots, \lambda_{2M})$  of size  $2M \times 2M$ , and the matrix of corresponding eigenmodes,  $\boldsymbol{\Theta} = [\boldsymbol{\theta}_1, \dots, \boldsymbol{\theta}_m, \dots, \boldsymbol{\theta}_{2M}]$ , of size  $2N \times 2M$ . The eigenvalues are reported as

$$\lambda_m = \psi_m + iv_m \quad \text{with} \quad \psi_m = (-1)^m \sqrt{1 - \xi_{j_m}^2} \omega_{j_m} \quad \text{and} \quad v_m = \xi_{j_m} \omega_{j_m} \quad (4.13)$$

where  $\omega_{j_m}$  and  $\xi_{j_m}$  are referred to as the  $j_m$ -th natural frequency and damping ratio of the structure with  $j_m = \lceil \frac{m}{2} \rceil$ . The real (resp. imaginary) part of the eigenvectors of odd (resp. even) rank are also set to a unit maximum absolute value. These notation, normalization and organization choices eventually imply that the eigensolutions come in pairs. In particular, they are such that  $\lambda_m = -\lambda_{m+1}^*$  and  $\boldsymbol{\theta}_m = -i\boldsymbol{\theta}_{m+1}^*$  when  $m$  is odd. Besides, according to the added state equations, the top and the bottom parts of the eigenmodes can also be related as follows



$$\boldsymbol{\theta}_m = \begin{bmatrix} \boldsymbol{\phi}_m \\ i\lambda_m \boldsymbol{\phi}_m \end{bmatrix} \quad (4.14)$$

where  $\boldsymbol{\phi}_m$  is a vector of size  $N \times 1$ .

Thanks to the symmetry and positive definiteness of the state-space formulation, the left eigenvectors can directly be identified as the transposes of the right ones. If not, the left eigenvectors are to be computed independently of the right eigenvectors. This is not detailed in here to keep clutter-free equations but it would not substantially modify the following procedure. In any case, the mode shapes are however not orthogonal through the state matrices because of their frequency dependent nature. Their projection into the modal basis thus reads

$$\boldsymbol{\Theta}^\top \mathbf{A}(\omega) \boldsymbol{\Theta} = \mathcal{D}^{-1} \mathcal{A}(\omega) \quad \text{and} \quad \boldsymbol{\Theta}^\top \mathbf{B}(\omega) \boldsymbol{\Theta} = \mathcal{D}^{-1} \mathcal{B}(\omega) \quad (4.15)$$

where the off-diagonal entries of  $\mathcal{A}(\omega)$  and  $\mathcal{B}(\omega)$  are not necessarily equal to zero. Meanwhile, their diagonal elements are given by

$$\mathcal{A}_{kk}(\omega = \psi_k) = \lambda_k \quad \text{and} \quad \mathcal{B}_{kk}(\omega = \psi_k) = i \quad (4.16)$$

but they drift away as soon as they are evaluated at another circular frequency. The matrix  $\mathcal{D} = \text{diag}(\mathcal{D}_1, \dots, \mathcal{D}_m, \dots, \mathcal{D}_{2M})$  is diagonal and is intended to contain the constants that normalize the eigenvectors as explained hereabove.

Introducing the modal projection of the state forces,  $\mathbf{p}(\omega) = \boldsymbol{\Theta}^\top \mathbf{g}(\omega)$ , and the modal decomposition of the state responses,  $\mathbf{y}(\omega) = \boldsymbol{\Theta} \mathbf{q}(\omega)$ , into Equation (4.10) consequently yields the modal state formulation of the governing equations

$$\mathbf{q}(\omega) = \mathcal{J}^{-1}(\omega) \mathbf{p}(\omega) \quad (4.17)$$

which indicates that the modal state responses are indeed not decoupled, as previously announced, because the dynamical flexibility matrix

$$\mathcal{J}(\omega) = \mathcal{D}^{-1} [\mathcal{A}(\omega) + i\omega \mathcal{B}(\omega)] \quad (4.18)$$

is still a full matrix to invert. From a stochastic point of view, these governing equations translate into the spectral densities of the modal state responses as follows

$$\mathbf{S}_q(\omega) = \mathcal{D} \mathcal{H}(\omega) \mathbf{S}_p(\omega) \mathcal{D} \mathcal{H}^\dagger(\omega) \quad (4.19)$$

where

$$\mathcal{H}(\omega) = [\mathcal{A}(\omega) + i\omega \mathcal{B}(\omega)]^{-1} \quad (4.20)$$

is the frequency response function matrix of the coupled system. As indicated in Section 4.2, the spectral densities of the forces are also initially expressed in the physical coordinates by the matrix  $\mathbf{S}_f(\omega)$ . According to Equation (4.9), the matrix  $\mathbf{S}_f(\omega)$  is then used to define the matrix

$$\mathbf{S}_g(\omega) = \begin{bmatrix} \mathbf{S}_f(\omega) & \mathbf{0} \\ \mathbf{0} & \mathbf{0} \end{bmatrix} \quad (4.21)$$

which gathers the spectral densities of the  $i$ -th and  $j$ -th state forces,  $S_{g,ij}(\omega)$ . The matrix  $\mathbf{S}_g(\omega)$  is subsequently projected into the modal basis to get the matrix

$$\mathbf{S}_p(\omega) = \boldsymbol{\Theta}^\top \mathbf{S}_g(\omega) \boldsymbol{\Theta} \quad (4.22)$$

which collects the spectral densities of the  $m$ -th and  $n$ -th modal state forces,  $S_{p,mn}(\omega)$ . Taking

advantage of the zero blocks in  $\mathbf{S}_g(\omega)$ , Equation (4.21) can be bypassed and the matrix  $\mathbf{S}_p(\omega)$  can alternatively be written

$$\mathbf{S}_p(\omega) = \Phi^\top \mathbf{S}_f(\omega) \Phi \quad (4.23)$$

by using the relation between the top and the bottom parts of the eigenmodes which is derived in Equation (4.14).

Globally, the good point is that the size of the matrices to be processed has been drastically reduced. But, although it is smaller than before, the full matrix  $\mathcal{J}(\omega)$  of size  $2M \times 2M$  still has to be inverted, and now the matrix  $\mathbf{S}_f(\omega)$  also has to be projected into the modal basis at each of the numerous integration points that are required to calculate the second moments of the modal state responses

$$\Sigma_q = \int_{-\infty}^{+\infty} \mathbf{S}_q(\omega) d\omega \quad (4.24)$$

with a sufficient resolution. This is problematic because both the inversions and the projections are computationally demanding tasks and should be avoided as much as possible. In order to get rid of the inversions, two decoupling strategies are detailed hereafter while the projections will be dealt with afterwards, in Chapter 5 and Chapter 6, by using the general framework of the Multiple Timescale Spectral Analysis.

## 4.4 Decoupling of the Equations - Scenario 1

The first decoupling strategy steps in even before the introduction of the state space formulation and consists in neglecting the frequency sensitivity of the three hydrodynamic matrices. To do so, they are respectively substituted by  $\mathbf{K}_h(\omega_0)$ ,  $\mathbf{C}_h(\omega_0)$  and  $\mathbf{M}_h(\omega_0)$ , which are constant over the whole range of circular frequencies. In order to limit the errors caused by this replacement, the parameter  $\omega_0$  usually chosen as the dominant frequency of the forces or of the motions [1, 83, 101, 102]. In these circumstances, Equation (4.1) becomes

$$\left[ \mathbf{K}_0 + i\omega \mathbf{C}_0 - \omega^2 \mathbf{M}_0 \right] \mathbf{x}_0(\omega) = \mathbf{f}(\omega) \quad (4.25)$$

where the global hydroelastic matrices read  $\mathbf{K}_0 = \mathbf{K}_s + \mathbf{K}_h(\omega_0)$ ,  $\mathbf{C}_0 = \mathbf{C}_s + \mathbf{C}_h(\omega_0)$ , and  $\mathbf{M}_0 = \mathbf{M}_s + \mathbf{M}_h(\omega_0)$ . It then percolates through Equation (4.10) and Equation (4.11) to finally arrive at the eigensystem

$$i\mathbf{A}_0 \Theta_0 = \Lambda \mathbf{B}_0 \Theta_0 \quad (4.26)$$

which is not only standard, but also linear given that the state matrices

$$\mathbf{A}_0 = \begin{bmatrix} \mathbf{K}_0 & \mathbf{0} \\ \mathbf{0} & -\mathbf{M}_0 \end{bmatrix} \quad \text{and} \quad \mathbf{B}_0 = \begin{bmatrix} \mathbf{C}_0 & \mathbf{M}_0 \\ \mathbf{M}_0 & \mathbf{0} \end{bmatrix} \quad (4.27)$$

are now constant. This complex eigenproblem will be designated as EVP-0 in the rest of the thesis. For the sake of conciseness in the developments, the same notation, normalization and organization choices as in Section 4.3 are adopted but it is important to notice that they should actually differ. Be careful to use the eigensolutions associated to either EVP- $\Omega$ , either EVP-0, depending on the scenario considered in the following sections and chapters.

In the context at stake, the mode shapes are by definition orthogonal to each other through the state matrices. Projecting these matrices into such a modal basis thus yields

$$\Theta_0^\top \mathbf{A}_0 \Theta_0 = \mathbf{D}^{-1} \Lambda \quad \text{and} \quad \Theta_0^\top \mathbf{B}_0 \Theta_0 = i\mathbf{D}^{-1} \quad (4.28)$$

which are therefore simultaneously diagonal. The modal projection and decomposition of the state forces and responses,  $\mathbf{p}_0(\omega) = \mathbf{\Theta}_0^\top \mathbf{g}(\omega)$  and  $\mathbf{y}_0(\omega) = \mathbf{\Theta}_0 \mathbf{q}_0(\omega)$ , are then injected into Equation (4.10). After left multiplication by  $\mathbf{\Theta}_0^\top$  and  $\mathbf{DH}(\omega)$ , this equation reads

$$\mathbf{q}_0(\omega) = \mathbf{DH}(\omega) \mathbf{p}_0(\omega) \quad (4.29)$$

where the matrix of generalized frequency response functions,  $\mathbf{H}(\omega) = \text{diag}(H_1(\omega), \dots, H_m(\omega), \dots, H_{2M}(\omega))$  is diagonal and is therefore not expensive to calculate anymore. As a consequence, Equation (4.29) can equivalently be written

$$q_{0,m}(\omega) = D_m H_m(\omega) p_{0,m}(\omega) \quad \text{with} \quad H_m(\omega) = (\lambda_m - \omega)^{-1} \quad (4.30)$$

in indicial format and, on top of being decoupled, the modal responses are additionally monochromatic because their respective frequency response functions contain a single pole.

As shown in Figure 4.1, the real part of  $H_m(\omega)$  hence exhibits a double peak, spiking just left and just right to  $\psi_m$  with a sign change in between. Meanwhile, the imaginary part of  $H_m(\omega)$  displays a single peak located at  $\psi_m$  as well. The position, the height and the width of these peaks are clearly indicated in Figure 4.1-(a) which pictures the real and the imaginary parts of  $H_m(\omega)$  in linear scales, with their signs. More specifically, both the half-width at half-height of the peak in  $\Im[H_m(\omega)]$  and the half-width between the maximum and the minimum of  $\Re[H_m(\omega)]$  are related to  $v_m$  which in turn depends on the damping ratio. Thus, the smaller the damping ratios, the sharper the peaks.

Meanwhile, Figure 4.1-(b) gives an overview of what happens far below and far above the poles by presenting the real and the imaginary parts of  $H_m(\omega)$  in absolute values and in logarithmic scales. In particular, the slopes of the straight lines drawn at both extremities of this log-log plot indicate that  $\Re[H_m(\omega)]$  and  $\Im[H_m(\omega)]$  are approximately constant when  $|\omega| \ll |\psi_m|$  and behave like monomials of degree  $(-1)$  or  $(-2)$ , respectively, when  $|\omega| \gg |\psi_m|$ .

As per Equation (4.30), the spectral density of the  $m$ -th and the  $n$ -th modal state responses can then be written in the canonical form

$$S_{q_0,mn}(\omega) = D_m D_n G_{mn}(\omega) S_{p_0,mn}(\omega) \quad (4.31)$$

where

$$G_{mn}(\omega) = H_m(\omega) H_n^*(\omega) \quad (4.32)$$

is used to define the structural kernel associated to the  $m$ -th and the  $n$ -th modal state responses. This function is illustrated in Figure 4.2 and Figure 4.3 for a few sets of parameters in order to get a picture of how the  $m$ -th and the  $n$ -th frequency response functions are supposed to interact in these various cases.

Integrating  $S_{q_0,mn}(\omega)$  instead of  $S_{y,ij}(\omega)$  is, in principle, easier to achieve as it features two sharp peaks at most, and no longer a multitude. These peaks are respectively associated to the resonance of the structure in the  $m$ -th and the  $n$ -th modes and come along some strong variations related to the particular energy content of the waves. However, despite their reduced number, the sharpness and the distinctness of these peaks imply that a large number of closely spaced integration points are still needed to determine the second moments of the modal state responses

$$\Sigma_{q_0,mn} = \int_{-\infty}^{+\infty} S_{q_0,mn}(\omega) d\omega \quad (4.33)$$

in an accurate way. Thanks to the method described above, the modal state equations are now

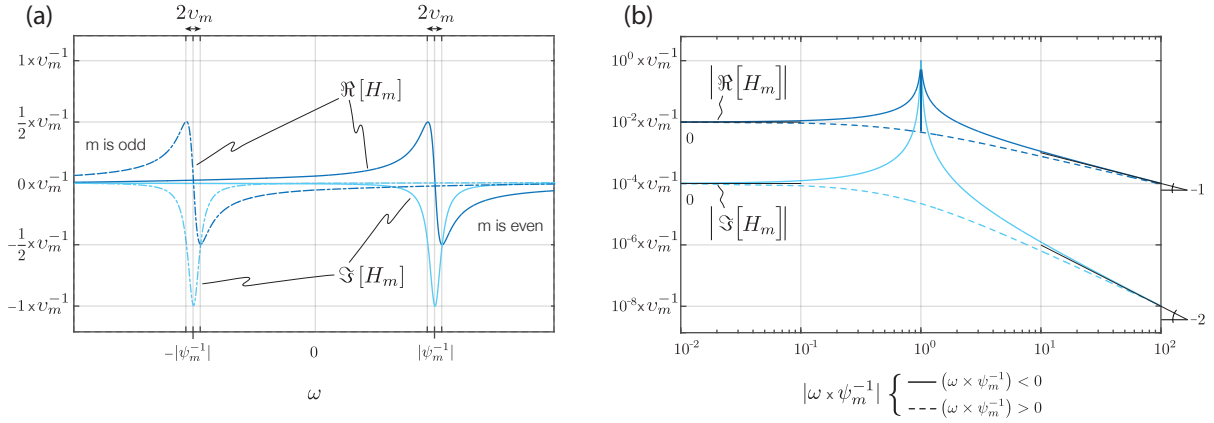


FIGURE 4.1: Real ( $\Re$ ) and imaginary ( $\Im$ ) parts of  $H_m(\omega)$ : (a) with their signs in linear scales, (b) in absolute values and logarithmic scales.

decoupled. They can therefore be solved independently of one another, without requiring to invert a full matrix anymore. Instead, the spectral densities of the modal state forces are computed and projected into the modal basis at each of the numerous integration points. Unfortunately, this operation is actually very costly as well, especially given the possibly large size of the system, meaning that the computational demand is not particularly reduced in overall. As previously mentioned, this problem will be dealt with in Chapter 5 for the decoupling strategy at hand. It will be addressed by applying the Multiple Timescale Spectral Analysis to the integral of Equation (4.33).

## 4.5 Decoupling of the Equations - Scenario 2

The eigenvalues and the eigenmodes considered in the upcoming section are obtained as the solutions of the EVP- $\Omega$  because the second decoupling strategy operates at the level of the dynamical flexibility matrix, by introducing the alternative expression

$$\mathcal{J}^{-1}(\omega) = \left[ \mathbf{I} + \sum_{k=1}^{+\infty} (-1)^k \left( \mathcal{J}_d^{-1}(\omega) \mathcal{J}_o(\omega) \right)^k \right] \mathcal{J}_d^{-1}(\omega) \quad (4.34)$$

where  $\mathcal{J}_d(\omega) = \text{diag}(\mathcal{J}(\omega))$  while  $\mathcal{J}_o(\omega) = \mathcal{J}(\omega) - \mathcal{J}_d(\omega)$  contains the off-diagonal entries of  $\mathcal{J}(\omega)$  and zeros anywhere else [96, 97, 103]. As a result, the inversion of a full matrix is no longer required. Inverting the diagonal part of the dynamical flexibility matrix suffices to obtain the transfer matrix

$$\mathcal{D}\mathcal{H}_d(\omega) = \mathcal{J}_d^{-1}(\omega) \quad (4.35)$$

where  $\mathcal{H}_d(\omega) = \text{diag}(\mathcal{H}_{d,1}, \dots, \mathcal{H}_{d,m}, \dots, \mathcal{H}_{d,2M})$ , and to correct it by a series of terms which do not depend on any other inverse. But even so, the computational demand is not substantially reduced when an infinite number of corrections is implemented.

It is therefore interesting to notice that the series presents a high convergence rate if the diagonality index of  $\mathcal{J}(\omega)$  is much smaller than unity for all  $\omega \in \mathbb{R}$ . This parameter measures the diagonal dominance of the matrix and is defined in [104] as

$$\rho(\mathcal{J}) = \sigma \left( \mathcal{J}_d^{-1}(\omega) \mathcal{J}_o(\omega) \right) \quad (4.36)$$

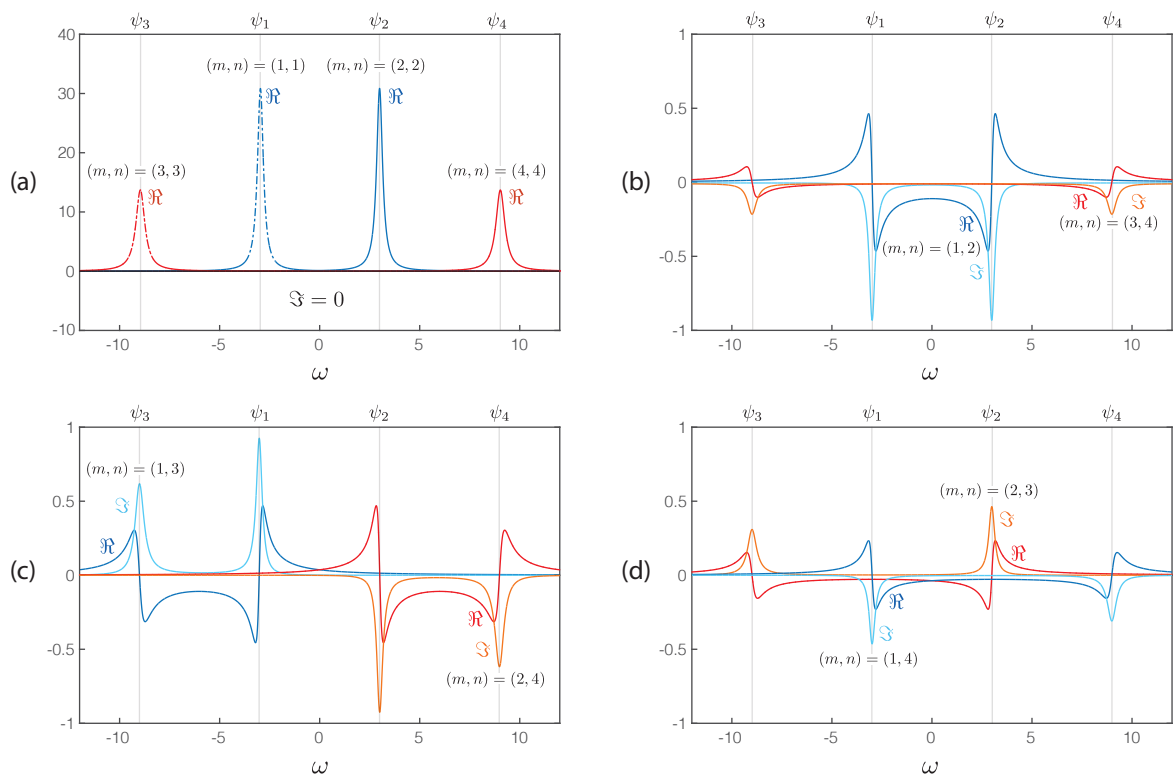


FIGURE 4.2: Real ( $\Re$ ) and imaginary ( $\Im$ ) parts of  $G_{mn}(\omega)$  when  $\omega_1 = 3$  rad/s,  $\omega_2 = 9$  rad/s,  $\xi_1 = 6\%$ , and  $\xi_2 = 3\%$ : (a)  $|\psi_m| = |\psi_n|$  and  $\psi_m\psi_n > 0$ , (b)  $|\psi_m| = |\psi_n|$  and  $\psi_m\psi_n < 0$ , (c)  $|\psi_m| \neq |\psi_n|$  and  $\psi_m\psi_n > 0$ , (d)  $|\psi_m| \neq |\psi_n|$  and  $\psi_m\psi_n < 0$ .

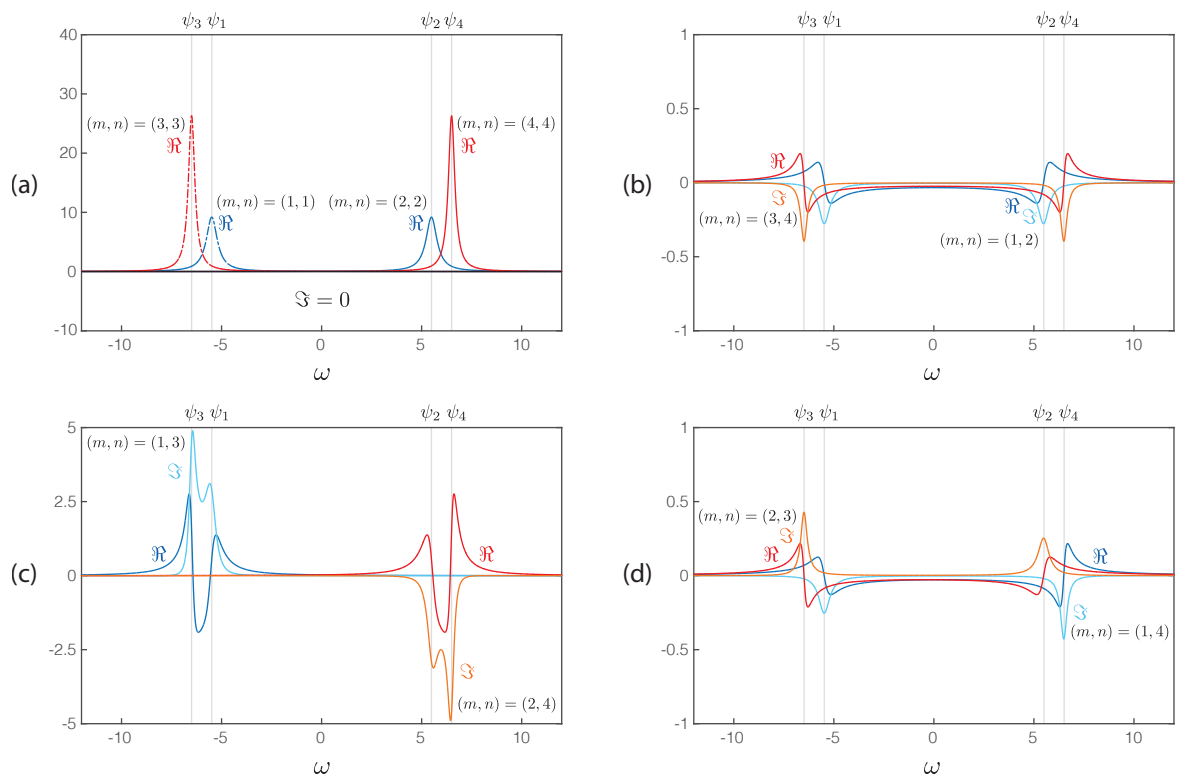


FIGURE 4.3: Real ( $\Re$ ) and imaginary ( $\Im$ ) parts of  $G_{mn}(\omega)$  when  $\omega_1 = 5.5$  rad/s,  $\omega_2 = 6.5$  rad/s,  $\xi_1 = 6\%$ , and  $\xi_2 = 3\%$ : (a)  $|\psi_m| = |\psi_n|$  and  $\psi_m \psi_n > 0$ , (b)  $|\psi_m| = |\psi_n|$  and  $\psi_m \psi_n < 0$ , (c)  $|\psi_m| \neq |\psi_n|$  and  $\psi_m \psi_n > 0$ , (d)  $|\psi_m| \neq |\psi_n|$  and  $\psi_m \psi_n < 0$ .

where  $\sigma$  stands for the spectral radius. Depending on its smallness, the series can thus be truncated after a given number of terms. Keeping only the leading term, for instance, amounts to neglect the off-diagonal entries in  $\mathcal{J}(\omega)$ . This approach is typically referred to as the decoupling approximation and is attributed to Lord Rayleigh [90].

In the following, the first order correction is considered as it partially accounts for the modal couplings which result from the frequency dependency. It complements the modal correlations which are due to the coherence of the modal forces. Hence, the transfer matrix is finally given by the series

$$\mathbf{H}_2(\omega) = [\mathbf{I} - \mathcal{D}\mathcal{H}_d(\omega)\mathcal{J}_o(\omega)]\mathcal{D}\mathcal{H}_d(\omega) \quad (4.37)$$

which is truncated at first order. Likewise, the modal state responses are supposed to be estimated precisely enough by the first order approximation

$$\mathbf{q}_2(\omega) = [\mathbf{I} - \mathcal{D}\mathcal{H}_d(\omega)\mathcal{J}_o(\omega)]\mathbf{q}_d(\omega) \quad (4.38)$$

where the leading order terms correspond to a set of decoupled modal state responses which can actually be obtained independently of one another, without having to invert any full matrix. They read

$$\mathbf{q}_d(\omega) = \mathcal{D}\mathcal{H}_d(\omega)\mathbf{p}(\omega) \quad (4.39)$$

and given that  $\mathcal{H}_d(\omega)$  collects the frequency response functions of these decoupled modal state responses

$$\mathcal{H}_{d,m}(\omega) = [\mathcal{A}_{mm}(\omega) + i\omega\mathcal{B}_{mm}(\omega)]^{-1} \quad (4.40)$$

on its diagonal but zeros everywhere else, Equation (4.39) can alternatively be written

$$q_{d,m}(\omega) = \mathcal{D}_m\mathcal{H}_{d,m}(\omega)p_m(\omega) \quad (4.41)$$

in indicial form.

Then, introducing the first order approximation of the transfer function into Equation (4.19) allows to estimate the spectral densities of the modal state responses as

$$\mathbf{S}_{q_2}(\omega) = \mathbf{S}_{q_1}(\omega) + [\Delta\mathbf{S}_{q_1}(\omega) + \Delta\mathbf{S}_{q_1}^\dagger(\omega)] \quad (4.42)$$

where the leading order term reads

$$\mathbf{S}_{q_1}(\omega) = \mathcal{D}\mathcal{H}_d(\omega)\mathbf{S}_p(\omega)\mathcal{D}\mathcal{H}_d^*(\omega) \quad (4.43)$$

and where the first order term is given by

$$\Delta\mathbf{S}_{q_1}(\omega) = -\mathcal{D}\mathcal{H}_d(\omega)\mathcal{J}_o(\omega)\mathcal{D}\mathcal{H}_d(\omega)\mathbf{S}_p(\omega)\mathcal{D}\mathcal{H}_d^*(\omega), \quad (4.44)$$

while the next corrective term

$$\Delta\mathbf{S}_{q_2}(\omega) = \mathcal{D}\mathcal{H}_d(\omega)\mathcal{J}_o(\omega)\mathbf{S}_{q_1}(\omega)\mathcal{J}_o^\dagger(\omega)\mathcal{D}\mathcal{H}_d^*(\omega) \quad (4.45)$$

is directly discarded on the basis that it is a second order term [97]. The corrections delivered by  $\Delta\mathbf{S}_{q_2}(\omega)$  are not significant when the diagonality index of the dynamical flexibility matrix is relatively small. Plus, it would not be consistent to keep them anyway since the series expansion of the transfer function has previously been truncated at first order.

As indicated in [97], the corrections provided by the first order terms,  $\Delta\mathbf{S}_{q_1}(\omega)$  and  $\Delta\mathbf{S}_{q_1}^\dagger(\omega)$ , are usually sufficient to ensure that  $\mathbf{S}_{q_2}(\omega)$  approximates  $\mathbf{S}_q(\omega)$  with a high level of accuracy. They are on the other hand necessary to achieve this objective for the off-diagonal elements of  $\mathbf{S}_{q_2}(\omega)$ , even though they are globally small with respect to the leading terms. If the modal forces are

uncorrelated, for instance,  $\mathbf{S}_p(\omega)$  and thus  $\mathbf{S}_{q_1}(\omega)$  are transformed into diagonal matrices. As a consequence, the off-diagonal elements of  $\mathbf{S}_{q_2}(\omega)$  are exclusively given by  $\Delta\mathbf{S}_{q_1}(\omega) + \Delta\mathbf{S}_{q_1}^\dagger(\omega)$ . In this specific case, the corrective terms are therefore not negligible, no matter their smallness because they are to be compared with zeros.

On the other hand, they completely disappear when the generalized flexibility matrix is either diagonal, either considered as such. Thus,  $\mathbf{S}_{q_1}(\omega)$  corresponds to the densities that are obtained when the modal responses are directly decoupled, or approximated as such. They are therefore solely influenced by the modal correlations, while the modal couplings are partially accounted for by the first order corrections.

Besides, in the above equations, the diagonal nature of the matrix  $\mathcal{D}$  and the matrix  $\mathcal{H}_d(\omega)$  is already accounted for. These matrices are hence symmetric and equivalent to their transposes. The elements of  $\mathcal{D}$  are also real-valued. Thus,  $\mathcal{D}$  corresponds to its hermitian conjugate and so does  $\mathbf{S}_p(\omega)$ , according to [105]. Rewriting Equation (4.42) in indicial form then yields

$$S_{q_2,mn}(\omega) = S_{q_1,mn}(\omega) + \Delta S_{q_1,mn}(\omega) + \Delta S_{q_1,nm}^*(\omega) \quad (4.46)$$

with the leading order term

$$S_{q_1,mn}(\omega) = \mathcal{D}_m \mathcal{D}_n G_{d,mn}(\omega) S_{p,mn}(\omega) \quad (4.47)$$

and the first order correction

$$\Delta S_{q_1,mn}(\omega) = \sum_{k=1}^{2M} \mathcal{D}_m \mathcal{D}_n \mathcal{D}_k G_{d,mnk}(\omega) \mathcal{J}_{o,mk}(\omega) S_{p,kn}(\omega) \quad (4.48)$$

being defined as functions of the structural kernels

$$G_{d,mn}(\omega) = \mathcal{H}_{d,m}(\omega) \mathcal{H}_{d,n}^*(\omega) \quad (4.49)$$

and

$$G_{d,mnk}(\omega) = \mathcal{H}_{d,m}(\omega) \mathcal{H}_{d,n}^*(\omega) \mathcal{H}_{d,k}(\omega) \quad (4.50)$$

which are respectively formed by the product of two or three frequency response functions. Provided that each of these functions contains a single pole,  $S_{q_1,mn}(\omega)$  and  $\Delta S_{q_1,mn}(\omega)$  are thus expected to exhibit the same amount of resonant peaks as the number of frequency response functions entering into their expression, at most. The former contains two peaks as is usually the case when the modal state responses are completely decoupled. The latter introduces small corrections in the form of additional peaks which make the spectral densities of the modal state responses look like those of coupled systems. However, instead of dealing with a multitude of peaks, they are to be handled two-by-two in Equation (4.46) or three-by-three in Equation (4.47). Being so readily identified, their contributions to the leading order terms

$$\Sigma_{q_1,mn} = \int_{-\infty}^{+\infty} S_{q_1,mn}(\omega) d\omega \quad (4.51)$$

and the first corrective terms

$$\Delta \Sigma_{q_1,mn} = \int_{-\infty}^{+\infty} \Delta S_{q_1,mn}(\omega) d\omega \quad (4.52)$$

are expected to be easily treated by the Multiple Timescale Spectral Analysis, see Chapter 6. But until then, the numerical integration of these functions requires to use an important number of



points and to project large matrices for each of them in order to get an accurate estimation for the second moments of the modal state responses which reads

$$\Sigma_{q_2, mn} = \Sigma_{q_1, mn} + \Delta \Sigma_{q_1, mn} + \Delta \Sigma_{q_1, mn}^\dagger \quad (4.53)$$

at last. Thus, although the current decoupling strategy allows to avoid the inversion of full matrices, the repeated projections of large matrices are still driving the computational cost up, and sometimes even out of reasonable ranges.

## 4.6 Recombination of the Modal Responses

At last, the spectral densities and the second moments of the modal state responses obtained in Section 4.3, Section 4.4 and Section 4.5 can finally be recombined by  $\mathbf{y}_*(\omega) = \Theta_{\mathbf{q}_*}(\omega)$  in order to get references and approximations for the spectral densities and the second moments of the nodal state responses. They thus read

$$\mathbf{S}_{y_*}(\omega) = \Theta_* \mathbf{S}_{q_*}(\omega) \Theta_*^\dagger \Leftrightarrow S_{y_*, ij}(\omega) = \sum_{m=1}^{2M} \sum_{n=1}^{2M} \Theta_{*, im} \Theta_{*, jn}^* S_{q_*, mn}(\omega) \quad (4.54)$$

where the star subscript denotes nothing, zero, one or two depending on the case considered here-above. They are known to fully describe the probabilistic features of the responses in the present linear, normal and zero-mean context. In particular, the second moments of the  $i$ -th and the  $j$ -th nodal state responses can be defined as the integrals of the corresponding spectral densities along the frequencies. They are hence expressed as

$$\Sigma_{y_*} = \Theta_* \Sigma_{q_*} \Theta_*^\dagger \Leftrightarrow \Sigma_{y_*, ij} = \sum_{m=1}^{2N} \sum_{n=1}^{2N} \Theta_{*, im} \Theta_{*, jn}^* \Sigma_{q_*, mn} \quad (4.55)$$

in matricial form and indicial form.

In order to identify the so-called square root of the sum of the squares (SRSS) and complete quadratic combination (CQC) rules, Equation (4.55) can also be rewritten as follows

$$\begin{aligned} \Sigma_{y_*, ij} &= \Theta_{*, im} \Theta_{*, jm}^* \Sigma_{q_*, mm} \\ &+ \sum_{m=1}^{2N} \sum_{n=1, n \neq m}^{2N} \Theta_{*, im} \Theta_{*, jn}^* \rho_{q_*, mn} \sqrt{\Sigma_{q_*, mm} \Sigma_{q_*, nn}} \end{aligned} \quad (4.56)$$

where

$$\rho_{q_*, mn} = \frac{\Sigma_{q_*, mn}}{\sqrt{\Sigma_{q_*, mm} \Sigma_{q_*, nn}}} \quad (4.57)$$

is the correlation coefficient of the modal state responses. By contrast with the second moments, these coefficients are dimensionless and bounded in the interval  $[-1, 1]$ . They thus enable a fair evaluation of the influence that the modal covariances might have on the nodal results, as regards to the modal variances. If the modal correlations are much smaller than unity in absolute value, the second line of Equation (4.56) drops. In this event, the SRSS, which is less burdensome as it considers the elements in the first line of Equation (4.56) only, is expected to be as accurate as the CQC, which includes the elements in both lines of Equation (4.56). Otherwise, the nodal results can be significantly affected by the choice of such a recombination rule.

Through the definition of the state variables,  $\mathbf{y}_*(\omega) = \begin{bmatrix} \mathbf{I} & i\omega \mathbf{I} \end{bmatrix}^\top \mathbf{x}_*(\omega)$ , the spectral densities and the second moments of the state responses also end up being related to those of the initial responses as follows

$$\mathbf{S}_{y_*}(\omega) = \begin{bmatrix} \mathbf{S}_{x_*}(\omega) & -i\omega\mathbf{S}_{x_*}(\omega) \\ i\omega\mathbf{S}_{x_*}(\omega) & \omega^2\mathbf{S}_{x_*}(\omega) \end{bmatrix} \quad (4.58)$$

where  $\omega^2\mathbf{S}_{x_*}(\omega) = \mathbf{S}_{\dot{x}_*}(\omega)$ . Hence, the top left and bottom right blocks of size  $N \times N$  in  $\mathbf{\Sigma}_{y_*}$  can readily be identified as containing the second moments of the initial responses and their time derivatives,  $\mathbf{\Sigma}_{x_*}$  and  $\mathbf{\Sigma}_{\dot{x}_*}$ , respectively. As mentioned earlier, these matrices and especially their diagonal elements, which represent the variances of the corresponding processes, are the quantities of interest for a design perspective. For instance, according to the conventional formula based on the Poisson assumption which has been widely adopted in most international codes and standards, the average of the extreme values encountered over windows of duration  $T$  in the response processes reads

$$\bar{z}_{x,i} = \left( \sqrt{2 \ln n_{x,i}} + \frac{\gamma}{\sqrt{2 \ln n_{x,i}}} \right) \sqrt{\Sigma_{x,i}} \quad (4.59)$$

for the  $i$ -th degree-of-freedom, where

$$n_{x,i} = \frac{T}{2\pi} \sqrt{\frac{\Sigma_{\dot{x},i}}{\Sigma_{x,i}}} \quad (4.60)$$

and  $\gamma \simeq 0.5572$  is the Euler constant [106]. When environmental loads are considered, these results are likely to be used by the wind engineering community to determine peak factors. In wave engineering, they are related to the short-term extreme responses whose cumulative distribution functions are then computed for many different sea states in order to derive the statistics of the long-term extreme responses. Although the state space formulation doubles the size of the matrices to be processed throughout the analysis, the extreme responses of the system are fully characterized by  $\mathbf{\Sigma}_y$  and thus by  $\mathbf{\Sigma}_q$ . In order to speed up the calculation of  $\mathbf{\Sigma}_q$  with the help of the Multiple Timescale Spectral Analysis, a single formula can be used for all of its elements, whereas in physical coordinates, two different expressions are needed: one is dedicated to the statistics of the modal responses and another one is required for the statistics of their derivatives [11].

## 4.7 Need for MTSA Extension

In comparison with the direct integration of the spectral densities presented in Equation (4.7), resorting to the modal state approach and the decoupling strategies, as detailed above, is already more efficient in computing the variances and the covariances of the initial responses and their time derivatives for several reasons. First, the size of the system has been drastically reduced by being projected into an appropriate basis composed of  $2M \ll 2N$  modes only. Second, the responses have been decoupled, at the expense of a small loss of accuracy or not depending on whether the frequency dependency of the hydroelastic matrices is significant or not.

As a result, their second order statistics can be obtained independently of one another, without requiring to invert a full matrix anymore, and the number of poles in the functions to integrate has been restricted to three at most instead of up to  $2N$ , provided that the frequency sensitivity of the hydroelastic matrices is relatively limited. But in return, the complexity of the stochastic analysis is now driven by the projections of the spectral densities of the modal state forces into the modal basis. This is indeed another computationally demanding task which additionally has to be repeated for a large number of integration points because the functions to be integrated feature sharp and distinct peaks.

Whereas the sharpness and the distinctness of the peaks constitute a huge drawback for the numerical integration, it can in fact be turned into an advantage as it provides a sound basis for the implementation of the Multiple Timescale Spectral Analysis. This general framework has

specifically been formulated to reduce the number of points that are needed to compute such integrals, and especially avoid to project the spectral densities of the forces into a modal basis so many times. This objective is typically achieved by deriving semi-analytical approximations for the main components of the corresponding statistics [11].

In ocean engineering applications though, the fast dynamics are not necessarily linked with the structural motions, especially when wave-loaded structures are compliant in surge, as floating offshore wind turbines or floating bridges. Such systems might therefore respond in the background and the resonant regimes, but also in the inertial one which is on the contrary hardly ever activated in land-based wind-loaded structures. The Multiple Timescale Spectral Analysis is therefore yet to take the inertial components into account.

In addition, fluid-structure interactions are also regarded for the first time. Given that we propose to handle the resulting non-classicality of the added damping and frequency dependency of the hydroelastic matrices by means of a modal state formulation, the consideration of complex eigenfrequencies and eigenmodes is expected to modify the expressions of the background and the resonant components which have been derived in the past for the second moments of the modal responses as well.

These are hence the two reasons why the method is extended in this thesis, in Chapter 5 and in Chapter 6 depending on whether the first or the second decoupling strategy is selected, before being finally applied on realistic wave-loaded structures in Chapter 7.



## Chapter 5

# Covariances, Excluding Frequency-Dependency

### 5.1 Introduction and Preliminary Considerations

In this chapter, the first decoupling strategy is supposed to have previously been implemented. It thus follows Section 4.4 and the integration of

$$S_{q_0, mn}(\omega) = D_m D_n G_{mn}(\omega) S_{p_0, mn}(\omega) \quad (5.1)$$

where the structural kernel reads

$$G_{mn}(\omega) = H_m(\omega) H_n^*(\omega) \quad (5.2)$$

is now tackled with the Multiple Timescale Spectral Analysis in order to accelerate the computation of the statistics, by reducing the number of times the spectral densities of the loading need to be projected.

Using this method first requires to formulate a few assumptions regarding the distinctness of the peaks observed in the integrands at stake. They are detailed in Section 5.2 and they consequently allow to identify the areas that contribute the most to the integrals. As in Chapter 2, these zones are readily identified as being twofold and related to either the peaks of the structural kernel, either the peaks of the loading spectrum. They are then focused in a sequential way in Section 5.3 and Section 5.4. In these regions, locally accurate approximations of the integrands are derived and are eventually integrated in an analytical way to provide a decomposition into two main components with simple formulas for the second order statistics of the modal state responses.

A realistic description of the wave loads will be considered later on, in Chapter 7, for validation. In this chapter, however, the spectral density of the  $m$ -th and  $n$ -th modal state forces are temporarily defined by using the following expression

$$S_{p_0, mn}(\omega) = P_{a, mn} |S_w(\omega)| + iP_{s, mn} S_w(\omega) \quad (5.3)$$

which is introduced in details in Appendix A. It allows to illustrate and to validate the mathematical developments presented in this chapter but also to study the influence that the natural frequencies, the damping ratios and the peak frequencies of the waves have on the results through a parametric analysis, in Section 5.5. Please note that the coefficients  $P_{a, mn}$  and  $P_{s, mn}$  are complex. Therefore and contrary to the spectral densities of real processes, the co- and quad-spectral densities of the modal state forces,  $\Re[S_{p_0, mn}(\omega)]$  and  $\Im[S_{p_0, mn}(\omega)]$ , are no longer even and odd because of the projection into a complex basis, see Appendix A for further explanations.

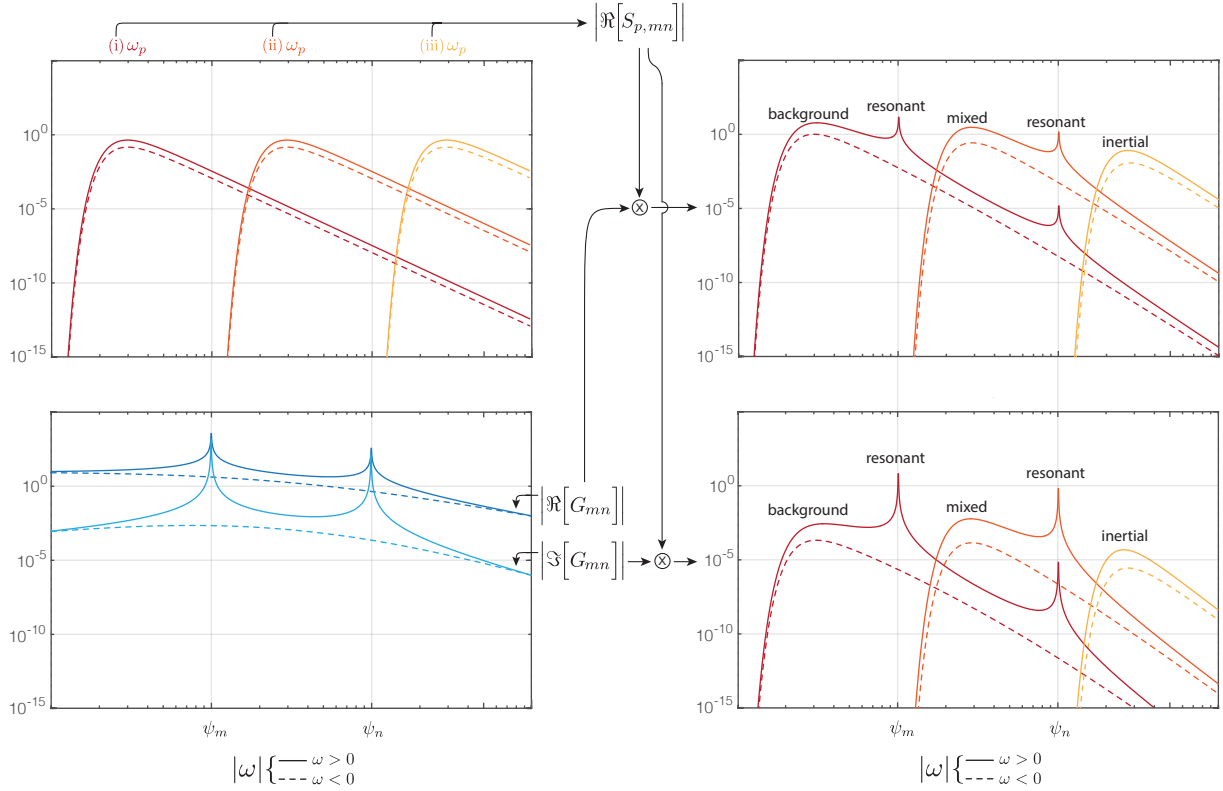


FIGURE 5.1: Origin of the peaks in the spectral density of the  $m$ -th and  $n$ -th modal state responses, with  $m$  and  $n$  being different even numbers. The natural frequencies and damping ratios are  $\omega_{j_m} = 0.1$  rad/s,  $\omega_{j_n} = 1$  rad/s,  $\xi_{j_m} = 1\%$  and  $\xi_{j_n} = 1\%$  while the spectral density of the  $m$ -th and  $n$ -th modal state forces is given by Equation (5.3) where  $P_{a,mn} = 1$ ,  $P_{s,mn} = -i/2$  and (i)  $\omega_p = 0.03$  rad/s for the red curves, (ii)  $\omega_p = 0.3$  rad/s for the orange curves or (iii)  $\omega_p = 3$  rad/s for the yellow curves.

## 5.2 Formulation of the Necessary Assumptions

In the current situation, the peaks in the spectral density of the  $m$ -th and  $n$ -th modal state responses are separated provided that a few conditions are verified. They read as follows and they can typically be linked to the existence of some small numbers which set the stage for a successful application of the perturbation theories.

- (i) The spectral density of the  $m$ -th and  $n$ -th modal state forces varies smoothly and moderately over the width of the resonant peaks. This is based on the fact that the derivatives of these functions are small with respect to the extent of the considered zone which scales with  $v_m \propto \xi_{j_m}$  and  $v_n \propto \xi_{j_n}$ . If the damping ratios are very small and the resonant peaks are very sharp, for instance, the spectral density of the  $m$ -th and  $n$ -th modal state forces is allowed to fluctuate more. Otherwise said, it will globally not change much between the two sides of an extremely narrow frequency interval.
- (ii) The characteristic frequency of the waves, which is denoted  $\omega_p$ , is significantly different from the  $m$ -th and  $n$ -th natural frequencies of the structure,  $\psi_m$  and  $\psi_n$ . The frequency ratios

$$\alpha_m = \frac{\omega_p}{|\psi_m|} \quad \text{and} \quad \alpha_n = \frac{\omega_p}{|\psi_n|} \quad (5.4)$$

are therefore much lower or much higher than one in absolute value. In the first case, the wave loading actually excites the corresponding mode in its background regime while it triggers the inertial regime in the second.

Under these assumptions, the Multiple Timescale Spectral Analysis can decompose the spectral densities of the modal state responses into two main parts. It yields

$$\tilde{S}_{q_0,mn}(\omega) = S_{r_0,mn}(\omega) + S_{\ell_0,mn}(\omega) \quad (5.5)$$

where the tilde symbol indicates that this is an approximate expression. On the one hand, the first term fits the initial spectral density (i.e. the non-tilde function) over the peaks that are caused by the poles of the frequency response functions. It is referred to as the *resonant* contribution and tagged by a subscript  $r$ . On the other hand, the second term approximates locally the spectral density of the response over the peaks that are related to the particular shape featured by the spectral densities of the modal state forces. Depending on the relative position of this peak with regard to the resonant ones, it is designated as the *background*, if both  $\omega_p < \omega_{j_m}$  and  $\omega_p < \omega_{j_n}$ , the *inertial*, if both  $\omega_p > \omega_{j_m}$  and  $\omega_p > \omega_{j_n}$ , or the *mixed* contribution, otherwise. These three eventualities are shown in Figure 5.1 and labelled (i), (ii), and (iii), respectively. In general, however, it can be identified as the *loading* contribution and this is denoted by the subscript  $\ell$ .

If these local approximations are sufficiently accurate in the regions considered, are integrable in the far field, and are such that the formulations of their integrals are explicit, the second moments of the modal state responses can be estimated through the use of the Multiple Timescale Spectral Analysis as the sum of two components

$$\tilde{\Sigma}_{q_0,mn} = \Sigma_{r_0,mn} + \Sigma_{\ell_0,mn} \quad (5.6)$$

whose expressions are derived in Section 5.3 and Section 5.4. It seems interesting to notice that dropping the loading component should suffice to get a correct estimation for the second moment when  $\alpha_m$  and/or  $\alpha_n$  approaches unity, even if Assumption (ii) is not met. Indeed, in this event, one or both natural frequencies are close to the characteristic frequency of the waves. The peak of the loading spectrum is stacked on one or both peaks of the structural kernel. Being in the same zones, they are all covered by the first local approximation of the response spectrum, which is herein the resonant one, when the Multiple Timescale Spectral Analysis is applied.

In brief, in Section 5.3 and Section 5.4, we demonstrate that  $\Sigma_{r_0,mn}$  and  $\Sigma_{\ell_0,mn}$  can respectively be expressed as

$$\Sigma_{r_0,mn} = i\pi \frac{D_m D_n}{\lambda_m - \lambda_n^*} [S_{p_0,mn}(\psi_m) + S_{p_0,mn}(\psi_n)] \quad (5.7)$$

and

$$\Sigma_{\ell_0,mn} = D_m D_n L_{mn} \sum_{l=1}^4 \left[ (+\omega_p)^{\beta_{mn}^{(l)}} \mathcal{G}_{mn}^{(l)} (+\omega_p) \Sigma_{p_0,mn}^{(l)(+)} + (-\omega_p)^{\beta_{mn}^{(l)}} \mathcal{G}_{mn}^{(l)} (-\omega_p) \Sigma_{p_0,mn}^{(l)(-)} \right] \quad (5.8)$$

where

$$L_{mn} = \left( 1 - \frac{S_{p_0,mn}(\psi_m)}{S_{p_0,mn}(\omega_p)} \right) \left( 1 - \frac{S_{p_0,mn}(\psi_n)}{S_{p_0,mn}(\omega_p)} \right) , \quad (5.9)$$

$$\Sigma_{p_0,mn}^{(l)(\pm)} = \pm \sum_{i=1}^N \sum_{j=1}^N \Phi_{im} \Phi_{in}^* \int_0^{\pm\infty} \omega^{-\beta_{mn}^{(l)}} S_{f,ij}(\omega) d\omega , \quad (5.10)$$

and

$l$	$\beta_{mn}^{(l)}$	$\mathcal{G}_{mn}^{(l)}(\omega)$
1	$\beta_m + \beta_n$	$\Re[H_m(\omega)] \Re[H_n^*(\omega)]$
2	$\beta_m + 2\beta_n$	$i\Re[H_m(\omega)] \Im[H_n^*(\omega)]$
3	$2\beta_m + \beta_n$	$i\Im[H_m(\omega)] \Re[H_n^*(\omega)]$
4	$2\beta_m + 2\beta_n$	$-\Im[H_m(\omega)] \Im[H_n^*(\omega)]$

as shown in Table 5.1.

### 5.3 Derivation of the Resonant Component

The resonant component is due to the poles of the frequency response functions,  $H_m(\omega)$  and  $H_n^*(\omega)$ . As shown in Figure 4.2 and Figure 4.3, the resulting peaks can interact differently –sometimes less, sometimes more– depending on how close  $\psi_m$  is to  $\psi_n$  and eventually merge if these eigenfrequencies are coalescent, e.g. when the auto-spectral densities and thus the variances are examined ( $m = n$ ).

Given that the denominator of the structural kernel is already factorized as the product of  $(\lambda_m - \omega)$  and  $(\lambda_n^* - \omega)$  being two first degree polynomials with single but complex roots, it is quite straightforward to expand it in partial fractions. Equation (5.2) is indeed expected to read

$$G_{mn}(\omega) = \frac{a}{\lambda_m - \omega} + \frac{b}{\lambda_n^* - \omega} \quad (5.11)$$

where  $a$  and  $b$  are constant but complex coefficients. Equation (5.11) can be rewritten as

$$b(\lambda_m - \omega) = 1 - a(\lambda_n^* - \omega) \quad (5.12)$$

which is subsequently evaluated at  $\omega = \lambda_n^*$  in order to get the following expression

$$b = \frac{1}{\lambda_m - \lambda_n^*} \quad (5.13)$$

for the first coefficient of the partial fraction expansion. Reintroducing Equation (5.13) into Equation (5.12) then yields

$$a = -b \quad (5.14)$$

for the second coefficient of the partial fraction expansion. These two coefficients are substituted back in the initial equation and the partial decomposition of the structural kernel is eventually given by

$$G_{mn}(\omega) = -\frac{1}{\lambda_m - \lambda_n^*} \left[ \frac{1}{\lambda_m - \omega} - \frac{1}{\lambda_n^* - \omega} \right] \quad (5.15)$$

or equivalently by

$$G_{mn}(\omega) = -\frac{H_m(\omega) - H_n^*(\omega)}{\lambda_m - \lambda_n^*} \quad (5.16)$$

in terms of the frequency response functions.

As a result, these functions are subtracted instead of being multiplied and the spectral density of the modal state responses becomes

$$S_{q_0, mn}(\omega) = -\frac{D_m D_n}{\lambda_m - \lambda_n^*} [H_m(\omega) S_{p_0, mn}(\omega) - H_n^*(\omega) S_{p_0, mn}(\omega)] \quad (5.17)$$

where the respective poles of  $H_m(\omega)$  and  $H_n^*(\omega)$  are now isolated, without any approximation, in two different parts of the function to integrate. The stretched coordinate  $\omega = \psi_m(1 + \varepsilon\eta)$  can then



be substituted into the first term of Equation (5.17) in order to focus on the pole of  $H_m(\omega)$  by placing it at  $\eta = 0$  and by zooming on the contributing area, where  $\eta \sim \text{ord}(1)$ , thanks to the smallness of the arbitrary parameter,  $\varepsilon \ll 1$ . Its value can actually be related to  $v_m$  which is the half width at half height of the peak in  $\Im[H_m(\omega)]$  or the half width between the positive and the negative maxima in  $\Re[H_m(\omega)]$ , as indicated in Figure 4.1-(a). Invoking Assumption (i), the derivatives of the loading spectrum are considered small enough to maintain the asymptoticness of its Taylor series expansion in the neighborhood of  $\eta = 0$ , or more formally  $\varepsilon^i \eta^i \partial_\eta^i S_{p_0, mn}(\psi_m) \ll S_{p_0, mn}(\psi_m)$ , see [11]. This spectral density can therefore be replaced by the constant value  $S_{p_0, mn}(\psi_m)$  on the region spanned by the strained coordinate while the frequency response function is expressed by

$$H_m(\eta) = -\frac{\varepsilon \eta \psi_m}{v_m^2 + (\varepsilon \eta \psi_m)^2} - \frac{i v_m}{v_m^2 + (\varepsilon \eta \psi_m)^2} \quad (5.18)$$

which is already integrable in closed-form and which is anyways not possible to further simplify on the basis of the hypotheses at stake.

Following the same path for the second term of Equation (5.17) with another but similar stretched coordinate,  $\omega = \psi_n(1 + \varepsilon \eta)$ , it yields

$$S_{r_0, mn}(\omega) = -\frac{D_m D_n}{\lambda_m - \lambda_n^*} [H_m(\omega) S_{p_0, mn}(\psi_m) - H_n^*(\omega) S_{p_0, mn}(\psi_n)] \quad (5.19)$$

to approximate locally the cross-spectral density of the response over the resonant peaks. Being sufficiently simple, locally accurate and bounded in the far field,  $S_{r_0, mn}(\omega)$  fits the requirements of the Multiple Timescale Spectral Analysis. It can finally be integrated in an explicit way to give the resonant component of the covariance

$$\Sigma_{r_0, mn} = i\pi \frac{D_m D_n}{\lambda_m - \lambda_n^*} [S_{p_0, mn}(\psi_m) + S_{p_0, mn}(\psi_n)] \quad (5.20)$$

which boils down, as expected, to the formulas derived in [13] and [11] under a few conditions, see Section 6.5.

## 5.4 Derivation of the Loading Component

As suggested in the presentation of the Multiple Timescale Spectral Analysis, Equation (5.19) is then subtracted from Equation (5.1) to give the residual function

$$\hat{S}_{q_0, mn}(\omega) = S_{q_0, mn}(\omega) - S_{r_0, mn}(\omega) \quad (5.21)$$

which yields

$$\hat{\Sigma}_{q_0, mn} = \Sigma_{q_0, mn} - \Sigma_{r_0, mn} \quad (5.22)$$

after integration. This remaining contribution is now solely due to the two peaks that are coming from the spectral density of the modal state responses. Although they are positioned symmetrically with respect to the origin (i.e. at  $\omega = \pm \omega_p$ ), they are however not supposed to reach the same maximum values. It is therefore not possible to treat them simultaneously as it was suggested for the variance of a wind-loaded oscillator in Section 2.4. Instead, in order to isolate these peaks into two different integrands again, the residual function is split into two parts as follows

$$\hat{S}_{q_0, mn}(\omega) = \hat{S}_{q_0, mn}^{(+)}(\omega) + \hat{S}_{q_0, mn}^{(-)}(\omega) \quad (5.23)$$

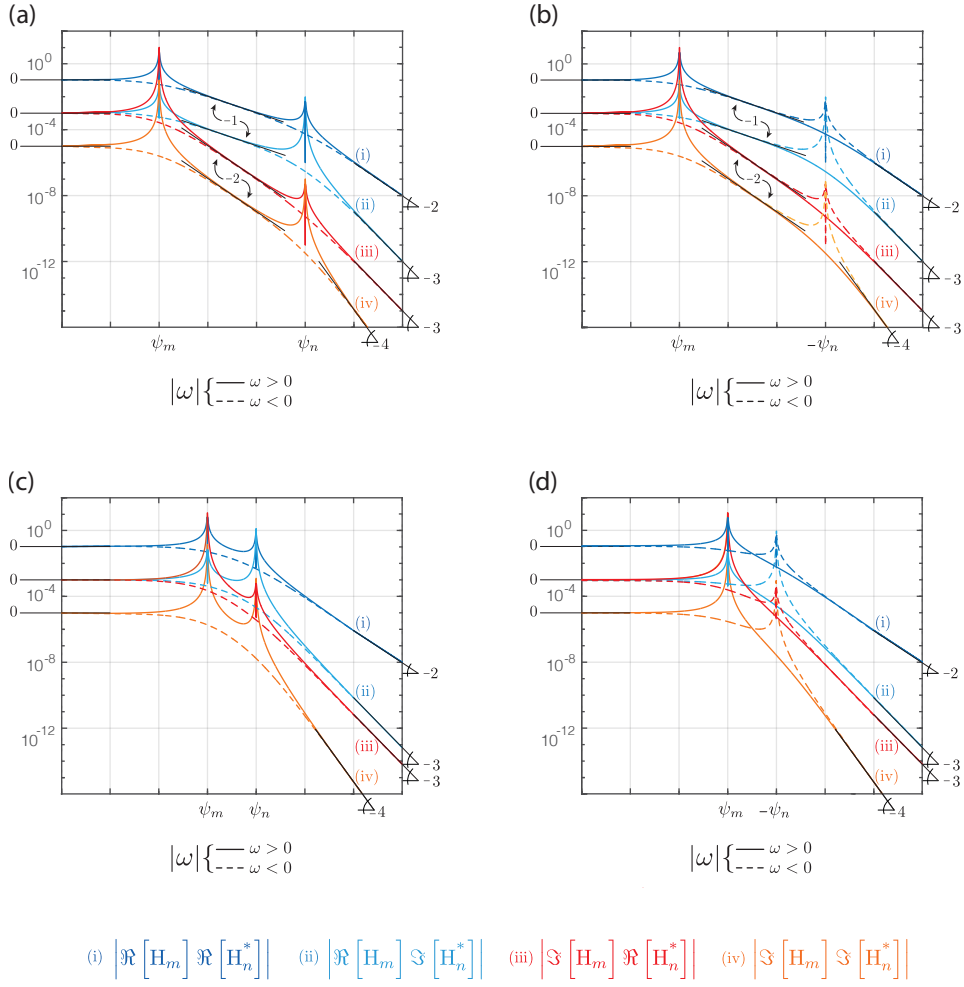


FIGURE 5.2: Decreasing trends observed in the structural kernel before, between, and after the poles of the frequency response functions: (a)  $\psi_m \psi_n > 0$  and  $|\psi_m| \ll |\psi_n|$ , (b)  $\psi_m \psi_n < 0$  and  $|\psi_m| \ll |\psi_n|$ , (c)  $\psi_m \psi_n > 0$  and  $|\psi_m| < |\psi_n|$ , (d)  $\psi_m \psi_n < 0$  and  $|\psi_m| < |\psi_n|$

where

$$\begin{cases} \hat{S}_{q_0, mn}^{(+)}(\omega) = \hat{S}_{q_0, mn}(\omega) & \text{if } \omega > 0 \\ \hat{S}_{q_0, mn}^{(+)}(\omega) = 0 & \text{if } \omega < 0 \end{cases} \quad (5.24)$$

and

$$\begin{cases} \hat{S}_{q_0, mn}^{(-)}(\omega) = 0 & \text{if } \omega > 0 \\ \hat{S}_{q_0, mn}^{(-)}(\omega) = \hat{S}_{q_0, mn}(\omega) & \text{if } \omega < 0 \end{cases} \quad (5.25)$$

respectively. This is just a mathematical trick which does not modify the residual function in overall.

The change of coordinate  $\omega = \omega_p (1 + \varepsilon \eta)$  is then introduced in the first integrand to focus on the peak located in the positive frequency range. Since this peak typically extends over a relatively large domain in contrast to the resonant ones, see Figure 5.1, the structural kernel cannot necessarily be replaced by a constant value across the whole area of interest unless the background regimes are activated in both the  $m$ -th and the  $n$ -th modes. Indeed, when  $\alpha_m \ll 1$  and  $\alpha_n \ll 1$ , the strained coordinate actually covers a domain where the frequency response functions are not varying much as  $\omega_p \ll |\psi_m|$  and  $\omega_p \ll |\psi_n|$ , see Figure 5.2.

In general, instead, the real and the imaginary parts of the  $m$ -th frequency response function can conveniently be approximated by a monomial which is equal to the initial function at the considered peak location and which is characterized by the same slope in logarithmic scales. They thus read

$$\Re [\tilde{H}_m(\eta)] = \left( \frac{1}{1 + \varepsilon\eta} \right)^{\beta_m} \Re [H_m(0)] \quad (5.26)$$

and

$$\Im [\tilde{H}_m(\eta)] = \left( \frac{1}{1 + \varepsilon\eta} \right)^{2\beta_m} \Im [H_m(0)] \quad (5.27)$$

where

$$\beta_m = \frac{\alpha_m}{\alpha_m - 1} \quad (5.28)$$

tends to 0 or 1 respectively when  $\alpha_m \ll 1$  or  $\alpha_m \gg 1$ , the two cases covered by Assumption (ii).

By comparing Equation (5.19) to Equation (5.17),  $S_{r_0, mn}(\omega)$  also appears to be negligible in relation to  $S_{q_0, mn}(\omega)$  in the region spanned by the stretched coordinate because  $S_{p_0, mn}(\psi_m) \ll S_{p_0, mn}(\omega_p)$  and  $S_{p_0, mn}(\psi_n) \ll S_{p_0, mn}(\omega_p)$  when the ratios  $\alpha_m$  and  $\alpha_n$  are either much lower, either much greater than one. If one of these inequalities is not verified, however, the loading component drops and even reaches zero in the limit case, i.e. when the cross-spectral density function is constant over the whole range of frequencies, meaning that the covariance of the modal responses is fully resonant. In order to comply with these observations while simplifying the expressions,  $S_{r_0, mn}(\omega)$  is removed from Equation (5.21) and replaced by the multiplicative form

$$L_{mn} = \left( 1 - \frac{S_{p_0, mn}(\psi_m)}{S_{p_0, mn}(\omega_p)} \right) \left( 1 - \frac{S_{p_0, mn}(\psi_n)}{S_{p_0, mn}(\omega_p)} \right) \quad (5.29)$$

which accordingly decreases down to zero when a frequency or a loading cross-spectrum ratio is getting close to one.

Proceeding with the same steps for the peak of the second integrand by using another but equivalent stretched coordinate,  $\omega = -\omega_p(1 + \varepsilon\eta)$ , the local approximation of the residual function eventually reads

$$S_{\ell_0, mn}^{(\pm)}(\omega) = D_m D_n L_{mn} \sum_{l=1}^4 \left[ (\pm \omega_p)^{\beta_{mn}^{(l)}} \mathcal{G}_{mn}^{(l)}(\pm \omega_p) \mathcal{S}_{p_0, mn}^{(l)}(\omega) \right] \quad (5.30)$$

after returning to the circular frequencies. The symbols (+) and (−) are selected in accordance with the sign of the frequencies because of the non-symmetric nature of the peaks at stake while  $\mathcal{G}_{mn}^{(l)}(\pm \omega_p)$  is defined in Table 5.1 and

$$\mathcal{S}_{p_0, mn}^{(l)}(\omega) = \omega^{-\beta_{mn}^{(l)}} S_{p_0, mn}(\omega) \quad (5.31)$$

is integrated over the positive or the negative frequency range to yield

$$\Sigma_{p_0, mn}^{(l)(\pm)} = \pm \int_0^{\pm\infty} \mathcal{S}_{p_0, mn}^{(l)}(\omega) d\omega \quad (5.32)$$

which is a part of the spectral (fractional) moment of order  $-\beta_{mn}^{(l)}$  associated to the  $m$ -th and  $n$ -th modal state forces. Interestingly enough, this last equation can alternatively be written

$$\Sigma_{p_0, mn}^{(l)(\pm)} = \pm \sum_{i=1}^N \sum_{j=1}^N \phi_{im} \phi_{in}^* \int_0^{\pm\infty} \omega^{-\beta_{mn}^{(l)}} S_{f,ij}(\omega) d\omega \quad (5.33)$$

when the modal decomposition of the spectral densities from Equation (4.23) is reintroduced, showing that the integration can actually be performed in the nodal basis, before the modal projection, in order to avoid doing so at each integration point with the spectral densities of the nodal state loadings. For each of these terms, the number of projections is therefore drastically reduced.

At last, the loading component of the modal covariance is given in an explicit way by

$$\Sigma_{\ell_0, mn} = D_m D_n L_{mn} \sum_{l=1}^4 \left[ (+\omega_p)^{\beta_{mn}^{(l)}} \mathcal{G}_{mn}^{(l)}(+\omega_p) \Sigma_{p_0, mn}^{(l)(+)} + (-\omega_p)^{\beta_{mn}^{(l)}} \mathcal{G}_{mn}^{(l)}(-\omega_p) \Sigma_{p_0, mn}^{(l)(-)} \right] \quad (5.34)$$

which boils down to the well-known background component when  $\alpha_m$  and  $\alpha_n$  are much lower than one ( $\beta_m = \beta_n = \beta_{mn}^{(l)} = 0$  and  $\omega_p = 0$ ). This expression additionally extends in a unified way to the inertial component or to the mixed background/inertial component which did not exist before. The next remainder can ultimately be neglected as it corresponds to the integral of a residual function which does no longer contain any significant contribution.

TABLE 5.1: Definitions for (5.30), (5.31) and (5.34)

$l$	$\beta_{mn}^{(l)}$	$\mathcal{G}_{mn}^{(l)}(\omega)$
1	$\beta_m + \beta_n$	$\Re[H_m(\omega)] \Re[H_n^*(\omega)]$
2	$\beta_m + 2\beta_n$	$i\Re[H_m(\omega)] \Im[H_n^*(\omega)]$
3	$2\beta_m + \beta_n$	$i\Im[H_m(\omega)] \Re[H_n^*(\omega)]$
4	$2\beta_m + 2\beta_n$	$-\Im[H_m(\omega)] \Im[H_n^*(\omega)]$

## 5.5 Verification with a Parametric Analysis

Globally, in Section 5.3 and Section 5.4, semi-analytical formulas have been established for the main components of the spectral densities, in Equation (5.19) and Equation (5.30), as well as the second statistics, in Equation (5.20) and Equation (5.34), of the  $m$ -th and the  $n$ -th modal state responses. They are now verified for different sets of parameters in the following section. To do so, the results they provide are compared with the references, a.k.a the spectral densities defined in Equation (4.31) and the second statistics obtained through the numerical integration of these functions with a sufficient number of points. This operation is performed hereafter by making use of the adaptive algorithm which is implemented in Version 12.0.0.0 of Wolfram Mathematica.

On the one hand, the adequacy of the expressions derived for the spectral densities in the previous sections is well confirmed by looking at the good agreement between the proposed decompositions and the numerical definitions of the co- and quad-spectral densities which is illustrated for all possible combinations of contributions in Figure 5.3 and Figure 5.4. Thanks to the color code adopted to represent them –green for the resonant, yellow for the inertial, orange for the mixed and red for the background component–, they are indeed identified as inertial and resonant in Figure 5.3-(a), mixed and resonant in Figure 5.3-(b), background and resonant in Figure 5.3-(c) but also in Figure 5.4. This background/resonant case is actually depicted for two different sets of parameters because the functions appear to be significantly different if the signs of the  $m$ -th and

the  $n$ -th eigenfrequencies are the same. It would however not change anything in Figure 5.3-(a) and the green bump would just flip side with respect to the  $y$ -axis in Figure 5.3-(b).

These figures can also be analyzed in the light of Equation (5.20) and Equation (5.34). Being simple, they allow to explain in a mathematical way the influence of some parameters, but also in which cases some components are specifically important to be taken into account. For instance, the resonant component is useless when the loading component is inertial because the frequency ratios are much lower than one,  $\alpha_m \ll 1$  and  $\alpha_n \ll 1$ . It implies that the eigenfrequencies are much smaller than the peak frequency of the waves in absolute value and the resonant peaks thus fall in a zone where  $S_{p_0,mn}(\psi_m)$  and  $S_{p_0,mn}(\psi_n)$  are extremely small because these functions exhibit an exponential decay in such a low frequency range. This is the reason why one or both resonant peaks disappear in Figure 5.3-(a) and Figure 5.3-(b). The loading component is also leading over the resonant one when the  $m$ -th and  $n$ -th natural frequencies are far away from each other, as shown in Figure 5.3. The opposite occurs when they are close to each other as in Figure 5.4. The interaction of the resonant peaks appear to be conditioned upon the damping ratios as well in this figure. The smaller the damping ratios, the sharper but also the more distinct the resonant peaks.

On the other hand, similar remarks can be formulated for the statistics obtained through the proposed decompositions and through the numerical integration. They are displayed in Figure 5.5 and they coincide quite well, except in the shaded area where a more important discrepancy is observed. This is to be expected because one of the natural frequencies is close to the peak frequency of the waves in this region, meaning that Assumption (ii) is actually not respected. Nevertheless, the errors remain reasonable thanks to the multiplicative factor  $L_{mn}$  which ensures that the loading component passes by zero when  $\alpha_n = 1$ , and thus does not grow unbounded. Overall, the proximity of the natural frequencies and the smallness of the damping ratios are necessary conditions to observe a burst in the resonant component, see Figure 5.5-(a), but this is not sufficient otherwise Figure 5.5-(b), (c) and (d) would exhibit a similar feature. In fact, the resonance in the  $m$ -th and  $n$ -th modes additionally needs to be activated by the loading but this is not the case when the loading component is inertial. Apart from that, the loading component also tends towards zero (resp. a non-zero constant value) when  $\alpha_n$  is far below one (resp. far above one) because  $\alpha_m$  and thus  $H_m(\pm\omega_p) = (\lambda_m \mp \omega_p)^{-1}$  are fixed but  $\psi_n$  increases (resp. decreases). This eigenfrequency eventually leads over  $\omega_p$  in  $H_n^*(\pm\omega_p) = (\lambda_n \mp \omega_p)^{-1}$  which is hence dropping to zero (resp. stabilizing at a constant value).

It is however not possible to conclude on the influence that these effects might have on the nodal results without referring to the correlation coefficients. Being dimensionless, they allow to assess the importance of taking the covariances of the modal state responses into account in relation to their variances. Indeed, they read

$$\rho_{q_0,mn} = \frac{\Sigma_{q_0,mn}}{\sqrt{\Sigma_{q_0,mm}\Sigma_{q_0,nn}}} \quad (5.35)$$

for the  $m$ -th and  $n$ -th modal state responses. Based on the proposed decomposition of the modal state variances and covariances, the correlation coefficient can first be written

$$\tilde{\rho}_{q_0,mn} = \frac{\Sigma_{r_0,mn} + \Sigma_{\ell_0,mn}}{\sqrt{\Sigma_{r_0,mm} + \Sigma_{\ell_0,mm}}\sqrt{\Sigma_{r_0,nn} + \Sigma_{\ell_0,nn}}} \quad (5.36)$$

and can then be estimated as the sum of a resonant and a loading component as well by using a similar derivation as in [13]:

$$\tilde{\rho}_{q_0,mn} = \gamma_{r_0}\rho_{r_0,mn} + \gamma_{\ell_0}\rho_{\ell_0,mn} \quad (5.37)$$

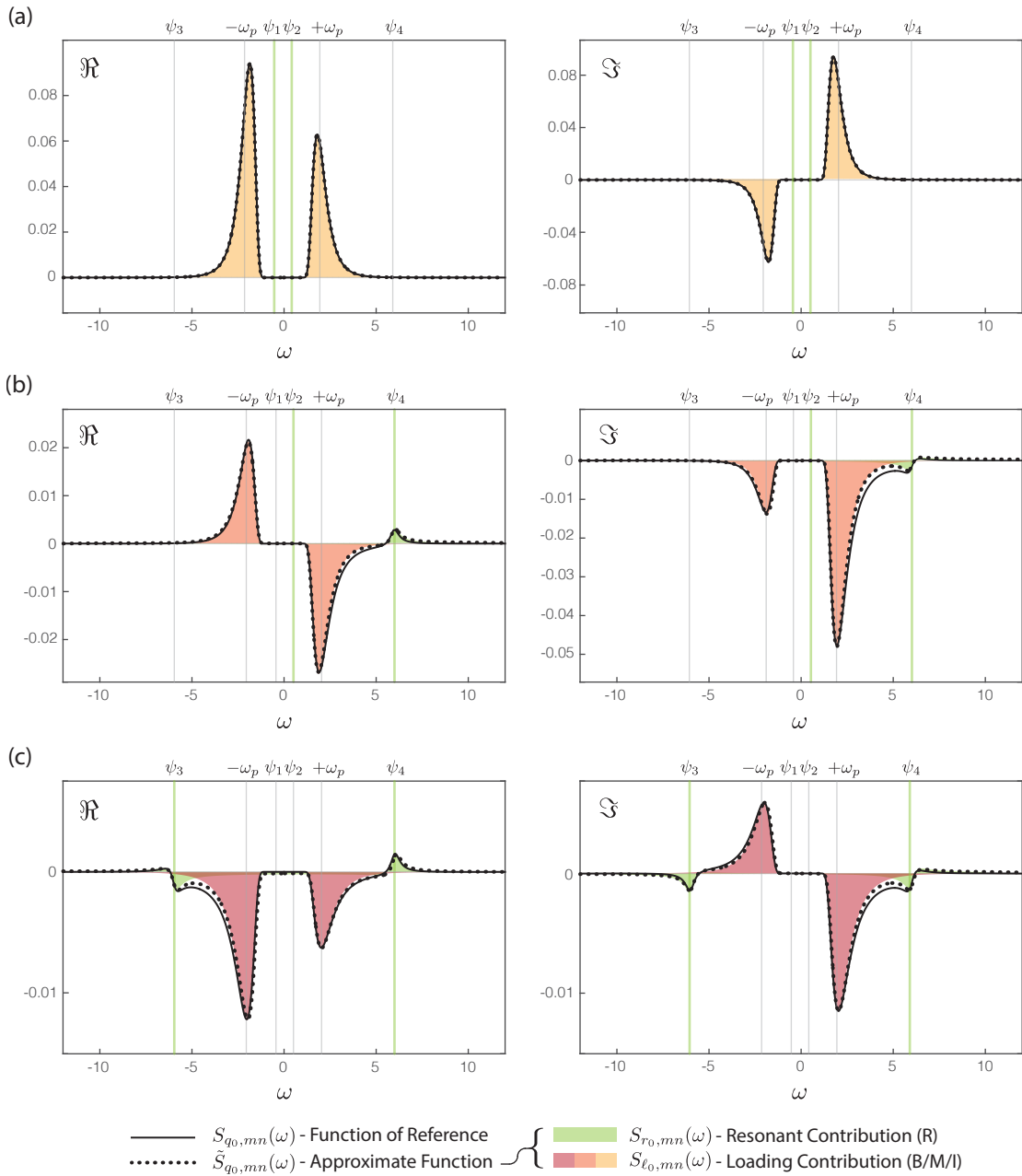


FIGURE 5.3: Spectral densities of the  $m$ -th and  $n$ -th modal state responses for all  $(m, n)$  pairs indicated by the green lines when  $P_a = (1 + 0.2i)$ ,  $P_s = (i - 0.2)$ ,  $\omega_1 = 0.1$  rad/s,  $\omega_2 = 6$  rad/s,  $\xi_1 = 5\%$  and  $\xi_2 = 5\%$ .

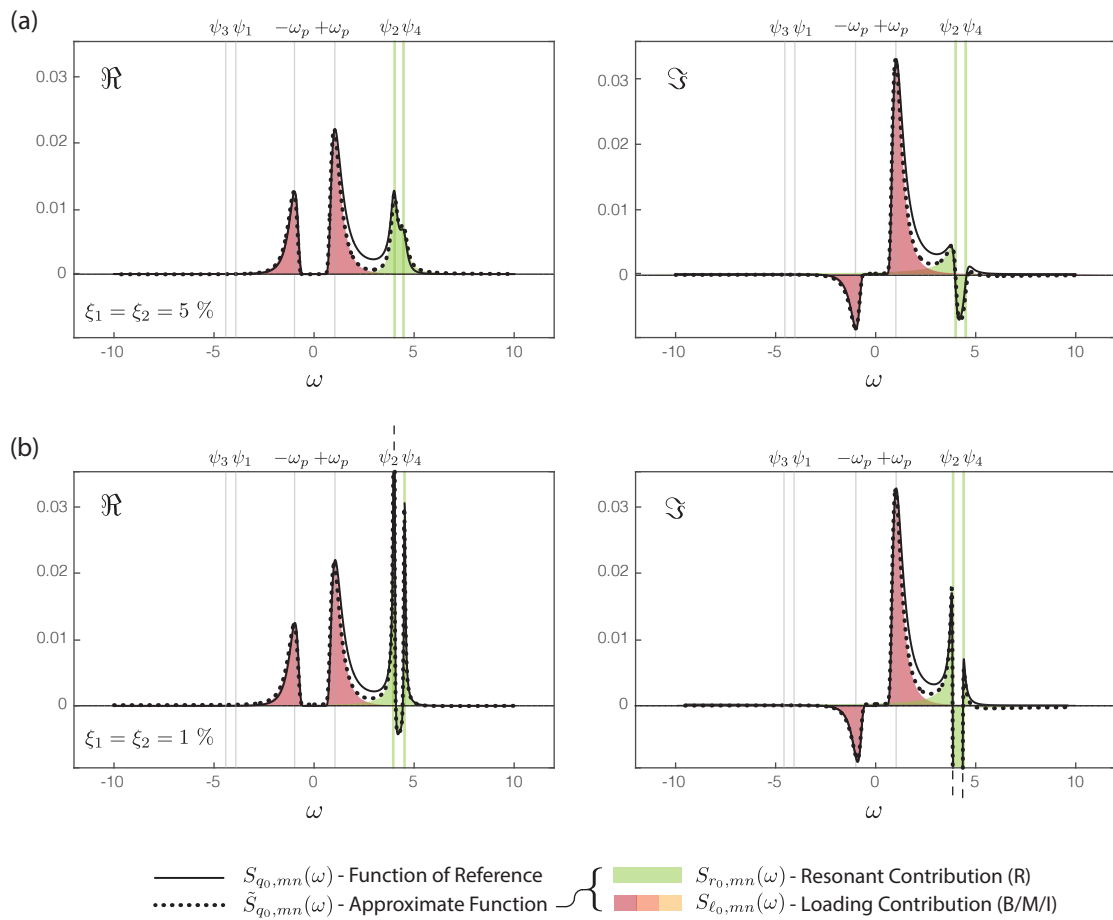


FIGURE 5.4: Spectral densities of the 2<sup>nd</sup> and 4<sup>th</sup> modal state responses when  $P_a = (1 + 0.2i)$ ,  $P_s = (i - 0.2)$ ,  $\omega_1 = 4$  rad/s and  $\omega_2 = 4.5$  rad/s.

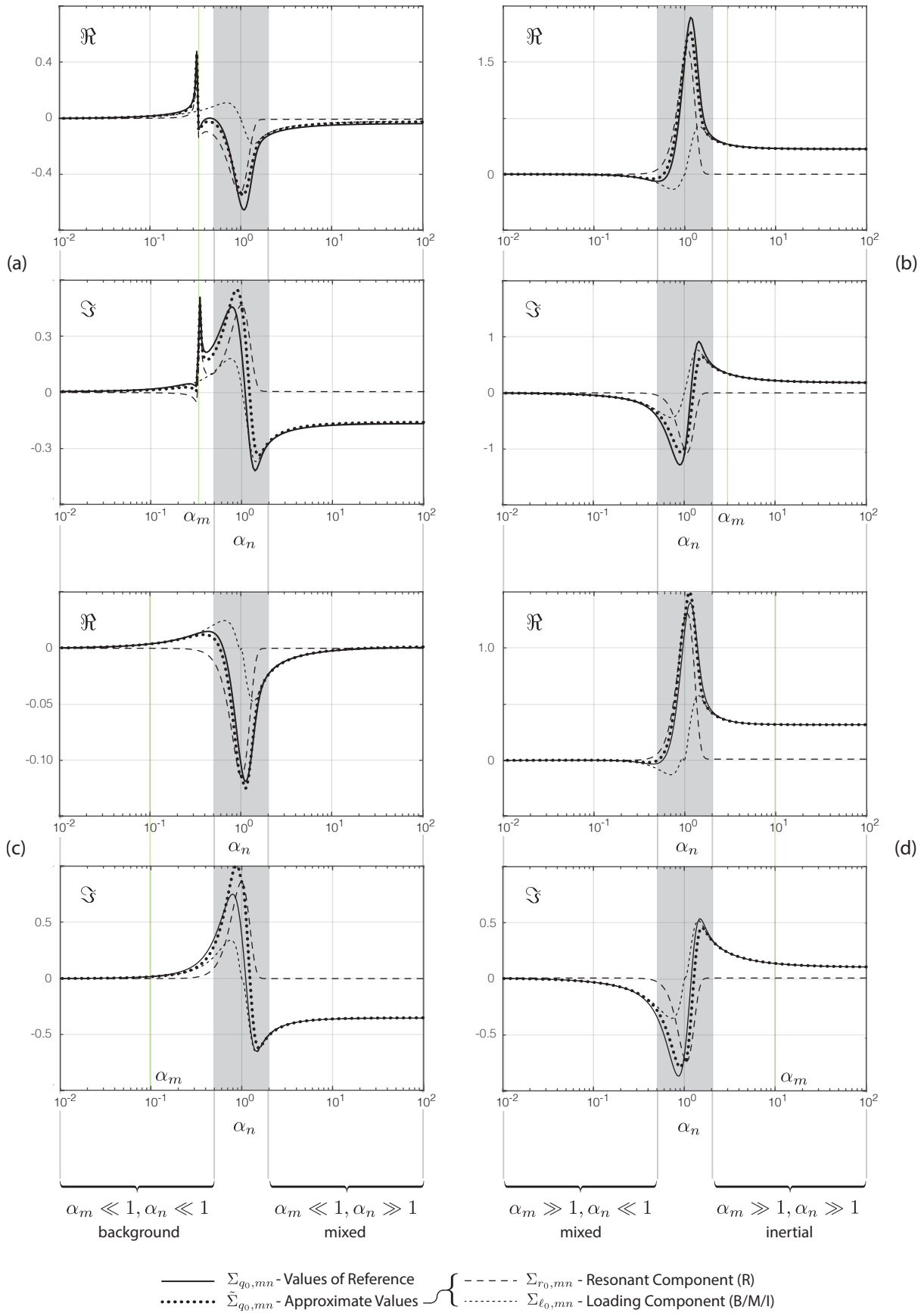


FIGURE 5.5: Covariances of the  $m$ -th and  $n$ -th modal state responses, with  $m$  and  $n$  being even numbers, when  $\xi_{j_m} = 1\%$ ,  $\xi_{j_n} = 1\%$ ,  $P_a = (1 + 0.2i)$ ,  $P_s = (i - 0.2)$ ,  $\omega_p = 1$  rad/s while (a)  $\alpha_m = 0.3$ , (b)  $\alpha_m = 3$ , (c)  $\alpha_m = 0.1$  and (d)  $\alpha_m = 10$ .



where

$$\gamma_{r_0} = \frac{1}{\sqrt{1+r_{0,m}^{-1}}\sqrt{1+r_{0,n}^{-1}}} \quad \text{and} \quad \gamma_{\ell_0} = \frac{1}{\sqrt{1+r_{0,m}}\sqrt{1+r_{0,n}}} \quad (5.38)$$

can be seen as a resonant and a loading weighting factors. They are related to the resonant-to-loading ratios

$$r_{0,m} = \frac{\Sigma_{r_0,mm}}{\Sigma_{\ell_0,mm}} \quad \text{and} \quad r_{0,n} = \frac{\Sigma_{r_0,nn}}{\Sigma_{\ell_0,nn}} \quad (5.39)$$

which are dimensionless and belong to the interval  $[0, +\infty[$ . If the responses are fully resonant in both modes, i.e.  $r_{0,m} \gg 1$  and  $r_{0,n} \gg 1$ ,  $\gamma_{r_0}$  tends towards unity and  $\gamma_{\ell_0}$  tends towards zero. On the contrary, if the loading component is leading in both modes, i.e.  $r_{0,m} \ll 1$  and  $r_{0,n} \ll 1$ ,  $\gamma_{r_0}$  tends towards zero and  $\gamma_{\ell_0}$  tends towards unity.

Substituting the appropriate components of the modal state variances and covariances into the general definition of the correlation coefficients

$$\rho_{(\cdot),mn} = \frac{\Sigma_{(\cdot),mn}}{\sqrt{\Sigma_{(\cdot),mm}\Sigma_{(\cdot),nn}}} \quad (5.40)$$

then yields

$$\rho_{r_0,mn} = \frac{\Sigma_{r_0,mn}}{\sqrt{\Sigma_{r_0,mm}\Sigma_{r_0,nn}}} \quad \text{and} \quad \rho_{\ell_0,mn} = \frac{\Sigma_{\ell_0,mn}}{\sqrt{\Sigma_{\ell_0,mm}\Sigma_{\ell_0,nn}}} \quad (5.41)$$

for the resonant and the loading components. The loading coefficient is unfortunately not easily interpretable unless the response is quasi-static in both modes. In this event, it boils down to the expression derived in [13] where it simply corresponds to the correlation coefficient of the  $m$ -th and  $n$ -th modal state forces,  $\rho_{\ell_0,mn} = \rho_{p,mn}$ .

Meanwhile, after some reformulations and manipulations, the resonant component is interestingly written as

$$\rho_{r_0,mn} = \varpi_{mn} [\Gamma_{mn}(\psi_m) S_{mn} + \Gamma_{mn}(\psi_n) S_{nm}] \quad (5.42)$$

where

$$\varpi_{mn} = i \frac{\sqrt{v_m v_n}}{\lambda_m - \lambda_n^*} \quad (5.43)$$

is a resonant interaction indicator. As shown in Figure 5.6 which illustrates the contours of its real and imaginary parts when  $\xi_{j_m} = \xi_{j_n} = \xi$  with  $m$  and  $n$  being even numbers, the value of this indicator actually increases if the resonant peaks are interacting. The crests of the first and the second plots are represented by white lines and are accordingly reached when the minima in the imaginary parts and the real parts, respectively, of the  $m$ -th and the  $n$ -th frequency response functions are aligned. Mathematically speaking, the equations of these lines respectively read

$$\zeta = 0 \quad \text{and} \quad \zeta = \pm \xi \quad (5.44)$$

where

$$\zeta = \frac{\psi_n - \psi_m}{\psi_n + \psi_m} \quad (5.45)$$

is a dimensionless measure of the relative distance between the resonant peaks.

Besides, the smaller the damping ratios, the sharper the resonant peaks, and thus the narrower the zone over which they blend. This is indicated in the figures by the faster decrease of the indicator with respect to  $\zeta$  when  $\xi$  tends towards zero. At last, the resonant part of the correlation

coefficient also increases if the values of the coherence function

$$\Gamma_{mn}(\omega) = \frac{S_{p_0,mn}(\omega)}{\sqrt{S_{p_0,mm}(\omega) S_{p_0,nn}(\omega)}} \quad (5.46)$$

at  $\omega = \psi_m$  and  $\omega = \psi_n$  or the spectral ratios

$$S_{mn} = \sqrt{\frac{S_{p_0,nn}(\psi_m)}{S_{p_0,nn}(\psi_n)}} \text{ and } S_{nm} = \sqrt{\frac{S_{p_0,mm}(\psi_n)}{S_{p_0,mm}(\psi_m)}} \quad (5.47)$$

grow as well. On the opposite, the coherence function and the spectral ratios drop to zero if the forces in two modes are not coherent or do not contain any energy in the frequency bands associated to the resonance of these modes.

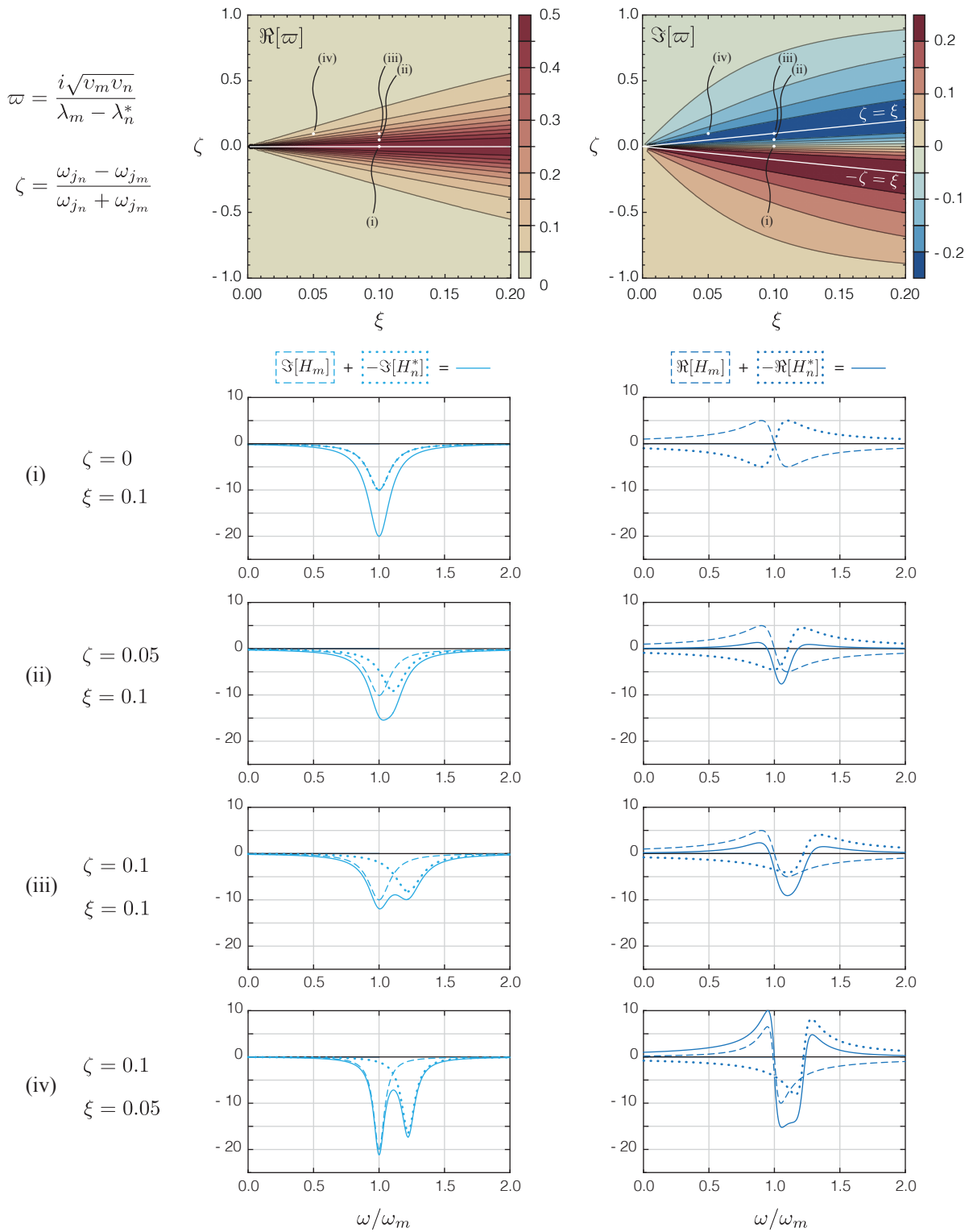


FIGURE 5.6: Real and imaginary parts of the resonant factor. White lines represent the crests of the contour plots. Below, the  $m$ -th and  $n$ -th frequency response functions obtained for a few sets of parameters are represented.



## Chapter 6

# Covariances, Including Frequency-Dependency

### 6.1 Introduction and Preliminary Considerations

In Chapter 4, the second decoupling strategy allowed to express the spectral densities of the modal state forces as the sum of the leading order function

$$S_{q_1, mn}(\omega) = \mathcal{D}_m \mathcal{D}_n G_{d, mn}(\omega) S_{p, mn}(\omega) \quad (6.1)$$

and the first order correction

$$\Delta S_{q_1, mn}(\omega) = \sum_{k=1}^{2M} \mathcal{D}_m \mathcal{D}_n \mathcal{D}_k G_{d, mnk}(\omega) \mathcal{J}_{o, mk}(\omega) S_{p, kn}(\omega) \quad (6.2)$$

where

$$G_{d, mn}(\omega) = \mathcal{H}_{d, m}(\omega) \mathcal{H}_{d, n}^*(\omega) \quad (6.3)$$

and

$$G_{d, mnk}(\omega) = \mathcal{H}_{d, m}(\omega) \mathcal{H}_{d, n}^*(\omega) \mathcal{H}_{d, k}(\omega) \quad (6.4)$$

are the structural kernels. The integration of these spectral densities is tackled with the help of the Multiple Timescale Spectral Analysis in this chapter, in order to rely on as few modal projections of the state forces as possible and to eventually speed up the computation.

Although they make use of the concepts that have already been introduced in Chapter 5, the decompositions of the spectral densities and the second moments are a bit more involved in this chapter, mathematically speaking. This is because the elements of the modal state matrices are now frequency dependent and the first order corrections contain many more terms. Explanations are provided when these two features lead to a significant modification of the previous developments. It is however not convenient to illustrate them by introducing a minimalistic loading spectrum anymore as it would require to arbitrarily define a lot of other parameters. Thus, the mathematical details regarding the preceding notions and results are deliberately kept short. For their better understanding, the reader is referred to Chapter 5.

In the following, the distinctness of the resonant and the loading peaks found in the integrands at stake is first ensured by formulating a number of assumptions in Section 6.2. As before, these peaks can then be sequentially targeted, in Section 6.3 and Section 6.4, to yield simple expressions for the two main components of the spectral densities and the second moments, which are again identified as resonant and loading.

## 6.2 Formulation of the Necessary Assumptions

In the present configuration, the separation of the peaks in the spectral densities of the modal state responses is conditioned upon the following list of assumptions, which can be associated to the existence of a few small parameters again.

- (i) The spectral densities of the modal state forces and the elements of the modal state matrices are varying smoothly and moderately over the width of the resonant peaks. In other words, the derivatives of these functions are small enough to maintain the asymptoticness of their Taylor series expansion near the natural frequencies of the structure. More formally, these conditions read

$$(\omega - \psi_k)^i \partial_\omega^i S_{p,mn}(\psi_k) \ll S_{p,mn}(\psi_k) \quad (6.5)$$

and

$$(\omega - \psi_k)^i \partial_\omega^i \mathcal{A}_{mn}(\psi_k) \ll \mathcal{A}_{mn}(\psi_k) \quad (6.6)$$

and

$$(\omega - \psi_k)^i \partial_\omega^i \mathcal{B}_{mn}(\psi_k) \ll \mathcal{B}_{mn}(\psi_k) \quad (6.7)$$

for all possible combinations of  $m$ ,  $n$  and  $k$  indices and for  $\omega$  taking values in an interval centered at  $\psi_k$  (the location of the  $k$ -th pole on the real axis) and extending over a range which is proportional to  $v_k$  (the imaginary part of the  $k$ -th eigenfrequency). This latter parameter decreases together with the corresponding damping ratio. According to Figure 4.1, the smaller it is, the sharper the corresponding peak and the narrower the zone where the functions are not supposed to change too much. In these equations, the symbol  $\partial_\omega^i$  also represents the  $i$ -th derivative with respect to the circular frequency.

- (ii) The spectral densities of the modal state forces reach their maximum value at a circular frequency which is designated by  $\omega_p$  and is significantly different from the natural frequencies of the structure. This hypothesis is formalized by acknowledging that the frequency ratios

$$\alpha_k = \frac{\omega_p}{|\psi_k|} \quad (6.8)$$

with  $k \in [1, \dots, 2M]$  are either much lower, either much greater than one. In the former case, the  $k$ -th mode is excited in its background regime by the loading while, in the latter case, the loading activates its inertial regime.

- (iii) The elements of the modal state matrices are almost constant in the zones where the spectral densities of the modal state forces are fluctuating a lot, i.e. when the circular frequency is getting close to the peak frequency of the modal state forces. In a formal way, it reads

$$(\omega \mp \omega_p)^i \partial_\omega^i \mathcal{A}_{mn}(\pm \omega_p) \ll \mathcal{A}_{mn}(\pm \omega_p) \quad (6.9)$$

and

$$(\omega \mp \omega_p)^i \partial_\omega^i \mathcal{B}_{mn}(\pm \omega_p) \ll \mathcal{B}_{mn}(\pm \omega_p) \quad (6.10)$$

with  $\omega$  taking values in the interval centered at  $\pm \omega_p$  and spread over the surrounding area. Its extent is complicated to define in a general sense because it does not scale with any structural parameter but it is typically wider than the resonant peaks.

Under these conditions,  $S_{q_1,mn}(\omega)$  and  $\Delta S_{q_1,mn}(\omega)$  can be decomposed into two main contributions as follows

$$\tilde{S}_{q_1,mn}(\omega) = S_{r_1,mn}(\omega) + S_{\ell_1,mn}(\omega) \quad (6.11)$$

and

$$\Delta\tilde{S}_{q_1,mn}(\omega) = \Delta S_{r_1,mn}(\omega) + \Delta S_{\ell_1,mn}(\omega) \quad (6.12)$$

by using the Multiple Timescale Spectral Analysis. These approximate functions are designated by a tilde symbol. The first terms provide a local approximation of the initial functions over the peaks that are coming from the structural kernels. They are called *resonant* and labeled by a  $r$  subscript. Meanwhile, the second terms approximate locally the initial functions over the peaks that are due to the spectral densities of the modal state forces. They are said *loading*-related and marked by a  $\ell$  subscript.

The Multiple Timescale Spectral Analysis requires them to be sufficiently accurate over the respective zones of interest, to be integrable in the far field, and to be simple enough so that they can be integrated in an explicit way. Under these conditions, the method is known to yield a similar decomposition for approximating the second moments with a controllable discrepancy. They are consequently expected to read

$$\tilde{\Sigma}_{q_1,mn} = \Sigma_{r_1,mn} + \Sigma_{\ell_1,mn} \quad (6.13)$$

and

$$\Delta\tilde{\Sigma}_{q_1,mn} = \Delta\Sigma_{r_1,mn} + \Delta\Sigma_{\ell_1,mn} \quad (6.14)$$

where the resonant and the loading contributions are indicated by the  $r$  and  $\ell$  subscripts again. They are intended to be given by means of simple formulas whose expressions are provided in Section 6.3 and Section 6.4, respectively. Although they are easy to understand and to interpret, they are unfortunately not so brief and are therefore not shown here as in the previous chapters.

### 6.3 Derivation of the Resonant Component

Starting with the resonant component, the peaks of concern are known to be caused by the poles of the frequency response functions, which enter into the definition of the structural kernels. Instead of being given by their product as in Equation (6.3) and Equation (6.4), the structural kernels can alternatively be expanded in partial fractions. They thus read

$$G_{d,mn}(\omega) = \frac{\mathcal{B}_{mm}(\omega)}{\mathcal{C}_{mn}(\omega)} \mathcal{H}_{d,m}(\omega) + \frac{\mathcal{B}_{nn}^*(\omega)}{\mathcal{C}_{nm}^*(\omega)} \mathcal{H}_{d,n}^*(\omega) \quad (6.15)$$

with

$$\mathcal{C}_{mn}(\omega) = \mathcal{A}_{mm}(\omega) \mathcal{B}_{nn}^*(\omega) + \mathcal{A}_{nn}^*(\omega) \mathcal{B}_{mm}(\omega) = \mathcal{C}_{nm}^*(\omega) \quad (6.16)$$

and

$$G_{d,mnk}(\omega) = \frac{\mathcal{B}_{kk}^2(\omega) \mathcal{H}_{d,k}(\omega)}{\mathcal{C}_{kn}(\omega) \mathcal{E}_{mk}(\omega)} - \frac{\mathcal{B}_{mm}^2(\omega) \mathcal{H}_{d,m}(\omega)}{\mathcal{C}_{mn}(\omega) \mathcal{E}_{mk}(\omega)} + \frac{\mathcal{B}_{nn}^{*2}(\omega) \mathcal{H}_{d,n}^*(\omega)}{\mathcal{C}_{nm}^*(\omega) \mathcal{C}_{nk}^*(\omega)} \quad (6.17)$$

with

$$\mathcal{E}_{mk}(\omega) = \mathcal{A}_{mm}(\omega) \mathcal{B}_{kk}(\omega) - \mathcal{A}_{kk}(\omega) \mathcal{B}_{mm}(\omega) \quad (6.18)$$

provided that the multiplicity of each pole is equal to one. Equation (6.17) is therefore not valid when  $k = m$ . This is however not much of a problem because  $G_{d,mnk}(\omega)$  will subsequently be multiplied by  $\mathcal{J}_{o,mk}(\omega)$ , which is actually equal to zero in this event.

As a consequence of the partial fraction expansion, each term of the sums in Equation (6.15) and Equation (6.17) contains a single frequency response function, e.g.  $H_{d,k}(\omega)$ , and thus a single pole which can be zoomed in on by introducing an appropriate stretched coordinate, e.g.  $\omega = \psi_k(1 + \varepsilon\eta)$ . Invoking Assumption (i), the spectral densities of the modal state forces and the elements of the modal state matrices can then be evaluated at the corresponding eigenfrequency

and replaced by these constant values on the region spanned by the strained coordinate. For the record, the diagonal elements of the modal state matrices are given by

$$\mathcal{A}_{kk}(\psi_k) = \lambda_k \quad \text{and} \quad \mathcal{B}_{kk}(\psi_k) = i \quad (6.19)$$

at these specific positions, as indicated in Section 4.3.

The spectral densities can therefore be estimated by

$$S_{r_1, mn}(\omega) = -\mathcal{D}_m \mathcal{D}_n \left[ \frac{S_{p, mn}(\psi_m)}{i\mathcal{C}_{mn}(\psi_m)} \mathcal{H}_m(\omega) - \frac{S_{p, mn}(\psi_n)}{i\mathcal{C}_{mn}(\psi_n)} \mathcal{H}_n^*(\omega) \right] \quad (6.20)$$

and

$$\begin{aligned} \Delta S_{r_1, mn}(\omega) = \mathcal{D}_m \mathcal{D}_n \sum_{\substack{k=1 \\ k \neq m}}^{2M} \mathcal{D}_k & \left[ \frac{\mathcal{J}_{o, mk}(\psi_m) S_{p, kn}(\psi_m)}{\mathcal{C}_{mn}(\psi_m) \mathcal{E}_{mk}(\psi_m)} H_m(\omega) \right. \\ & \left. - \frac{\mathcal{J}_{o, mk}(\psi_n) S_{p, kn}(\psi_n)}{\mathcal{C}_{nm}^*(\psi_n) \mathcal{C}_{nk}^*(\psi_n)} H_n^*(\omega) - \frac{\mathcal{J}_{o, mk}(\psi_k) S_{p, kn}(\psi_k)}{\mathcal{E}_{mk}(\psi_k) \mathcal{C}_{kn}(\psi_k)} H_k(\omega) \right] \end{aligned} \quad (6.21)$$

over the width of the resonant peaks with

$$H_k(\omega) = \left( \frac{1}{\lambda_k - \omega} \right) \quad (6.22)$$

being an approximation of the frequency response function. It is actually defined as the frequency response function obtained with the first decoupling strategy, except that the eigenvalue is now the solution of another eigenvalue problem, EVP- $\Omega$  instead of EVP-0. Given that its integral yields

$$\int_{-\infty}^{+\infty} H_k(\omega) d\omega = i\pi \frac{\Im(\lambda_k)}{|\Im(\lambda_k)|} \quad (6.23)$$

by applying the residue theorem, the local approximations derived in Equation (6.20) and Equation (6.21) are sufficiently simple, locally accurate and seemingly integrable to meet the requirements of the Multiple Timescale Spectral Analysis. In consequence, they finally provide the explicit formulas

$$\Sigma_{r_1, mn} = i\pi \mathcal{D}_m \mathcal{D}_n \left[ \frac{S_{p, mn}(\psi_m)}{i\mathcal{C}_{mn}(\psi_m)} + \frac{S_{p, mn}(\psi_n)}{i\mathcal{C}_{mn}(\psi_n)} \right] \quad (6.24)$$

and

$$\begin{aligned} \Delta \Sigma_{r_1, mn} = i\pi \mathcal{D}_m \mathcal{D}_n \sum_{\substack{k=1 \\ k \neq m}}^{2M} \mathcal{D}_k & \left[ \frac{\mathcal{J}_{o, mk}(\psi_m) S_{p, kn}(\psi_m)}{\mathcal{C}_{mn}(\psi_m) \mathcal{E}_{mk}(\psi_m)} \right. \\ & \left. + \frac{\mathcal{J}_{o, mk}(\psi_n) S_{p, kn}(\psi_n)}{\mathcal{C}_{nm}^*(\psi_n) \mathcal{C}_{nk}^*(\psi_n)} - \frac{\mathcal{J}_{o, mk}(\psi_k) S_{p, kn}(\psi_k)}{\mathcal{E}_{mk}(\psi_k) \mathcal{C}_{kn}(\psi_k)} \right] \end{aligned} \quad (6.25)$$

for the resonant components of the second order statistics.

## 6.4 Derivation of the Loading Component

As it is recommended by the procedure detailed in the introduction, the local approximations derived in Equation (6.20) and Equation (6.21) are subtracted from the exact spectral densities



found in Equation (6.1) and Equation (6.2) in order to define the residuals

$$\hat{S}_{q_1, mn}(\omega) = S_{q_1, mn}(\omega) - S_{r_1, mn}(\omega) \quad (6.26)$$

and

$$\Delta \hat{S}_{q_1, mn}(\omega) = \Delta S_{q_1, mn}(\omega) - \Delta S_{r_1, mn}(\omega) \quad (6.27)$$

which do no longer contain any significant contribution near the poles of the frequency response functions. Up to this point,  $\Sigma_{q_1, mn}$  and  $\Delta \Sigma_{q_1, mn}$  can be totally recovered by complementing the resonant components presented in Equation (6.24) and Equation (6.25) with the respective integrals of the two residuals introduced hereabove. In this section, however, a simple but approximate formula is sought for these additional contributions.

Given that the remaining peaks in the residuals are generated by the spectral densities of the modal state forces, they are located at a frequency which is close to the peak frequency of the loading in absolute value. Focusing on the positive frequency range first, the change of coordinate  $\omega = \omega_p (1 + \varepsilon \eta)$  is introduced to center the corresponding peak at the abscissa  $\eta = 0$  and to zoom in on the area of interest by means of an appropriate small number.

As mentioned earlier, this peak usually extends over a relatively wide zone. Under Assumption (iii), the elements of the modal state matrices can be calculated at the position  $\eta = 0$  and substituted by these constant values over the whole area of interest. The same rationale is also supposed to hold for the elements of the dynamical flexibility matrix. Nevertheless, this approach cannot be satisfactorily applied to the frequency response functions. At first, they thus read

$$\mathcal{H}_{\ell, k}(\eta) = \frac{1}{\mathcal{A}_{kk}(0) + i\omega_p(1 + \varepsilon \eta) \mathcal{B}_{kk}(0)} \quad (6.28)$$

when they are expressed with respect to the strained coordinates.

Once the frequency dependency of the modal state coefficients is ignored, the real and the imaginary parts of the resulting functions can adequately be approached by the following monomials

$$\Re[\tilde{\mathcal{H}}_{\ell, k}(\eta)] = \left(\frac{1}{1 + \varepsilon \eta}\right)^{\beta_k} \Re[\mathcal{H}_{\ell, k}(0)] \quad (6.29)$$

and

$$\Im[\tilde{\mathcal{H}}_{\ell, k}(\eta)] = \left(\frac{1}{1 + \varepsilon \eta}\right)^{2\beta_k} \Im[\mathcal{H}_{\ell, k}(0)] \quad (6.30)$$

where

$$\beta_k = \frac{\alpha_k}{\alpha_k - 1} \quad (6.31)$$

is equal to 0 and 1 in the two limit cases,  $\alpha_k \ll 1$  and  $\alpha_k \gg 1$ , which can respectively be encountered according to Assumption (ii). These approximate frequency response functions have been tailored to be equal to the original functions at the peak frequency of the waves, i.e. when  $\omega = \omega_p$  or equivalently  $\eta = 0$ . Likewise, they have also been customized to exhibit the same decreasing trend in logarithmic scales when the evolution of the structural properties with the frequency is disregarded.

Under these conditions, the resonant approximations of the spectral densities are readily shown to be negligible in the region spanned by the strained coordinates if  $S_{p, mn}(\psi_m) \ll S_{p, mn}(\omega_p)$  and  $S_{p, mn}(\psi_n) \ll S_{p, mn}(\omega_p)$ . These conditions are supposed to be verified when the ratios  $\alpha_m$  and  $\alpha_n$  are either much lower, either much greater than one on the basis that the spectral densities of the modal state forces decrease rapidly on both sides of their peaks. Otherwise, the loading component

drops down to zero because the contributions provided by  $S_{q_1, mn}(\omega)$  and  $S_{r_1, mn}(\omega)$  are of the same order of magnitude but of opposite sign. As it allows to account for these remarks while reducing the complexity of the formulations, the multiplicative term

$$\mathcal{L}_{mn} = \left(1 - \frac{S_{p, mn}(\psi_m)}{S_{p, mn}(\omega_p)}\right) \left(1 - \frac{S_{p, mn}(\psi_n)}{S_{p, mn}(\omega_p)}\right) \quad (6.32)$$

is introduced to replace the resonant approximations of the spectral densities into the equations. This reasoning is however more difficult to justify clearly now that the elements of the modal state matrices are depending on the frequencies as well. For further explanations, the reader is invited to go back to the previous chapter.

Implementing the same procedure for the peak positioned in the negative frequency range with another but similar stretching,  $\omega = -\omega_p(1 + \varepsilon\eta)$ , the local approximations of the residuals over the peaks associated to the spectral densities of the modal state forces finally read

$$S_{\ell_1, mn}^{(\pm)}(\omega) = \mathcal{D}_m \mathcal{D}_n \mathcal{L}_{mn} \sum_{l=0}^4 \left[ (\pm \omega_p)^{\beta_{mn}^{(l)}} \mathcal{G}_{mn}^{(l)}(\pm \omega_p) \mathcal{S}_{p, mn}^{(l)}(\omega) \right] \quad (6.33)$$

and

$$\Delta S_{\ell_1, mn}^{(\pm)}(\omega) = \mathcal{D}_m \mathcal{D}_n \mathcal{L}_{mn} \sum_{k=1}^{2M} D_k \sum_{l=1}^8 \left[ (\pm \omega_p)^{\beta_{mnk}^{(l)}} \mathcal{G}_{mnk}^{(l)}(\pm \omega_p) \mathcal{J}_{o, mk}(\pm \omega_p) \mathcal{S}_{p, mnk}^{(l)}(\omega) \right] \quad (6.34)$$

in the initial coordinates. Because of the projection in a complex basis, the real and imaginary parts of the spectral densities have lost their symmetry properties. Their values are no longer the same or the opposite, respectively, for similar absolute frequencies located in either the positive, either the negative frequency range. Therefore, the symbols (+) and (-) have to be selected in line with the sign of the considered circular frequency as before. Alternatively, this idea can also be formalized by using the same mathematical trick as in the previous chapter, Section 5.4.

When integrated, the functions

$$\mathcal{S}_{p, mn}^{(l)}(\omega) = \omega^{-\beta_{mn}^{(l)}} S_{p, mn}(\omega) \quad \text{and} \quad \mathcal{S}_{p, mnk}^{(l)}(\omega) = \omega^{-\beta_{mnk}^{(l)}} S_{p, kn}(\omega) \quad (6.35)$$

yield

$$\Sigma_{p, mn}^{(l)(\pm)} = \pm \int_0^{\pm\infty} \mathcal{S}_{p, mn}^{(l)}(\omega) \quad \text{and} \quad \Sigma_{p, mnk}^{(l)(\pm)} = \pm \int_0^{\pm\infty} \mathcal{S}_{p, mnk}^{(l)}(\omega) \quad (6.36)$$

which can be referred to as the spectral (fractional moments) of order  $-\beta_{mn}^{(i)}$  and the  $-\beta_{mni}^{(i)}$  of the  $m$ -th and  $n$ -th modal state forces.

In the end, integrating the local approximations of the residuals as well thus provides some explicit expressions for the loading components of the second order statistics. Indeed, they are given by

$$\Sigma_{\ell_1, mn} = \mathcal{D}_m \mathcal{D}_n \mathcal{L}_{mn} \sum_{l=1}^4 \left[ (+\omega_p)^{\beta_{mn}^{(l)}} \mathcal{G}_{mn}^{(l)}(+\omega_p) \Sigma_{p, mn}^{(l)(+)} + (-\omega_p)^{\beta_{mn}^{(l)}} \mathcal{G}_{mn}^{(l)}(-\omega_p) \Sigma_{p, mn}^{(l)(-)} \right] \quad (6.37)$$

TABLE 6.1: Definitions for Equations (5.30), (5.31) and (5.34)

$l$	$\beta_{mnk}^{(l)}$	$\mathcal{G}_{mnk}^{(l)}(\omega)$		
1	$\beta_m + \beta_n + \beta_k$	$\Re[\mathcal{H}_{\ell,m}(\omega)] \Re$	$\mathcal{H}_{\ell,n}^*(\omega)$	$\Re[\mathcal{H}_{\ell,k}(\omega)]$
2	$\beta_m + \beta_n + 2\beta_k$	$i\Re[\mathcal{H}_{\ell,m}(\omega)] \Re$	$\mathcal{H}_{\ell,n}^*(\omega)$	$\Im[\mathcal{H}_{\ell,k}(\omega)]$
3	$\beta_m + 2\beta_n + \beta_k$	$i\Re[\mathcal{H}_{\ell,m}(\omega)] \Im$	$\mathcal{H}_{\ell,n}^*(\omega)$	$\Re[\mathcal{H}_{\ell,k}(\omega)]$
4	$2\beta_m + \beta_n + \beta_k$	$i\Im[\mathcal{H}_{\ell,m}(\omega)] \Re$	$\mathcal{H}_{\ell,n}^*(\omega)$	$\Re[\mathcal{H}_{\ell,k}(\omega)]$
5	$\beta_m + 2\beta_n + 2\beta_k$	$-\Re[\mathcal{H}_{\ell,m}(\omega)] \Im$	$\mathcal{H}_{\ell,n}^*(\omega)$	$\Im[\mathcal{H}_{\ell,k}(\omega)]$
6	$2\beta_m + 2\beta_n + \beta_k$	$-\Im[\mathcal{H}_{\ell,m}(\omega)] \Im$	$\mathcal{H}_{\ell,n}^*(\omega)$	$\Re[\mathcal{H}_{\ell,k}(\omega)]$
7	$2\beta_m + \beta_n + 2\beta_k$	$-\Im[\mathcal{H}_{\ell,m}(\omega)] \Re$	$\mathcal{H}_{\ell,n}^*(\omega)$	$\Im[\mathcal{H}_{\ell,k}(\omega)]$
8	$2\beta_m + 2\beta_n + 2\beta_k$	$-i\Im[\mathcal{H}_{\ell,m}(\omega)] \Im$	$\mathcal{H}_{\ell,n}^*(\omega)$	$\Im[\mathcal{H}_{\ell,k}(\omega)]$

and

$$\Delta\Sigma_{\ell_1,mn} = \mathcal{D}_m \mathcal{D}_n \mathcal{L}_{mn} \sum_{k=1}^{2M} \mathcal{D}_k \left[ \sum_{l=1}^8 (+\omega_p)^{\beta_{mnk}^{(l)}} \mathcal{G}_{mnk}^{(l)}(+\omega_p) \mathcal{J}_{o,mk}(+\omega_p) \Sigma_{p,mnk}^{(l)(+)} + \sum_{l=1}^8 (-\omega_p)^{\beta_{mnk}^{(l)}} \mathcal{G}_{mnk}^{(l)}(-\omega_p) \mathcal{J}_{o,mk}(-\omega_p) \Sigma_{p,mnk}^{(l)(-)} \right] \quad (6.38)$$

respectively. Interestingly enough, Equation (6.36) can alternatively be written

$$\Sigma_{p,mn}^{(l)(\pm)} = \pm \sum_{i=1}^N \sum_{j=1}^N \phi_{im} \phi_{in}^* \int_0^{\pm\infty} \omega^{-\beta_{mn}^{(l)}} S_{f,ij}(\omega) d\omega \quad (6.39)$$

and

$$\Sigma_{p,mnk}^{(l)(\pm)} = \pm \sum_{i=1}^N \sum_{j=1}^N \phi_{ik} \phi_{in}^* \int_0^{\pm\infty} \omega^{-\beta_{mnk}^{(l)}} S_{f,ij}(\omega) d\omega \quad (6.40)$$

when the modal decomposition of the spectral densities from Equation (4.23) is reintroduced, showing that the integration can actually be performed in the nodal basis, before the modal projection, in order to avoid doing so at each integration point with the spectral densities of the nodal state loadings. For each of these terms, the modal projections required to compute the loading components are therefore reduced to none.

## 6.5 Specialization to Former Approximations

In order to verify somehow the consistency of the expressions proposed in this chapter, they are shown to degenerate into the expressions that have formerly been developed in more restrictive circumstances. It is quite straightforward for the background components since fixing  $\beta_m = \beta_n = \beta_k = 0$  and  $\omega_p = 0$  is sufficient to recover the expression of Davenport. For the resonant component, however, it is a little bit more complicated and the additional assumptions formulated in the previous chapter, in [13], and in [11] are thus implemented the one after the other in the following, starting from Equation (6.24) and Equation (6.25).

### 1. The frequency-dependency of the hydroelastic matrices is disregarded.

In this event, the off-diagonal entries of the modal state matrices are nil. Thus, Equation (6.25) directly drops. Besides, the diagonal elements of the modal state matrices are also given by the constant values

$$\mathcal{A}_{kk} = \lambda_k \quad \text{and} \quad \mathcal{B}_{kk} = i \quad (6.41)$$

over the whole range of circular frequencies. Substituting these coefficients into Equation (6.24) yields

$$\mathcal{C}_{mn} = -i(\lambda_m - \lambda_n^*) = \mathcal{C}_{nm}^* \quad (6.42)$$

and thus

$$\Sigma_{r_1, mn} = i\pi \frac{D_m D_n}{\lambda_m - \lambda_n^*} [S_{p, mn}(\psi_m) + S_{p, mn}(\psi_n)] \quad (6.43)$$

which corresponds well to the resonant component of the covariances between the  $m$ -th and  $n$ -th modal state responses obtained in Chapter 5. Meanwhile, the corrective terms readily disappear because the off-diagonal elements of the dynamical flexibility matrix are now strictly equal to zero.

### 2. The off-diagonal terms of the modal damping matrix are negligible.

Given that the top and the bottom parts of the complex eigenmodes can be related by

$$\boldsymbol{\theta}_m = \begin{bmatrix} \boldsymbol{\phi}_m \\ i\lambda_m \boldsymbol{\phi}_m \end{bmatrix} \quad (6.44)$$

where  $\boldsymbol{\phi}_m$  is a vector of size  $N$ , the modal state matrices can actually be expanded as

$$\begin{cases} \boldsymbol{\theta}_m^T \mathbf{A} \boldsymbol{\theta}_m = \boldsymbol{\phi}_m^T \mathbf{K} \boldsymbol{\phi}_m + \lambda_m^2 \boldsymbol{\phi}_m^T \mathbf{M} \boldsymbol{\phi}_m \\ \boldsymbol{\theta}_m^T \mathbf{B} \boldsymbol{\theta}_m = \boldsymbol{\phi}_m^T \mathbf{C} \boldsymbol{\phi}_m + 2i\lambda_m \boldsymbol{\phi}_m^T \mathbf{M} \boldsymbol{\phi}_m \end{cases} \quad (6.45)$$

where  $\boldsymbol{\theta}_m^T \mathbf{A} \boldsymbol{\theta}_m = \lambda_m D_m^{-1}$  and  $\boldsymbol{\theta}_m^T \mathbf{B} \boldsymbol{\theta}_m = iD_m^{-1}$ .

Then, under the assumption that has just been introduced, the stiffness, the mass and the damping matrices are simultaneously diagonalized by being projected into the basis formed by the top parts of the complex eigenmodes. As a consequence, it yields

$$\begin{cases} D_m = \lambda_m (k_m + \lambda_m^2 m_m)^{-1} \\ 0 = k_m + i\lambda_m c_m - \lambda_m^2 m_m \end{cases} \quad (6.46)$$

for the normalization coefficients, where the modal properties

$$k_m = \boldsymbol{\phi}_m^T \mathbf{K} \boldsymbol{\phi}_m \quad ; \quad m_m = \boldsymbol{\phi}_m^T \mathbf{M} \boldsymbol{\phi}_m \quad \text{and} \quad c_m = \boldsymbol{\phi}_m^T \mathbf{C} \boldsymbol{\phi}_m \quad (6.47)$$

are respectively referred to as the modal stiffnesses, masses and damping coefficients.

### 3. The damping ratios are much smaller than one, $\xi_{j_m} \ll 1$ and $\xi_{j_n} \ll 1$ .

By truncating the above equations at leading order in  $\xi_{j_m}$  and  $\xi_{j_n}$ , the natural frequencies and the damping ratios of the undamped structure read

$$\omega_{j_m} = \sqrt{\frac{k_m}{m_m}} \quad (6.48)$$

and

$$\xi_{j_m} = \frac{c_m}{2\sqrt{k_m m_m}} \quad (6.49)$$

respectively. Given that the  $m$  and  $n$  indices are both odd, doing so with Equation (6.43) as well yields

$$\Sigma_{r_1, mn} = \frac{\pi}{4k_m k_n} \frac{\omega_{j_m} \omega_{j_n}}{(\xi_{j_m} \omega_{j_m} + \xi_{j_n} \omega_{j_n}) + i(\omega_{j_m} - \omega_{j_n})} [S_{p, mn}(\omega_{j_m}) + S_{p, mn}(\omega_{j_n})] \quad (6.50)$$

for the resonant component of the modal state covariances.

#### 4. The damping ratios are the same in both modes, $\xi_m = \xi_n = \xi$ .

Under this condition, the covariance reads

$$\Sigma_{r_1, mn} = \frac{\pi}{4k_m k_n} \left( \frac{\xi - i\zeta}{\xi^2 + \zeta^2} \right) \left( \frac{\omega_m \omega_n}{\omega_m + \omega_n} \right) [S_{p, mn}(\omega_m) + S_{p, mn}(\omega_n)] \quad (6.51)$$

where the parameter

$$\zeta = \frac{\omega_n - \omega_m}{\omega_n + \omega_m} \quad (6.52)$$

as defined in [11] is introduced. This dimensionless number measures the relative distance between the two natural frequencies.

#### 5. The natural frequencies are close to each other, $\omega_n = \omega_m (1 + 2\zeta)$ with $\zeta \ll 1$ .

The covariance is finally expressed by

$$\Sigma_{r_1, mn} = \frac{\pi}{4k_m k_n} \left( \frac{\xi - i\zeta}{\xi^2 + \zeta^2} \right) \left( \frac{\omega_m + \omega_n}{2} \right) \left( \frac{S_{p, mn}(\omega_m) + S_{p, mn}(\omega_n)}{2} \right) \quad (6.53)$$

as in [11]. However, by contrast with these previous developments, the arithmetic mean between the cross-spectral densities comes out from the equations and are not due to further arbitrary simplifications.

#### 6. The indices $m$ and $n$ are equal to each other.

At last, the resonant component of the variance

$$\Sigma_{r_1, mm} = \frac{\pi \omega_{j_m}}{4\xi k_{j_m}^2} S_{p, mm}(\omega_{j_m}) \quad (6.54)$$

is also well recovered [14].

All in all, the demonstration provided hereabove confirms that the formulas derived in this thesis are in fact more general and can be used in an even broader domain of application than before.



## Chapter 7

# Applications

This chapter tackles the stochastic analysis of multi-degree-of-freedom structures subjected to hydrodynamic loads with the methodologies developed in this thesis and aims at validating them. Given that the first application is very detailed, the second one is deliberately kept short.

### 7.1 Bergsøysund Bridge

The first example deals with a simplified and adapted version of the Bergsøysund Bridge. This bridge is located in Norway and is one of the longest end-anchored floating bridges in the world. With its total length of 933 m, it crosses a 300-m deep strait. It is currently regarded by the Norwegian Public Road Administration as an inspiration for the very long floating bridges that they are planning to build to complete their impressive E39 Coastal Highway Route project. The dynamic behavior of this bridge has therefore been studied in many publications over the past years. In particular, K. A. Kvåle et al. performed the stochastic analysis of this specific bridge as explained in Section 4.3. These authors are gratefully acknowledged for having provided us with the material, the code, and the data associated to their work as it constituted the starting point for evaluating the accuracy and the efficiency of the approaches proposed in the previous chapters.

To start, the validity of the two decoupling strategies presented in Chapter 4 is assessed. To do so, the spectral densities and the second moments of the modal state responses are computed as explained in Section 4.4 and Section 4.5. These *approximations* are then to be compared with the spectral densities and the second moments of reference which are obtained by using the expressions presented in Section 4.3. These results are all supposed to match provided that the frequency sensitivity of the hydrodynamic matrices is negligible in the first scenario, or limited in the second scenario.

The *decompositions* derived with the help of the Multiple Timescale Spectral Analysis for the spectral densities and the second moments of the modal state responses, in Chapter 5 and Chapter 6, are then validated as well. In both scenarios, the resonant contributions are displayed in green while the loading contributions are drawn in yellow, orange or red, depending on whether they are referring to an inertial, a mixed or a background case. At start, the errors originating from the approximations and the decompositions are analyzed the one after the other but they are eventually examined as a whole when the spectral densities and the second moments of the nodal state responses are reconstructed.

To be clear, Table 7.1 and Table 7.2 contain a summary of the spectral densities and the statistics that are going to be shown in the sequel, along with the equation numbers, the line styles, and the various figures they are associated to.

As shown in Figure 7.1, the Bergsøysund Bridge is composed of 7 pontoons made of concrete. They are linked together and to the shore by steel truss segments of approximately 105 meters in length. As indicated in Kvåle's paper, the water depth reaches 100 m or more at the locations of all but one of the pontoons. They are thus considered as being subjected to deep water waves. Thanks to the absence of mooring, the dynamics of this bridge are likely to be correctly described

by means of the linear equations of motion introduced in Section 4.2. For the record, they read

$$\left[ \mathbf{K}(\omega) + i\omega\mathbf{C}(\omega) - \omega^2\mathbf{M}(\omega) \right] \mathbf{x}(\omega) = \mathbf{f}(\omega) \quad (7.1)$$

where  $\mathbf{K}(\omega) = \mathbf{K}_s$ ,  $\mathbf{C}(\omega) = \mathbf{C}_s + \mathbf{C}_h(\omega)$ , and  $\mathbf{M}(\omega) = \mathbf{M}_s + \mathbf{M}_h(\omega)$  are the global hydroelastic matrices of the structure. Except for the stiffness matrix, the damping and the mass matrices are composed of a static and a hydrodynamic contribution which are respectively denoted by the  $s$  and the  $h$  subscripts.

In the following, a low-dimensional model is used for the superstructure instead of the Abaqus model employed by Kvåle and his coworkers. It allows to tackle the analysis of the bridge with a limited number of modes and to better understand how they interact with each other as it includes the horizontal degrees-of-freedom only. Given that the pontoons are almost aligned with respect to the  $y$  axis, these movements are regarded as the sway ( $x$ ), the surge ( $y$ ), and the yaw ( $\varphi$ ) responses of the pontoons – see Figure 7.1. The stiffness and the mass matrices of the steel truss segments are thus built in these global coordinates with BeamZ, the in-house finite element software created by Prof. Denoël. They are then combined with the buoyancy and the inertia of the pontoons delivered by Abaqus in order to form the static matrices,  $\mathbf{K}_s$  and  $\mathbf{M}_s$ .

For the sake of simplicity, the deck of the bridge is represented by equivalent beam elements. Their properties are listed in Table 7.3. Despite being realistic, they have been chosen to illustrate the capabilities of both the background and the inertial components in capturing the loading-related features of the responses. For the same reason, the hydrodynamic matrices and the hydrodynamic forces are defined as in Kvåle's paper but using as the one-dimensional wave spectral density a two-parameter Pierson-Moskovitz spectrum

$$S_{pm}(\omega) = \frac{5h_s}{16\omega_p} \left( \frac{\omega_p^5}{\omega^5} \right) \exp \left( -\frac{5}{4} \frac{\omega_p^4}{\omega^4} \right) \quad (7.2)$$

with  $h_s = 2.4$  m being the significant wave height and  $\omega_p = 2.2$  rad/s being the peak wave frequency, as introduced in Chapter 1. The wave period is therefore equal to  $T_p = 2.85$  seconds. A spreading parameter of 3 is also selected, meaning that the waves are short-crested. The correlations between the loads applied on different pontoons can hence be neglected. Otherwise, the spectral densities of the forces might exhibit some rapid oscillations which cannot theoretically be handled by the Multiple Timescale Spectral Analysis for the moment, see Assumption (i) in Chapter 5 and Chapter 6.

As a consequence of these specific choices, a few natural frequencies are below, close to, or above the peak frequency of the loading. They are obtained together with the damping ratios by solving the eigenproblem

$$i\mathbf{A}(\psi_m)\boldsymbol{\theta}_m = \lambda_m\mathbf{B}(\psi_m)\boldsymbol{\theta}_m \quad (7.3)$$

for the eigenmodes  $\boldsymbol{\theta}_m$  and the eigenvalues  $\lambda_m = \psi_m + i\nu_m$  with the appropriate set of state matrices first, and second by identifying them as

$$\omega_{j_m} = |\lambda_m| \quad \text{and} \quad \xi_{j_m} = \Im[\lambda_m]/|\lambda_m| \quad (7.4)$$

after a simple algebraic manipulation of Equation (4.13). In the first scenario, the state matrices are considered as being constant with respect to the circular frequencies and replaced by  $\mathbf{A}(\omega_0)$  and  $\mathbf{B}(\omega_0)$  where the dominant frequency  $\omega_0$  is set equal to the peak frequency of the waves. In the second scenario, however, the frequency dependent nature of the state matrices is kept as is.



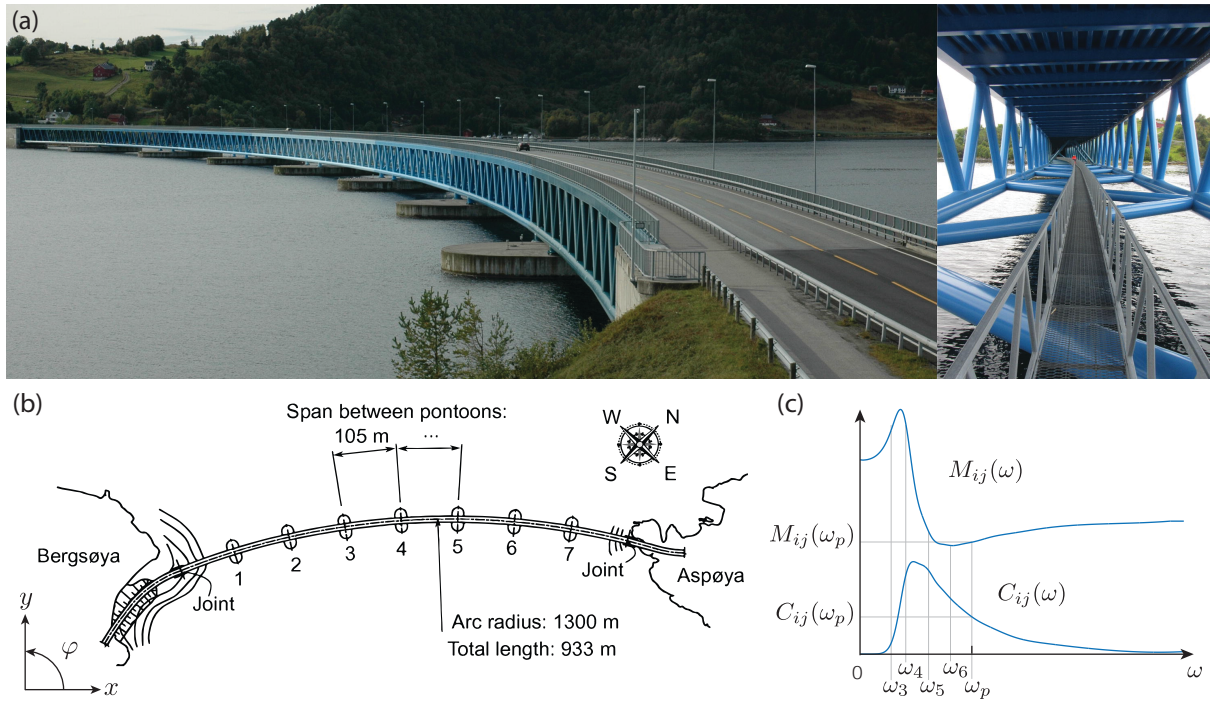


FIGURE 7.1: (a) Picture of the Bergsøysund Bridge [107]; (b) Top view of the Bergsøysund Bridge [83]; (c) Typical evolution of the hydrodynamic mass and damping elements along the circular frequencies [15].

TABLE 7.1: Spectral Densities – Legend for the following figures.

















	Scenario 0	Scenario 1	Scenario 2	
Ultimate Reference	$S_{q,mn}(\omega)$	$S_{q_0,mn}(\omega)$	$S_{q_1,mn}(\omega)$	$\Delta S_{q_1,mn}(\omega)$
	Eq. (4.19)	Eq. (4.31)	Eq. (4.47)	Eq. (4.48)
				
Asymptotic Approximation	$S_{q_2,mn}(\omega)$	$\tilde{S}_{q_0,mn}(\omega)$	$\tilde{S}_{q_1,mn}(\omega)$	$\Delta \tilde{S}_{q_1,mn}(\omega)$
	Eq. (4.46)	Eq. (5.5)	Eq. (6.11)	Eq. (6.12)
				
Leading Contribution	$S_{q_1,mn}(\omega)$	$S_{r_0,mn}(\omega)$	$S_{r_1,mn}(\omega)$	$\Delta S_{r_1,mn}(\omega)$
	Eq. (4.47)	Eq. (5.19)	Eq. (6.20)	Eq. (6.21)
				
First Correction	$\Delta S_{q_1,mn}(\omega)$	$S_{\ell_0,mn}(\omega)$	$S_{\ell_1,mn}(\omega)$	$\Delta S_{\ell_1,mn}(\omega)$
	Eq. (4.48)	Eq. (5.30)	Eq. (6.33)	Eq. (6.34)
				
Auto-spectrum	Figure 7.4	Figure 7.3	Figure 7.5	Figure 7.6
Co-spectrum	Figure 7.9	Figure 7.8	Figure 7.9	Figure 7.9
Quad-spectrum	Figure 7.10	Figure 7.8	Figure 7.10	Figure 7.10

TABLE 7.2: Second Moments – Legend for the following figures.













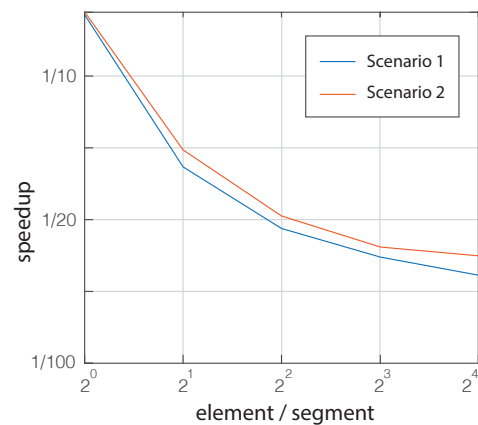
	Scenario 1	Scenario 2	
	$\Sigma_{q_0,mn}$	$\Sigma_{q_2,mn}$	
Numerical Solution	Eq. (4.33)	Eq. (4.53)	
			
		$\Sigma_{q_1,mn}$	$\Delta\Sigma_{q_1,mn}$
		Eq. (4.51)	Eq. (4.52)
			
MTSA Decomposition	$\tilde{\Sigma}_{q_0,mn}$	$\tilde{\Sigma}_{q_2,mn}$	
	Eq. (5.6)	Eq. (6.13) + Eq. (6.14)	
			
Resonant Contribution	$\Sigma_{r_0,mn}$	$\Sigma_{r_1,mn}$	$\Delta\Sigma_{r_1,mn}$
	Eq. (5.20)	Eq. (6.24)	Eq. (6.25)
			
Loading Contribution	$\Sigma_{\ell_0,mn}$	$\Sigma_{\ell_1,mn}$	$\Delta\Sigma_{\ell_1,mn}$
	Eq. (5.34)	Eq. (6.37)	Eq. (6.38)
			

TABLE 7.3: Parameters of the model.

Name	Value	Unit
Segment Length	105	m
Inertia Moment	12.36	m <sup>4</sup>
Young Modulus	2.10 <sup>10</sup>	N/m <sup>2</sup>
Cross-Section	0.6	m <sup>2</sup>
Density of Steel	7850	kg/m <sup>3</sup>
Significant Wave Height	2.4	m
Peak Wave Frequency	2.2	rad/s
Spreading Wave Constant	3	-

FIGURE 7.2: Speedup with MTSA.



The resulting natural frequencies and damping ratios are listed in Table 7.4, next to the associated mode shapes. These modal parameters are equal to the reference values in the second scenario. Meanwhile, they are almost systematically overestimated in the first scenario because the added masses are depleted, i.e.  $M_{ij}(\omega_0 = \omega_p) < M_{ij}(\omega)$ , and the damping coefficients are amplified, i.e.  $C_{ij}(\omega_0 = \omega_p) > C_{ij}(\omega)$ , over a broad frequency range. The only exceptions concern the damping ratios associated to the 5<sup>th</sup>, 6<sup>th</sup> and 7<sup>th</sup> modes for which the mass elements  $M_{ij}(\omega_0 = \omega_p)$  are nearly unchanged in relation to  $M_{ij}(\omega_{j_m})$  and the damping coefficients  $C_{ij}(\omega_0 = \omega_p)$  are smaller than  $C_{ij}(\omega_{j_m})$ . These observations are in accordance with the typical evolution of the mass and the damping entries along the circular frequencies, which is schematically represented in Figure 7.1-(c).

Thanks to the proposed decompositions, these modifications of the damping ratios are clearly shown to be responsible for the reduction and the augmentation of the resonant contributions in the approximate spectral densities and second moments obtained in the first scenario, with respect to the reference ones.

The attenuation effects are however exclusively observed in the higher modes (8<sup>th</sup> to 15<sup>th</sup>) but not in the lower ones (1<sup>th</sup> to 4<sup>th</sup>) because they are responding in the inertial regime only and their resonant regimes are simply not activated by the loading, see the yellow patches in the 1<sup>th</sup> to 4<sup>th</sup> graph of Figure 7.3. As a consequence, the resonant peaks of the reference auto- and cross-spectral densities associated to the higher modes respectively vanish in the first scenario, see the light blue lines versus the dark blue lines in the 8<sup>th</sup> to 15<sup>th</sup> graphs of Figure 7.3 and Figure 7.4, or in the last rows of Figure 7.8 and Figure 7.9-7.10. Please notice that the full scale values of the vertical axes are not always the same for a given pair of graphs. The smallest of the two values is thus represented by an horizontal grey line on the companion graph to ease their comparison.

In parallel to these disappearances, the resonant components of the variances and the correlations relative to the higher modes are smaller in the first scenario than in the second, see the color repartition in the respective stacks of Figure 7.7-(b) and Figure 7.7-(c), or the top right parts of Figure 7.11-(a) and Figure 7.11-(k), respectively. This is also the reason why the errors on these results are more important in the first scenario, see the gaps between the light and dark blue symbols in Figure 7.7-(a), and the locations of the darker spots in Figure 7.11-(f).

Regarding the magnification effects, all but the last of the above remarks can just be reversed and applied to the 5<sup>th</sup>, the 6<sup>th</sup> and the 7<sup>th</sup> modes. They appear to be milder because the dominant frequency is closer to their natural frequencies. Thus, the modal parameters are closer to the reference values. But, given that the dominant frequency is equal to the peak frequency, Assumption (ii) is not respected for these modal state responses. It implies that the decompositions of their spectral densities and their second moments are less accurate for these few modes, see the discrepancies between the stacks and the light blue line in the shaded area of Figure 7.7-(b), and the errors in the cross-shaped zone of Figure 7.11-(c). In particular, the variance of the 5<sup>th</sup> modal response is substantially undervalued whereas the variances of the 6<sup>th</sup> and the 7<sup>th</sup> modal responses are significantly larger than the exact ones.

Being the most contributing modes, the balance between the decreasing and the increasing effects eventually tips in favor of the latter. This is quite straightforward to understand for the sway ( $x$ ) and the surge ( $y$ ) motions because they are almost not responding in the high frequency range. They are hence mainly subject to the latter changes and they are consequently overestimated, see the differences between the light blue dots and the dark blue lines in the first and the second columns of Figure 7.13 and Figure 7.14. The yaw ( $z$ ) responses, however, are affected by both types of modifications. The peaks of their spectral densities are simultaneously flattened in the high frequencies and sharpened below. But globally, their variances are overvalued as well, see the same lines as before in the third columns of Figure 7.13 and Figure 7.14.

All in all, the errors are principally due to the implementation of the decoupling strategy in the first scenario because of how it impacts the modal parameters. Meanwhile, the validity of

the formulas derived in Chapter 5 with the Multiple Timescale Spectral Analysis is confirmed by looking at the good agreement between the spectral densities and the second statistics of the modal state responses that they provide and the approximated ones for all types and combinations of responses (inertial in yellow, mixed in orange, background in red, and resonant in green), see the light blue dots and lines in Figure 7.3 and Figure 7.8, the light blue dots and circles in Figure 7.7, and the smallness of the errors in Figure 7.11-(c).

Moreover, although the correlations of the modal state responses are often related to the interactions between the resonance in two different modes and neglected provided that their natural frequencies are sufficiently distant from each other, as shown in Figure 7.11-(e), they appear to be significantly influenced by the loading components, see Figure 7.11-(d). As indicated in Section 5.5, they are particularly important when the forces in two different modes are coherent, which happens when their mode shapes are similar. The 1<sup>st</sup> and 8<sup>th</sup> modes, for instance, are strongly correlated as they are both symmetric, they change sign at mid-length and they possess two half waves. On all of these subfigures, the coefficients are divided into five categories and said partly inertial in the bottom-left corners, partly background in the top-right corners, and partly mixed in the two remaining corners, bottom-right and top-left, while the loading and resonant peaks interact in the cross-shaped areas. Last but not least, it seems interesting to notice that the diagonal elements in greyscale colors refer to the weighting factors  $\gamma_r$  and  $\gamma_\ell$  in Figure 7.11. The same comments obviously hold in the second scenario.

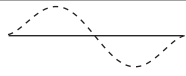

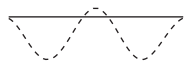

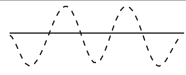
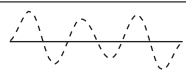
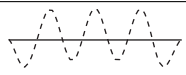
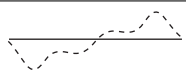
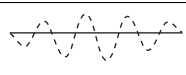
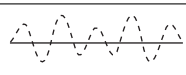
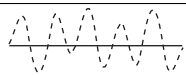
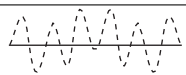
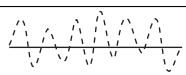
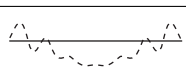
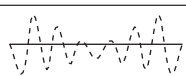
As shown by the matching of the dashed and the solid dark blue lines in Figure 7.4, 7.9 and 7.10, the reproduction of the resonant peaks by the approximate spectral densities is actually greatly improved in the second scenario. It means that the frequency sensitivity of the hydrodynamic matrices is not really negligible, otherwise the first scenario would provide better results, but it is indeed limited. Truncating the series expansion of the spectral densities at first order is therefore fully justified. Beyond that, it appears that the series can even be stopped before in the example at hand and this is hence what is done afterwards when reconstructing the spectral densities and the second moments of the nodal state responses. Indeed, be it for the auto-spectral densities of the modal state responses in Figure 7.4 or for the variances in Figure 7.7-(c), the first order corrections, in pink, are most often negligible in relation to the leading order contributions, in purple. In the first few modes, they even take the results away from the exact value which is represented by a thin line. The smallness of these contributions is even more pronounced for the cross-spectral densities. This is the reason why the first order correlation coefficients are not illustrated in Figure 7.11.

But before that, the decompositions provided in Chapter 6 for the leading order and the first order spectral densities are compared to the approximations discussed above in order to be validated, no matter if they are going to be neglected afterwards. Overall, they fit sufficiently well to conclude that the formulas developed with the Multiple Timescale Spectral Analysis are adequate in all of the cases treated so far, see the dotted and the solid lines of the same colors in Figure 7.4, 7.9 and 7.10.

As a result, the variances and the covariances of the modal state responses are correctly estimated again, unless the natural frequencies of the corresponding modes approach the peak frequency of the waves, see the dark blue symbols in Figure 7.7-(a), the similarity between the stacks and the horizontal lines in Figure 7.7-(c), and the few errors in the cross-shaped area of Figure 7.11-(m).

In the end, the spectral densities and the second moments of the nodal responses are more accurate in the second scenario, see the purple dotted lines and the dark blue lines in Figure 7.13 and Figure 7.14, although the analysis does not take much longer than in the first scenario, provided that the first order corrections are omitted, see Figure 7.2. The computational time is divided by 20 at least and this ratio further decreases when the model contains more degrees-of-freedom. The decoupling strategies and the semi-analytical formulas proposed in this thesis are therefore providing an interesting balance between precision and efficiency.

TABLE 7.4: Modal analysis of the Bergsøysund Bridge.

$j_m$	Scenario 1			Scenario 2			Mode Shape
	$\omega_{j_m}$	$f_{j_m}$	$\xi_{j_m}$	$\omega_{j_m}$	$f_{j_m}$	$\xi_{j_m}$	
	Unit	[rad/s]	[Hz]	[%]	[rad/s]	[Hz]	
1	0.27	0.04	16.5	0.25	0.04	0.01	
2	0.42	0.06	10.1	0.38	0.06	0.12	
3	0.68	0.11	5.93	0.62	0.10	1.08	
4	0.88	0.14	5.27	0.78	0.12	2.43	
5	1.32	0.21	3.64	1.23	0.19	5.05	
6	1.77	0.28	2.78	1.75	0.28	3.86	
7	2.07	0.33	2.19	2.06	0.32	2.43	
8	2.73	0.43	5.58	2.68	0.42	4.13	
9	3.21	0.51	2.84	3.12	0.49	1.16	
10	3.75	0.59	2.65	3.59	0.57	0.71	
11	4.32	0.68	2.51	4.08	0.64	0.43	
12	4.85	0.77	2.38	4.54	0.72	0.25	
13	5.33	0.85	2.28	4.96	0.78	0.24	
14	5.38	0.85	2.56	4.87	0.77	0.15	
15	5.77	0.92	2.36	5.28	0.84	0.18	

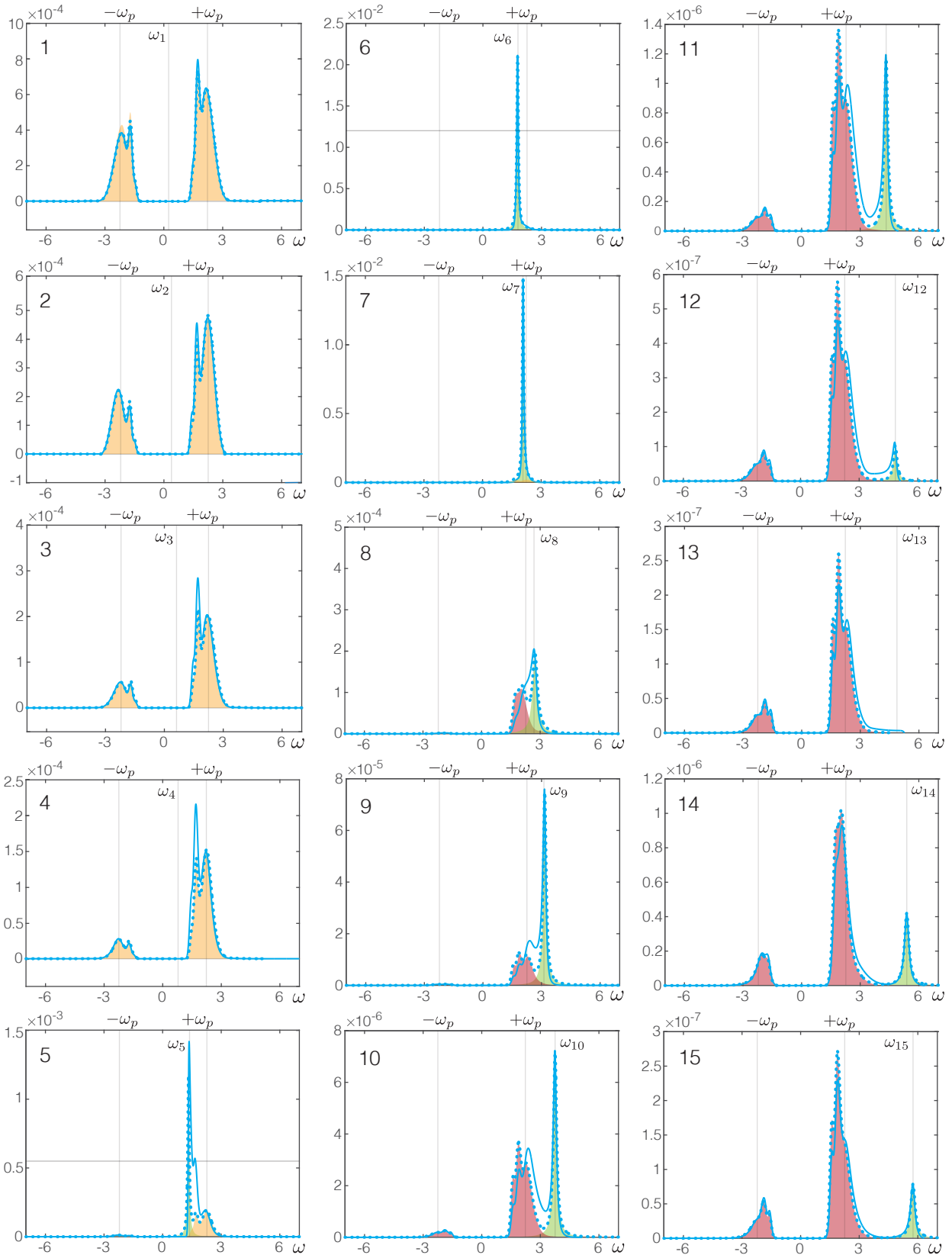


FIGURE 7.3: Scenario 1 – Auto-spectral densities of the modal state responses associated to the  $j_m$ -th modes, with  $m$  being an even number. See the legend in Table 7.1.

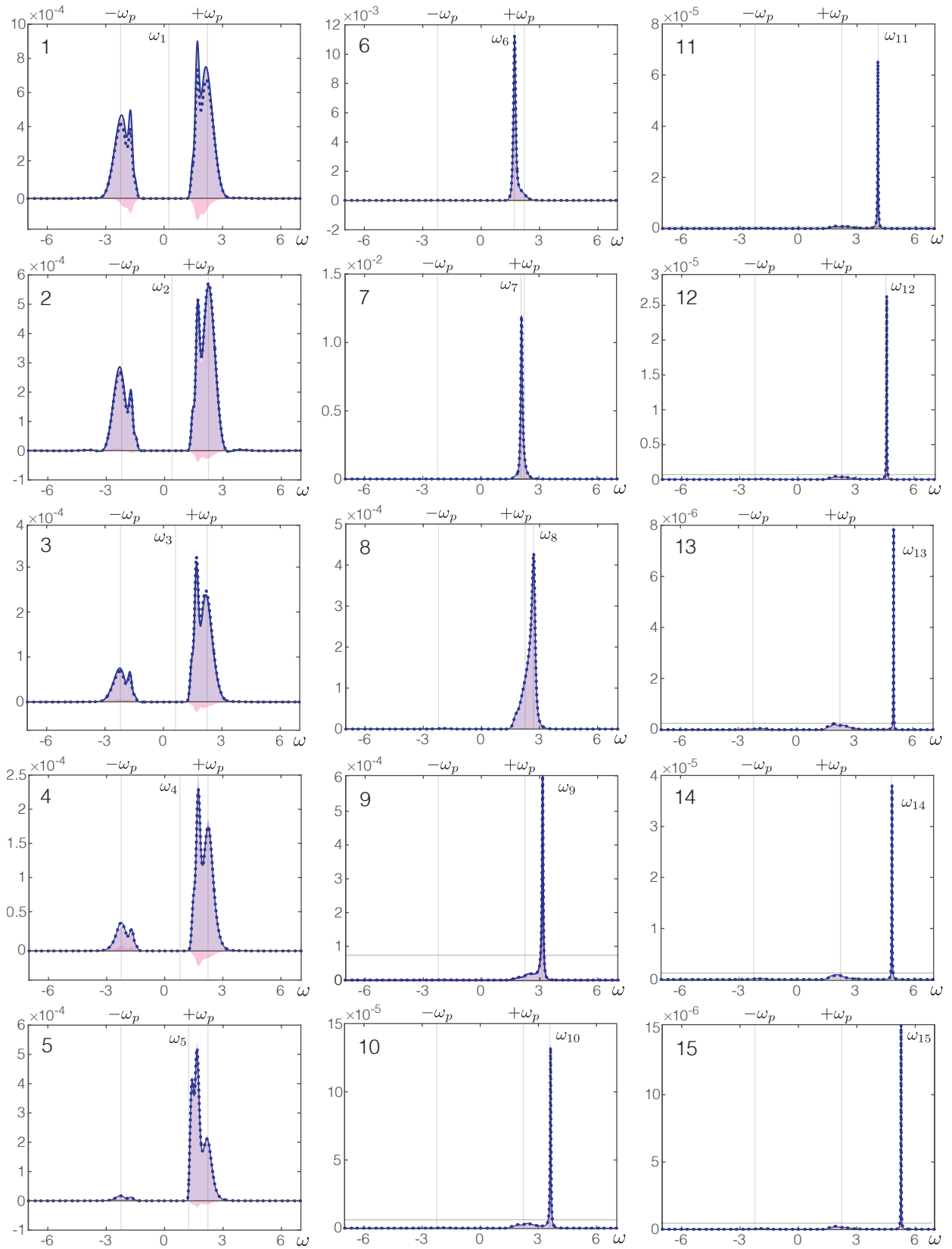


FIGURE 7.4: Reference & Scenario 2 – Auto-spectral densities of the modal state responses associated to the  $j_m$ -th modes, with  $m$  being an even number. See the legend in Table 7.1.

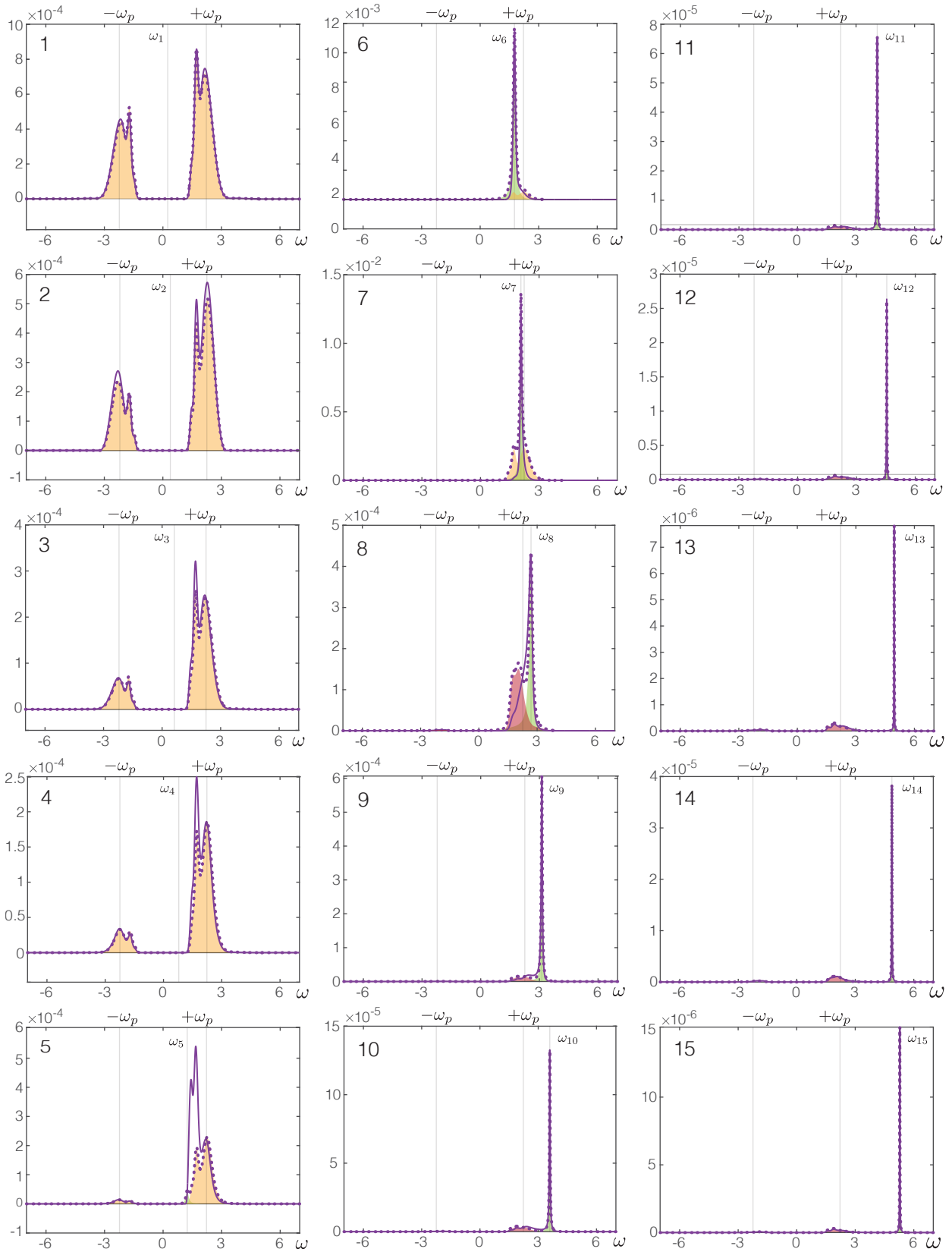


FIGURE 7.5: Scenario 2 – Leading order auto-spectral densities of the modal state responses associated to the  $j_m$ -th modes, with  $m$  being an even number. See the legend in Table 7.1.



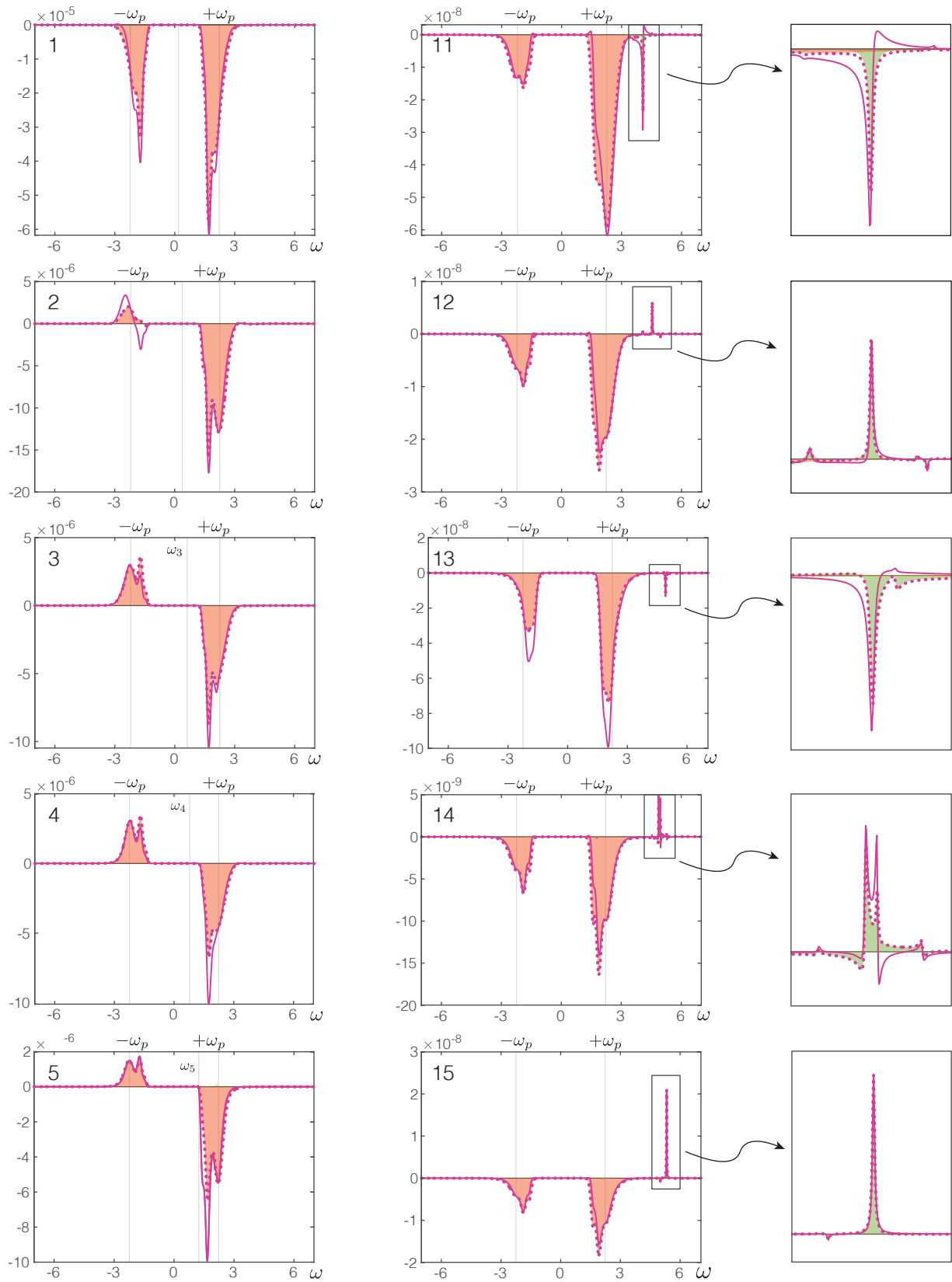


FIGURE 7.6: Scenario 2 – First order auto-spectral densities of the modal state responses associated to the  $j_m$ -th modes, with  $m$  being an even number. See the legend in Table 7.1.

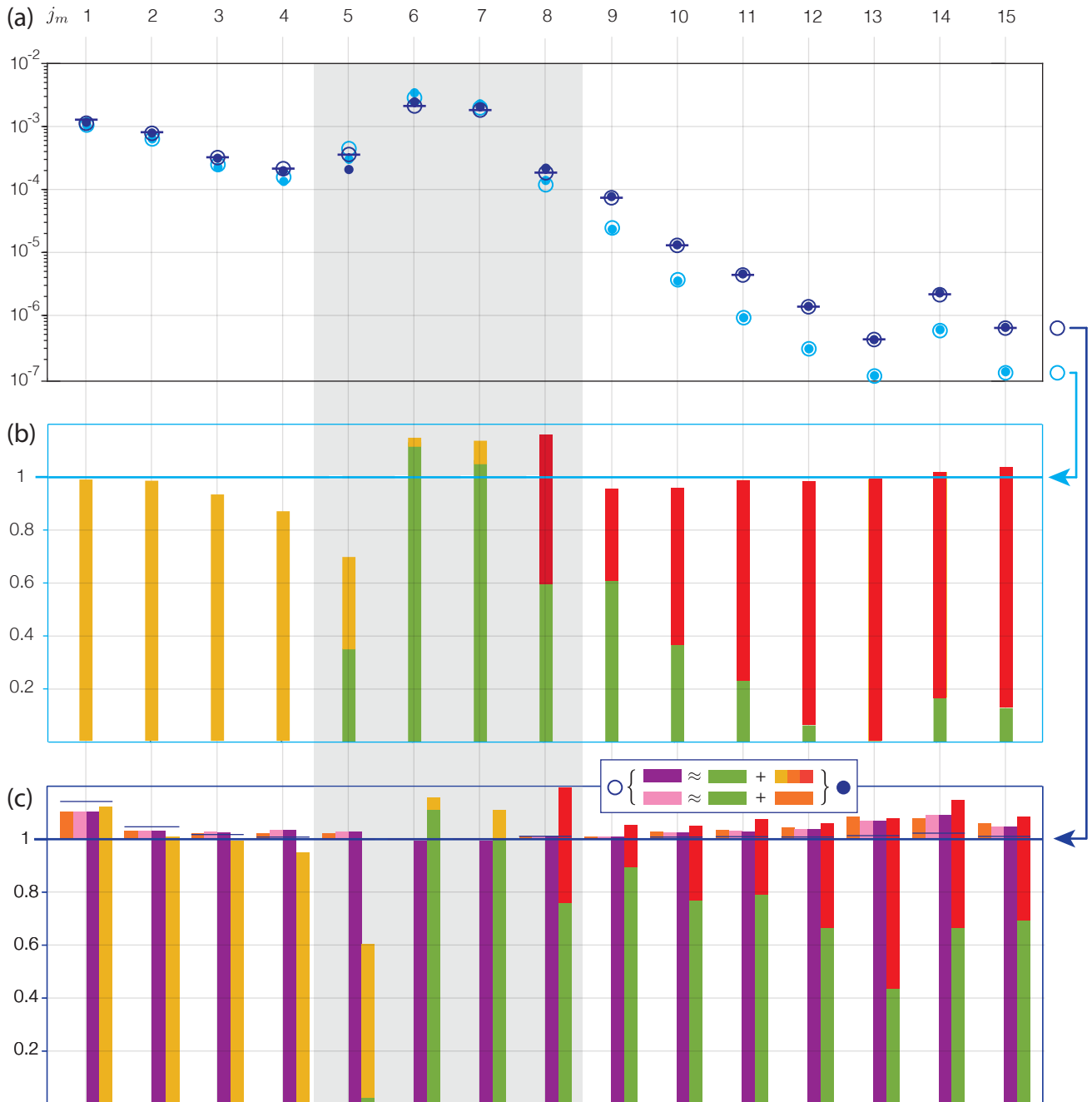


FIGURE 7.7: On top, the variances of the modal state responses associated to the  $j_m$ -th modes and obtained in both scenarios, with  $m$  being an even number. Below, the repartition between the resonant and the loading components, the leading order and the first order terms, depending on the scenario. See the legend in Table 7.2.

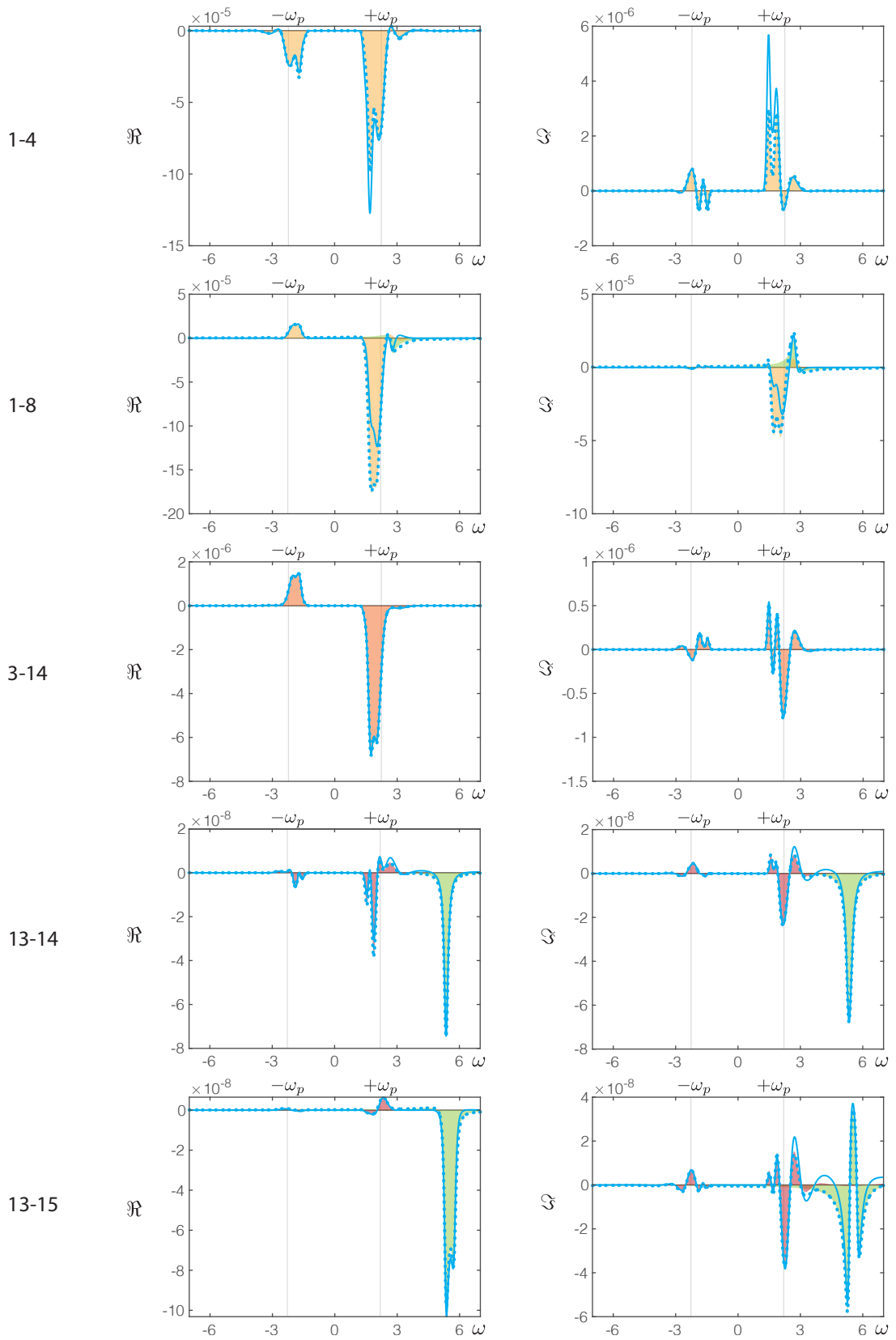


FIGURE 7.8: Scenario 1 – Co- and quad-spectral densities of the modal state responses associated to the  $j_m$ -th modes, with  $m$  being an even number. See the legend in Table 7.1.

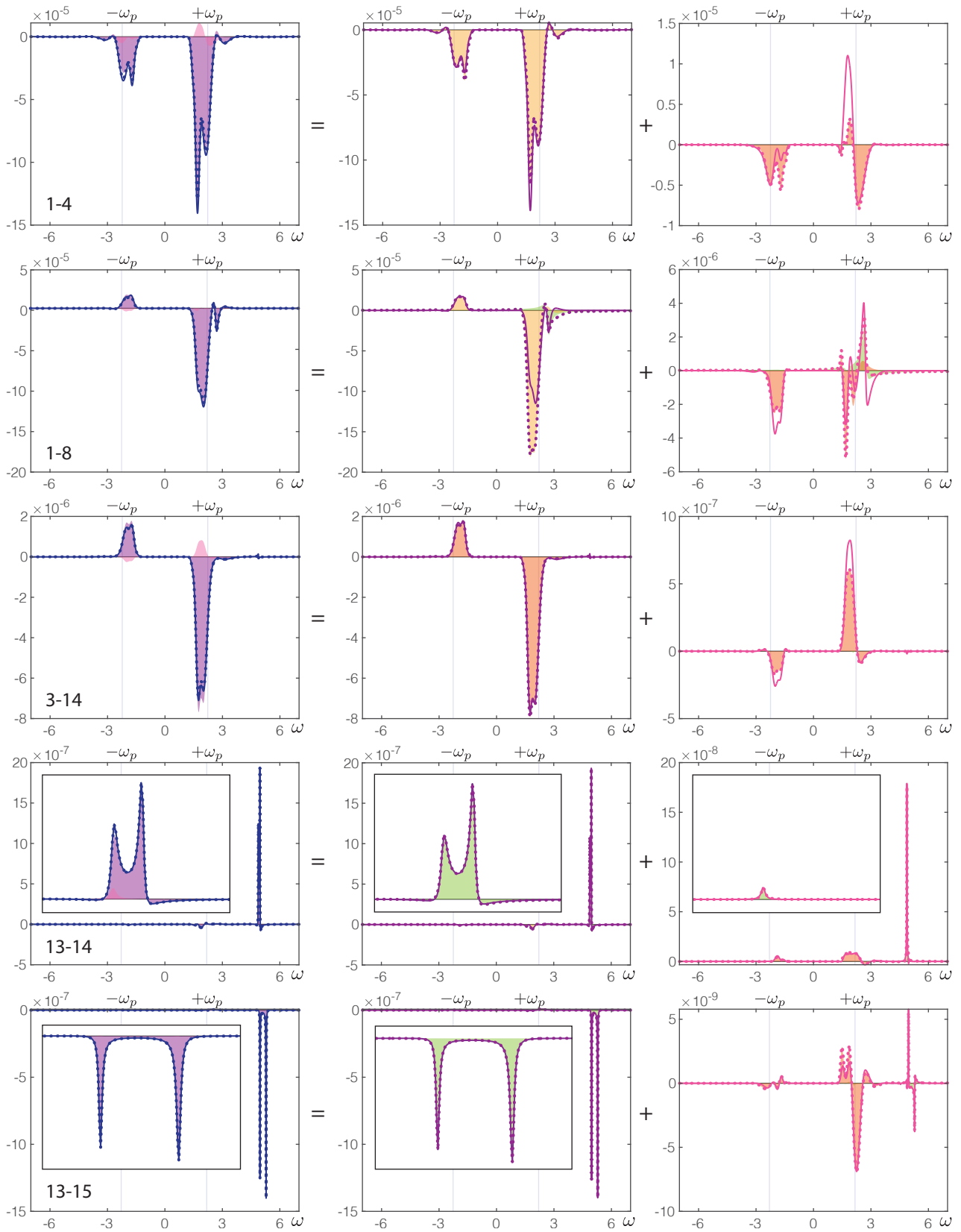


FIGURE 7.9: Scenario 2 – Co-spectral densities of the modal state responses associated to the  $j_m$ -th modes, with  $m$  being an even number. See the legend in Table 7.1.

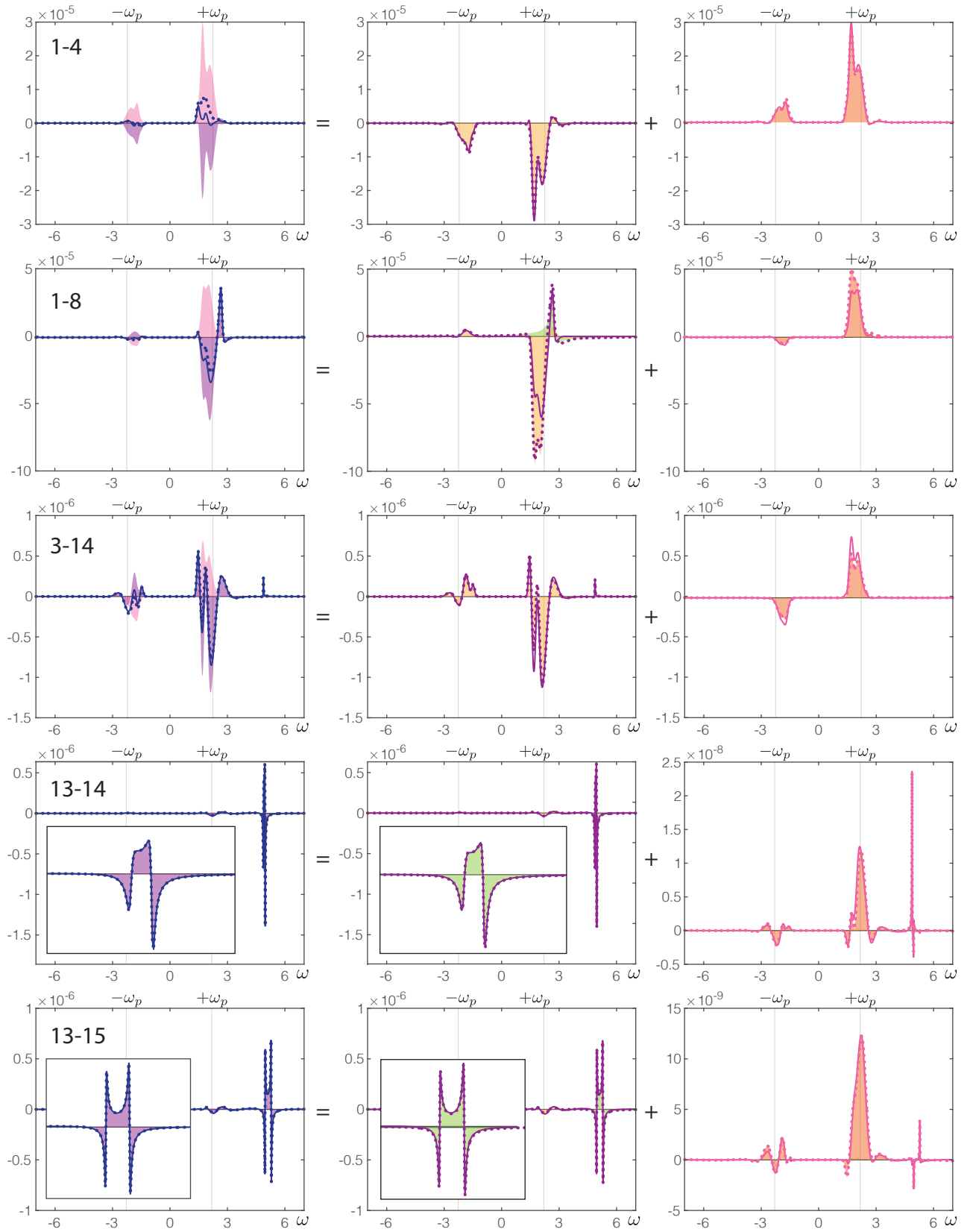


FIGURE 7.10: Scenario 2 – Quad-spectral densities of the modal state responses associated to the  $j_m$ -th modes, with  $m$  being an even number. See the legend in Table 7.1.

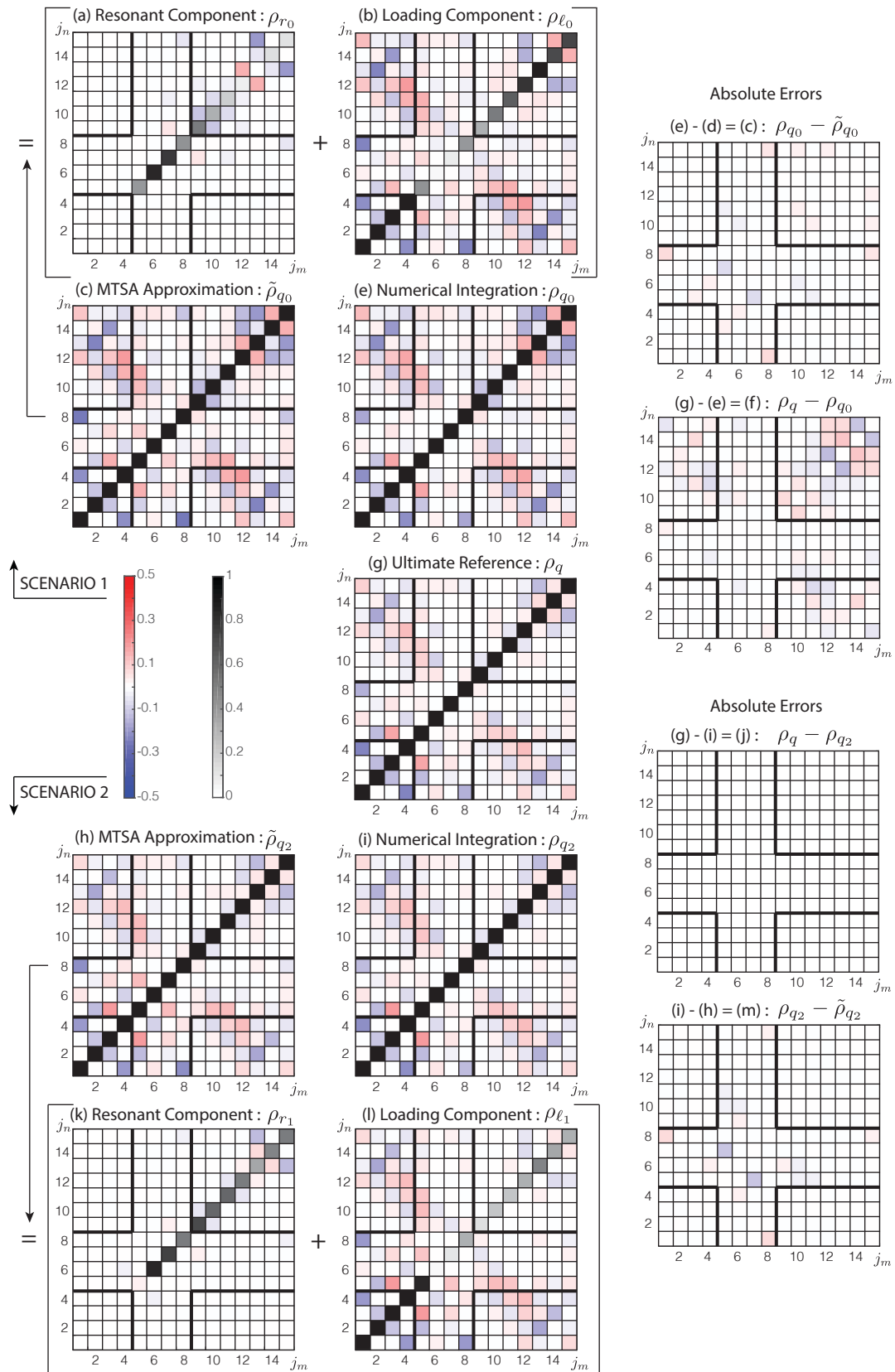


FIGURE 7.11: Real parts of the correlation coefficients between the modal state responses with  $m$  and  $n$  being even numbers. In the subfigures (a)/(k) and (b)/(l), the shades of grey respectively represent the resonant and the loading ratios.

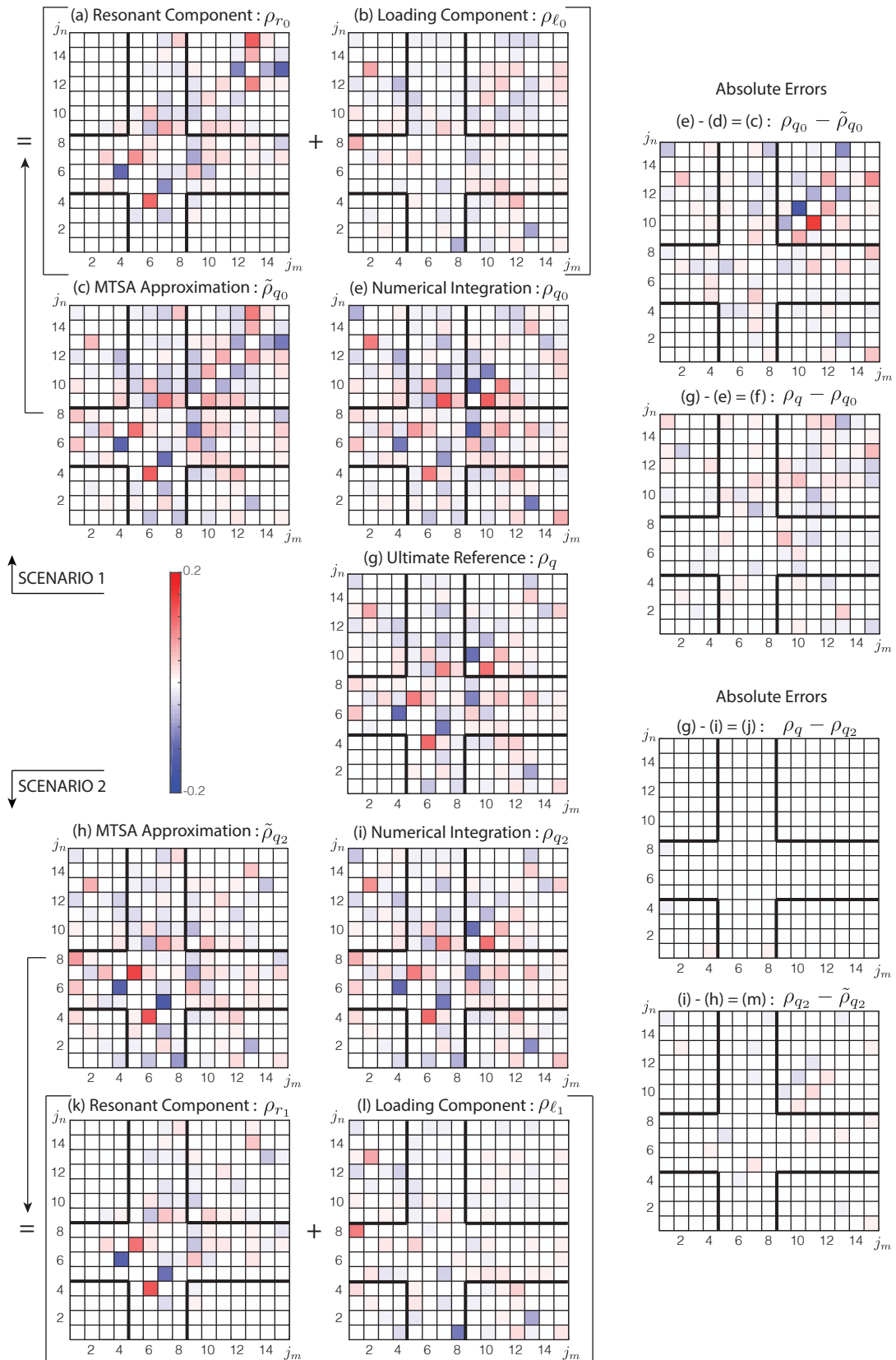


FIGURE 7.12: Imaginary parts of the correlation coefficients between the modal state responses with  $m$  and  $n$  being even numbers.

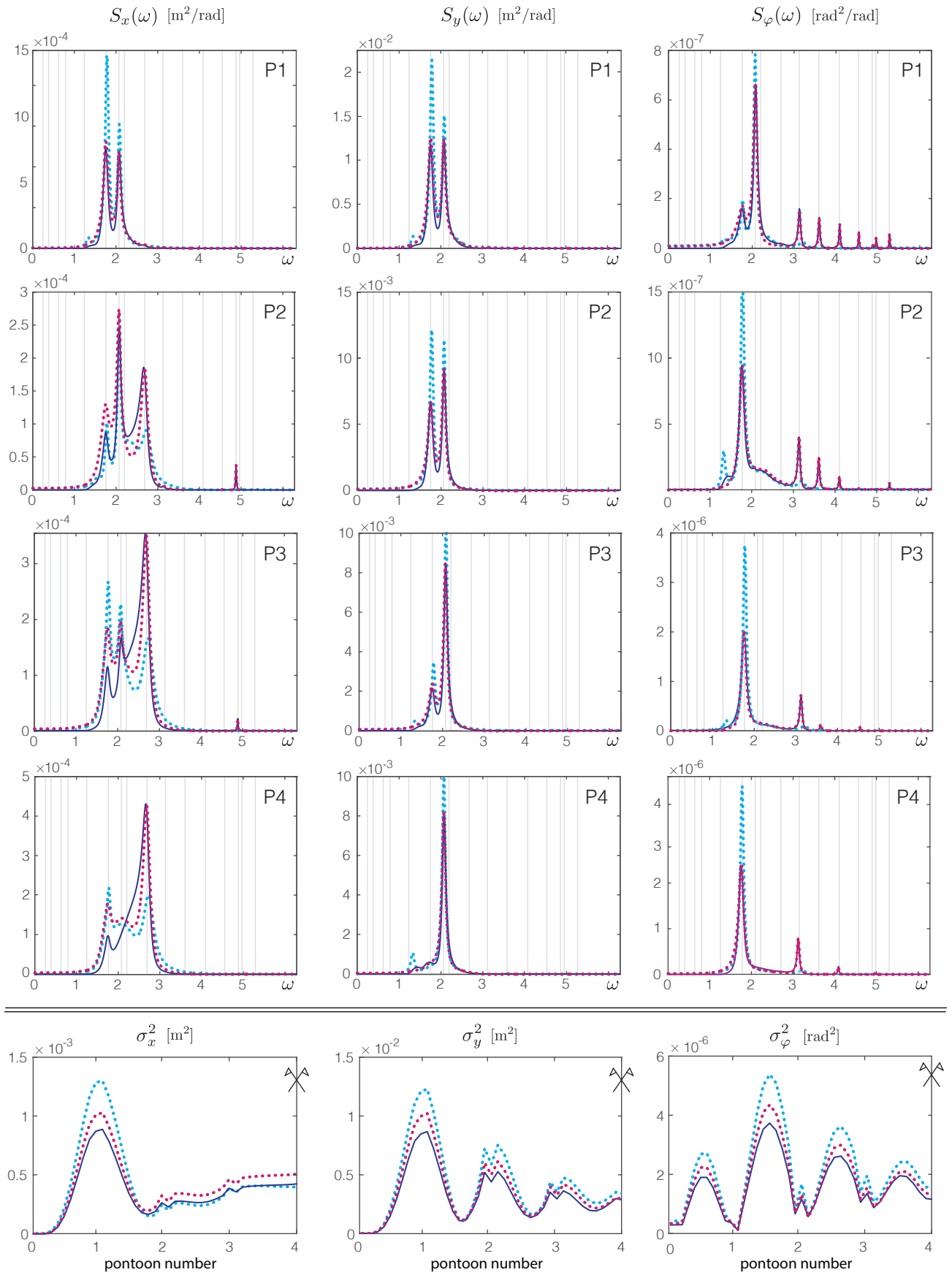


FIGURE 7.13: Auto-spectral densities and variances of the responses computed at the locations of the pontoons in both scenarios. Grey lines indicate the positions of the natural frequencies. See the legends in Table 7.1 and Table 7.2.



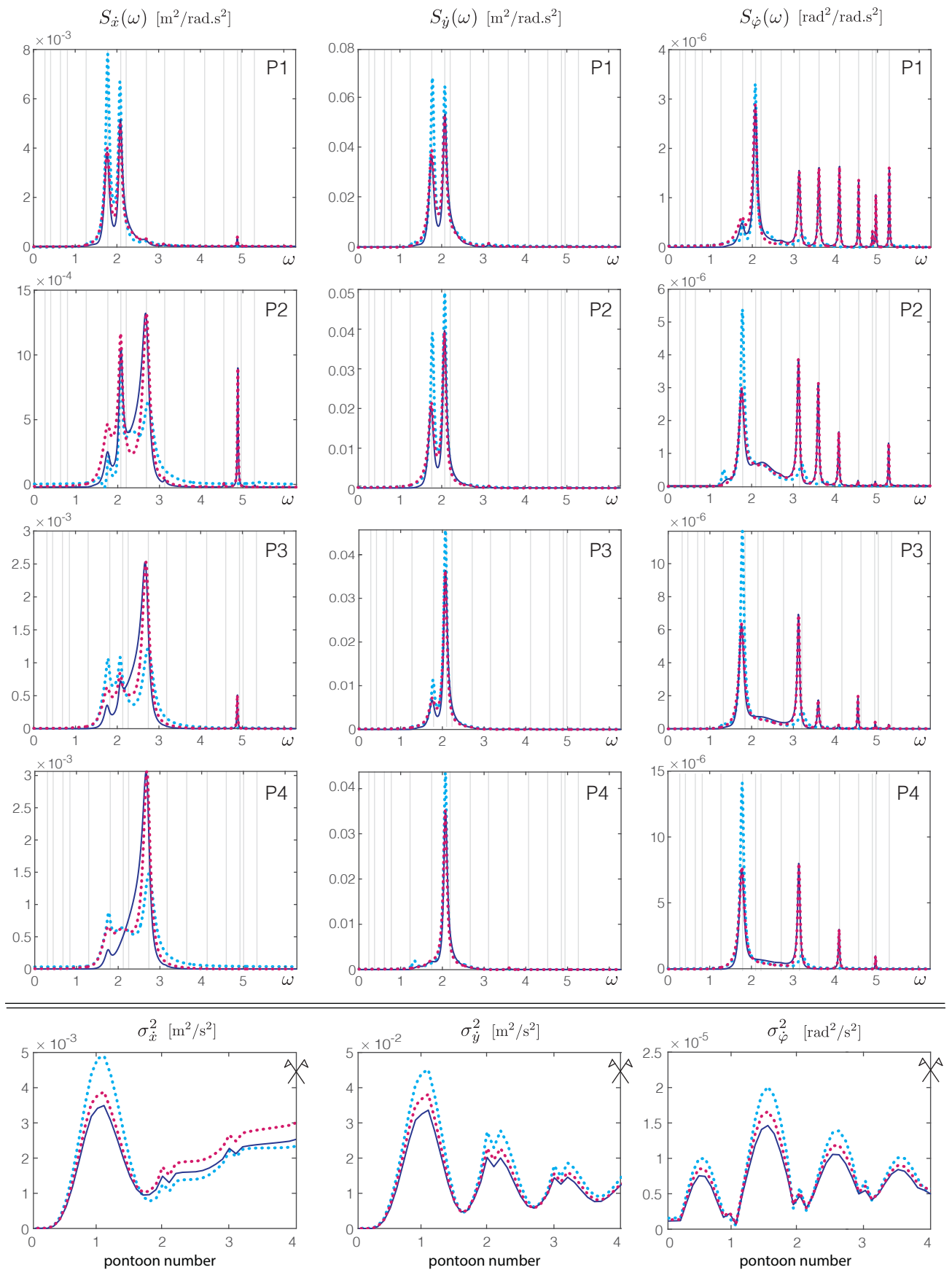


FIGURE 7.14: Auto-spectral densities and variances of the responses obtained at the locations of the pontoons in both scenarios. Grey lines indicate the positions of the natural frequencies. See the legends in Table 7.1 and Table 7.2.

## 7.2 Bjørnafjorden Bridge

The Bjørnafjorden Bridge is a floating arch bridge as well. It is approximately 5 km long and so is its radius of curvature. It is supported by 46 steel pontoons of  $58 \times 10$  m, whose layout is represented in Figure 7.15. The hydrodynamic behavior of this bridge is currently studied by the Norwegian Public Road Administration in the context of the E39 Coastal Highway Project. It is actually one of the possible future constructions that were evoked in the previous section. It has therefore been the subject of many recent publications, and in particular the latest one [108] to which the reader is referred for further details about the geometries of the elements, the properties of the materials, etc. Aksel Fenerci is sincerely thanked for having given us access to the static and the hydrodynamic matrices, as well as the spectral densities of the wave loads associated to the model that he and his colleagues created at the Norwegian University of Science and Technology.

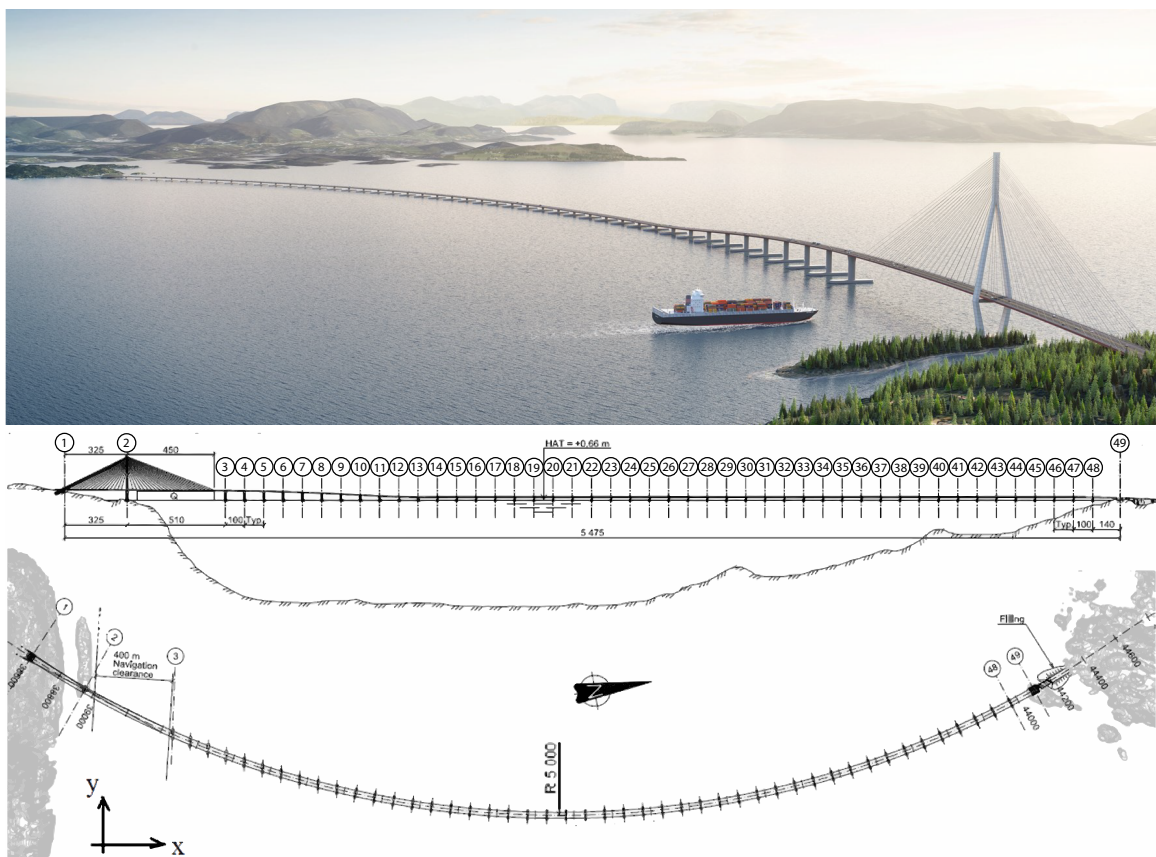


FIGURE 7.15: Artistic view and technical drawings of the Bjørnafjorden Bridge [108].

The standard deviations of the pontoon motions are reported in Figure 7.16 for a given sea state,  $h_s = 2.4$  m and  $\omega_p = 0.93$  rad/s ( $T_p = 6.75$  s). They are computed following the same procedure as in Section 7.1. The only difference concerns the origin of the structural matrices, which come from Abaqus instead of BeamZ. Otherwise, the dominant frequency is set equal to the peak frequency of the waves in the first scenario and the asymptotic series expansion is stopped at leading order in the second scenario. For each of these two scenarios, the standard deviations obtained through the numerical integration of the approximate spectral densities or through the proposed decompositions of the second statistics are represented by blue circles and red crosses in either the first, either the second column of Figure 7.16, respectively, whereas the reference results are designated by blue plus symbols. A few natural frequencies and damping ratios are also listed in Table 7.5 in order to provide a glimpse into the dynamical properties of the structure.

TABLE 7.5: Modal analysis of the Bjørnafjorden Bridge.

$j_m$	Scenario 1			Scenario 2			Mode Type H = horizontal V=vertical
	$\omega_{j_m}$	$f_{j_m}$	$\xi_{j_m}$	$\omega_{j_m}$	$f_{j_m}$	$\xi_{j_m}$	
Unit	[rad/s]	[Hz]	[%]	[rad/s]	[Hz]	[%]	
1	0.054	0.009	92.87	0.053	0.009	0.752	H
2	0.102	0.016	30.23	0.102	0.016	0.453	H
3	0.181	0.029	16.23	0.182	0.029	0.320	H
4	0.262	0.042	9.066	0.262	0.041	0.308	H
5	0.380	0.060	6.729	0.379	0.060	0.398	H
6	0.447	0.071	4.548	0.447	0.071	0.511	H
7	0.543	0.086	3.539	0.542	0.086	0.769	H
8	0.644	0.102	3.358	0.641	0.102	1.240	H
9	0.700	0.111	2.545	0.698	0.111	1.361	H
10	0.792	0.126	2.181	0.791	0.126	1.588	H
11	0.825	0.131	2.266	0.824	0.132	1.781	H
12	0.947	0.151	5.524	0.949	0.151	5.407	V
13	0.962	0.153	5.227	0.965	0.153	5.573	V
14	0.967	0.154	1.873	0.966	0.153	1.983	H
15	0.999	0.159	18.56	1.039	0.165	4.826	H

Overall, the good agreement between the various results presented in Figure 7.16 confirms again the validity of the methodologies proposed in this thesis. In particular, the statistics of the sway ( $x$ ) and the heave ( $z$ ) motions are very well reproduced in the first scenario. The approximations are however less precise for the other degrees-of-freedom and especially for the roll ( $\varphi_z$ ) motion. In this specific case, the approximate standard deviations are also less closely fitted by the proposed decomposition. Instead of being neglected, the frequency dependency of the hydrodynamic matrices is partially taken into account in the second scenario. It is shown to improve the accuracy of the approximations for all but the sway ( $x$ ) motions. The second decoupling strategy and the subsequent decompositions derived for the spectral densities and the second moments with the Multiple Timescale Spectral Analysis were therefore worth being considered and developed in this thesis.

In the framework of a joint publication at the 41<sup>st</sup> International Conference on Ocean, Offshore & Artic Engineering, Aksel Fenerci also used the formulas and the codes developed in this thesis in order to calculate the statistics of the responses obtained under many different sea states and eventually estimate their long-term extreme distributions [52]. Then, he compared them to the outcomes of the conventional spectral approach that he usually adopts. It indicated that, even though some discrepancies were observed when using the Multiple Timescale Spectral Analysis, these errors attenuate when computing the long-term extremes. In addition, they were shown to be sensitive to changes in the peak period but not in the significant wave height. This was to be expected because the former parameter is the only one which is supposed to influence the accuracy of the Multiple Timescale Spectral Analysis, through Assumption (ii).

These results were however referring to a case in which the frequency sensitivity of the hydrodynamic matrices is completely neglected. A further collaboration with Aksel Fenerci and Ole Øiseth is planned for the near future. It will aim at tackling such a long-term analysis by using the second decoupling strategy and the associated decompositions in order to take the frequency dependent nature of the fluid-structure interactions into account as well.

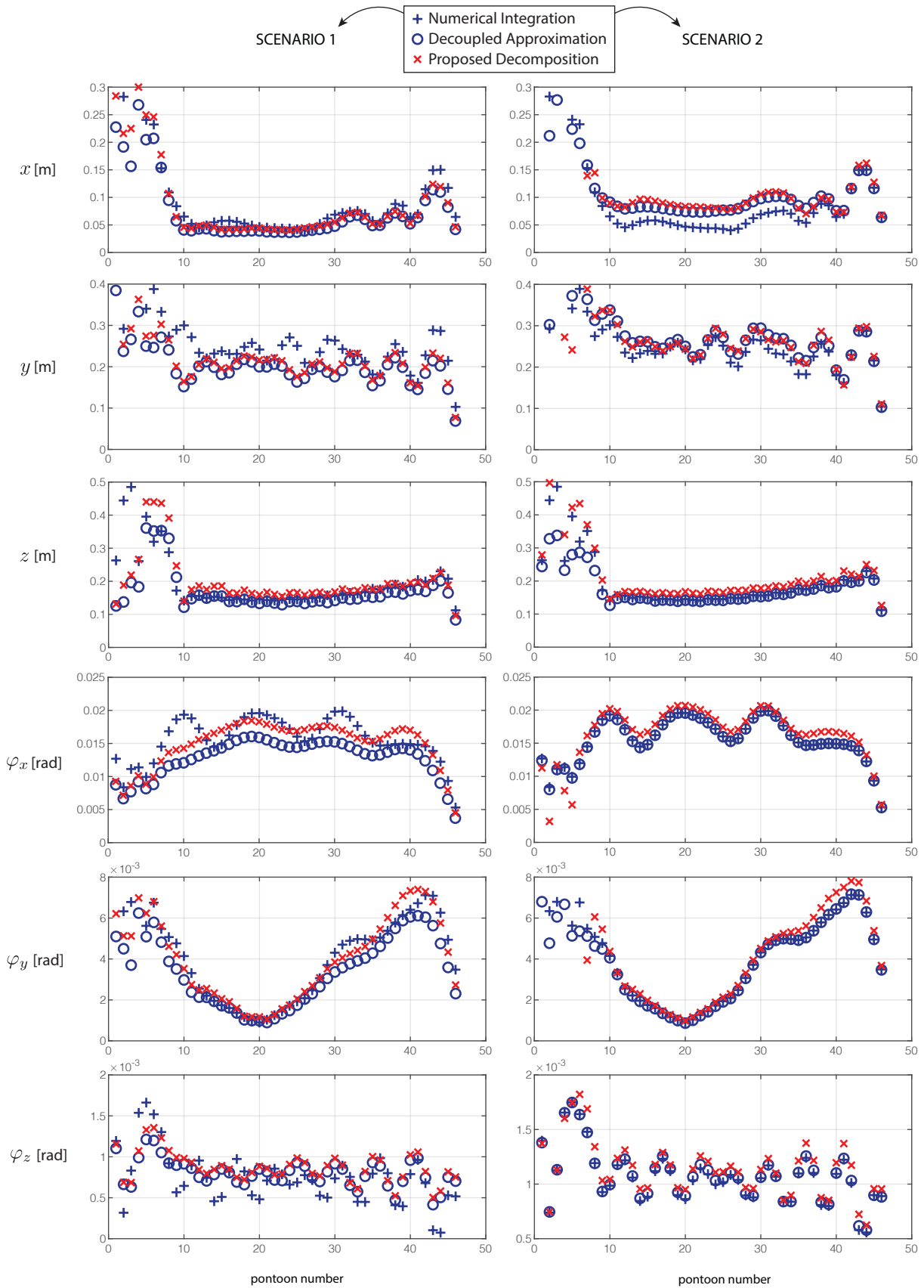


FIGURE 7.16: Standard deviations of the pontoon motions.





# CONCLUSION

## Contributions and Limitations

**In Part 1**, the second and third order responses of a linear system with a single degree-of-freedom, subjected to several versions of the Morison wave forces, are investigated.

Regarding the second statistical moments of the response, in Chapter 2, a new way of deriving their resonant component is proposed and compared to the usual one, which is used for example in [12, 36, 13, 11, 10]. It consists in expanding the structural kernels in partial fractions. This is the first time such a local approximation technique is employed in the history of the Multiple Timescale Spectral Analysis. Overall, both approaches provide the same final expressions for the resonant components of the second order moments but not for the local approximations of the power spectral densities, and thus not for the residual functions either. It is then demonstrated that the new residual function is more amenable to being simplified in the vicinity of the loading peaks, without the need for extra assumptions. It is therefore considered in the sequel to derive two different expressions for the inertial components, depending on whether the power spectral density of the loading is exponentially small near the origin or not.

The conditions for using the first formulation are consequently more restrictive but, interestingly enough, this expression eventually depends on the integral of a function which is totally independent of the structural characteristics. This is unfortunately not the case with the second formulation. Nevertheless, the function to be integrated does no longer exhibit peaks at the poles of the structural kernel, meaning that the number of integration points can anyway be reduced at these locations. As a next step, unified formulas are developed for the so-called loading components, i.e. background and inertial, to be treated as a single unit. They are eventually validated and verified against the integration of the response spectra obtained under a linearized, a quadratized and a non-polynomial wave loading, whose power spectral density is based on analytical definitions or numerical simulations.

Regarding the third statistical moments of the response, several components are formulated for the first time in Chapter 3, see Figure C. They depend on the values of the response bispectrum which are located along a few lines of the two dimensional domain only. Globally, it means that the order of integration is decreased by one at least when using these expressions. They are therefore extremely efficient in estimating the third central moments, and thus the skewness, of an oscillator's response under both a background and an inertial loading, whose bispectrum contains a real part, and possibly an imaginary part as well, which was hitherto always ignored.

Since the wave load models that are currently available always result in a real-valued bispectrum, the validations and the verifications of the new formulations proposed in Chapter 3 are only conducted for the contributions that are not associated to a complex-valued bispectrum of loading. Finally, the results obtained for different definitions of this bispectrum highlight the fact that it cannot be simplified on the basis that the turbulence intensity is small when the loading is inertial, contrary to what is usually done in a wind engineering context where the loading is quasi-static.

**In Part 2**, the second order responses of a multi-degree-of-freedom system are examined. Besides, the loading of the waves is supposed to be linear but to include fluid-structure interaction forces. These effects are hence transcribed in the equations of motion by frequency-dependent stiffness, damping and mass matrices.

Due to these specific features, the equations of motion cannot be decoupled in a satisfactory way, unless additional conditions as regards to the frequency sensitivity of the matrices are met. Two decoupling strategies are thus proposed in Chapter 4. They are respectively expected to work well provided that the frequency dependency of the matrices result in a negligibly or a slightly coupled set of modal state responses.

Their two-by-two power spectral densities are consequently made independent of one another in both scenarios. In the latter, their expression are however more involved, mathematically speaking. This is because of two reasons. First, the diagonal elements of the modal state matrices, which enter into the definition of the frequency response functions, are no longer constant. Second, in order to partially account for the modal coupling, the leading order term, which depends on only two frequency response functions, has to be complemented by a first order correction, which depends on all combinations of three frequency response functions. But, apart from occasionally replacing the diagonal elements of the modal state matrices with constant values, the main contributions to the modal state variances and covariances of the modal state responses are derived in a similar fashion, regardless of whether they are related to the first, in Chapter 5, or the second, in Chapter 6, decoupling strategy.

The resonant components are expressed by using the new local approximation technique introduced in Chapter 2. As a result, the resonant components require to project the spectral densities of the forces at the natural frequencies of the structure only. The loading components, in turn, are uniformly determined by approximating the two, or three, frequency response functions found in the structural kernels by monomials. As a consequence, the loading components do not involve any modal projection of the loading spectra. At last, the expressions given in Chapter 5 and Chapter 6 are respectively validated by being applied on a minimalistic example and by being reduced to the formulas derived under more restrictive assumptions in [12, 13, 11].

Overall, the spectral densities and the second moments of the modal and the nodal responses obtained after each step, first with the decoupled approximations and second with the suggested decompositions, are eventually computed to verify these developments on two realistic floating bridges. As it is to be expected, the first decoupling strategy is however less precise than the second whose use is therefore recommended. Except for the solution of an iterative eigenvalue problem, it does not cost much more to be implemented if the correction terms do not provide a significant improvement of the accuracy and are thus discarded. In this event, the statistics are shown to be computed 20 to 30 times faster than through the numerical integration of the corresponding spectra in both scenarios.

The limitations of the expressions proposed in this thesis are naturally related to the conditions that need to be fulfilled in order to allow for a successful application of the Multiple Timescale Spectral Analysis. They are listed in the beginning of each chapter with such a derivation, in Section 2.2, 3.3, 5.2 and 6.2. In essence, they ensure that (i) the loading spectra evolve slowly at the peaks of the structural kernels, the so-called resonant peaks, and (ii) the frequencies at which these resonant peaks occur are significantly different from those associated with the peaks of the loading spectra.



Nevertheless, the transgression of the second condition is shown to produce larger discrepancies, of course, but these errors are mitigated by the introduction of a new multiplicative factor in the expressions of the loading components, which consequently decrease the closer (a) the peak frequencies of the structure and the loading, and (b) the values of the loading spectra at these peak frequencies. If the loading spectrum is completely flat, indeed, the sole non-zero component is in effect the resonant one. In a perturbation perspective, this multiplicative factor seems to act as if the limit cases of the background and the inertial components were matched.

### Future Perspectives, see White Boxes in Figure C

This feature is implemented for the second-order statistics but not for the third-order statistics yet, since their loading components are not expressed by means of a unified function. Similarly, none of their components have been expressed for the response of a system with frequency dependent parameters, and/or with multiple degrees of freedom. This could be the subject of future developments. Meanwhile, the response of a single-degree-of-freedom system can actually be formulated in state space as well and is thus expressed in the exact same way as the responses of a multi-degree-of-freedom system. The components derived for the second order statistics in the second part of this thesis can therefore be applied without modification to compute the variance of such an oscillator whose parameters might as well depend on the frequency.

In parallel, there is also a whole other branch of the literature which concerns the structural nonlinearities and which is still in the same status as before. For the moment, the background resonant decomposition of the second, third and fourth statistical moments of an oscillator’s response to a buffeting wind loading with a structural velocity feedback has already been studied. Regarding the inertial components, they have been derived for the variance of the response in a similar context, except that the oscillator is subjected to a wave loading. The inertial components of higher order statistics, the frequency dependent nature of the parameters and the correlations between multiple degrees-of-freedom could hence be explored in the future as well.

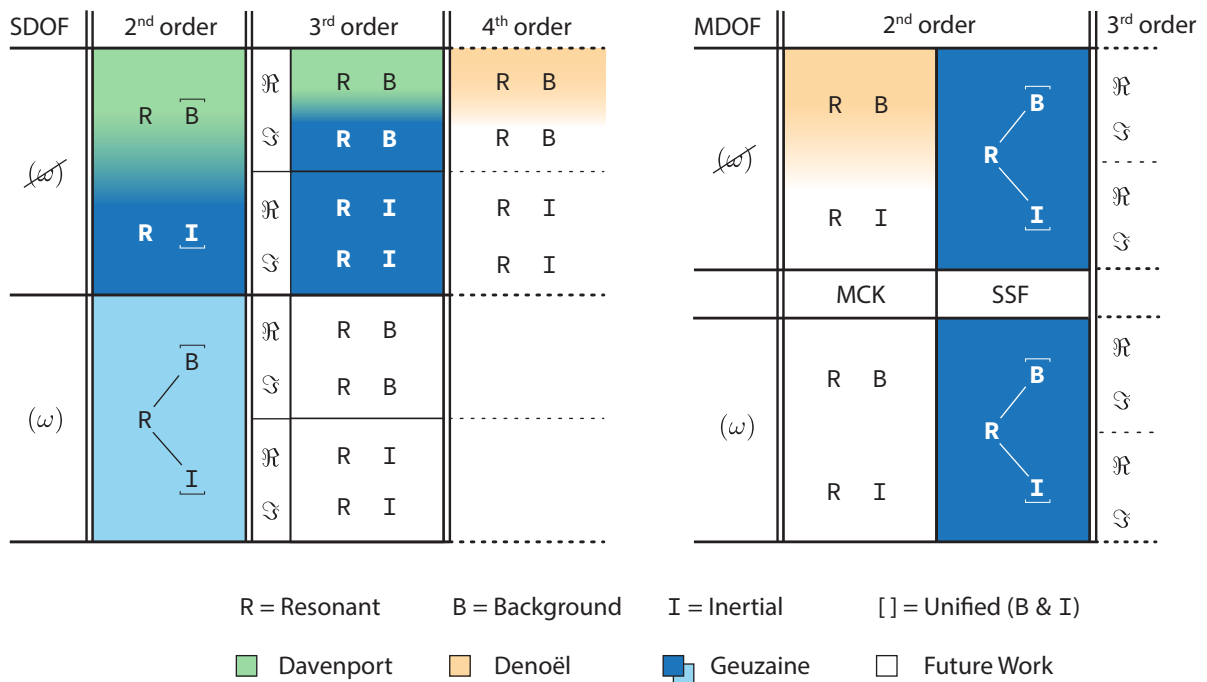


Figure C







# APPENDICES



# Appendix A

## Simple Expression of the Loading Spectra

In this thesis, the loading processes are deemed to be zero-mean, stationary over a given time interval and Gaussian. Under such conditions, they are completely described, in a probabilistic sense, by the matrix  $\mathbf{S}_f(\omega)$  which gathers the cross-spectral densities of all  $i$ -th and  $j$ -th nodal forces,  $S_{f,ij}(\omega)$ . In brief, they are typically obtained by using a wave elevation spectrum whose unified expression reads

$$S_w(\omega) = \left( \frac{\omega_p^5}{\omega^5} \right) \exp \left( -\frac{5}{4} \frac{\omega_p^4}{\omega^4} \right) \quad (7.5)$$

and whose maximum is reached at  $\omega_p$  in the positive frequency range [61]. This equation is then commonly multiplied by some filters, which include for instance the influence of directional spreading effects, spatial correlations, and wave elevation-to-force amplitude operators.

However, these frequency-dependent effects can first be discarded to get a simple expression for the spectral densities of the forces which aims at illustrating the mathematical developments presented in Chapter 5. As a result, the spectral densities of the forces read

$$\mathbf{S}_f(\omega) = \mathbf{F}_a |S_w(\omega)| + i\mathbf{F}_s S_w(\omega)$$

where the coefficients in the matrices  $\mathbf{F}_a$  and  $\mathbf{F}_s$  are chosen as constant, real and such that  $\mathbf{F}_a = \mathbf{F}_a^T$  and  $\mathbf{F}_s = -\mathbf{F}_s^T$  in order to ensure that they verify the following properties

$$\begin{cases} \Re [S_{f,mn}(\omega)] = +\Re [S_{f,mn}(-\omega)] \\ \Im [S_{f,mn}(\omega)] = -\Im [S_{f,mn}(-\omega)] \end{cases} \quad \text{and} \quad S_{f,mn}(\omega) = S_{f,mn}^*(\omega) \quad (7.6)$$

according to [105]. In particular, the auto-spectral densities are real and positive over the whole range of circular frequencies, as it is expected for any real loading process.

After projection into the modal basis, it thus yields

$$\mathbf{S}_{p_0}(\omega) = \mathbf{P}_a |S_w(\omega)| + i\mathbf{P}_s S_w(\omega) \quad (7.7)$$

where

$$\mathbf{P}_a = \mathbf{\Theta}_0^T \mathbf{F}_a \mathbf{\Theta}_0^* \quad \text{and} \quad \mathbf{P}_s = \mathbf{\Theta}_0^T \mathbf{F}_s \mathbf{\Theta}_0^* \quad (7.8)$$

are now filled with complex entries, such that  $\mathbf{P}_a = \mathbf{P}_a^\dagger$  and  $\mathbf{P}_s = -\mathbf{P}_s^\dagger$ . It implies that the symmetry properties listed hereabove do not stand for the generalized cross-spectral densities because their real and imaginary parts respectively read

$$\begin{cases} \Re [\mathbf{S}_{p_0}(\omega)] = \Re [\mathbf{P}_a] |S_w(\omega)| - \Im [\mathbf{P}_s] S_w(\omega) \\ \Im [\mathbf{S}_{p_0}(\omega)] = \Im [\mathbf{P}_a] |S_w(\omega)| + \Re [\mathbf{P}_s] S_w(\omega) \end{cases} \quad (7.9)$$

and are given by the sum of symmetric and anti-symmetric functions of the circular frequencies.





# Nomenclature

$i$	= imaginary unit
$t$	= dimensional time variable
$\omega$	= dimensional circular frequency
$\tau$	= dimensionless time variable
$\Omega$	= dimensionless circular frequency
$\eta$	= dimensional stretched coordinate
$\Upsilon$	= dimensionless stretched coordinate
$\varepsilon$	= arbitrary small number
$\omega_0$	= natural frequency of the oscillator in Part 1
$\omega_0$	= predominant frequency of the response in Part 2
$\omega_p$	= maximum of the wave elevation spectrum in the positive frequency range
$k$	= stiffness of the oscillator
$c$	= viscosity of the oscillator
$m$	= effective mass of the oscillator
$m_s$	= mass of the oscillator itself
$m_a$	= added mass of the moving fluid
$k_m$	= inertia force coefficient
$k_d$	= drag force coefficient
$u_c$	= constant current speed
$h_s$	= significant wave height
$t_r$	= time duration of reference
$u_r$	= water velocity of reference
$x_r$	= structural response of reference
$\lambda_u$	= turbulence intensity
$\xi_s$	= structural damping ratio
$\xi_a$	= added damping ratio

---

$\kappa_u$	= loading ratio
$\alpha_v$	= frequency ratio
$\omega_{(.)}$	= peak frequency of the (.) process, see below
$S_{(.)}(\dots)$	= power spectral density of the (.) process, see below
$B_{(.)}(\dots, \dots)$	= bispectrum of the (.) process, see below
$\sigma_{(.)}^2$	= second central moment of the (.) process, see below
$\beta_{(.)}$	= third central moment of the (.) process, see below
$\gamma_{(.)}$	= skewness coefficient of the (.) process, see below
$h(t)$	= water wave elevation
$u(t)$	= water velocity fluctuation
$f_m(t)$	= inertia wave force
$f_d(t)$	= drag wave force
$f(t)$	= Morison wave force
$x(t)$	= displacement of the oscillator
$\dot{x}(t)$	= velocity of the oscillator
$\ddot{x}(t)$	= acceleration of the oscillator
$v(\tau)$	= nondimensional water velocity fluctuation
$\varphi_d(\tau)$	= alternative nondimensional drag force
$\varphi_f(\tau)$	= simplified nondimensional drag force
$\varphi_p(\tau)$	= polynomialized nondimensional drag force
$\chi(\tau)$	= nondimensional response of the oscillator
$\chi'(\tau)$	= nondimensional velocity of the oscillator
$\chi''(\tau)$	= nondimensional acceleration of the oscillator
$\sigma_{\varrho}^2$	= resonant component of $\sigma_{\chi}^2$
$\sigma_{\zeta}^2$	= inertial component of $\sigma_{\chi}^2$ if $\alpha_v > 1$
$\sigma_{\xi}^2$	= background component of $\sigma_{\chi}^2$ if $\alpha_v < 1$

---

$S_\rho(\Omega)$	= resonant component of $S_\chi(\Omega)$
$S_\zeta(\Omega)$	= inertial component of $S_\chi(\Omega)$ if $\alpha_v > 1$
$S_\varsigma(\Omega)$	= background component of $S_\chi(\Omega)$ if $\alpha_v < 1$
$\sigma_r^2$	= resonant component of $\sigma_x^2$
$\sigma_i^2$	= inertial component of $\sigma_x^2$
$\sigma_b^2$	= background component of $\sigma_x^2$
$S_r(\omega)$	= resonant component of $S_x(\omega)$
$S_i(\omega)$	= inertial component of $S_x(\omega)$
$S_b(\omega)$	= background component of $S_x(\omega)$
$H_{(\cdot)}(\dots)$	= frequency response function
$G_s(\Omega)$	= structural kernel at second order
$G_b(\Omega_{1,2})$	= structural kernel at third order
$p_1$	= first degree coefficient of the polynomialization
$p_2$	= second degree coefficient of the polynomialization
$P_0$	= zeroth degree coefficient of the Padé approximant
$P_2$	= second degree coefficient of the Padé approximant
$\sigma_{\iint_\varphi}^2$	= approximate spectral moment of $\varphi(\tau)$
$\sigma_{\iint_f}^2$	= approximate spectral moment of $f(t)$
$C_\varphi$	= dimensionless structural kernel coefficient
$C_f$	= dimensional structural kernel coefficient
$\beta_{bbb}$	= tri-background component of $\Re \times \Re \Im \times \Im - \beta_\chi$
$\beta_{\Re[brr]}$	= background bi-resonant component of $\Re \times \Re - \beta_\chi$
$\beta_{\Im[brr]}$	= background bi-resonant component of $\Im \times \Im - \beta_\chi$
$\beta_{rr}$	= global bi-resonant component of $\Re \times \Re \Im \times \Im - \beta_\chi$
$\beta_{\Re[rii]}$	= resonant bi-inertial component of $\Re \times \Re - \beta_\chi$

---

$\beta_{\mathfrak{S}[rii]}$	= resonant bi-inertial component of $\mathfrak{S} \times \mathfrak{S} - \beta_{\chi}$
$\mathbf{K}_s$	= static stiffness matrix
$\mathbf{C}_s$	= static damping matrix
$\mathbf{M}_s$	= static mass matrix
$\mathbf{K}_h(\omega)$	= hydrodynamic stiffness matrix
$\mathbf{C}_h(\omega)$	= hydrodynamic damping matrix
$\mathbf{M}_h(\omega)$	= hydrodynamic mass matrix
$\mathbf{K}(\omega)$	= hydroelastic stiffness matrix
$\mathbf{C}(\omega)$	= hydroelastic damping matrix
$\mathbf{M}(\omega)$	= hydroelastic mass matrix
$\mathbf{K}_0$	= hydroelastic stiffness matrix at $\omega_0$
$\mathbf{C}_0$	= hydroelastic damping matrix at $\omega_0$
$\mathbf{M}_0$	= hydroelastic mass matrix at $\omega_0$
$\mathbf{A}(\omega)$	= first state matrix
$\mathbf{B}(\omega)$	= second state matrix
$\mathbf{A}_0$	= first state matrix at $\omega_0$
$\mathbf{B}_0$	= second state matrix at $\omega_0$
$\Theta_0$	= matrix of eigenmodes (EVP-0)
$\Phi_0$	= top part of the eigenmodes (EVP-0)
$\Lambda_0$	= matrix of eigenfrequencies (EVP-0)
$\mathbf{D}$	= normalization constants (EVP-0)
$\mathbf{H}(\omega)$	= matrix of frequency response functions (EVP-0)
$\Theta$	= matrix of eigenmodes (EVP- $\Omega$ )

---

$\Phi$	= top part of the eigenmodes (EVP- $\Omega$ )
$\Lambda$	= matrix of eigenfrequencies (EVP- $\Omega$ )
$\mathcal{D}$	= normalization constants (EVP- $\Omega$ )
$\mathcal{A}(\omega)$	= first generalized state matrix
$\mathcal{B}(\omega)$	= second generalized state matrix
$\mathcal{J}(\omega)$	= dynamical flexibility matrix
$\mathcal{H}(\omega)$	= matrix of frequency response functions
$\mathcal{J}_o(\omega)$	= off-diagonal dynamical flexibility matrix
$\mathcal{J}_d(\omega)$	= diagonal dynamical flexibility matrix
$\mathcal{H}_d(\omega)$	= diagonal frequency response matrix
$\mathbf{S}_{(.)}(\omega)$	= power spectral density matrix of $(.)$ , see below
$\Sigma_{(.)}$	= variance and covariance matrix of $(.)$ , see below
$\mathbf{f}(\omega)$	= nodal forces
$\mathbf{g}(\omega)$	= nodal state forces
$\mathbf{p}_*(\omega)$	= modal state forces
$\mathbf{x}_*(\omega)$	= nodal responses
$\dot{\mathbf{x}}_*(\omega)$	= nodal response derivatives
$\mathbf{y}_*(\omega)$	= nodal state responses
$\mathbf{q}_*(\omega)$	= modal state responses
$\star \rightarrow \emptyset$	= reference results
$\star \rightarrow 0$	= approximation in $(\omega)$ scenario
$\star \rightarrow 1$	= leading order approximation
$\star \rightarrow 2$	= first order approximation
$\Delta \mathbf{S}_{q_1}(\omega)$	= corrective terms of the power spectral densities
$\Delta \Sigma_{q_1}(\omega)$	= corrective terms of the second central moments

---

$S_w(\omega)$	= wave elevation spectrum, see Appendix A
$F_{a,mn}$	= constant antimetric coefficient, see Appendix A
$F_{s,mn}$	= constant symmetric coefficient, see Appendix A
$P_{a,mn}$	= generalized antimetric coefficient, see Appendix A
$P_{s,mn}$	= generalized symmetric coefficient, see Appendix A
$m$	= index for the modal basis matrices and vectors
$n$	= index for the modal basis matrices and vectors
$k$	= index for the modal basis matrices and vectors
$i$	= index for the nodal basis matrices and vectors
$j$	= index for the nodal basis matrices and vectors
$M$	= number of modal responses
$N$	= number of nodal responses
$\lambda_m$	= $m$ -th eigenfrequency
$\psi_m$	= real part of $\lambda_m$
$v_m$	= imaginary part of $\lambda_m$
$\alpha_m$	= $m$ -th frequency ratio
$\omega_{j_m}$	= $j_m$ -th natural frequency
$\xi_{j_m}$	= $j_m$ -th damping ratio
$G_{mn}(\omega)$	= structural kernel in $(\omega)$ scenario
$G_{d,mn}(\omega)$	= leading order structural kernel
$G_{d,mnk}(\omega)$	= first order structural kernel
$S_{r_0,mn}(\omega)$	= resonant component of the power spectral density
$S_{\ell_0,mn}(\omega)$	= loading component of the power spectral density
$\Sigma_{r_0,mn}$	= resonant component of the second central moment
$\Sigma_{\ell_0,mn}$	= loading component of the second central moment

---

$L_{mn}$	= multiplicative factor
$\beta_{mn}^{(l)}$	= asymptotic slope of the structural kernel
$\beta_m, \beta_n$	= asymptotic slope of the transfer functions
$\Sigma_{p_0, mn}^{(l)(\pm)}$	= spectral moment of order $\beta_{mn}^{(l)}$
$\mathcal{G}_{mn}^{(l)}(\omega)$	= structural kernel approximation
$\mathcal{S}_{p_0, mn}^{(l)}(\omega)$	= loading spectrum approximation
$\mathcal{L}_{mn}$	= multiplicative factor
$\beta_{mnk}^{(l)}$	= asymptotic slope of the structural kernel
$\beta_m, \beta_n, \beta_k$	= asymptotic slope of the transfer functions
$\mathcal{G}_{mnk}^{(l)}(\omega)$	= structural kernel approximation
$\mathcal{S}_{p, mnk}^{(l)}(\omega)$	= loading spectrum approximation
$\Sigma_{p, mnk}^{(l)(\pm)}$	= spectral moment of order $\beta_{mnk}^{(l)}$
$\rho_{q_0, mn}$	= correlation coefficient of the modal state responses
$\rho_{r_0, mn}$	= resonant component of the correlation coefficient
$\rho_{\ell_0, mn}$	= loading component of the correlation coefficient
$\gamma_{r_0}$	= resonant weighting factor
$\gamma_{\ell_0}$	= loading weighting factor
$r_{0, m}$	= resonant-to-loading ratio
$\varpi_{mn}$	= resonant interaction indicator
$\zeta_{mn}$	= distance between $\omega_{j_m}$ and $\omega_{j_n}$
$\Gamma_{mn}$	= coherence function
$S_{mn}$	= spectral ratio





# Bibliography

- [1] C. M. Wang and B. T. Wang. *Large Floating Structures*. Springer, 2015.
- [2] J. Ding, Y. Wu, Z. Xie, W. Yang, S. Wang, J. Yu, and T. Yu, “Overview: Research on hydroelastic responses of VLFS in complex environments,” *Marine Structures*, vol.78, no. March, p.102978, 2021.
- [3] T. Moan and M. E. Eidem, “Floating bridges and submerged tunnels in Norway - the history and future outlook,” in *WCFS2019*, pp.81–111, Springer, 2020.
- [4] F. Brancaleoni. *The Messina Strait Bridge: A challenge and a dream*. CRC Press, 2009.
- [5] E. Watanabe, “Floating bridges: past and present,” *Structural engineering international*, vol.13, no.2, pp.128–132, 2003.
- [6] F. Perotti, F. Foti, L. Martinelli, and M. Tomasin, “Sfts under dynamic loads: new design issues and numerical simulation,” in *Maintenance, Safety, Risk, Management and Life-Cycle Performance of Bridges*, pp.885–892, CRC Press, 2018.
- [7] D. G. Quirk, J. R. Underhill, J. G. Gluyas, H. A. Wilson, M. J. Howe, and S. Anderson, “The north sea through the energy transition,” *First Break*, vol.39, no.4, pp.31–43, 2021.
- [8] E. Watanabe, T. Utsunomiya, and C. M. Wang, “Hydroelastic analysis of pontoon-type VLFS: A literature survey,” *Engineering Structures*, vol.26, no.2, pp.245–256, 2004.
- [9] E. Watanabe, C. M. Wang, T. Utsunomiya, and T. Moan, “Very large floating structures: applications, analysis and design,” *Core report of centre for offshore research and engineering national university of Singapore*, no.2, pp.1–30, 2004.
- [10] V. Denoël, “Multiple timescale spectral analysis of a linear fractional viscoelastic system under colored excitation,” *Probabilistic Engineering Mechanics*, vol.53, no. May, pp.66–74, 2018.
- [11] V. Denoël, “Multiple timescale spectral analysis,” *Probabilistic Engineering Mechanics*, vol.39, pp.69–86, 2015.
- [12] V. Denoël, “On the background and biresonant components of the random response of single degree-of-freedom systems under non-Gaussian random loading,” *Engineering Structures*, vol.33, no.8, pp.2271–2283, 2011.
- [13] V. Denoël, “Estimation of modal correlation coefficients from background and resonant responses,” *Structural Engineering and Mechanics*, vol.32, no.6, pp.725–740, 2009.
- [14] A. G. Davenport, “The spectrum of horizontal gustiness near the ground in high winds,” *Quarterly Journal of the Royal Meteorological Society*, vol.87, no.372, pp.194–211, 1961.
- [15] Y. Xu, O. Øiseth, and T. Moan, “Time domain simulations of wind-and wave-induced load effects on a three-span suspension bridge with two floating pylons,” *Marine Structures*, vol.58, pp.434–452, 2018.
- [16] X. Chen and A. Kareem, “Nonlinear response analysis of long-span bridges under turbulent winds,” *Journal of Wind Engineering and Industrial Aerodynamics*, vol.89, no.14-15, pp.1335–1350, 2001.

- [17] V. Denoël and H. Degée, “Influence of the non-linearity of the aerodynamic coefficients on the skewness of the buffeting drag force,” *Wind and Structures*, vol.9, no.6, pp.457–471, 2006.
- [18] J. Morison, J. Johnson, and S. Schaaf, “The force exerted by surface waves on piles,” *Journal of Petroleum Technology*, vol.2, no.05, pp.149–154, 1950.
- [19] E. de Sá Caetano. *Cable vibrations in cable-stayed bridges*, vol.9. IABSE, 2007.
- [20] I. Langen and R. Sigbjörnsson, “On stochastic dynamics of floating bridges,” *Engineering Structures*, vol.2, no.4, pp.209–216, 1980.
- [21] C. Jin, M. Kim, W. C. Chung, and D.-S. Kwon, “Time-domain coupled analysis of curved floating bridge under wind and wave excitations,” *Ocean Systems Engineering*, vol.10, no.4, pp.399–414, 2020.
- [22] J. Wang, E. Cheynet, J. Þ. Snæbjörnsson, and J. B. Jakobsen, “Coupled aerodynamic and hydrodynamic response of a long span bridge suspended from floating towers,” *Journal of Wind Engineering and Industrial Aerodynamics*, vol.177, pp.19–31, 2018.
- [23] S. M. Han and H. Benaroya. *Nonlinear and stochastic dynamics of compliant offshore structures*, vol.98. Springer Science & Business Media, 2002.
- [24] M. Shinozuka, “Stochastic fields and their digital simulation,” in *Stochastic methods in structural dynamics*, pp.93–133, Springer, 1987.
- [25] E. Marino, C. Borri, and U. Peil, “A fully nonlinear wave model to account for breaking wave impact loads on offshore wind turbines,” *Journal of Wind Engineering and Industrial Aerodynamics*, vol.99, no.4, pp.483–490, 2011.
- [26] M. D. Shields and H. Kim, “Simulation of higher-order stochastic processes by spectral representation,” *Probabilistic Engineering Mechanics*, vol.47, pp.1–15, 2017.
- [27] R. Adrezin, P. Bar-Avi, and H. Benaroya, “Dynamic response of compliant offshore structures,” *Journal of aerospace engineering*, vol.9, no.4, pp.114–131, 1996.
- [28] A. Naess and J. Johnsen, “Response statistics of nonlinear, compliant offshore structures by the path integral solution method,” *Probabilistic Engineering Mechanics*, vol.8, no.2, pp.91–106, 1993.
- [29] A. Larsen. *Aerodynamics of large bridges*. Routledge, 2017.
- [30] K. Aas-Jakobsen and E. Strømmen, “Time domain buffeting response calculations of slender structures,” *Journal of Wind Engineering and Industrial Aerodynamics*, vol.89, no.5, pp.341–364, 2001.
- [31] S. Quek, X. Li, and C. Koh, “Stochastic response of jack-up platform by the method of statistical quadratization,” *Applied ocean research*, vol.16, no.2, pp.113–122, 1994.
- [32] A. Naess and S. C. Yim, “Stochastic response of offshore structures excited by drag forces,” *Journal of engineering mechanics*, vol.122, no.5, pp.442–448, 1996.
- [33] M. Schetzen, “The volterra and wiener theories of nonlinear systems,” 1980.
- [34] A. Kareem and J. Zhao, “Analysis of non-gaussian surge response of tension leg platforms under wind loads,” 1994.

- [35] C. E. Larsen and L. D. Lutes, "Predicting the fatigue life of offshore structures by the single-moment spectral method," in *Stochastic Structural Dynamics 2*, pp.91–120, Springer, 1991.
- [36] V. Denoël and L. Carassale, "Response of an oscillator to a random quadratic velocity-feedback loading," *Journal of Wind Engineering and Industrial Aerodynamics*, vol.147, pp.330–344, 2015.
- [37] A. Naess and T. Moan. *Stochastic dynamics of marine structures*. Cambridge University Press, 2013.
- [38] X. Pitoiset and A. Preumont, "Spectral methods for multiaxial random fatigue analysis of metallic structures," *International Journal of Fatigue*, vol.22, no.7, pp.541–550, 2000.
- [39] N. D. P. Barltrop and A. J. Adams. *Dynamics of fixed marine structures*, vol.91. Butterworth-Heinemann, 2013.
- [40] M. Palmieri, F. Cianetti, G. Zucca, G. Morettini, and C. Braccesi, "Spectral analysis of sine-sweep vibration: A fatigue damage estimation method," *Mechanical Systems and Signal Processing*, vol.157, p.107698, 2021.
- [41] M. Borg, L. Manuel, M. Collu, and J. Liu, "Long-term global performance analysis of a vertical-axis wind turbine supported on a semi-submersible floating platform," in *International Conference on Offshore Mechanics and Arctic Engineering*, vol.56574, p.V009T09A066, American Society of Mechanical Engineers, 2015.
- [42] F. I. G. Giske, K. A. Kvåle, B. J. Leira, and O. Øiseth, "Long-term extreme response analysis of a long-span pontoon bridge," *Marine Structures*, vol.58, no.December 2017, pp.154–171, 2018.
- [43] F.-I. G. Giske, B. J. Leira, and O. Øiseth, "Long-term extreme response analysis of marine structures using inverse SORM," *Journal of Offshore Mechanics and Arctic Engineering*, vol.140, no.5, 2018.
- [44] F.-I. G. Giske, B. J. Leira, and O. Øiseth, "Full long-term extreme response analysis of marine structures using inverse FORM," *Probabilistic Engineering Mechanics*, vol.50, pp.1– 8, 2017.
- [45] Y. Xu, A. Fenerci, O. Øiseth, and T. Moan, "Efficient prediction of wind and wave induced long-term extreme load effects of floating suspension bridges using artificial neural networks and support vector machines," *Ocean Engineering*, vol.217, p.107888, 2020.
- [46] T. M. Lystad, A. Fenerci, and O. Øiseth, "Long-term extreme buffeting response of cable-supported bridges with uncertain turbulence parameters," *Engineering Structures*, vol.236, p.112126, 2021.
- [47] O. Gramstad, C. Agrell, E. Bitner-Gregersen, B. Guo, E. Ruth, and E. Vanem, "Sequential sampling method using Gaussian process regression for estimating extreme structural response," *Marine Structures*, vol.72, p.102780, 2020.
- [48] F.-I. G. Giske, B. J. Leira, and O. Øiseth, "Efficient computation of cross-spectral densities in the stochastic modelling of waves and wave loads," *Applied Ocean Research*, vol.62, pp.70–88, 2017.
- [49] M. Gu and X. yi Zhou, "An approximation method for resonant response with coupling modes of structures under wind action," *Journal of Wind Engineering and Industrial Aerodynamics*, vol.97, no.11-12, pp.573–580, 2009.

- [50] E. Hinch. *Perturbation Methods*. Cambridge: Cambridge University Press, 1995.
- [51] M. Geuzaine, A. Fenerci, O. Øiseth, and V. Denoël, “Importance of the inertial components in modal state covariances,” *Proceedings of the forty-first International Conference on Ocean, Offshore and Arctic Engineering (OMAE 2022)*, 2022.
- [52] A. Fenerci, M. Geuzaine, V. Denoël, and O. Øiseth, “Efficient long-term extreme response analysis of floating bridges using multiple timescale spectral analysis,” *Proceedings of the forty-first International Conference on Ocean, Offshore and Arctic Engineering (OMAE 2022)*, 2022.
- [53] M. Geuzaine and V. Denoël, “Efficient estimation of the skewness of the response of a wave-excited oscillator,” *Proceedings of the eleventh International Conference on Structural Dynamics (EURODYN 2020)*, pp.3467–3480, 2020.
- [54] M. Geuzaine, M. Esposito Marzino, and V. Denoël, “Efficient estimation of the skewness of the response of a linear oscillator under a non-gaussian loading,” *Proceedings of the Engineering Mechanics Institute Conference and Probabilistic Mechanics & Reliability Conference, New York, United States*, 2020.
- [55] M. Geuzaine and V. Denoël, “A framework for the efficient spectral analysis of large wind- and wave-loaded structures,” *Proceedings of the fifteenth International Conference on Wind Engineering, Beijing, China*, 2019.
- [56] M. Geuzaine and V. Denoël, “Estimation of modal correlation coefficients in wind buffeting spectral analysis,” *Proceedings of the second Romanian National Conference on Wind Engineering, Bucharest, Romania*, 2019.
- [57] M. Geuzaine, J.-P. Jaspard, J.-F. Demonceau, and V. Denoël, “Influence of a small flexibility of connections on the elastic structural response of frames,” *Journal of Structural Engineering*, vol.148, no.5, p.04022033, 2022.
- [58] M. Geuzaine, F. Foti, and V. Denoël, “Minimal requirements for the vibration-based identification of the axial force, the bending stiffness and the flexural boundary conditions in cables,” *Journal of Sound and Vibration*, vol.511, p.116326, 2021.
- [59] F. Foti, M. Geuzaine, and V. Denoël, “On the identification of the axial force and bending stiffness of stay cables anchored to flexible supports,” *Applied Mathematical Modelling*, vol.92, pp.798–828, 2021.
- [60] S. Felder, M. Geuzaine, B. Dewals, and S. Erpicum, “Nappe flows on a stepped chute with prototype-scale steps height: Observations of flow patterns, air-water flow properties, energy dissipation and dissolved oxygen,” *Journal of Hydro-Environment Research*, vol.27, pp.1–19, 2019.
- [61] S. K. Chakrabarti. *Hydrodynamics of offshore structures*. WIT press, 1987.
- [62] L. Carassale and A. Kareem, “Modeling nonlinear systems by volterra series,” *Journal of engineering mechanics*, vol.136, no.6, pp.801–818, 2010.
- [63] G. Najafian, “Probability models for offshore structural response due to morison wave loading: Part 1: Drag-only response,” *Ocean engineering*, vol.34, no.17-18, pp.2277–2288, 2007.
- [64] G. Najafian, “Probability models for offshore structural response due to morison wave loading: Part 2: Inertia-only and total responses,” *Ocean engineering*, vol.34, no.17-18, pp.2289–2299, 2007.

- [65] G. H. Keulegan, L. H. Carpenter, *et al.*, “Forces on cylinders and plates in an oscillating fluid,” *Journal of research of the National Bureau of Standards*, vol.60, no.5, pp.423–440, 1958.
- [66] J. Penzien. *Structural dynamics of fixed offshore structures*. Norwegian Institute of Technology, 1976.
- [67] D. R. Brillinger, “An introduction to polyspectra,” *The Annals of mathematical statistics*, pp.1351–1374, 1965.
- [68] D.-h. Tsaur and Y.-H. Chen, “Bispectrum and Trispectrum of Wave Current Force on Offshore Structure,” *Proceedings of the 14th Conference on Ocean Engineering in Republic of China*, pp.444–469, 1992.
- [69] A. Kareem, J. Zhao, and M. A. Tognarelli, “Surge response statistics of tension leg platforms under wind and wave loads: a statistical quadratization approach,” *Probabilistic Engineering Mechanics*, vol.10, no.4, pp.225–240, 1995.
- [70] J. M. Nichols, C. C. Olson, J. V. Michalowicz, and F. Bucholtz, “The bispectrum and bicoherence for quadratically nonlinear systems subject to non-gaussian inputs,” *IEEE Transactions on signal processing*, vol.57, no.10, pp.3879–3890, 2009.
- [71] H. Kikuchi, Y. Tamura, H. Ueda, and K. Hibi, “Dynamic wind pressures acting on a tall building model: proper orthogonal decomposition,” *Journal of Wind Engineering and Industrial Aerodynamics*, vol.69, pp.631–646, 1997.
- [72] M. Esposito Marzino *et al.*, “Bispectrum and bicoherence: a higher order stochastic approach to non-gaussian dynamic wind loading,” 2019.
- [73] M. Geuzaine, M. Esposito Marzino, and V. Denoël, “Efficient estimation of the skewness of the response of a linear oscillator under non-gaussian loading,” 2020.
- [74] G. Dong, H. Chen, and Y. Ma, “Parameterization of nonlinear shallow water waves over sloping bottoms,” *Coastal engineering*, vol.94, pp.23–32, 2014.
- [75] A. Masuda and Y.-Y. Kuo, “A note on the imaginary part of bispectra,” *Deep Sea Research Part A. Oceanographic Research Papers*, vol.28, no.3, pp.213–222, 1981.
- [76] S. Elgar and R. Guza, “Observations of bispectra of shoaling surface gravity waves,” *Journal of Fluid Mechanics*, vol.161, pp.425–448, 1985.
- [77] K. Hasselmann, W. Munk, and G. MacDonald, “Bispectra of ocean waves,” in *Symposium on Time Series Analysis*, pp.125–139, New York, 1963.
- [78] The Mathworks, Inc., Natick, Massachusetts, *MATLAB version 9.3.0.713579 (R2017b)*, 2017.
- [79] A. Haldar. *Recent developments in reliability-based civil engineering*. World Scientific, 2006.
- [80] O. C. Zienkiewicz, R. L. Taylor, P. Nithiarasu, and J. Z. Zhu. *The finite element method*, vol.3. McGraw-hill London, 1977.
- [81] Y. Bai. *Marine structural design*. Elsevier, 2003.
- [82] O. M. Faltinsen, “Sea Loads on Ships and Offshore Structures,” 1990.
- [83] K. A. Kvåle, R. Sigbjörnsson, and O. Øiseth, “Modelling the stochastic dynamic behaviour of a pontoon bridge: A case study,” *Computers and Structures*, vol.165, pp.123–135, 2016.

- [84] F.-I. G. Giske, B. J. Leira, and O. Øiseth, “Stochastic Modelling of Wave Loads on Floating Bridges : Efficient Calculation of Cross-Spectral Densities,” *19th Congress of IABSE, Challenges in Design and Construction of an Innovative and Sustainable Built Environment*, no. September, pp.48–56, 2016.
- [85] S. R. Winterstein, “Nonlinear vibration models for extremes and fatigue,” *Journal of Engineering Mechanics*, vol.114, no.10, pp.1772–1790, 1988.
- [86] A. G. Davenport, “Note on the distribution of the largest value of a random function with application to gust loading,” *Proceedings of the Institution of Civil Engineers*, vol.28, no.2, pp.187–196, 1964.
- [87] J. B. Roberts and P. D. Spanos. *Random vibration and statistical linearization*. Courier Corporation, 2003.
- [88] M. Grigoriu. *Stochastic calculus: applications in science and engineering*. Springer, 2002.
- [89] J. Penzien and R. W. Clough, “Dynamics of structures,” *Earthquake Engineering Handbook*, pp.3–1–3–40, 2002.
- [90] J. W. S. B. Rayleigh. *The theory of sound*, vol.2. Macmillan, 1896.
- [91] S. Adhikari, “Damping modelling using generalized proportional damping,” *Journal of Sound and Vibration*, vol.293, no.1-2, pp.156–170, 2006.
- [92] A. Ibrahimbegovic and E. L. Wilson, “Simple numerical algorithms for the mode superposition analysis of linear structural systems with non-proportional damping,” *Computers and Structures*, vol.33, no.2, pp.523–531, 1989.
- [93] P. Lancaster and I. Zaballa, “Diagonalizable quadratic eigenvalue problems,” *Mechanical Systems and Signal Processing*, vol.23, no.4, pp.1134–1144, 2009.
- [94] T. K. Caughey and M. E. O’Kelly, “Classical normal modes in damped linear dynamic systems,” *Journal of Applied Mechanics, Transactions ASME*, vol.32, no.3, pp.583–588, 1965.
- [95] D. L. Cronin, “Approximation for determining harmonically excited response of nonclassically damped systems,” *Journal of Engineering for Industry Transactions of the ASME*, vol.98, no.1, pp.43–47, 1976.
- [96] V. Denoël and H. Degée, “Asymptotic expansion of slightly coupled modal dynamic transfer functions,” *Journal of Sound and Vibration*, vol.328, no.1-2, pp.1–8, 2009.
- [97] T. Canor, N. Blaise, and V. Denoël, “Efficient uncoupled stochastic analysis with non-proportional damping,” *Journal of Sound and Vibration*, vol.331, no.24, pp.5283–5291, 2012.
- [98] F. Tisseur, “Backward error and condition of polynomial eigenvalue problems,” *Linear Algebra and Its Applications*, vol.309, no.1-3, pp.339–361, 2000.
- [99] K. A. Foss, “Co-ordinates which uncouple the equations of motion of a damped linear systems,” *Journal of Applied Mechanics*, vol.25, no. May, pp.361–364, 1967.
- [100] B. N. Parlett and H. C. Chen, “Use of indefinite pencils for computing damped natural modes,” *Linear Algebra and Its Applications*, vol.140, no. C, pp.53–88, 1990.
- [101] R. Taghipour, T. Perez, and T. Moan, “Hybrid frequency-time domain models for dynamic response analysis of marine structures,” *Ocean Engineering*, vol.35, no.7, pp.685–705, 2008.

- [102] A. Kappos. *Dynamic loading and design of structures*. CRC Press, 2001.
- [103] T. Canor, N. Blaise, and V. Denoël, “An asymptotic expansion-based method for a spectral approach in equivalent statistical linearization,” *Probabilistic Engineering Mechanics*, vol.38, pp.1–12, 2014.
- [104] R. A. Horn and C. R. Johnson. *Matrix analysis*. Cambridge university press, 2012.
- [105] R. Sigbjörnsson, “Stochastic theory of wave loading processes,” *Engineering Structures*, vol.1, pp.58–64, 1979.
- [106] D. K. Kwon and A. Kareem, “Peak factors for non-gaussian load effects revisited,” *Journal of Structural Engineering*, vol.137, no.12, pp.1611–1619, 2011.
- [107] Ø. W. Petersen, O. Øiseth, T. S. Nord, and E. Lourens, “Estimation of the full-field dynamic response of a floating bridge using kalman-type filtering algorithms,” *Mechanical Systems and Signal Processing*, vol.107, pp.12–28, 2018.
- [108] A. Fenerci, K. A. Kvåle, X. Xiang, and O. Øiseth, “Hydrodynamic interaction of floating bridge pontoons and its effect on the bridge dynamic responses,” *Marine Structures*, vol.83, p.103174, 2022.
- [109] S. Deng, Y. Xu, H. Ren, S. Fu, S. Li, T. Moan, and Z. Gao, “Numerical simulation of wave-induced hydroelastic response and flow-induced vibration of a twin-tube submerged floating tunnel,” *Marine Structures*, vol.82, no.September 2021, p.103124, 2022.
- [110] V. Denoël, “Multiple timescale spectral analysis of a linear fractional viscoelastic system under colored excitation,” *Probabilistic Engineering Mechanics*, vol.53, no.December 2017, pp.66–74, 2018.
- [111] DNV, “Offshore Standard DNV-RP-H103 -Modelling And Analysis Of Marine Operations,” *Det Norske Veritas*, no.April, p.150, 2011.
- [112] I. P. Mitseas and M. Beer, “Modal decomposition method for response spectrum based analysis of nonlinear and non-classically damped systems,” *Mechanical Systems and Signal Processing*, vol.131, pp.469–485, 2019.
- [113] Z. Cheng, Z. Gao, and T. Moan, “Hydrodynamic load modeling and analysis of a floating bridge in homogeneous wave conditions,” *Marine Structures*, vol.59, no.January, pp.122–141, 2018.
- [114] M. K. Ochi and E. N. Hubble, “Chapter 18 Six-Parameter Wave Spectra,”
- [115] T. J. Agar, “Aerodynamic flutter analysis of suspension bridges by a modal technique,” *Engineering Structures*, vol.11, no.2, pp.75–82, 1989.
- [116] L. Wan, D. Jiang, and J. Dai, “Numerical modelling and dynamic response analysis of curved floating bridges with a small rise-span ratio,” *Journal of Marine Science and Engineering*, vol.8, no.6, 2020.
- [117] W. Yin and A. S. Mehr, “Stochastic analysis of the normalized subband adaptive filter algorithm,” *IEEE Transactions on Circuits and Systems I: Regular Papers*, vol.58, no.5, pp.1020–1033, 2011.
- [118] R. Taghipour, T. Perez, and T. Moan, “Hybrid frequency-time domain models for dynamic response analysis of marine structures,” *Ocean Engineering*, vol.35, no.7, pp.685–705, 2008.

- [119] T. Viuff, X. Xiang, B. Leira, and O. Øiseth, “Code-to-code verification of end-anchored floating bridge global analysis,” *Proceedings of the International Conference on Offshore Mechanics and Arctic Engineering - OMAE*, vol.11A, pp.1–9, 2018.
- [120] C. Chen, P. Duffour, K. Dai, Y. Wang, and P. Fromme, “Identification of aerodynamic damping matrix for operating wind turbines,” *Mechanical Systems and Signal Processing*, vol.154, p.107568, 2021.
- [121] M. Heuberger, “Assessment of the dynamic response of a floating pontoon bridge with a fiber reinforced polymer superstructure,” *Msc Thesis*, 2018.
- [122] E. Mackay, “A unified model for unimodal and bimodal ocean wave spectra,” *International Journal of Marine Energy*, vol.15, no.April 2016, pp.17–40, 2016.
- [123] X. Xiang, T. Viuff, B. Leira, and O. Øiseth, “Impact of hydrodynamic interaction between pontoons on global responses of a long floating bridge under wind waves,” *Proceedings of the International Conference on Offshore Mechanics and Arctic Engineering - OMAE*, vol.7A, pp.1–10, 2018.
- [124] L. S. Silva, B. S. Cazzolato, N. Y. Sergiienko, and B. Ding, “Efficient estimation of the nonlinear aerodynamic loads of floating offshore wind turbines under random waves and wind in frequency domain,” *Journal of Ocean Engineering and Marine Energy*, vol.7, no.3, pp.287–303, 2021.
- [125] J. Heremans, A. Mayou, and V. Denoël, “Background/Resonant decomposition of the stochastic torsional flutter response of an aeroelastic oscillator under buffeting loads,” *Journal of Wind Engineering and Industrial Aerodynamics*, vol.208, no.July, 2021.
- [126] M. J. Patil, “Decoupled second-order equations and modal analysis of a general nonconservative system,” *Collection of Technical Papers - AIAA/ASME/ASCE/AHS/ASC Structures, Structural Dynamics and Materials Conference*, vol.5, pp.220–229, 2000.
- [127] A. Naess and T. Moan. *Stochastic Dynamics of Marine Structures*. Cambridge University Press, 2012.
- [128] S. Schubert. *Analysis of Coupling Techniques for Overset-Grid Finite-Volume Methods*, vol.M. 2019.
- [129] R. Sigbjörnsson and M. Mörch, “Spectral analysis of nonlinear wave load effects on offshore platforms,” *Engineering Structures*, vol.4, no.1, pp.29–36, 1982.
- [130] S. Fu, T. Moan, X. Chen, and W. Cui, “Hydroelastic analysis of flexible floating interconnected structures,” *Ocean Engineering*, vol.34, no.11-12, pp.1516–1531, 2007.
- [131] F.-I. G. Giske, K. A. Kvåle, B. J. Leira, and O. Øiseth, “Long-term extreme response analysis of a long-span pontoon bridge,” *Marine Structures*, vol.58, pp.154–171, 2018.
- [132] W. Chai and B. J. Leira, “Environmental contours based on inverse SORM,” *Marine Structures*, vol.60, pp.34–51, 2018.
- [133] F. M. Mazzolani, R. Landolfo, B. Faggiano, M. Esposito, F. Perotti, and G. Barbella, “Structural analyses of the submerged floating tunnel prototype in Qiandao Lake (PR of China),” *Advances in structural engineering*, vol.11, no.4, pp.439–454, 2008.
- [134] E. Morris, V. Szabo, G. Yang, and M. Isaacson, “Frequency domain analysis of a floating bridge,” *Coastal Structures*, 2003.



- 
- [135] F.-I. G. Giske. *Long-Term Extreme Response Analysis of Marine Structures Using Inverse Reliability Methods*. no. December, 2017.
- [136] J.-S. Hwang, D.-K. Kwon, and A. Kareem, “Frequency Domain State Space-Based Mode Decomposition Framework,” *Journal of Engineering Mechanics*, vol.145, no.7, p.04019051, 2019.
- [137] W. R. Inc., “Mathematica, Version 12.0,” 2019. Champaign, IL.
- [138] K. A. Kvåle, R. Sigbjörnsson, and O. Øiseth, “Modelling the stochastic dynamic behaviour of a pontoon bridge: A case study,” *Computers & Structures*, vol.165, pp.123–135, 2016.
- [139] O. Gaidai and A. Naess, “Extreme response statistics for drag dominated offshore structures,” *Probabilistic engineering mechanics*, vol.23, no.2-3, pp.180–187, 2008.
- [140] A. Totsky and K. Egiazarian, “Bispectrum-and bicoherence-based discriminative features used for classification of radar targets and atmospheric formations,” in *Topics in Radar Signal Processing*, pp.243–269, IntechOpen, 2018.
- [141] A. Masuda and Y.-Y. Kuo, “Bispectra for the surface displacement of random gravity waves in deep water,” *Deep Sea Research Part A. Oceanographic Research Papers*, vol.28, no.3, pp.223–237, 1981.
- [142] S. R. Massel. *Ocean surface waves: their physics and prediction*, vol.11. World scientific, 1996.